UNIVERSITY OF CALIFORNIA

Los Angeles

Modeling and Control of Particulate Processes:

High-Velocity Oxygen Fuel Thermal Spray and Protein Crystallization

A dissertation submitted in partial satisfaction of the

requirements for the degree Doctor of Philosophy

in Chemical Engineering

by

Dan Shi

2005

UMI Number: 3196339

INFORMATION TO USERS

The quality of this reproduction is dependent upon the quality of the copy submitted. Broken or indistinct print, colored or poor quality illustrations and photographs, print bleed-through, substandard margins, and improper alignment can adversely affect reproduction.

In the unlikely event that the author did not send a complete manuscript and there are missing pages, these will be noted. Also, if unauthorized copyright material had to be removed, a note will indicate the deletion.

UMI®

UMI Microform 3196339

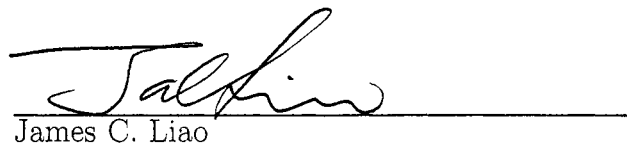Copyright 2006 by ProQuest Information and Learning Company.

All rights reserved. This microform edition is protected against unauthorized copying under Title 17, United States Code.

ProQuest Information and Learning Company
300 North Zeeb Road
P.O. Box 1346
Ann Arbor, MI 48106-1346

The dissertation of Dan Shi is approved.

Jane P. Chang

James C. Liao

Fernando G. Paganini

Panagiotis D. Christofides, Committee Chair

University of California, Los Angeles

2005

Contents

v

List of Figures

ix

List of Tables

ACKNOWLEDGEMENTS

I am grateful to my advisor, Professor Panagiotis D. Christofides, for his guidance, support, encouragement and confidence in me throughout the course of the project.

I would also like to thank Professor Jane P. Chang and Professor James C. Liao of the Department of Chemical Engineering, and Professor Fernando Paganini of the Department of Electrical Engineering for participating in my examination committee.

The friendship of the many wonderful graduate students of Professor Christofides' group is much appreciated. This includes Nael El-Farra, Yiming Lou, Mingheng Li, Prasenjit Ray, Dong Ni, Prashant Mhaskar, Stevan Dubljevic and Adiwinata Gani.

I would like to thank my parents. Their support was absolutely indispensable and I am indebted to them for all my accomplishments.

VITA

April 23, 1977   Born, Hangzhou, Zhejiang Province, China

1999   B. S., Control Science & Engineering
                Zhejiang University
                Hangzhou, Zhejiang, China

2001   M. S., Control Science & Engineering
                Zhejiang University
                Hangzhou, Zhejiang, China

2001-05   Doctoral candidate
                Department of Chemical Engineering
                University of California, Los Angeles, CA

PUBLICATIONS

Shi, D.; Zhang H.; Yang, L. "Time-delay Neural Network for the Prediction of Carbonation Tower's Temperature", *IEEE Transactions on Instrumentation and Measurement*, **52** 1125-1129, 2003.

Shi, D.; Li, M.; Christofides, P. D. "Diamond Jet Hybrid HVOF Thermal Spray: Rule-based Modeling of Coating Microstructure," *Industrial and Engineering Chemistry Research*, **43**, 3653-3665, 2004.

Shi, D.; El-Farra, N. H.; Li, M.; Mhaskar, P.; Christofides, P. D. "Predictive Control of Particle Size Distribution in Particulate Processes," *Chemical Engineering Science*, to appear.

Shi, D.; El-Farra, N. H.; Mhaskar, P.; Christofides, P. D. "Predictive Control of Crystal Size Distribution in Protein Crystallization," *Nanotechnology*, accepted.

Li, M.; Shi, D.; Christofides, P. D. "Diamond Jet Hybrid HVOF Thermal Spray: Gasphase and Particle Behavior Modeling and Feedback Control Design," *Industrial and*

Engineering Chemistry Research, **43**, 3632-3652, 2004.

Li, M.; Shi, D.; Christofides, P. D. "Model-based Estimation and Control of Particle Velocity and Melting in HVOF Thermal Spray," *Chemical Engineering Science*, **59**, 5647-5656, 2004.

Li, M.; Shi, D.; Christofides, P. D. "Modeling and Control of HVOF Thermal Spray Processing of WC-Co Coatings," *Powder Technology*, 2005. (in press)

Shi, D.; Mhaskar, P.; El-Farra, N. H.; Christofides, P. D. "Predictive Control of Crystal Size Distribution in Protein Crystallization," *Proceedings of the American Control Conference*, to appear, Portland, Oregon, 2005.

Shi, D.; El-Farra, N. H.; Li, M.; Mhaskar, P.; Christofides, P. D. "Predictive Control of Particle Size Distribution in Particulate Processes," *Proceedings of 2nd International Conference on Population Balance Modeling*, 17 pages, Valencia, Spain, 2004.

Shi, D.; Li, M.; Christofides, P. D. "Feedback Control of HVOF Thermal Spray Process: A Study of the Effect of Process Variations on Closed-loop Performance," *Proceedings of 8th International Symposium on Process Systems Engineering*, 1193-1198, Kunming, P. R. China, 2004.

Li, M.; Shi, D.; Christofides, P. D. "Modeling and Control of an Experimental HVOF Thermal Spray Process," *Proceedings of American Control Conference*, 3973-3979, Denver, Colorado, 2003.

ABSTRACT OF THE DISSERTATION

Modeling and Control of Particulate Processes:

High-Velocity Oxygen Fuel Thermal Spray and Protein Crystallization

by

Dan Shi

Doctor of Philosophy in Chemical Engineering

University of California, Los Angeles, 2005

Professor Panagiotis D. Christofides, Chair

Particulate processes play an important role in a number of process industries including agricultural, chemical, food, minerals and pharmaceuticals. By some estimates, 60% of the products in the process industries are manufactured as particulates with an additional 20% using powders as ingredients. Examples of particulate processes include the crystallization of proteins for pharmaceutical applications, the emulsion polymerization reactors for the production of latex, and the thermal spray processing of nanostructured coatings used as thermal and mechanical barriers. From a control point of view, the distinguishing feature of particulate processes is that they give rise to nonlinear control problems that involve the regulation of the particle size distribution (PSD) by using a finite number of control actuators and measurement sensors. This is because the shape of the PSD strongly influences the product properties.

This doctoral thesis focuses on modeling and control of two important classes of

particulate processes: high-velocity oxygen fuel (HVOF) thermal spray and protein crystallization. In particular, the first part of this thesis focuses on the modeling and feedback control of the HVOF thermal spray processing of nanostructured coatings; this research work is motivated by the superior qualities of nanostructured coatings and high sensitivity of the coated material to arbitrary variation in the operating environment. The second part of this thesis presents a novel and practical framework for the synthesis of practically-implementable predictive controllers for regulation of particle size distribution (PSD) in particulate processes.

Specifically, in the area of modeling and control of HVOF thermal spray, we developed a comprehensive multiscale model, which includes continuum type differential equations that describe the evolution of gas and particle temperature and velocity, and a rule-based stochastic simulator that predicts the evolution of coating microstructure. Based on the process model, a detailed comprehensive parametric analysis is carried out to study the relationship between the key process parameters and the particle inflight behavior as well as the resulting coating properties. This analysis shows that the particle velocity and melting ratio play a very important role in the formation of coating microstructure, which in turn, can be almost independently adjusted by manipulating the combustion pressure and the fuel/oxygen ratio. To develop a feedback controller that can be readily implemented in practice, the control problem is formulated as the one of regulating volume-based averages of the melting ratio and velocity of the particles at the point of impact on the substrate by directly manipulating the flow rate of fuel, oxygen and air at the entrance of the HVOF gun. A multivariable model-based feedback control system is developed and applied to a fundamental process model. Closed-loop simulations demonstrate that the proposed control system is effective in driving the particle velocity and melt-

ing ratio at impact to set-point values and is also robust with respect to various disturbances in the operating environment.

In the second part of this thesis, we focus on the development and application of predictive-based strategies for control of PSD in continuous and batch particulate processes described by population balance models (PBMs). The control algorithms are developed on the basis of reduced-order models that capture the dominant dynamics of the particulate process, utilize measurements of principle moments of the PSD, and are tailored to address different control objectives for the continuous and batch processes. For continuous particulate processes, we consider the control objective of asymptotic stabilization under constraints and develop a hybrid predictive control strategy that employs logic-based switching between model predictive control (MPC) and a fall–back controller with a well-defined stability region. The strategy is shown to provide a safety net for the implementation of MPC algorithms to particulate processes, and is successfully used to stabilize a continuous crystallizer at an open-loop unstable steady-state. For batch particulate processes, the control objective is to achieve PSD with desired characteristics subject to both manipulated input and product quality constraints. An optimization-based predictive control strategy that incorporates these constraints explicitly in the controller design is formulated. The developed control methods are successfully applied via computer simulations to batch cooling crystallizers which produce inorganic and protein (tetragonal hen egg-white lysozyme) crystals.

Chapter 1

Introduction

1.1 High-velocity oxygen fuel thermal spray process

1.1.1 Nanostructured coatings

Nanostructured (also called nanoscale, nanophase or nanocrystalline) materials are materials with grain sizes less than about 100 nm, and are generally obtained by processing of nanosize powders. Currently, there is a great interest in the understanding and processing of nanostructured materials which stems from the cost-effective production of high-quality nanosize powders as well as the discovery that such materials have properties superior to those of conventional bulk materials, including strength, hardness, ductility, sinterability, size-dependent light absorption, reactivity, etc. (see, for example, [58, 69, 76, 101, 194, 156, 3, 193, 89, 90, 100, 88, 166].) The superior properties of nanostructured materials motivate their use in a wide variety of applications such as protective coatings for heat engines and gas turbines, hard materials for machine tools, ductile ceramics, catalysts, new electronic and optical devises, etc.

With prompt advances in the production of high quality unagglomerated nanoscale

powders, including atomization, colloidal precipitation, mechanical milling, and vapor phase nucleation and growth (see, for example, [135, 136, 190, 197]), the focus of nanostructured materials research is now shifting from synthesis to processing, for example, the fabrication of nanostructured coatings using the so-called thermal spray technology [101, 68, 1]. Figure 1.1 shows two typical dark field Transmission Electron Microscopy (TEM) images of the nanocrystalline CoCr coating prepared by plasma thermal spraying [101] and the nanocrystalline Ni coating prepared by high-velocity oxygen fuel (HVOF) thermal spraying [1], illustrating an average grain size smaller than 100 nm. Compared to the traditional counterparts, the nanostructured coatings exhibit superior qualities in several aspects including increased hardness and strength, improved ductility, and enhanced diffusivity and sinterability [182, 81, 97, 98]. Nowadays, the nanostructured coatings are widely used in many industries as thermal-barrier, wear-resistant and corrosion-protective surface layers to extend product life, increase performance and reduce production and maintenance costs. Other primary uses of nanostructured coatings include dimensional restoration, maintaining precise clearances, and modifying thermal and electrical properties.

1.1.2 Thermal spray process

In the simplest terms possible, the thermal spray processes represent a group of particulate deposition processes in which materials, in powder or wire form, are propelled and heated in a gas/plasma stream and deposited on a given substrate in a molten or semi-molten state, and the coating microstructure results from the solidification and sintering of the particles [141]. Thermal spray processes provide a low-cost and energy-efficient route for the processing of nanostructured coatings be-
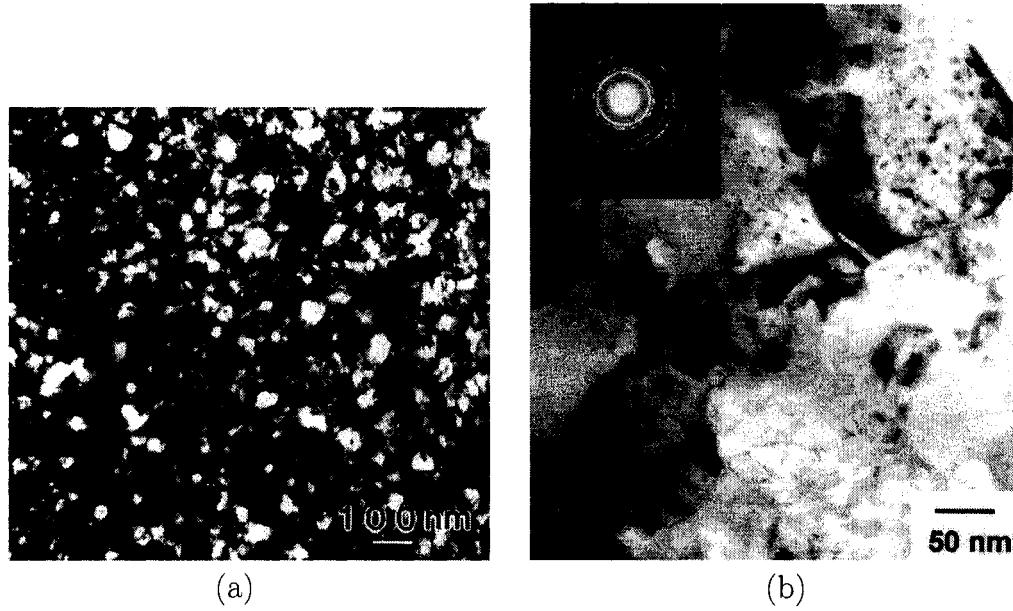
Figure 1.1: TEM dark images of (a) plasma sprayed nanocrystalline CoCr and (b) HVOF sprayed nanocrystalline Ni coatings [101, 1].

cause they require significantly fewer manufacturing steps than conventional welding processes. They are also characterized by zero dilution of the substrate as a result of mechanical bonding, the ability to apply thin coatings, and a high rate of area coverage, compared to arc welding processes. Thermal spray processes of most commercial interest include high-velocity oxygen fuel (HVOF) and atmospheric plasma arc spraying (PAS) (see Figure 1.2 for a schematic of these two processes). In the HVOF thermal spray process, the fuel is burnt with oxygen at a high pressure and generate a sonic or supersonic exhaust jet, which heats up the powders and propels them to the substrate. Currently, there is an increasing interest in the HVOF thermal spray processing of nanostructured coatings, which owes to its unique process characteristics - very high gas/particle velocity and relatively low gas/particle temperature, as compared to those in plasma spray process. On the one hand, extremely high particle velocity helps to densify the coating and to increase the deposition rate.

3

Combustion
Chamber Nozzel Barrel

Oxygen

Fuel

Powder
Injection

Cooling
Water In

Cooling
Water Out

Spray
Stream

Spray
Deposit

Prepared
Substrate

(a)

Tungsten
Cathode

Nozzle
Copper
Anode

Plasma

Spray
Deposit

Spray
Stream

Electric Arc

Arc gas

Electrical (-)
Connection
and Water Out

Electrical (+)
Connection
and Water In

Powder and
Carrier Gas

Prepared
Substrate

(b)
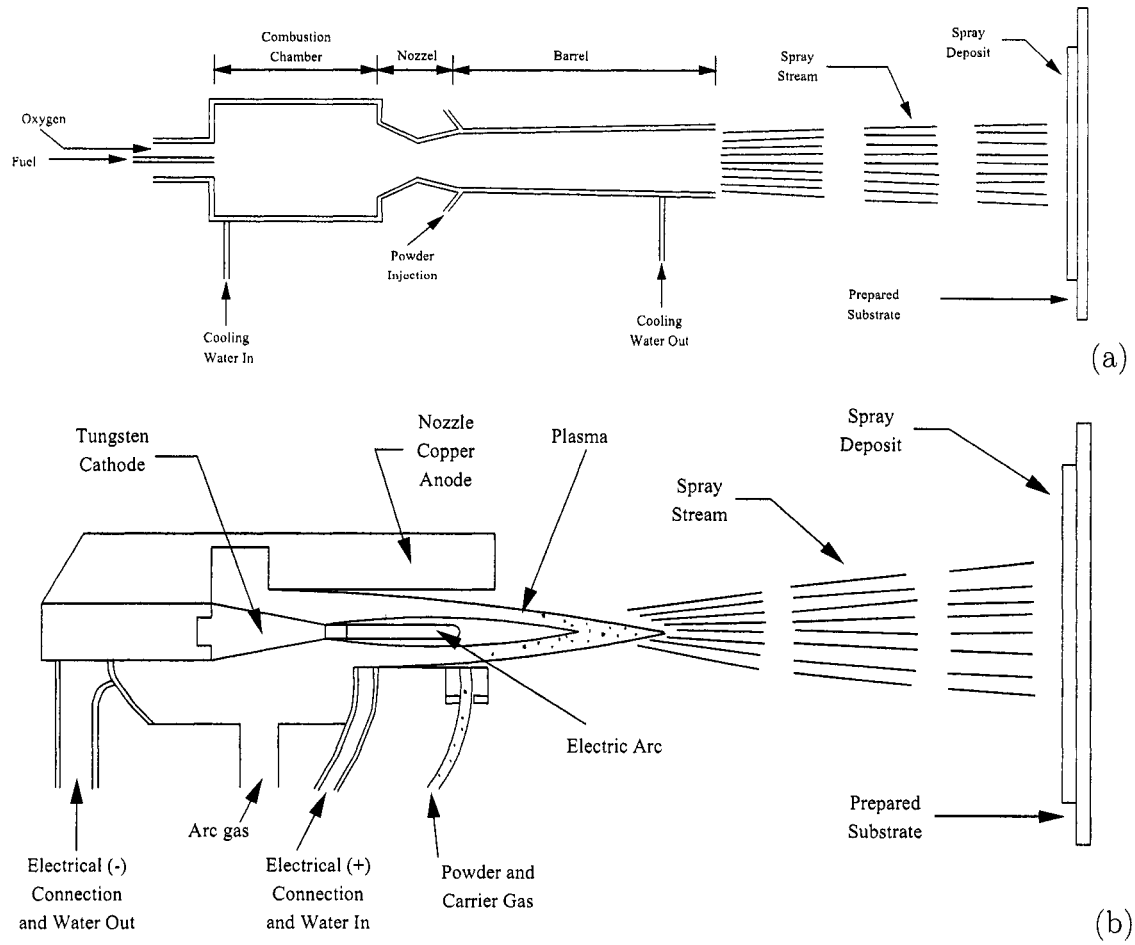
Figure 1.2: (a) HVOF thermal spray processing and (b) plasma thermal spray processing.

On the other hand, very short residence time in the relatively low temperature gas flame makes the powder particles highly plastic and superheating or vaporization is prevented [22, 24].

Figure 1.3 shows a schematic diagram of the Diamond Jet hybrid HVOF thermal spray gun (Sulzer Metco, Westbury, NY), which is currently used in industry. In this process, the premixed fuel (typically propylene or hydrogen) and oxygen are fed from the annular gap to the air cap (also referred to as convergent-divergent nozzle), where they react to produce high temperature combustion gases. The exhaust gases, together with the air injected from the annular inlet orifice, expand through the nozzle

4
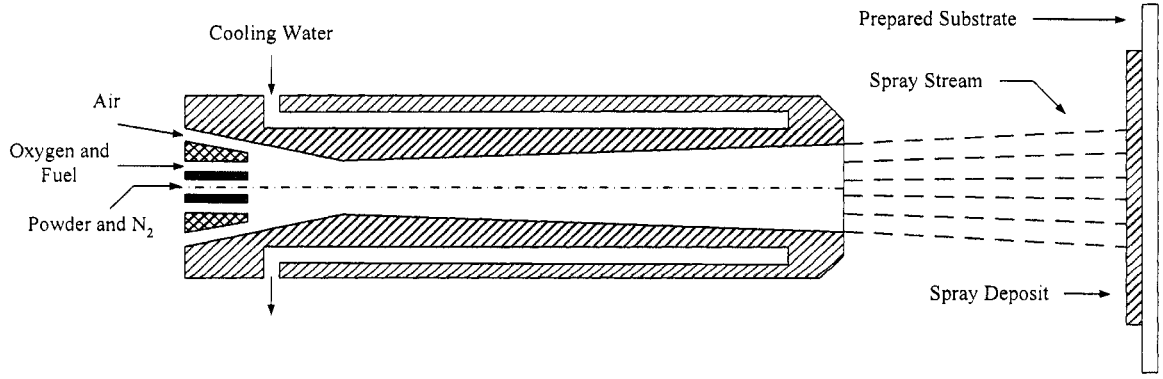
Figure 1.3: A schematic of the Diamond Jet hybrid HVOF thermal spray process.

to reach supersonic velocity. The air cap is water-cooled to prevent from being melted. The powder particles are injected from the central inlet hole using nitrogen as the carrier gas. Consequently, rapid momentum and heat transfer between the gas and the powder particles leads to acceleration and heating of the powder particles. The molten or semi-molten particles exit the air cap and move towards the substrate. The particles hit the substrate, cool and solidify, forming a thin layer of dense and hard coating. The typical operating conditions and main characteristics of the Diamond Jet Hybrid HVOF thermal spray process are given in Table 1.1. It should be noted that although the gain size of nanostructured coatings is about 100 nm, the powders used for coating processing are actually nanostructured agglomerates whose sizes are typically on the magnitude of 10 μm (see Figures 1.4 and 1.5 for SEM images of the flake-shaped Cu-10 wt.% Al agglomerates produced by methanol- and cryo-milling and TEM images of the corresponding TEM images illustrating nanosize grains). This is because, in the thermal spray processing, very small particles usually follow the gas stream and do not stick on the substrate [110].
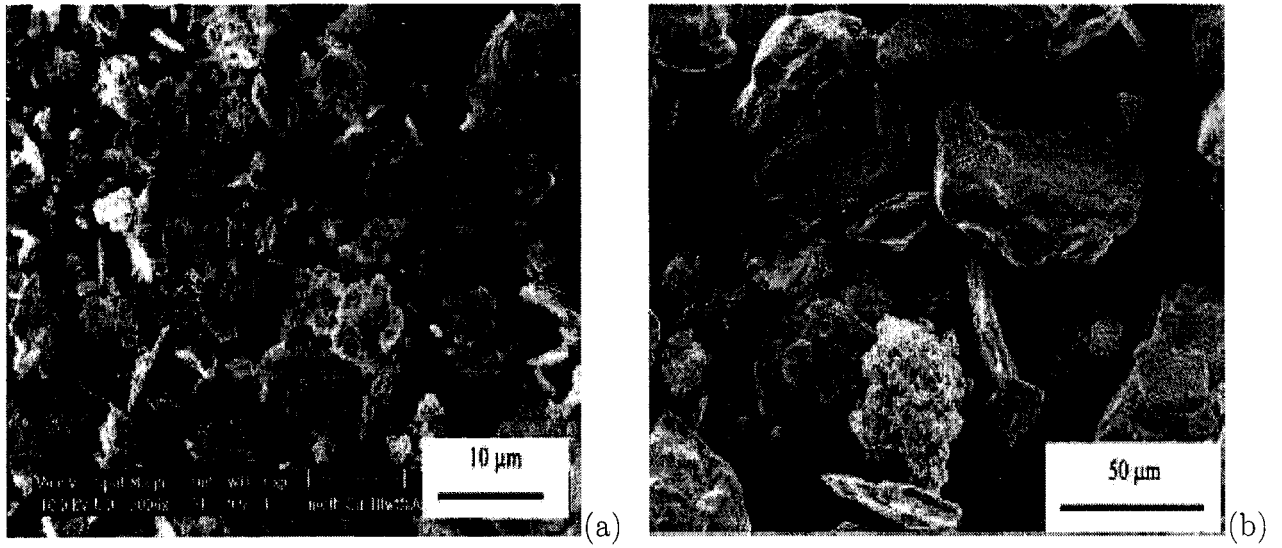
Figure 1.4: SEM images of Cu-10 wt.% Al powders milled for 10 hours in (a) methanol, and (b) liquid nitrogen [99].
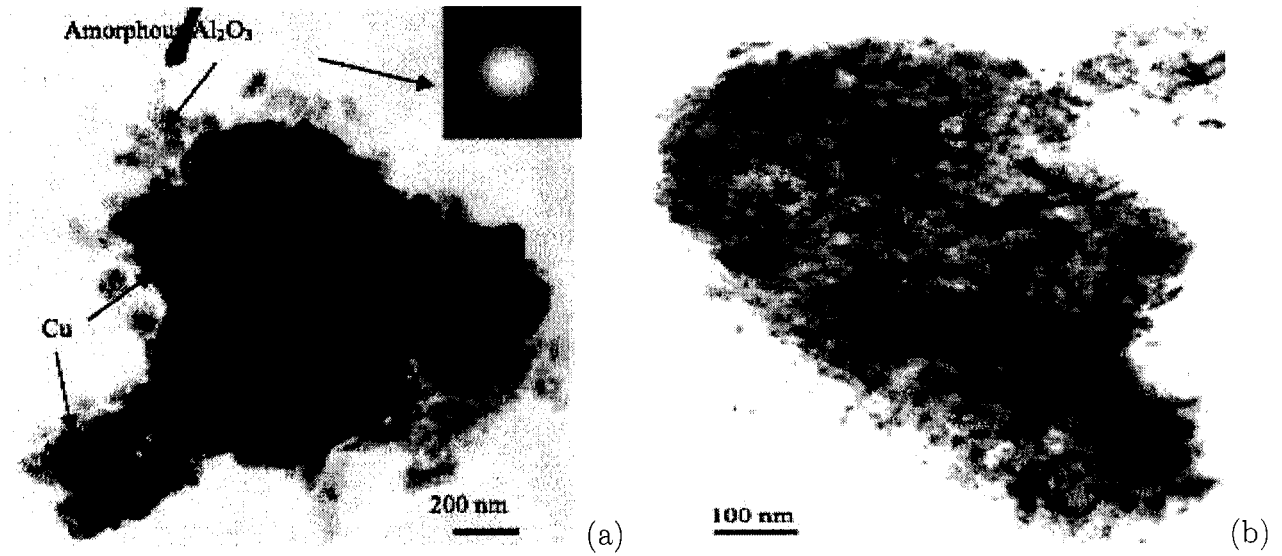
Figure 1.5: Bright field TEM images of Cu-10 wt.% Al powders for 20 hours in (a) methanol, and (b) liquid nitrogen [99].

Table 1.1: Typical operating conditions and main characteristics of the Diamond Jet Hybrid HVOF thermal spray process.

Typical operating conditions		Main process characteristics	
Gas flow rate	18 g/s (12 l/s)	Flame temperature	2800 ^{0}C
Powder feed rate	20 - 80 g/min	Exit Mach number	2
Powder size	5 - 45 μm	Exit gas velocity	2000 m/s
Coating thickness	100 - 300 μm	Deposition efficiency	70 %
Spray distance	150 - 300 mm	Coating porosity	1 - 2 %

1.1.3 Motivation for process control

Although applications of thermal spray processes as a means of material processing in many industries have been widely used in the past three decades, it is only recently that there have been great interests in the processing of nanostructured materials [22]. In order for these practical applications to be realized in a broad industrial scale, the basic engineering problem of controlled processing of the nanopowders into useful nanostructured materials has to be addressed. Whereas thermal spray processing provides a natural way for the processing of nanopowders to useful nanostructured materials with desired properties, for the most part, they have been developed through costly trial and error procedures. In many cases, a general knowledge of the overall behavior has been attained, but fundamental understanding and critical parameters that affect the final product are not clearly defined. Consequently, the final product yield and precise regulation of final product properties has been low due to the lack of tight monitoring and control of the critical parameters. For example, the work of Khor et al. [91] shows that the particle melting ratio plays a very important role in the formation of coating microstructure and resulting coating properties (see Figure 1.6). Therefore, this parameter should be precisely controlled

7

during deposition process to achieve coating uniformity.

Over the last decade, the need to optimally design and operate thermal spray processes has motivated significant research on the development of fundamental mathematical models for thermal spray processes that explicitly account for various physico-chemical phenomena and the dynamic behavior of various process components. Specifically, fundamental models have been developed targeting the complex gas/particle flow behavior involved in the internal and external flow field of the HVOF gun (see review papers [175, 22]); molten droplet formation, motion, impact and deposition [119, 118, 11, 196]; droplet solidification, microstructure development, surface roughness and coating porosity [181, 81, 14, 105, 188]; phase transformations of nanocrystalline powders [28]; and the relationship between the nanostructure and the mechanical properties of the end-product [61, 15, 14, 37]. In addition, research has been carried out in the integration of the detailed models of the aforementioned components to develop general simulators that describe the behavior of entire thermal spray processes [199, 110].

These modeling efforts have been complemented with significant research on the development of intelligent measurement sensors for thermal spray process monitoring including laser light scattering techniques for ensemble and single particle sizing [9, 164, 6, 7, 72, 9, 80, 102, 16, 73, 74, 167, 104, 18]; optical methods for particle velocity [187, 50] and particle temperature [140, 48] and measurement of melt flowrate [62, 73, 74, 104]. Comprehensive reviews of results in this area can be found in [80, 72, 102, 13]. An effort to integrate real-time diagnostic techniques with simple control schemes has been done in the context of expert systems (e.g., [176]). However, expert systems provide simple supervisory control and cannot deal with the critical issue of precise control of the size distribution of the droplets impinging on the substrate
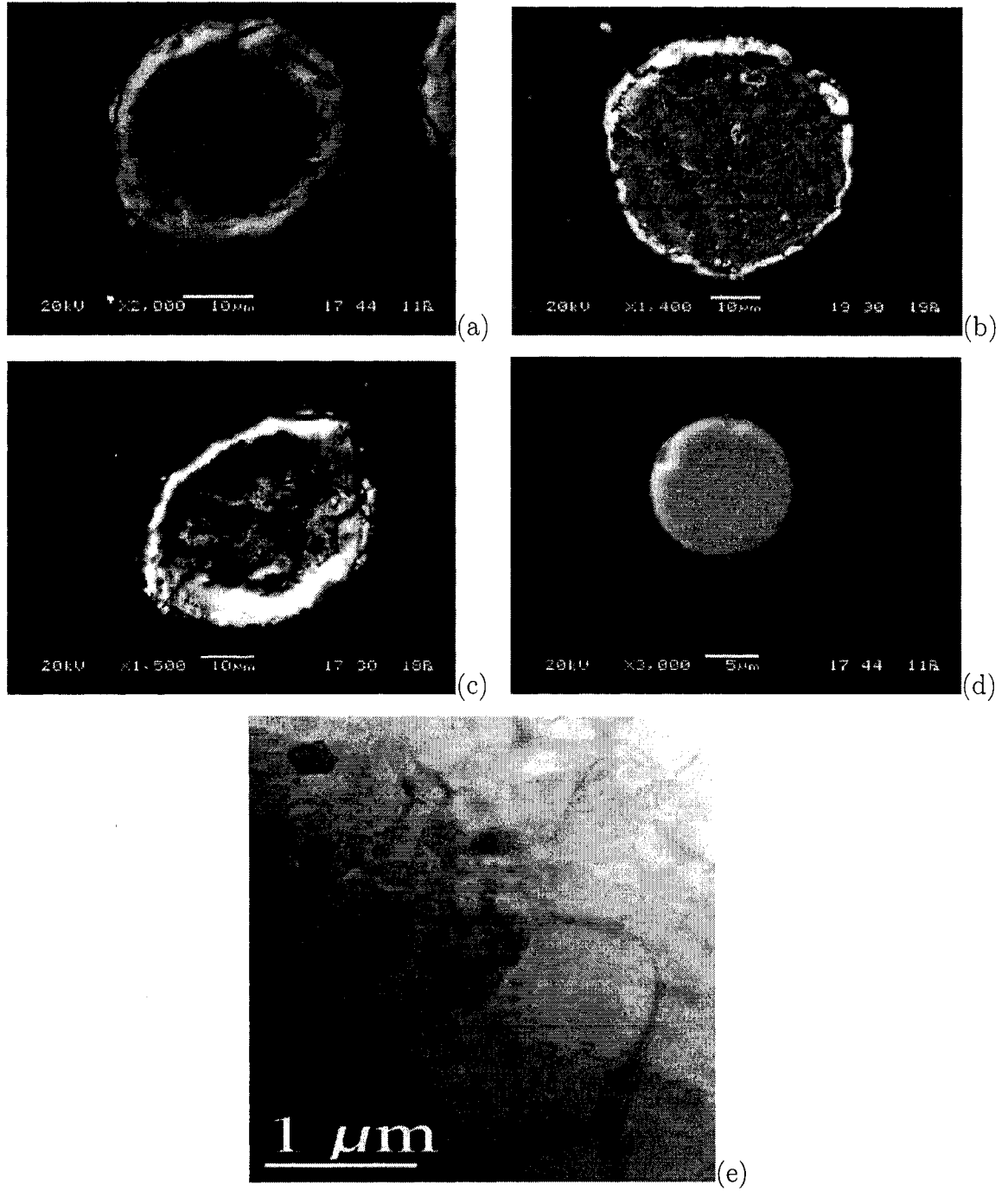
Figure 1.6: Cross-sectional morphology of four HVOF sprayed hydroxyapatite (HA) particles with different melting degrees and a TEM image of the as-sprayed HA coating showing the interface between melted and unmelted parts of HA splat [91].

which affects the structure and end-properties of the nanostructured coatings.

In order for HVOF thermal spray process to be widely used in industry for the processing of nanostructured coatings, it is important to achieve excellent real-time diagnosis and control of the processing stage which will allow to obtain coatings with nanostructures that yield the desired thermal and mechanical properties. Despite the recent progress on modeling of the various phenomena that affect droplet motion, deposition, solidification and microstructure development in HVOF thermal spray process, at this stage, there exists no systematic framework for integrated on-line diagnosis and control of the HVOF thermal spray processing which will be capable of achieving precise regulation of the microstructure and ultimate mechanical properties of the sprayed materials and coatings. Since the incorporation of the advanced feedback control on thermal spray processes has been reported to lead to significant improvements in their operation and performance [2, 125], it is of great significance to close this gap by integrating fundamental models that accurately describe the inherent relationships between the coating micro- and nano-structure and the processing parameters (such as substrate surface condition, gas flow rate, and fuel/oxygen ratio etc.) with on-line state-of-the-art diagnostic techniques and advanced nonlinear control algorithms, to develop high-performance real-time computer control systems for thermal spray processes which on-line manipulate process variables flow rate, gas pressure, spray motion and angle, substrate motion, to regulate the microstructure and end-properties of the deposits. In addition, incorporation of advanced real-time diagnosis and control schemes into thermal spray processes is expected to reduce operational cost and environmental impact, and improve end-product properties and yield. Recent efforts in this direction have mainly focused on diagnostics and control of plasma thermal spray (see [49]); the reader may also refer to [133] for a discussion

of various process optimization and control issues.

1.2 Particle size distribution in particulate processes

1.2.1 Particulate processes

Particulate processes are prevalent in a number of process industries including agricultural, chemical, food, minerals, and pharmaceuticals. By some estimates, 60% of the products in the chemical industry are manufactured as particulates with an additional 20% using powders as ingredients. Examples of particulate processes include the crystallization of proteins for pharmaceutical applications, the emulsion polymerization reactors for the production of latex, and the titania powder aerosol reactors used in the production of white pigments. Figure 1.7 shows a schematic illustration of a batch particulate process. One of the key attributes of particulate systems is the co–presence of continuous phase and dispersed phase, which leads to the occurrence of physico–chemical phenomena such as particle nucleation, growth, coagulation, and breakage which are absent in homogeneous processes and lead to a distributed characterization of the physical and chemical properties of the particulate product such as particle size, shape, morphology, porosity, molecular weight, etc.

It is now well understood that the physico–chemical and mechanical properties of materials made with particulates are strongly dependent on the characteristics of the corresponding particle size distribution (PSD). For example, a nearly mono–disperse PSD is required for titania pigments to obtain the maximum hiding power per unit mass. Also, in coatings the product's composition, molecular weight and particle size distributions often need to be maintained in specific ranges to ensure the coating has a desired level of film formation, film strength, and gloss. In all of these instances, the PSD provides the critical link between the product quality indices and the operating

Figure 1.7: Schematic illustration of a batch particulate process.

process variables; and, therefore, the ability to effectively manipulate the PSD is essential for our ability to control the end product quality in these processes. In this light, the problem of synthesizing and implementing high-performance model-based feedback control systems on particulate processes to achieve PSDs with desired characteristics has significant industrial value.

The mathematical models of particulate processes are typically obtained through the application of population, material and energy balances and consist of systems of nonlinear partial integro-differential equations that describe the evolution of the PSD, coupled with systems of nonlinear ordinary differential equations (ODEs) that describe the evolution of the state variables of the continuous phase. There is an extensive literature on population balance modeling, numerical solution, and dynamical analysis of particulate processes, see, for example, [153, 142, 124, 53, 57, 150, 75, 95, 79, 154, 152]; see also [30] for further details and references. Early work on control of particulate processes focused mainly on the understanding of fundamen-

tal control-theoretic properties of PBMs [170], and the application of conventional control schemes to crystallizers and emulsion polymerization processes [171, 158, 39], and the references therein. More recently, the realization that PBMs – owing to their infinite-dimensional nature – cannot be used directly for the synthesis of practically implementable controllers, has motivated significant research work on the development of a general order reduction procedure, based on combination of the method of weighted residuals and approximate inertial manifolds, which allows deriving low-order ODE approximations that capture the dominant dynamics of particulate processes and can, therefore, serve as an appropriate basis for the design of low-order controllers that can be readily implemented in practice [26]. This approach subsequently laid the foundation for the development of a systematic framework for solving a number of important control problems for particulate processes, including the problem of dealing with the highly nonlinear behavior, e.g., owing to complex growth, nucleation, agglomeration and breakage mechanisms, and the Arrhenius dependence of nucleation laws on solute concentration in crystallizers [26], the problem of model uncertainty [27], and the problem of control under actuator constraints [43].

1.2.2 Protein crystallization process

Proteins play a vital role in most biological processes. In addition to constructing large-scale biological structures, such as muscle fibers, smaller protein molecules can function as antibodies, which help the immune system to destroy invading substances like viruses and bacteria, and enzymes, which can catalyze the synthesis of complex compounds, the transformation of complex substances into simpler ones, or the generation of energy in organisms. A protein molecule is a chain of amino acids that are linked by peptide bonds formed by dehydration synthesis. Many pharmaceuticals act

by binding to and blocking an active site (the active site is a region on the protein composed of some of the protein's amino acids which have a specific three dimensional arrangement to which a molecule can bind) of a protein [160]. The three-dimensional arrangement of amino acids, especially, at the active site, determines the specific biological function of the protein molecule. Figure 1.8 shows the space-filling model of hen egg-white (HEW) lysozyme molecule and the tetragonal form of HEW lysozyme crystal. HEW lysozyme is composed of 129 amino acids, with a molecular weight of 14,388.
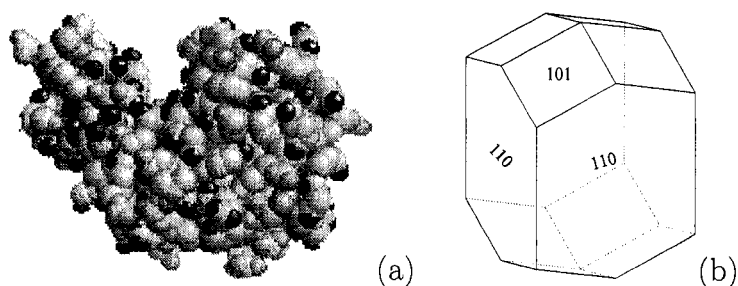
Figure 1.8: Hen egg-white lysozyme: (a) the space-filling model of the molecule and (b) the structure of the tetragonal HEW lysozyme crystal.

X-ray and neutron diffraction techniques are the only available methods that can be used to obtain structural information of proteins with molecular weight over 20,000. To be able to study the structure of proteins using these techniques, large protein crystals of high structural perfection, typically with diameters of several hundred microns, are needed. Extensive research studies, using model proteins, such as ferritin, insulin, haemoglobin and lysozyme, that are able to crystallize easily under normal operating conditions, have focussed on growing large protein crystals of high structural perfection under various operating conditions, including low gravity [17], different pressure conditions [138], flow condition of the solution [149], purity [186], temperature [35] and concentrations of precipitants and buffers [148, 111].

In addition, numerous research studies have considered the problem of modeling of protein nucleation [54, 147] and growth [42, 96, 51]. The reader may also refer to [127, 163, 192, 185] for excellent reviews on this subject. Among these model proteins, the tetragonal form of HEW lysozyme is most popular and widely used [19]. HEW lysozyme is composed of 129 amino acids, with a molecular weight of 14,388. It is a naturally occurring enzyme, and has antibacterial activity against gram-positive bacteria.

The experimental studies not only benefit the determination of the protein structure, but also provide, through an understanding of the nucleation and growth mechanism of protein crystallization, a means for determining the operating conditions necessary to achieve protein crystals of desired properties, which can often be expressed in the form of a desired size distribution. In the pharmaceutical industry, the size distribution of the protein crystal is a very critical variable and in many applications a predetermined, typically narrow, crystal size distribution is necessary in order to guarantee a desired drug delivery performance.

Protein crystals intrinsically grow much slower than most inorganic crystals at the same supersaturation [161]. This is probably one of the reasons why it has been widely believed that implementation of advanced control algorithms is not important for growing perfect crystals in protein crystallization. However, experimental results show that even in protein crystallization processes, certain growth conditions lead to crystal defect formation (for example, the structural defect density increases when the growth rate is relatively high [132]), which necessitates appropriately choosing the operating conditions. Furthermore, for a given choice of operating conditions, it is critical to implement real-time control to mitigate the affect of disturbances that might throw the operating conditions off the desired values.

1.2.3 Motivation of predictive control

In the operation of particulate processes, constraints typically arise due to physical limitations on the capacity of control actuators and/or desired restrictions on the process state variables, such as temperature and certain properties of the PSD (e.g., crystal concentration and total particle size), in order to meet some safety or product quality requirements. In current industrial practice, the achievement of optimal performance, subject to input and state constraints, relies to a large extent on the use of model predictive control (MPC) policies which are well known for their ability to handle multi-variable interactions, constraints, and optimization requirements, all in a consistent, systematic manner. Unlike open-loop model-based optimal control policies (where the optimal operating conditions are calculated off-line), in MPC, the control action is computed by solving repeatedly, on–line, a constrained optimization problem at each sampling time. Owing to this, MPC has the ability to suppress the influence of external disturbances and tolerate model inaccuracies (because of the use of feedback) and force the system to follow the optimal trajectory that respects constraints on the operating conditions.

Significant previous works have focused on PSD control in the batch crystallizers [153, 195, 10]. [137] derived an open-loop optimal control strategy where the objective function involves maximization of the crystal size and the cooling curve is the decision variable. [130] developed a method for assessing parameter uncertainty and studied its effects on the open-loop optimal control strategy, which maximized the weight mean size of the product. [201] developed an on-line optimal control methodology for a seeded batch cooling crystallizer to improve the product quality expressed in terms of the mean size and the width of the distribution. [78] designed a hierarchical multiobjective strategy to control the PSD in semi-batch emulsion polymerization.

In these previous works, most efforts were focused on the open-loop optimal control of the batch crystallizer, i.e., the optimal operating condition was calculated off-line and based on mathematical models. The successful application of such a control strategy relies, to a large extent, on the accuracy of the models.

1.3 Research objective and thesis structure

The objective of the present research is to develop a novel and practical framework for the modeling and control of particulate processes, including HVOF thermal spray and protein crystallization processes. First, we developed a computational methodology to precisely control the coating micro- or nano-structure produced by HVOF thermal spray process, by manipulating macro-scale operating conditions such as the gas flow rate and spray distance, etc. The major challenge on this problem lies in the development of multiscale models linking the macroscopic scale process behavior (i.e., gas dynamics and particle inflight behavior) and the microscopic scale process characteristics (evolution of coating microstructure), and the integration of models, measurements, and control theory to develop measurement/model-based control strategies [29]. The underlying multiscale behavior of the HVOF process is shown in Figure 1.9 [112]. On one hand, the microstructure of thermally sprayed coatings results from the deformation, solidification and sintering of the deposited particles, which are dependent on the substrate properties (e.g., substrate temperature) as well as the physical and chemical state (e.g., temperature, velocity, melting ratio, and oxidant content) of the particles at the point of impact on the substrate. On the other hand, the particle inflight behavior, however, is coupled with the gas dynamics, which can be manipulated by adjusting operating conditions such as the total gas flow rate and the fuel/oxygen ratio. While the macroscopic thermal/flow field can be
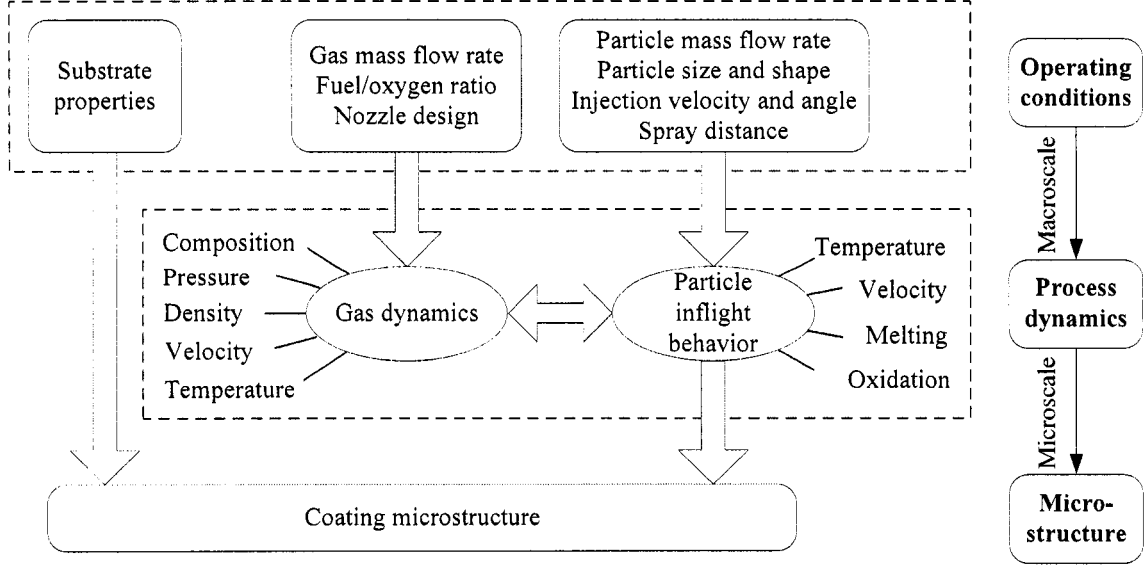
Figure 1.9: Multiscale character of the HVOF thermal spray process [112].

readily described by continuum type differential equations governing the compressible two-phase flow, the process of particle deposition is stochastic and discrete in nature, and thus, it can be best described by stochastic simulation methods [94]. By manipulating macroscopic operating conditions, such as gas flow rate, fuel/oxygen ratio, and spray distance, one can adjust gas and particle dynamics, and eventually, control coating microstructure.

To address these problems, we conducted research in the following areas:

- **Diamond Jet Hybrid HVOF Thermal Spray Process: Control-relevant Modeling and Analysis of Gas-phase and Particle Behavior [112]**

This work focuses on the extensive control relevant parametric analysis of the industrial HVOF thermal spray process. At this point, it is important to note that a comprehensive computational fluid dynamic (CFD) model is not practical for the development of control system to be implemented in practice. (However, for off-line

18

optimization and analysis, a comprehensive CFD based modeling work will be presented at the end of this thesis.) To address this issue, a one-dimensional model for the industrial Diamond Jet Hybrid HVOF thermal spray process is initially developed. The model describes the evolution of the gas thermal and velocity fields, the motion and temperature of agglomerate particles of different sizes, and explicitly accounts for the effect of powder size distribution. A contribution of this work is to take into account the particle melting behavior during flight. In addition to providing useful insight into the in-flight behavior of different size particles, the model is used to make a comprehensive parametric analysis of the HVOF process. This analysis allows us to systematically characterize the influence of controllable process variables such as combustion pressure, oxygen/fuel ratio, as well as the effect of powder size distribution, on the values of particle velocity and temperature (or melting ratio) at the point of impact on substrate. Specifically, the study shows that the gas momentum flux (ρu^2) and the gas temperature, which provide driving forces for particle motion and particle heating, can be almost independently adjusted by manipulating the chamber pressure and the fuel oxygen ratio. These findings are consistent with existing experimental studies and set the basis for the formulation of the control problem for the HVOF thermal spray process.

- **Diamond Jet Hybrid HVOF Thermal Spray Process: Rule-based Modeling and Analysis of Coating Microstructure [173]**

This work focuses on the computational modeling and simulation of microstructure of coatings prepared by the industrial Diamond Jet Hybrid HVOF thermal spray process. Based on the understanding of coating structure and mechanisms of pore formation inside of the coating obtained from experimental studies, a stochastic simulation procedure is used to explore the evolution of the microstructure of the coatings.

In the coating growth model, the velocity, temperature and degree of melting of particles hitting on the substrate are determined by a previously developed mathematical model [112] describing gas and particle behavior, and the complex characteristics of the thermally sprayed coatings are captured by applying certain basic rules that encapsulate the main physical features of the deposition process. In addition to providing useful insight into the pore formation and coating growth, the model is used to make a comprehensive parametric analysis, which allows us to systematically characterize the influence of operating conditions, such as the gas flow rate, spray distance, as well as the effect of particle size, on the particle melting behavior, coating porosity, surface roughness and deposition efficiency. Comparison of simulation results and experimental studies shows that the proposed model can reasonably predict the relationship between macroscopic processing conditions and coating microstructure.

To control the particle size distribution in particulate processes, predictive-based strategies are developed and implemented to control continuous and batch crystallizers described by population balance models. Because of the high dimensionality (population balance model is typically described by PDE) and nonlinearity (such as the nonlinear dependence of nucleation rate and growth rate on the solute concentration), the population balance model cannot be used in the controller design directly, therefore, model reduction techniques must be introduced for the purpose of controller design. Furthermore, the controller design should also explicitly incorporate the constraints on the manipulated input variables (which reflect physical limitations of control actuators) and on the process state variables (which reflect performance considerations). Under the predictive control strategy, a constrained optimization problem is solved repeatedly at each sampling time. The practical implementation of predictive control to control the PSD in particulate processes is limited by: (1) the

computational difficulties of solving a nonlinear and nonconvex optimization problem at each time step, and (2) the difficulty of characterizing, *a priori*, the set of initial conditions starting from where a given nonlinear predictive controller is guaranteed to be feasible and/or stabilize continuous particulate processes. To address these problems, we conducted research in the following areas:

- **Predictive Control of Particle Size Distribution in Particulate Processes [172]**

In this work, we focus on the development and application of predictive-based strategies for control of PSD in continuous and batch particulate processes described by population balance models (PBMs). The control algorithms are designed on the basis of reduced-order models, utilize measurements of principle moments of the PSD, and are tailored to address different control objectives for the continuous and batch processes. For continuous particulate processes, we develop a hybrid predictive control strategy to stabilize a continuous crystallizer at an open-loop unstable steady-state. The hybrid predictive control strategy employs logic-based switching between MPC and a fall–back bounded controller with a well-defined stability region. The strategy is shown to provide a safety net for the implementation of MPC algorithms with guaranteed stability region. For batch particulate processes, the control objective is to achieve a final PSD with desired characteristics subject to both manipulated input and product quality constraints. An optimization-based predictive control strategy that incorporates these constraints explicitly in the controller design is formulated and applied to a seeded batch cooling crystallizer example. The strategy is shown to be able to reduce the total volume of the fines by 13.4% compared to a linear cooling strategy, and is shown to be robust with respect to modeling errors.

- **Predictive Control of Crystal Size Distribution in Protein Crystallization [174]**

This work focuses on the modeling, simulation and control of a batch protein crystallization process that is used to produce the crystals of tetragonal hen egg-white (HEW) lysozyme. First, a model is presented that describes the formation of infinitesimal size protein crystals via nucleation and the subsequent growth of the crystals via condensation, and predicts the temporal evolution of the crystal size distribution in the size range of $0 - 300$ μm. To this end, existing experimental data are used to develop empirical models of the nucleation and growth mechanisms of the tetragonal HEW lysozyme crystal. The developed growth and nucleation rate expressions are used within a population balance model to simulate a batch crystallization process that produces the tetragonal HEW lysozyme crystals. Then, model reduction techniques are used to derive a reduced-order moments model for the purpose of controller design. Online measurements of the solute concentration and reactor temperature are assumed to be available, and a Luenberger-type observer is developed to estimate the moments of the crystal size distribution based on the available measurements. A predictive controller, that uses the available state estimates, is designed to achieve the objective of maximizing the volume-averaged crystal size while respecting constraints on the manipulated input variables (which reflect physical limitations of control actuators) and on the process state variables (which reflect performance considerations). Simulation results demonstrate that the proposed predictive controller is able to increase the volume-averaged crystal size by 30% and 8.5% compared to Constant Temperature Control (CTC) and Constant Supersaturation Control (CSC) strategies, respectively, while reducing the number of fine crystals produced. Furthermore, a comparison of the crystal size distributions (CSDs) indicates that the

product achieved by the proposed predictive control strategy has larger total volume and lower polydispersity compared to the CTC and CSC strategies. Finally, the robustness of the proposed method with respect to plant-model mismatch is evaluated. The proposed method is demonstrated to successfully achieve the task of maximizing the volume-averaged crystal size in the presence of plant-model mismatch, and is found to be robust in comparison to open-loop optimal control strategies.

Chapter 2

Diamond Jet Hybrid HVOF Thermal Spray: Gas-Phase and Particle Behavior Modeling and Feedback Control Design

This chapter focuses on modeling and control of an industrial high-velocity oxygen fuel (HVOF) thermal spray process (Diamond Jet hybrid gun, Sulzer Metco, Westbury, NY). We initially develop a fundamental model for the process which describes the evolution of the gas thermal and velocity fields, the motion and temperature of particles of different sizes, and explicitly accounts for the effect of powder size distribution. Based on the proposed model, a comprehensive parametric analysis is made to systematically characterize the influence of controllable process variables such as combustion pressure, oxygen/fuel ratio, as well as the effect of powder size distribution, on the values of particle velocity, temperature and degree of melting at the point of impact on substrate (these are the variables that directly influence coating microstructure and porosity, which, in turn, determine coating strength and hard-

ness, see Chapter 3 for details). A feedback control system, which aims to control the volume-based average of particle velocity and melting ratio by directly manipulating the flow rate of fuel, oxygen and air at the entrance of the HVOF gun, is developed and applied to a detailed mathematical model of the process. Closed-loop simulations show that the feedback controller is effective in driving the controlled outputs to the desired set-point values and also robust with respect to various kinds of disturbances in the operating environment.

2.1 Introduction

The last two decades have witnessed the wide application of the high-velocity oxygen fuel (HVOF) thermal spray technology (see Figure 2.1 for a schematic of this process) as a means for depositing coatings of cermets, metallic alloys and composites in order to modify the surface properties of a base material (substrate). Using the thermal energy produced by the combustion of fuel with oxygen to heat and propel the powder particles, the HVOF thermal spray provides a highly efficient way to modify the surface properties of a substrate to extend product life, increase performance and reduce maintenance costs. Recently, there is an increasing interest in the HVOF thermal spray processing of nanostructured coatings, whose grain size is less than about 100 nm [100]. This interest has been motivated by several factors, including: (1) the cost-effective production of high-quality nanosize powders; (2) the superior qualities of coatings made with the HVOF process [21]; and (3) the discovery that nanostructured coatings exhibit superior qualities over traditional counterparts (made of materials with micro-sized grains) in several aspects including hardness, strength, ductility and diffusivity [100, 182].

Over the last decade, the need to optimally design and operate thermal spray

Cooling Water

Air

Oxygen and
Fuel

Powder and N_2

Prepared Substrate

Spray Stream

Spray Deposit
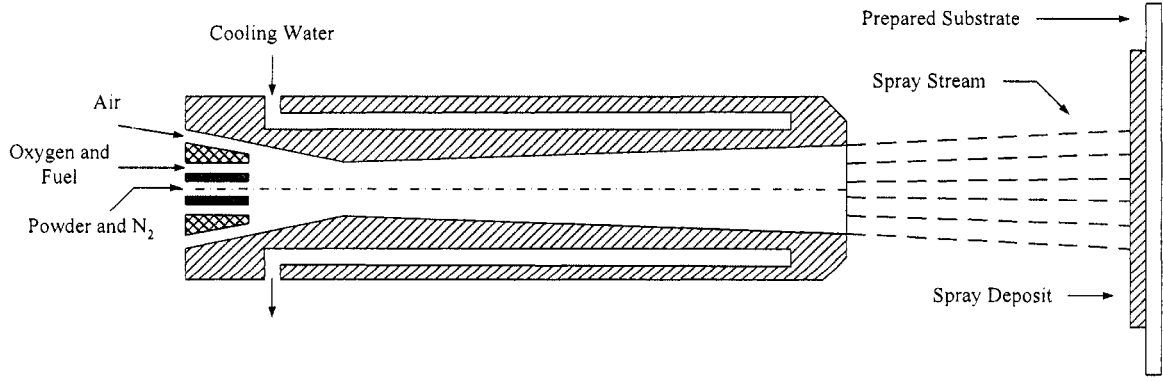
Figure 2.1: A schematic of the Diamond Jet hybrid HVOF thermal spray process.

processes has motivated significant research on the development of fundamental mathematical models to capture the various physicochemical phenomena taking place in thermal spray processes and to describe the dynamic behavior of various process components. Specifically, fundamental models have been developed describing the gas dynamics and particle in-flight behavior inside of the gun and in the free jet [143, 198, 67]; molten drop deposition, solidification and microstructure development [188, 134]; and the relationship between coating microstructure and mechanical properties [64]. In addition, research has been carried out in the integration of the detailed models of the aforementioned components to develop general simulators that describe the behavior of entire thermal spray processes [134, 199].

In order to reduce product variability and to improve robustness with respect to variations in the operating conditions in industrial HVOF thermal spray processes, it is important to implement excellent real-time process diagnosis and control which could lead to the fabrication of coatings with microstructures that yield the desired properties. Despite the recent progress on the modeling of the various phenomena that affect droplet motion, deposition, solidification and microstructure development in HVOF thermal spray processes, at this stage, there exists no systematic framework

26

for integrated on-line diagnosis and control of the HVOF thermal spray process which will be capable of achieving precise regulation of the microstructure and ultimate mechanical and thermal properties of the sprayed coatings. In addition, incorporation of advanced real-time diagnosis and control schemes into thermal spray processes is expected to reduce operational cost and environmental impact, and allow depositing nanostructured and complex (multi-material) coatings with very low variability. Since the application of optimization and control techniques to spray casting processes has been reported to lead to significant improvements in their operation and performance [2, 125], it is important to develop real-time computer control systems for thermal spray processes by integrating fundamental models that accurately describe the inherent relationships between the coating microstructure and the processing parameters with on-line state-of-the-art diagnostic techniques and control algorithms. Recent efforts in this direction have mainly focused on diagnostics and control of plasma thermal spray [49]; the reader may also refer to Moreau and Leblanc [133] for a discussion of various process optimization and control issues. In our previous work (see [108, 109]), we performed a comprehensive control-relevant parametric analysis and proposed a novel formulation of the control problem that accounts for the important effect of powder size distribution for an HVOF process in which air is used as oxidant and propane is used as fuel gas.

The objective of the present research is to develop a computational methodology to precisely control the coating micro- or nano-structure which determines the coating mechanical and physical properties by manipulating macro-scale operating conditions such as the gas flow rate and spray distance. The major challenge on this problem lies in the development of multiscale models linking the macroscopic scale process behavior (i.e., gas dynamics and particle inflight behavior) and the microscopic scale

27
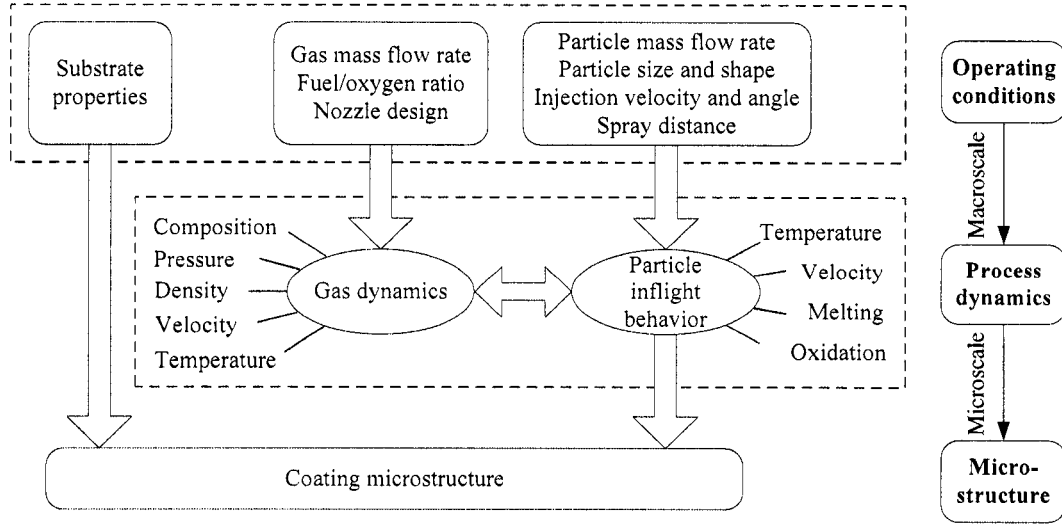
Figure 2.2: Multiscale character of the HVOF thermal spray process.

process characteristics (evolution of coating microstructure), and the integration of models, measurements, and control theory to develop measurement/model-based control strategies [29]. The underlying multiscale behavior of the HVOF process is shown in Figure 2.2. On the one hand, the microstructure of thermally sprayed coatings results from the deformation, solidification and sintering of the deposited particles, which are dependent on the substrate properties (e.g., substrate temperature) as well as the physical and chemical state (e.g., temperature, velocity, melting ratio, and oxidant content) of the particles at the point of impact on the substrate. On the other hand, the particle inflight behavior, however, is coupled with the gas dynamics, which can be manipulated by adjusting operating conditions such as the total gas flow rate and the fuel/oxygen ratio. While the macroscopic thermal/flow field can be readily described by continuum type differential equations governing the compressible two-phase flow, the process of particle deposition is stochastic and discrete in nature, and thus, it can be best described by stochastic simulation methods [94].

This work focuses on modeling and control of an industrial high-velocity oxygen

fuel (HVOF) thermal spray process (Diamond Jet hybrid gun, Sulzer Metco, Westbury, NY). We initially develop a fundamental model for the process which describes the evolution of the gas thermal and velocity fields, the motion and temperature of agglomerate particles of different sizes, and explicitly accounts for the effect of powder size distribution. In addition to providing useful insight into the in-flight behavior of different-size particles, the model is used to make a comprehensive parametric analysis of the HVOF process. This analysis allows us to systematically characterize the influence of controllable process variables such as combustion pressure, oxygen/fuel ratio, as well as the effect of powder size distribution, on the values of particle velocity and temperature at the point of impact on substrate. Specifically, the study shows that the particle velocity is primarily influenced by the combustion pressure, and the particle temperature is strongly dependent on the fuel/oxygen ratio. These findings are consistent with existing experimental studies and set the basis for the formulation of the control problem for the HVOF thermal spray process. To develop a feedback controller that can be readily implemented in practice, the control problem is formulated as the one of regulating volume-based averages of the melting ratio and velocity of the particles at the point of impact on the substrate (these are the variables that directly influence coating microstructure and porosity, which, in turn, determine coating strength and hardness) by directly manipulating the flow rate of fuel, oxygen and air at the entrance of the HVOF thermal spray gun. A feedback control system is developed and applied to a detailed mathematical model of the process. Closed-loop simulations demonstrate that the particle velocity and melting ratio at the point of impact on the substrate reach the desired set-point values in a short time, which validates the feasibility of real-time implementation of feedback control on the HVOF thermal spray system. It is also shown that the proposed control problem formulation and the feedback control system are robust with respect

29

to disturbances in spray distance and particle injection velocity, and variations in powder size distribution.

In the next chapter, we present a mechanistic model which uses information about particle velocity, temperature and degree of melting at the point of impact on substrate from the model developed in this chapter to predict coating porosity and microstructure.

2.2 Modeling of gas thermal and flow fields

2.2.1 Process description and modeling procedure

Figure 2.1 shows a schematic diagram of the Diamond Jet hybrid gun. The premixed fuel (typically propylene or hydrogen) and oxygen are fed from the annular gap to the air cap (also referred to as convergent-divergent nozzle, whose dimensions are shown in Table 2.1), where they react to produce high temperature combustion gases. The exhaust gases, together with the air injected from the annular inlet orifice, expand through the nozzle to reach supersonic velocity. The air cap is water-cooled to prevent from being melted. The powder particles are injected from the central inlet hole using nitrogen as the carrier gas. Consequently, rapid momentum and heat transfer between the gas and the powder particles leads to acceleration and heating of the powder particles. The molten or semi-molten particles exit the air cap and move towards the substrate. The particles hit the substrate, cool and solidify, forming a thin layer of dense and hard coating. In the remainder of this section, we present the procedure that we follow for modeling as well as the equations describing the gas flow and thermal fields.

Roughly speaking, there are three major physicochemical processes involved in

Table 2.1: Dimensions of the air cap.

Inlet Diameter (mm)	14
Nozzle Diameter (mm)	7.16
Outlet Diameter (mm)	11
Inlet half angle (deg)	12
Outlet half angle (deg)	2
Length of convergent part (mm)	16
Length of divergent part (mm)	54

the HVOF thermal spray process: transformation of chemical energy into thermal energy by the combustion of the fuel, conversion of thermal energy into kinetic energy of the burning gases by passing through the nozzle, and transfer of momentum and heat from the gases to the powder particles. These processes occur simultaneously and make the fundamental modeling of the HVOF process a very difficult task. For example, detailed fundamental modeling of the gas flow and thermal fields requires state-of-the-art Computational Fluid Dynamics (CFD) methodologies and leads to complex two- or three-dimensional time-dependent partial differential equations [40, 67, 144]. For the purposes of control system design and implementation, a compromise between the model complexity, computational cost and model ability to capture the dominant (from a control point of view) phenomena occurring in the process is essential. To simplify the analysis, the process model used here is based on the one-way coupling assumption, i.e., the existence of particles has a minimal influence on the gas dynamics while the particle inflight behavior is dependent on the gas thermal/flow field. This assumption is reasonably accurate because the particle loading in the HVOF process, which is defined as the ratio of mass flow rate of particles to that of gases, is typically less than 4% [198]. In addition, the assumptions of instantaneous equilibrium at the entrance of the HVOF gun and frozen isentropic

flow during passage through the nozzle are made. These assumptions were initially proposed and justified by Swank et al [178]. based on the comparison of numerical simulations and experimental results, and later also recommended by Cheng et al. [21] Comparisons of simulation results and experimental data which will be shown later in this chapter further substantiate the validity of these assumptions (see discussion in subsections 2.4.1 and 2.4.2).

Regarding the role of the air stream, it is really hard to predict what portion of the air takes part in the reaction. Whereas the air was treated as coolant solely to isolate the wall from the high temperature flame gases in some references [24, 139], it was assumed in others [40, 64, 144] that all the oxygen coming from the air participates in the reaction. The latter assumption is employed here, since it is pointed out clearly by Gourlaouen et al. [64] that the airflow mixing with the oxygen/propylene mixture should be more effective in the currently used Diamond Jet hybrid gun (which is the process under consideration in this work) than the previous Diamond Jet gun, as implied by the "water-cooled" (not "air-cooled") nozzle. Other assumptions in the modeling include: (1) all the gases obey ideal gas law; (2) the combustion gases behave like a perfect gas during isentropic compression and expansion, and the specific heat ratio is nearly constant; and (3) the friction and cooling water effects along the nozzle and barrel are negligible so that laws of isentropic flow of compressible fluids apply.

Because the flow is chocked at the throat of the nozzle, the convergent part of the air cap and the divergent one can be solved separately [144]. The modeling procedure that is followed in the simulation is based on the sequential modular method. Specifically, given the mass flow rates of each stream (fuel, oxygen, air, and carrier gas) and a postulated combustion pressure, the temperature and gas composition at

the entrance of the nozzle is calculated using an instantaneous equilibrium model, and then the nozzle flow using standard isentropic compressible flow relationships is solved. The total mass flow rate at the throat of the nozzle is then calculated and compared with the one at the entrance. The combustion pressure is then adjusted using the shooting method [146], until the discrepancy between the calculated and specified values of the total mass flow rate falls below the specified tolerance. After the gas properties at the nozzle throat are determined, the divergent part is solved using isentropic flow relationships. The external thermal/flow field in the free jet is described by empirical formulas.

2.2.2 Modeling of gas thermal and flow fields inside the gun

To calculate the equilibrium composition and temperature of the combustion gases, the method of minimization of the Gibbs free energy under adiabatic conditions is employed. This approach is advantageous compared to the equilibrium constant method because it can track a large number of species simultaneously without specifying a set of reactions a priori [63]. Under the assumption of adiabatic combustion under constant pressure, the calculation of equilibrium temperature and composition can be formulated as an optimization problem of the following form:

$$\min G = \sum_{j \in pr} \mu_i \xi_i$$

$$\text{s.t.}$$

$$0 = \sum_{j \in pr} a_{ij}\xi_j - b_i^0, \quad (i = 1, ..., l) \quad \text{(Mass Balance)} \tag{2.1}$$

$$0 = \sum_{j \in pr} \xi_j H_j^0(T_{eq}) + \frac{1}{2}v_{eq}^2 - h_0 - E_0 \quad \text{(Energy Balance)}$$

where G is the Gibbs free energy of the product mixture (including inert gases and excess reactants), pr stands for products, ξ_i, H_i and μ_i correspond to the stoichiometric coefficient, enthalpy and chemical potential of species i, respectively, T_{eq} is

33

the equilibrium temperature (subscript eq represents equilibrium), a_{ij} is the number of element i in species j, l is the total number of chemical elements involved in the system, and the superscript ^{0} stands for the standard condition. $b_i^0 = \sum_{k \in re} a_{ik}\xi_k$ is the number of moles of elements i per kilogram reactants (subscript re represents reactants), $h_0 = \sum_{k \in re} \xi_k H_k^0(T_{in})$ is the enthalpy per kilogram of reactants (subscript in represents inlet), and $E_0 = \sum_{k \in re} \frac{1}{2}\xi_k M_k v_k^2$ is the kinetic energy per kilogram of reactants (M_k is the molecular weight and v_k is the velocity of species k). For a gas obeying the ideal gas law, the chemical potential can be determined by the following expression:

$$\mu_i(T) = \mu_i^0(T) + RT \ln \frac{P}{P^0} + RT \ln \frac{\xi_i}{\sum\limits_{i \in pr} \xi_i} \tag{2.2}$$

where R is the gas constant and P is the pressure. Due to continuity, the gas velocity after the combustion reaction is given by the following expression:

$$v_{eq} = \frac{\dot{m}_g}{\rho A_{in}} = \frac{\dot{m}_g R T_{eq}}{P A_{in} \bar{M}_{pr}} = \frac{\dot{m}_g \xi_T R T_{eq}}{P A_{in}} \tag{2.3}$$

where $\dot{m}_g$ is the total mass flow rate of the gas, A_{in} is the cross sectional area at the inlet of the air cap, $\bar{M}_{pr}$ is the average molecular weight of the product mixture, and $\xi_T = \sum\limits_{j \in pr} \xi_j$. From Eq.2.3, it follows that:

$$\frac{1}{2}v_{eq}^2 = \frac{\dot{m}_g^2 \xi_T^2 R^2 T_{eq}^2}{2P^2 A_{in}^2} \tag{2.4}$$

Defining $f = G + \sum\limits_{i=1}^{l} \lambda_i \left[\sum\limits_{j \in pr} a_{ij}\xi_j - b_i^0 \right]$, where λ_i are the Lagrangian multipliers, the optimal solution of the optimization problem of Eq.2.1 can be determined by

34

solving the following nonlinear algebraic equations:

$$0 = \mu_j^0 + RT_{eq}\ln(P/P^0) + RT_{eq}\ln(\xi_j/\xi_T) + \sum_{i\in l}\lambda_i a_{ij} \quad (j = 1, ..., s)$$

$$0 = \sum_{j\in pr} a_{ij}\xi_j - b_i^0 \quad (i = 1, ..., l)$$

$$0 = \sum_{j\in pr}\xi_j - \xi_T \quad\quad\quad (2.5)$$

$$0 = \sum_{j\in pr}\xi_j H_j^0(T_{eq}) + \frac{\dot{m}_g^2\xi_T^2 R^2 T_{eq}^2}{2P^2 A_{in}^2} - h_0 - E_0$$

The variables to be determined are equilibrium compositions ξ_j $(j = 1, ..., s)$, Lagrangian multipliers λ_i $(i = 1, ..., l)$, total number of moles ξ_T, and equilibrium temperature T_{eq}. The set of $s + l + 2$ nonlinear algebraic equations of Eq.2.5 are solved using the decent Newton-Raphson method. The central idea of Newton-Raphon method is to apply multivariable Taylor series expansion to a nonlinear vector function and truncate all terms that contain derivatives of second order and higher, and then use the resulting expression to build an iterative formula which can be used to compute the solution given an initial guess that is close to the solution; the reader may refer to the book [146] for details.

Because ξ_j, ξ_T and T should be positive numbers, in order to avoid taking the logarithm of negative numbers in the iteration procedure, we have chosen $\Delta\ln\xi_j$ $(j = 1, ..., s)$, $\Delta\ln\xi_T$, $\Delta\ln T$ and $-\lambda_i/RT$ $(i = 1, ..., l)$ as the solution variables at each iteration step. In the above equations, the thermodynamic data, such as the heat capacity, enthalpy, entropy and chemical potential of each species are calculated

35

by the following equations [63]:

$$\frac{c_p^0(T)}{R} = \frac{a_1}{T^2} + \frac{a_2}{T} + a_3 + a_4 T + a_5 T^2 + a_6 T^3 + a_7 T^4$$

$$\frac{H^0(T)}{RT} = -\frac{a_1}{T^2} + \frac{a_2}{T}\ln T + a_3 + \frac{a_4}{2}T + \frac{a_5}{3}T^2 + \frac{a_6}{4}T^3 + \frac{a_7}{5}T^4 + \frac{a_8}{T}$$

$$\frac{S^0(T)}{R} = -\frac{a_1}{2T^2} - \frac{a_2}{T} + a_3 \ln T + a_4 T + \frac{a_5}{2}T^2 + \frac{a_6}{3}T^3 + \frac{a_7}{4}T^4 + a_9 \qquad (2.6)$$

$$\frac{\mu_j^0}{RT} = \frac{H^0(T)}{RT} - \frac{S^0(T)}{R}$$

where $a_1, \ldots, a_9$ are constants for a given species. It usually takes about 10 iterations to get a convergent solution.

Under the assumption of isentropic frozen flow, the properties of gas phase during passage through the nozzle (both the convergent part and the divergent part) can be solved using the following equations (which are derived by solving conservation equations governing compressible flow) [157]:

$$\frac{A_2}{A_1} = \frac{\mathbf{M}_1}{\mathbf{M}_2}\left\{\frac{1 + [(\gamma-1)/2]\mathbf{M}_2^2}{1 + [(\gamma-1)/2]\mathbf{M}_1^2}\right\}^{(\gamma+1)/2(\gamma-1)} \qquad (2.7)$$

$$\frac{T_2}{T_1} = \frac{1 + [(\gamma-1)/2]\mathbf{M}_1^2}{1 + [(\gamma-1)/2]\mathbf{M}_2^2} \qquad (2.8)$$

$$\frac{P_2}{P_1} = \left\{\frac{1 + [(\gamma-1)/2]\mathbf{M}_1^2}{1 + [(\gamma-1)/2]\mathbf{M}_2^2}\right\}^{\gamma/(\gamma-1)} \qquad (2.9)$$

$$\frac{\rho_2}{\rho_1} = \left\{\frac{1 + [(\gamma-1)/2]\mathbf{M}_1^2}{1 + [(\gamma-1)/2]\mathbf{M}_2^2}\right\}^{1/(\gamma-1)} \qquad (2.10)$$

where A is the cross-sectional area perpendicular to the flow direction, ρ is the gas density, γ is the specific heat ratio calculated by the expression $\gamma = \bar{c}_p/(\bar{c}_p - R)$ where $\bar{c}_p = \sum_i \xi_i c_p^i / \sum_i \xi_i$, and $\mathbf{M}$ is the mach number defined by the ratio of gas velocity to the local sonic velocity ($a = \sqrt{\gamma P/\rho}$). At the throat of the nozzle, where the mach number is 1 [157], the mass flow rate can be calculated using the formula:

$$\dot{m}_g = \rho_t v_t A_t = \sqrt{\gamma P_t \rho_t} A_t \qquad (2.11)$$

where the subscript g stands for gas and the subscript t stands for throat. With a postulated combustion pressure, the calculated mass flow rate at the throat is usually different from the one at the entrance of the gun. The shooting method is then applied to adjust the combustion pressure until these two flow rates match.

We note that the isentropic relationships (Eqs.2.7-2.10) are valid only if there is no shock inside of the nozzle. This can be guaranteed as long as the following inequity holds:

$$\frac{P_b}{P_e} \;<\; \frac{2\gamma}{\gamma+1}\mathrm{M}_e^2 - \frac{\gamma-1}{\gamma+1} \tag{2.12}$$

where P_b is the back pressure (ambient pressure), and P_e is the gas pressure at the exit of the nozzle. For the experimental Diamond Jet hybrid gun system, our calculations show that the right hand side of the above equation is about 5, and therefore no shock will ever occur inside of the nozzle as long as the exit pressure is larger than one fifth of the back pressure; a condition which is always satisfied under industrial operating conditions.

We have applied the above modeling procedure and equations to analyze the Diamond Jet HVOF process [144], which is similar to the one shown in Figure 2.1 but whose nozzle has only a convergent part. The combustion products considered in our numerical simulation are Ar, CO, CO_2, H, H_2, H_2O, NO, N_2, O, O_2, and OH. It is worth pointing out that C_3H_6 is not part of the products under normal operating conditions. For the given four different operating conditions, the combustion pressures predicted by the above procedure are all within 6% of the experimentally measured values (see Table 2.2); this result is more accurate than the one obtained with the two step chemical kinetics model [144] and implies that the combustion model should take into account the dissociation of the combustion products.

37

Table 2.2: Comparison of computational and experimental results for a Diamond Jet process [144].

Case	O_2 scfh	C_3H_6 scfh	Air scfh	N_2 scfh	P_{eq}^e psia	P_{eq}^c psia	error %
1	635	185	790	29.4	69.7	68.7	-1.4
2	635	185	395	29.4	59.7	56.1	-6.0
3	879	185	795	29.4	76.7	77.6	1.2
4	347	110	632	29.4	44.7	44.8	0.2

2.2.3 Modeling of gas thermal and flow fields outside the gun

At the exit of the nozzle, the Reynolds number based on the diameter and the gas velocity is about 3×10^4, and the flow is fully turbulent. Depending on the magnitude of the gas pressure at the exit of the air cap and of the back pressure, the flow outside the nozzle may be under-expanded, ideally expanded or over-expanded. Usually the velocity and temperature of the gas in the free jet are lower than the ones at the nozzle exit [82, 25]. From the exit of the nozzle to a position whose distance is not larger than the potential core length (L_{pc}), the gas velocity and temperature can be considered almost constant [180]. Further downstream, the gas velocity and temperature decay rapidly because of the entrainment of the surrounding air. This decay of the gas velocity and temperature can be described by the following empirical formulas [180]:

$$\frac{v}{v_e} = 1 - \exp\left(\frac{\alpha}{1 - x/L_{pc}}\right) \qquad (2.13)$$

and

$$\frac{T - T_a}{T_e - T_a} = 1 - \exp\left(\frac{\beta}{1 - x/L_{pc}}\right) \qquad (2.14)$$

where x is the axial distance from the exit of the gun barrel ($x > L_{pc}$) and α and β are parameters obtained from experimental measurements. L_{pc} is a function of the

mach number at the exit of the gun barrel ($\mathbf{M}_e$) and of the barrel diameter (D) of the following form [180]:

$$L_{pc}/D = 3.5 + 1.0\mathbf{M}_e^2 \qquad (2.15)$$

2.3 Modeling of particle motion and temperature

The particle trajectories and temperature histories in the gas field are computed by the momentum and heat transfer equations. Since the acceleration and deceleration of particles in the moving gas in the HVOF process are dominated by the drag force [141], other forces applied on the particles can be neglected and the particle motion can be adequately described by the following two first-order ordinary differential equations:

$$
\begin{aligned}
m_p \frac{dv_p}{dt} &= \frac{1}{2}C_D\rho_g A_p(v_g - v_p)|v_g - v_p|, \ \ v_p(0) = v_{p_0} \\
\frac{dx_p}{dt} &= v_p, \ \ x_p(0) = 0
\end{aligned}
\qquad (2.16)
$$

where m_p is the mass of the particle, v_p is the axial velocity of the particle, A_p is the projected area of the particle on the plane perpendicular to the flow direction, ρ_g is the density of the gas, C_D is the drag coefficient, and x_p is the position of the particle. The absolute sign in the relative velocity between particle and gas implies that a particle is accelerated if its velocity is less than that of the gas and decelerated otherwise. In order to take into consideration the fact that many powders used in the HVOF process are not spherical, a formula for the drag coefficient C_D, which accounts for the particle shape using the concept of sphericity ϕ (defined as the ratio of the surface area of a sphere with equivalent volume to the actual surface area of the particle) is used here, which has the following form [23, 55]:

$$\frac{C_D}{K_2} = \frac{24}{ReK_1K_2}\left[1 + 0.1118(ReK_1K_2)^{0.6567}\right] + \frac{0.4305}{1 + 3305/ReK_1K_2} \qquad (2.17)$$

where K_1 and K_2 are two sphericity-related factors. The local Reynolds number (Re) for this two phase flow problem is defined based on the relative velocity $Re = d_p \mid v_g - v_p \mid \rho_g / \eta_g$, where d_p is either the particle diameter if the particle is spherical or an appropriate equivalent diameter if the particle is not spherical and η_g is the gas viscosity.

In the HVOF process, the Biot number of the particles ($Bi = hL/\lambda_p$, h is the heat transfer coefficient, L is a characteristic dimension defined by the ratio of particle volume to its surface area, and λ_p is the thermal conductivity of the particle) is typically less than 0.1 [23], which means that the particles are heated with negligible internal resistance and that the temperature gradients inside them can be neglected [56]. Consequently, the equation describing the heat transfer between a single particle and the gas reduces to a first-order ordinary differential equation. Depending on the value of particle temperature, different equations are used. With the assumption of negligible particle vaporization, the particle heating can be described as follows:

$$
hA_p'(T_g - T_p) = \begin{cases} m_p c_{p_p} \dfrac{dT_p}{dt}, & (T_p \neq T_m) \\[2ex] \Delta H_m m_p \dfrac{df_p}{dt}, & (T_p = T_m) \end{cases} \tag{2.18}
$$

where T_p is the temperature of the particle, A_p' is the surface area of the particle, T_m is the melting point of the particle, ΔH_m is the enthalpy of melting and f_p is the melting ratio, or the ratio of the melted mass to the total mass of the particle ($0 \leq f_p \leq 1$). The heat transfer coefficient h is computed by the Ranz-Marshall empirical equation [8]:

$$
\frac{hd_p}{\bar{\lambda}_g} = Nu = 2 + 0.6Re^{\frac{1}{2}}Pr^{\frac{1}{3}} \tag{2.19}
$$

where the Prandtl number (Pr) is calculated by $Pr = \bar{c}_{p_g}\bar{\eta}_g/\bar{\lambda}_g$.

In the above equations, the viscosity and thermal conductivity of each species are

calculated by the following formulas [63]:

$$
\begin{aligned}
\ln(\eta) &= b_1 \ln(T) + b_2/T + b_3/T^2 + b_4 \\
\ln(\lambda) &= c_1 \ln(T) + c_2/T + c_3/T^2 + c_4
\end{aligned}
\tag{2.20}
$$

where $b_1, \ldots, b_4, c_1, \ldots, c_4$ are constants for a specific species. For gas mixtures, the average viscosity and thermal conductivity are calculated by the following mixing rules [63]:

$$
\begin{aligned}
\bar{\eta} &= \sum_i \frac{x_i \eta_i}{x_i + \sum_{j \neq i} x_i \psi_{ij}} \\
\bar{\lambda} &= \sum_i \frac{x_i \lambda_i}{x_i + \sum_{j \neq i} x_i \varsigma_{ij}}
\end{aligned}
\tag{2.21}
$$

where the interaction coefficients ψ_{ij} and ς_{ij} are obtained from the following formulas:

$$
\begin{aligned}
\psi_{ij} &= \frac{1}{4} \left[1 + \left(\frac{\eta_i}{\eta_j} \right)^{1/2} \left(\frac{M_j}{M_i} \right)^{1/4} \right]^2 \left[\frac{2M_j}{M_i + M_j} \right]^{1/2} \\
\varsigma_{ij} &= \psi_{ij} \left[1 + \frac{2.41(M_i - M_j)(M_i - 0.142 M_j)}{(M_i + M_j)^2} \right]
\end{aligned}
\tag{2.22}
$$

At each step, we integrate Eqs.2.16 and 2.18 with a small enough time-step such that the gas velocity, gas temperature, and the local Reynolds number can all be considered constant over this interval. After one integration step, we update the gas velocity and gas temperature according to the new particle position and then apply the same strategy for the next time-step. This methodology was proposed by Crowe and Stock [34] and was found to be computationally less expensive and accurate. To account for the particle melting behavior, we modified this approach and check the molten state of the particle at each time-step and applied different formulas for the particle heating. Specifically, the iterative formulas for particle velocity, position and

41

temperature are:

$$
\begin{aligned}
v_p^{i+1} &= v_g^i - (v_g^i - v_p^i) \exp(-\Delta t/\tau_p) \\
x_p^{i+1} &= x_p^i + v_p^i \Delta t \\
T_p^{i+1} &= T_g^i - (T_g^i - T_p^i) \exp(-\Delta t/\omega_p), \quad (T_p^i, T_p^{i+1} > T_m \text{ or } T_p^i, T_p^{i+1} < T_m) \quad (2.23) \\
f_p^{i+1} &= f_p^i + \frac{c_{p_p}(T_g - T_m)}{\Delta H_m} \frac{\Delta t}{\omega_p}, \quad (0 < f_p^i, f_p^{i+1} < 1)
\end{aligned}
$$

where $\tau_p = \dfrac{4\rho_p d_p^2}{3\eta_g C_D Re}$ and $\omega_p = \dfrac{\rho_p c_p d_p^2}{6 Nu \lambda_g}$. In the four possible phase transition points, in which the current step and the next step correspond to different particle molten states, the successive formulas for particle temperature and melting ratio take the following form:

1. $T_p^i < T_m$ $(f_p^i = 0)$, $T_p^{i+1} > T_m$, from totally solid state to partially melted state

$$
\begin{aligned}
f_p^{i+1} &= f_p^i + \frac{c_{p_p}(T_p^{i+1} - T_m)}{\Delta H_m} \\
T_p^{i+1} &= T_m
\end{aligned}
\quad (2.24)
$$

2. $T_p^i > T_m$ $(f_p^i = 1)$, $T_p^{i+1} < T_m$, from totally liquid state to partially melted state

$$
\begin{aligned}
f_p^{i+1} &= f_p^i + \frac{c_{p_p}(T_p^{i+1} - T_m)}{\Delta H_m} \\
T_p^{i+1} &= T_m
\end{aligned}
\quad (2.25)
$$

3. $T_p^i = T_m$ $(0 < f_p^i < 1)$, $T_p^{i+1} > T_m$, from partially melted state to totally liquid state

$$
\begin{aligned}
T_p^{i+1} &= T_m + \frac{\Delta H_m(f^{i+1} - 1)}{c_{p_p}} \\
f_p^{i+1} &= 1
\end{aligned}
\quad (2.26)
$$

4. $T_p^i = T_m$ $(0 < f_p^i < 1)$, $T_p^{i+1} < T_m$, from partially melted state to totally solid state

$$
\begin{aligned}
T_p^{i+1} &= T_m + \frac{\Delta H_m f^{i+1}}{c_{p_p}} \\
f_p^{i+1} &= 0
\end{aligned}
\quad (2.27)
$$

To reduce the computation time and to maintain accuracy at the same time, a time varying time-step is used of the following form:

$$\Delta t = \min\{\tau_p/100, \omega_p/100, \Delta x_{max}/v_p\} \qquad (2.28)$$

where Δx_{max} is chosen to be 10^{-4} m, which is the maximum flight distance in each time interval. The first two constraints guarantee that the gas velocity and temperature will change little in each time-step.

2.4 Analysis of gas and particle behavior

2.4.1 Analysis of gas dynamics without the air stream

Initially, we only included propylene and oxygen as feed to the system and tested the influence of combustion pressure and oxygen/fuel ratio on the gas temperature, velocity, density, and momentum flux (ρu^2) in the internal field. The reasons are the following: (1) the influence of the process parameters on the gas dynamics and the particle infight behavior is apparent in this simplified case; (2) a bijection of pressure and equivalence ratio to fuel and oxygen flow rates is possible, and calculation starting from either side is equivalent to the other, which facilitates the numerical calculation; and (3) there are many HVOF processes whose feed consists of only fuel and oxygen (i.e., without air); see, for example, Gu et al. [65] and Yang and Eidelman [198] etc. The process model was based on the assumptions of negligible injection gas velocity, instantaneous equilibrium under constant enthalpy and pressure in the injection interface, and frozen isentropic flow during passage through the nozzle. To account for the dissociation of gaseous products, the model included nine species (CO, CO_2, H, H_2, H_2O, O, O_2, and OH) in the product mixture. The equilibrium temperature and composition of combustion was solved by minimizing the total Gibbs free energy, and
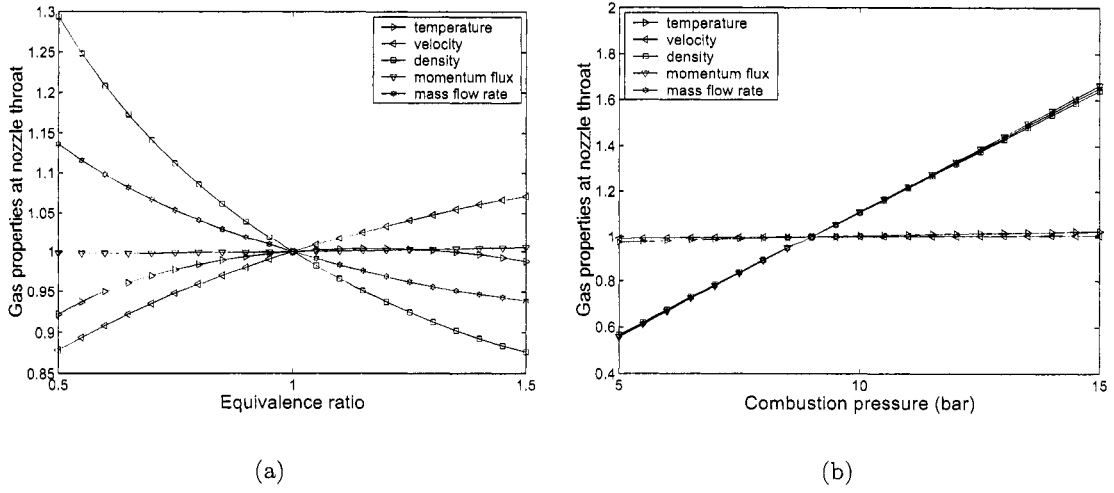
Figure 2.3: Normalized gas temperature, velocity, momentum flux, and mass flow rate in the internal field under operating conditions: $P = 5 - 15\ bar$ and $\varphi = 0.5 - 1.6$. Normalization is done with respect to the corresponding gas properties under operating conditions: $P = 9\ bar$ and $\varphi = 1.0$ (Table 2.3).

the gas properties during passage through the nozzle were determined by standard laws governing compressible flows described in subsection 2.2.2.

Table 2.3: Gas properties under operating conditions: $P = 9\ bar$ and $\varphi = 1.0$.

Properties	Inlet	Throat	Exit
Temperature (K)	3486.7	3120.7	2222.6
Velocity (m/s)	–	1147.0	2150.8
Density (kg/m^3)	0.7535	0.4688	0.1073
Momentum flux $(10^5 kg \cdot m/s^2)$	–	6.1673	4.9627
Mass flow rate $(10^{-3} kg/s)$	21.65	21.65	21.65
Average molecular weight $(10^{-3} kg/mol)$	24.15	24.15	24.15

In Figure 2.3(a), the combustion pressure is fixed to be 9 bar and the equivalence ratio varies from 0.5 to 1.6. In this range, it is found that there is a peak in each of the temperature vs. equivalence ratio plot. As the equivalence ratio increases,
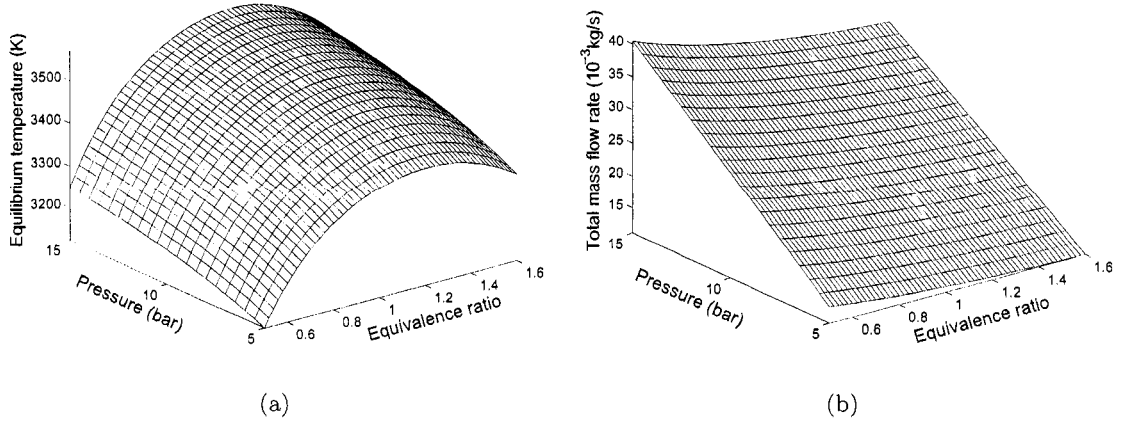
Figure 2.4: Profile of equilibrium temperature and total mass flow rate with respect to P and φ. Operating conditions: $P = 5$ - 15 bar and $\varphi = 0.5$ - 1.6.

the temperature at the entrance, the throat and the exit increase first, reaching a maximum value, and then decrease. However, the equivalence ratio associated with each peak temperature is about 1.2 (or fuel rich system), which is somewhat different from a fuel/air system [108], whose optimal value is close to 1.05. It can also be seen that as the equivalence ratio increases from 0.5 to 1.6, the gas velocity both at the throat and at the exit increase by about 22-23%, while the gas density decreases by about 33%. As a result, the momentum flux keeps almost constant at these two positions. In Figure 2.3(b), the equivalence ratio is kept at 1.0 and the combustion pressure varies from 5 to 15 bar. In the combustion pressure range of interest, it is found that both gas velocity and gas temperature change little (about 2% and 5%, respectively), however, the gas density and momentum flux change almost linearly with respect to the combustion pressure, by about 190% and 200%, respectively. We also computed 3D profiles of gas properties under different combustion pressures and equivalence ratios, as shown in Figures 2.4-2.6. Further analysis reveals the following:

45
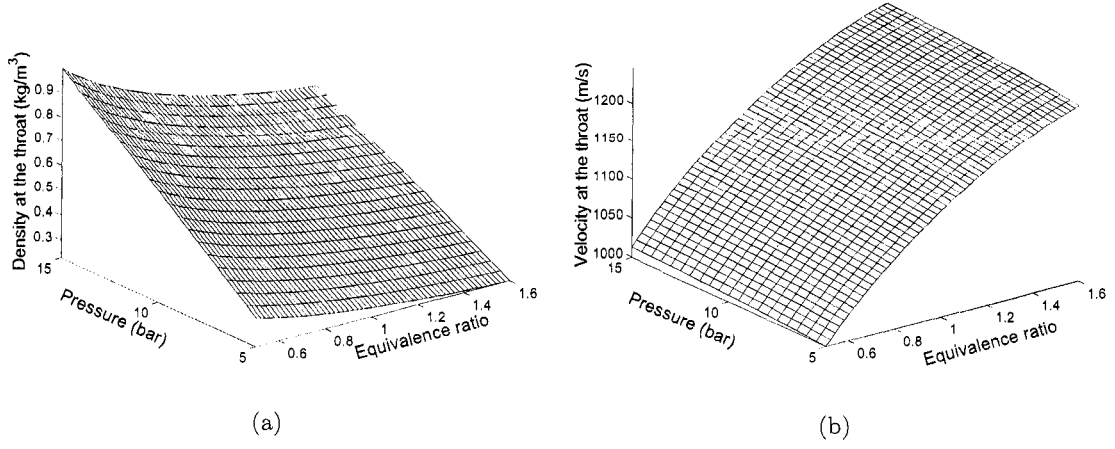
Figure 2.5: Profile of gas density and velocity at the throat with respect to P and φ. Operating conditions: $P = 5 - 15$ *bar* and $\varphi = 0.5 - 1.6$.
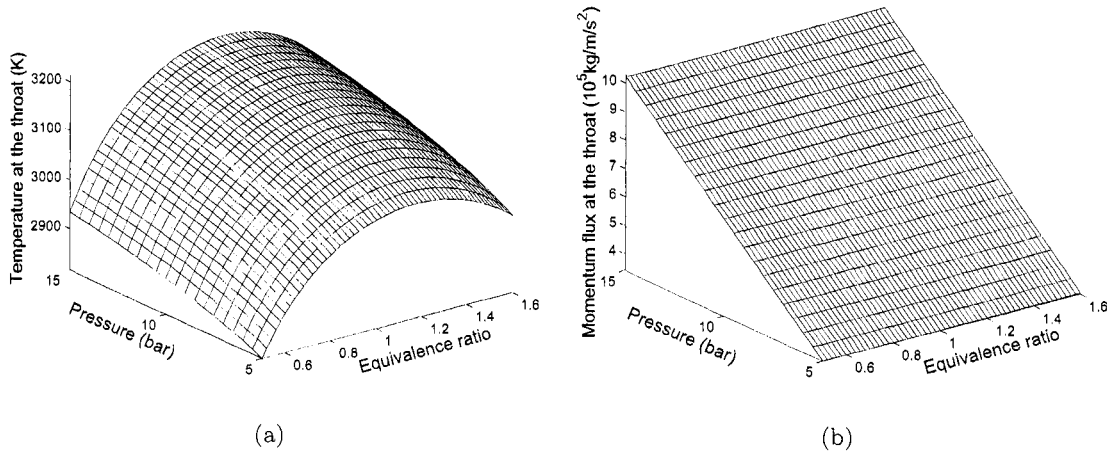
Figure 2.6: Profile of temperature and momentum flux at the throat with respect to P and φ. Operating conditions: $P = 5 - 15$ *bar* and $\varphi = 0.5 - 1.6$.

1. At a fixed pressure, there is a peak in the equilibrium temperature vs. equivalence ratio plot, whose value is about 1.2. It is worth noting that the peak flame temperature occurs not at stoichiometric, but at a fuel rich condition. This is because the equilibrium temperature is determined not only by the heat generated by the exothermic reaction process, but also by the heat capacity of the product mixture as well. As the equivalence ratio becomes slightly above 1, the gas temperature increases further with the equivalence ratio; this is because the heat capacity of products decreases more rapidly than the heat released. Beyond the equivalence ratio associated with the peak temperature (about 1.2), the heat generated falls more rapidly than does the heat capacity, and the temperature decreases. On the other hand, when the equivalence ratio is fixed, the equilibrium temperature increases with pressure. The primary cause of the equilibrium temperature variation with pressure is the product dissociation because higher pressure favors larger molecules (Le Chatelier's principle). Further increase in pressure results in an increase in H_2O with respect to H_2 and O and helps to increase temperature.

2. The higher the equivalence ratio, the smaller the total mass flow rate is needed to achieve the same combustion pressure to choke the flow. On the other hand, under the same equivalence ratio, the combustion pressure increases linearly with the total mass flow rate. These observations can be explained by the following equation:

$$\dot{m}_g \;=\; \rho_g v_g A \;=\; \mathrm{M}P\sqrt{\frac{\gamma \bar{M}_{pr}}{RT_g}}A \;=\; \frac{\mathrm{M}P\gamma A}{a} \qquad (2.29)$$

Note that the combustion process tends to increase the total number of moles in the product mixture and to decrease the average molecular weight. In the fuel rich case, the total amount of dissociation becomes significant and the molecular

47
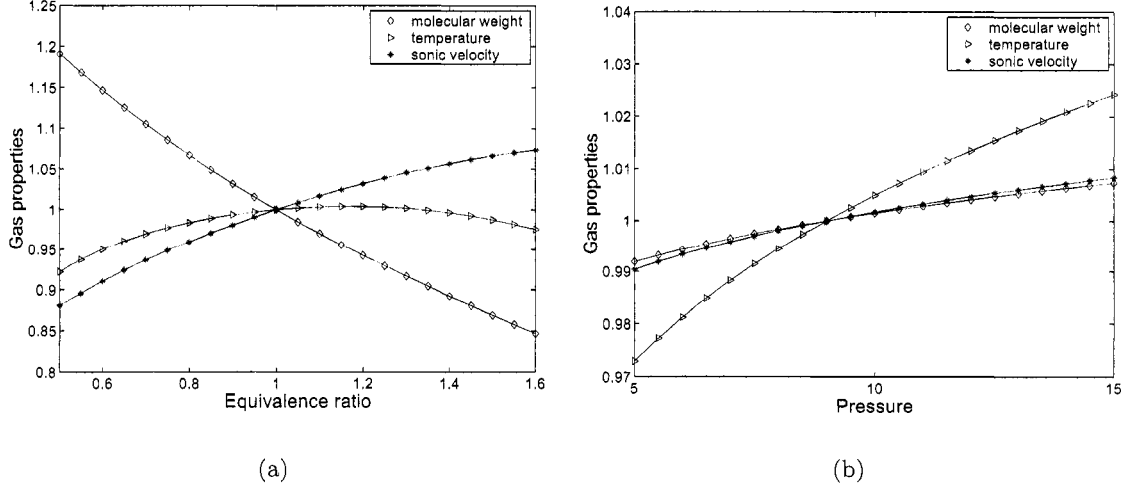
Figure 2.7: Normalized average molecular weight, temperature, and sonic velocity at the throat of the nozzle under operating conditions: $P = 5$ - 15 bar and $\varphi = 0.5$ - 1.6. Normalization is done with respect to the corresponding gas properties under operating conditions: $P = 9$ bar and $\varphi = 1.0$ (Table 2.3).

weight decreases continuously as φ increases. Referring to Figure 2.7, when φ increases from 0.5 to 1.6 with a fixed P, while T varies less than 10%, $\bar{M}_{pr}$ decreases about 30% following a nearly linear function, and as a consequence, M_{pr}/T decreases monotonically. Therefore, $\dot{m}_g$ decreases monotonically as φ increases. When the combustion pressure increases with a fixed φ, both $\bar{M}_{pr}$ and T increase slightly because the product dissociation is suppressed. Because $\sqrt{\bar{M}_{pr}/T}$ varies less than 2% in the pressure range of interest, the total mass flow rate of gas is roughly proportional to the combustion pressure. Eq.2.29 also indicates that the pressure can be increased by (1) increasing the total mass flow rate of the gas, and (2) increasing the equivalence ratio.

3. The gas density at the nozzle throat can increase by increasing the combustion pressure and decreasing the equivalence ratio. This can be explained by the

expression $\rho = \gamma P / a^2$. However, the gas velocity at the nozzle throat, where the Mach number is one, is mainly a function of the equivalence ratio and changes little with the combustion pressure, as previously discussed.

4. The momentum flux at the throat of the nozzle is independent of the equivalence ratio and is a linear function of the combustion pressure. The influence of pressure on momentum flux can be explained by the following equation:

$$\rho_g v_g^2 = \rho_g \mathbf{M}^2 a^2 = \rho_g \mathbf{M}^2 \left(\sqrt{\gamma P / \rho_g} \right)^2 = \mathbf{M}^2 \gamma P \qquad (2.30)$$

where γ is nearly a constant and $\mathbf{M}$ mainly depends on the geometrical configuration of the nozzle. As a consequence, the momentum flux is a nearly linear function of the gas pressure. Eq.2.30 is also applicable to the HVOF systems which include air in the feed stream.

Because the drag force, which is the dominant force that determines the motion of the particles in the gas field, is approximately proportional to the gas momentum flux, and the gas temperature, whose difference from the particle temperature provides the driving force for particle heating, it follows from the above analysis that particle temperature and velocity can be nearly independently adjusted by manipulating the equivalence ratio and the combustion pressure, respectively.

2.4.2 Analysis of gas dynamics with the air stream

Motivated by the conclusions drawn from the above parametric analysis, we included air in the feed stream to the HVOF process; this makes the process analysis more difficult. Assuming the air is composed by O_2, N_2, and Ar only, the reaction formula becomes

$$\varphi C_3 H_6 + 4.5 O_2 + x[N_2 + 1/78 Ar] \Rightarrow \sum_{i \in pr} \xi_i (PR)_i \qquad (2.31)$$

49
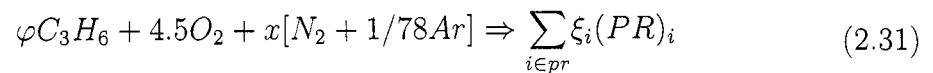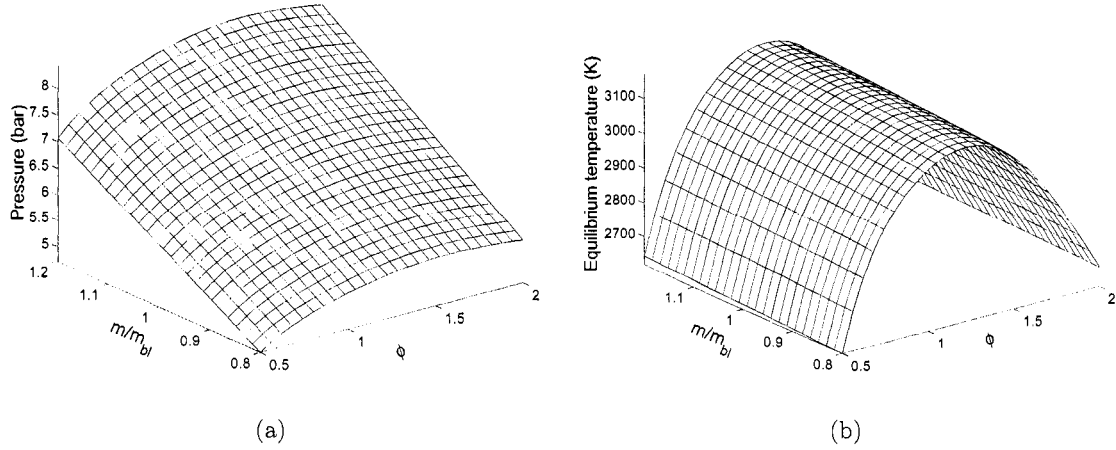
Figure 2.8: Profile of pressure and equilibrium temperature with respect to φ and m/m_{bl}. Operating conditions: x the same as the one in the baseline condition (Propylene: 176 $scfh$ (standard cubic feet per hour), Oxygen: 578 $scfh$, Air: 857 $scfh$, Nitrogen: 28.5 $scfh$), total mass flow rate varying from 0.8 to 1.2 times the one of the baseline value (18.1 g/s), and $\varphi = 0.5 - 2.0$.

where x can be any number from 0 to 16.7, corresponding to the cases of pure oxygen as oxidant and pure air as oxidant, respectively. Obviously, in this case, the equilibrium temperature is not only dependent on φ, but also on x. Furthermore, because the pressure depends on the temperature, the average molecular weight and the mass flow rate (Eq.2.29), the air stream plays an important role in achieving a high pressure.

Figure 2.8 shows the combustion pressure and equilibrium temperature under different total mass flow rates and equivalence ratios for a fixed $x = 3.97$. It can been seen that the process behavior is very similar to the one without air if x is kept constant (compare Figure 2.8 and Figure 2.4). The pressure contour in Figure 2.8(a) shows that the total mass flow rate required to achieve the same combustion pressure decreases as the equivalence ratio increases. The total mass flow rate increases linearly
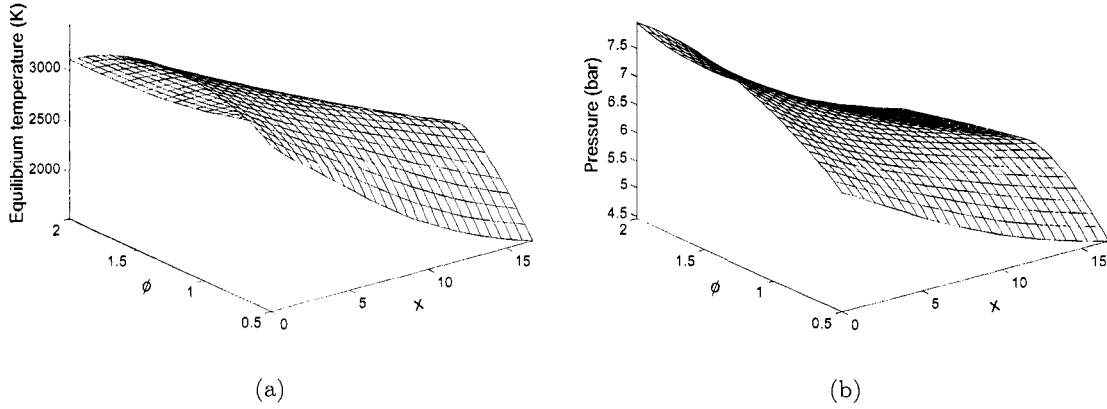
Figure 2.9: Profile of equilibrium temperature and pressure with respect to φ and x. Operating conditions: total mass flow rate the same as the one in the baseline condition, $\varphi = 0.5 - 2.0$, and $x = 0 - 16.7$.

with pressure when the equivalence ratio is fixed. The equilibrium temperature is significantly dependent on the equivalence ratio, but varies slightly with the total mass flow rate. This also implies that pressure variations do not significantly affect the equilibrium temperature.

Figure 2.9 shows the combustion pressure and equilibrium temperature under different equivalence ratios and oxygen/nitrogen ratios with a fixed total mass flow rate that is equal to the one in the baseline condition. It can been seen that as the fraction of air in the whole reactant mixture increases, both pressure and temperature drop. As x varies from 0 (pure oxygen as oxidant) to 16.7 (pure air as oxidant), the equivalence ratio corresponding to the peak equilibrium temperature decreases from 1.23 to 1.05 (see Figure 2.10); this result provides a way to optimally manipulate the relative flow rate of oxygen to air.

We tested the gas dynamics under nine different operating conditions shown in
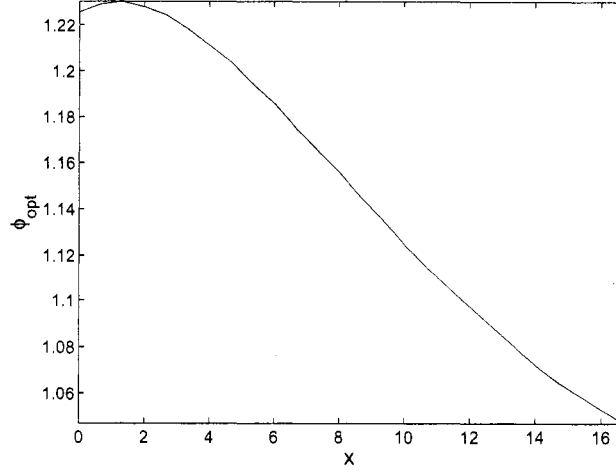
Figure 2.10: Profile of optimal equivalence ratio corresponding to the peak temperature of the gas with respect to x. Operating conditions: total mass flow rate the same as the one in the baseline condition, $x = 0$ - 16.7.

Table 2.4. The baseline condition is recommended by the manufacturer. The simulation results are given in Table 2.5. Under the baseline conditions, the pressure at the exit of the air cap calculated by the proposed procedure is 0.63 *bar*, which implies that the flow outside the gun is overexpanded. The manufacturer, Sulzer Metco measured a gauge pressure of -4 *psig* (-0.3 *bar*, or the absolute pressure is about 0.7 *bar*) at the nozzle exit under the same operating conditions [131], which validated the model and assumption applied in this work. In fact, the overexpanded flow condition gives a slightly higher gas velocity.

In the nine different operating conditions, the equilibrium temperature is a function of the total mass flow rate, as well as a function of φ and x. For instance, cases 1, 6, 7, 8, 9 have the same x (about 4.0), under which the equivalence ratio associated with the peak temperature is around 1.2 according to our previous discussion. Equilibrium temperature in case 7 is the lowest because its equivalence ratio is only 0.7. Although the equivalence ratios in cases 2 and 6 are quite different, the

52

Table 2.4: Different operating conditions.

Case	O_2 scfh	C_3H_6 scfh	Air scfh	N_2 scfh	$\dot{m}$ kg/s	φ	x
1 (baseline)	578.0	176.0	857.0	28.5	18.10	1.045	3.969
2 ($Air\uparrow$ 33%)	578.0	176.0	1139.8	28.5	20.98	0.969	4.895
3 ($Air\downarrow$ 33%)	578.0	176.0	574.2	28.5	15.22	1.134	2.885
4 ($O_2\uparrow$ 33%)	768.7	176.0	857.0	28.5	20.24	0.835	3.171
5 ($O_2\downarrow$ 33%)	387.3	176.0	857.0	28.5	15.95	1.396	5.303
6 ($C_3H_6\uparrow$ 33%)	578.0	234.1	857.0	28.5	18.95	1.390	3.969
7 ($C_3H_6\downarrow$ 33%)	578.0	117.9	857.0	28.5	17.24	0.700	3.969
8 ($\dot{m}\uparrow$ 33%)	768.7	234.1	1139.8	37.9	24.07	1.045	3.969
9 ($\dot{m}\downarrow$ 33%)	387.3	117.9	574.2	19.1	12.13	1.045	3.969

Table 2.5: Gas properties for different operating conditions.

Case	P_{eq} bar	T_{eq} K	M_{pr} $10^{-3}kg/mol$	T_t K	ρ_t kg/m^3	v_t m/s	$(\rho v^2)_t$ $10^5 kg/m/s^2$
1 (baseline)	6.79	3128	26.1	2812	0.428	1050	4.72
2 ($Air\uparrow$ 33%)	7.66	3056	26.8	2747	0.509	1023	5.33
3 ($Air\downarrow$ 33%)	5.89	3197	25.0	2874	0.349	1083	4.09
4 ($O_2\uparrow$ 33%)	7.47	3112	26.8	2802	0.487	1032	5.19
5 ($O_2\downarrow$ 33%)	5.98	3008	25.0	2693	0.376	1054	4.18
6 ($C_3H_6\uparrow$ 33%)	7.34	3128	24.4	2805	0.433	1087	5.11
7 ($C_3H_6\downarrow$ 33%)	6.05	2925	27.9	2630	0.436	982	4.21
8 ($\dot{m}\uparrow$ 33%)	9.06	3159	26.1	2842	0.567	1054	6.30
9 ($\dot{m}\downarrow$ 33%)	4.52	3084	26.0	2772	0.288	1045	3.15

temperatures are almost the same. This is because these two equivalence ratios are located in opposite sides of the optimal equivalence ratio and the total mass flow rates differ slightly. Temperatures are quite different in cases 5 and 6 although the equivalence ratios are very close because the mass flow rates are different. Note that a higher mass flow rate favors higher pressure, and accordingly, higher equilibrium temperature. Case 3 has the lowest x and an equivalence ratio close to the optimal one, as a consequence; its equilibrium temperature is the highest, compare to cases 1 and 2, even when the total mass flow rate is low.

On the other hand, the combustion pressure under the above operating conditions is roughly a linear function of the total mass flow rate and changes little with the gas composition. This is because the average molecular weight of the reaction product mixture is 24-28$\times 10^{-3}$ kg/mol, and the temperature is 2.9-3.1$\times 10^3$ K. Consequently, the sonic velocity does not vary much and the pressure is proportional to the total mass flow rate (which is in agreement with Eq. 2.29).

2.4.3 Analysis of particle velocity and temperature

In the fabrication of nanostructured coatings, it is crucial to maintain high particle temperature at the point of impact on the substrate and to prevent particles from being superheated at the same time, because it is precisely the small grain size that contributes to the superior qualities of nanostructured coatings [23]. It is also of great importance to maintain high particle velocity at the point of impact on substrate since the higher the particle velocity, the denser the coating. We simulated the Diamond Jet hybrid HVOF process model under the baseline operating conditions given in Table 2.4 for Nickel (particle properties are given in Table 2.6) and the results for the in-flight particle velocity, temperature and melting ratio are shown

Table 2.6: Thermophysical properties of powder particles.

Powder	Ni
Density (kg/m^3)	8900
Specific heat$(J/kg/K)$	471
Melting point (K)	1727
Latent heat (J/kg)	3×10^5
Diameter (μm)	1-100

in Figure 2.11. Particles of small sizes may reach very high velocities during flight, however, their velocities drop more sharply than those of larger particles because of their smaller momentum inertias. Furthermore, they may be heated to the melting point in a short time and be fully melted during flight, however, they may eventually be in a coexistence state of liquid and solid or even in a solid state after a long enough distance. Smaller particles tend to change their temperatures easily because of their smaller thermal inertias. For particles of large sizes, however, their period for acceleration and heating are both longer, and their velocity (or temperature) profiles become nearly flat as they approach the same velocity (or temperature) of the gas. In addition, they may not reach the melting point and be in solid state during the entire flight. However, particles of medium sizes may become partially melted during flight.

To further understand the behavior of particles in the HVOF process, we also plotted the velocity, temperature and melting ratio at the 0.254 m standoff as a function of particle size, shown in Figure 2.12 (note the configuration of each figure may vary with different spray distances). Under the baseline operating conditions, particles in the size range of 9 - 30 μm hit the substrate as liquid droplets. Particles of sizes larger than 49 μm or less than 5 μm are in solid state at the point of impact on substrate. Other particles, however, when reach the substrate, are in a semi-molten

55
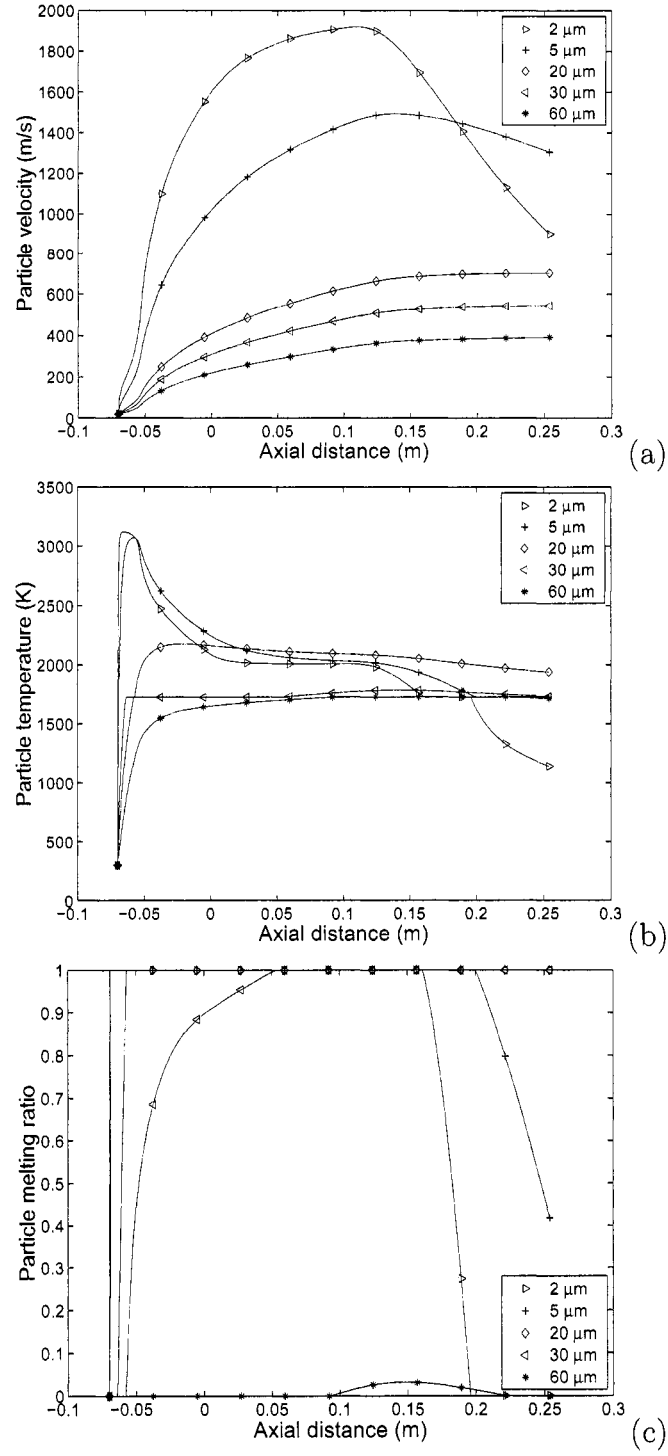
Figure 2.11: Profiles of particle velocity, temperature, and melting ratio along the flow field ($x = 0$ corresponds to the nozzle exit).
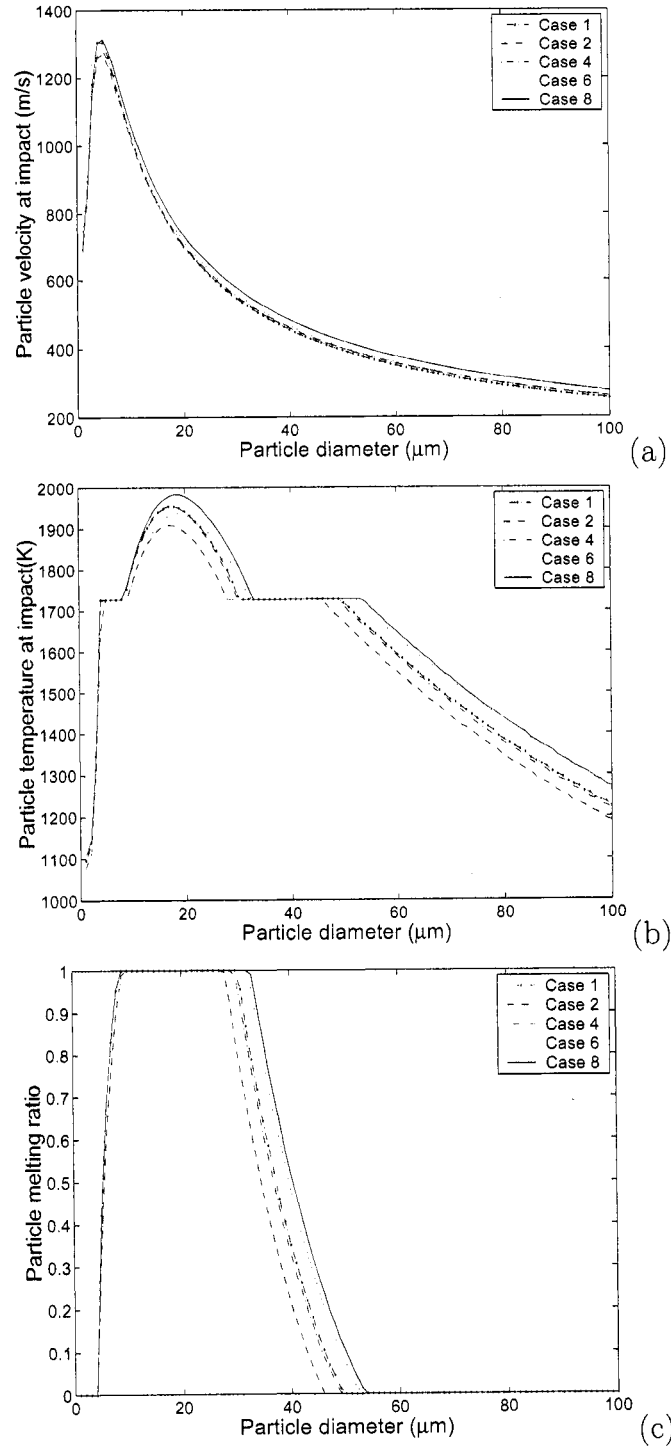
Figure 2.12: Velocity, temperature and melting ratio at the 0.254 m standoff (point of impact on substrate) as a function of particle size.

state (where both liquid and solid coexist). It is worth pointing out that, although both very small particles and very big particles hit the substrate in partially molten state or even solid state, their microstructure is not the same because the former ones have been fully melted during flight.

Figure 2.13 shows the influences of particle injection velocity and spray distance on the profiles of particle velocity and temperature and flight time. It is shown that both disturbances have a minimal effect on particle velocity. However, their influence on particle temperature and melting behavior, can not be neglected. This behavior can be explained by the changes of residence time of particles in the gas flow field. An increase in the particle injection velocity will result in a decrease of particle residence time, especially in the high temperature zone. This is why larger size particles are affected to a larger extent. An increase in the spray distance, however, has a greater influence on the temperature of smaller particles. This is because larger particles have greater thermal inertia and do not change their temperature very much after they reach the gas temperature.

2.4.4 Modeling of powder size distribution

The fact that particle temperature and velocity at the point of impact on substrate depend strongly on particle size implies that particle size of the feedstock is one of the key parameters deciding coating quality. This property, together with the significant polydispersity of most powders used in the thermal spray process, motivates accounting for the effect of powder size distribution in the process model, the control problem formulation and the controller design. Previous experimental work [114, 103]) has shown that lognormal functions can adequately describe the size distribution of many powders used in the HVOF process. To this end, a lognormal
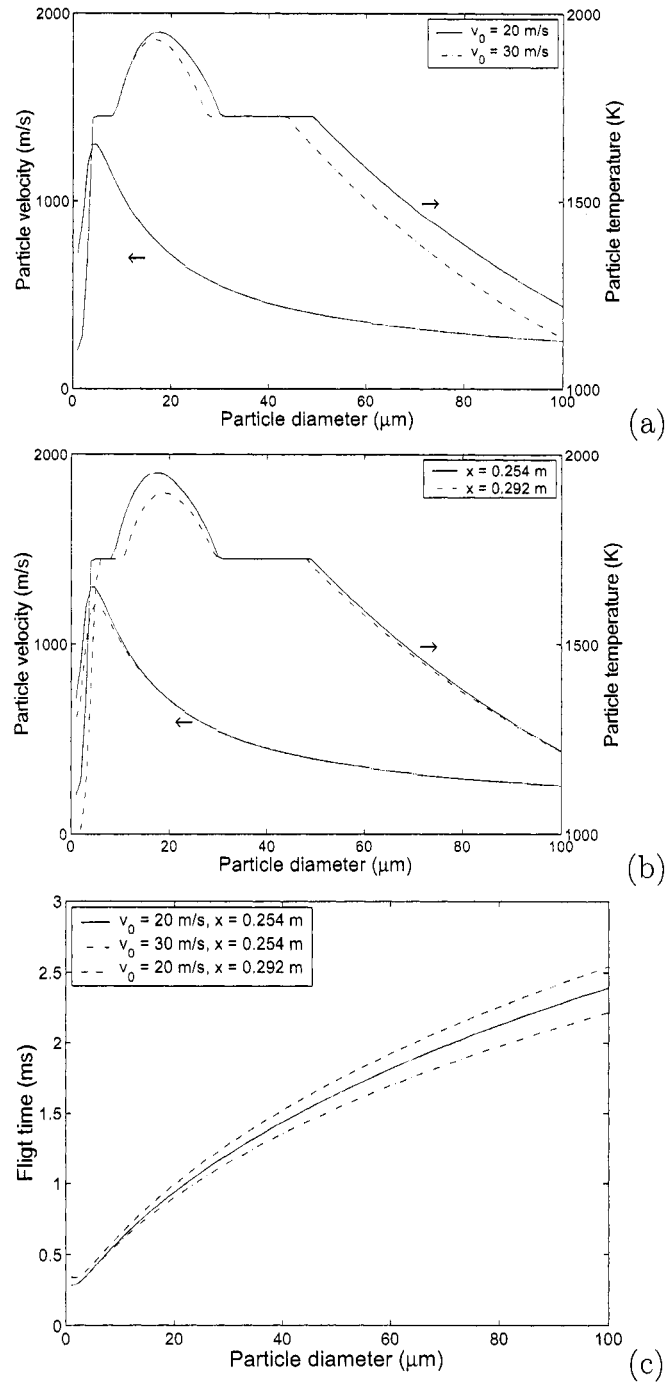
Figure 2.13: Effect of disturbances on operating conditions (particle injection velocity and spray distance) on particle velocity, temperature and flight time.

function is used to describe the powder size distribution with the following form [32]:

$$f(d_p) = \frac{1}{\sqrt{2\pi}\sigma d_p} \exp\left[-\frac{(\ln d_p - \mu)^2}{2\sigma^2}\right] \tag{2.32}$$

where $f(d_p)$ is the size distribution function, μ and σ^2 are two dimensionless parameters corresponding to the mean and the variance of $\ln d_p$, which obeys the normal distribution. For particles that are lognormally distributed, μ and σ can be determined using the following formulas:

$$\begin{aligned}
\mu &= \ln \sqrt[3]{d_{10}d_{50}d_{90}} - 1.831 \left(\ln \sqrt{\frac{d_{90}}{d_{10}}}\right)^2 \\
\sigma &= 0.781 \ln \sqrt{\frac{d_{90}}{d_{10}}}
\end{aligned} \tag{2.33}$$

where d_{10}, d_{50} and d_{90} are three characteristic diameters which can be obtained experimentally [100]. Particle coagulation in the HVOF thermal spray process has not been reported in the literature, which may be explained by the following argument. The average distance between individual particles in the HVOF thermal spray process can be estimated based on the analysis of Crowe et al. [33]. Specifically,

$$\frac{L_d}{d_p} = \left[\frac{\pi}{6}\frac{1+\kappa}{\kappa}\right]^{1/3} \tag{2.34}$$

where L_d is the distance between two particles and κ is the ratio of particle loading to particle/gas density ratio. Usually the particle loading is about 4%, the density ratio is about 10^{3-4}, therefore L_d/d_p is about 20-50, which implies that the individual powder particles can be considered isolated from each other. Therefore, in this work, we assume that particle coagulation is negligible and the powder size distribution does not change during flight.

There are many ways to define average powder properties. For example, they can be averaged with respect to particle number or particle volume. In this work, the average powder properties $(\overline{PP})$ are calculated based on particle volume because

larger particles have a stronger influence on coating properties than smaller ones. Volume-based average powder properties can be computed as follows:

$$\overline{PP} \ = \ \frac{\int_0^\infty \frac{1}{6}\pi d_p^3 PP(d_p)f(d_p)d(d_p)}{\int_0^\infty \frac{1}{6}\pi d_p^3 f(d_p)d(d_p)} \tag{2.35}$$

2.5 Feedback control of HVOF thermal spray process

2.5.1 Control problem formulation and controller design

Based on model predictions and available experimental observations, the control problem for the HVOF process is formulated as the one of regulating the volume-based averages of melting ratio and velocity of particles at the impact on substrate (these are the variables that directly influence coating microstructure and porosity, see modeling and analysis in Chapter 3) by manipulating the flow rates of propylene, oxygen and air at the entrance of the HVOF thermal spray gun. From the analysis in the previous sections, it follows that the gas momentum flux, which is approximately proportional to the drag force, and the gas temperature, whose difference between the particle temperature provides the driving force for particle heating, can be almost independently adjusted by manipulating the combustion pressure and the equivalence ratio. To develop a feedback controller that can be readily implemented in practice, the manipulation of combustion pressure and equivalence ratio is realized by adjusting the flow rate of propylene, $u_1(t)$, oxygen, $u_2(t)$, and air $u_3(t)$. Owing to the almost decoupled nature of the manipulated input/controlled output pairs, two proportional integral (PI) controllers are used to regulate the process. Specially, the

controllers have the following form:

$$\dot{\zeta}_i \;=\; y_{sp_i} - y_i, \;\; \zeta_i(0) = 0, \;\; i = 1, 2$$

$$u'_i \;=\; K_{c_i}\left[(y_{sp_i} - y_i) + \frac{1}{\tau_{c_i}}\zeta_i\right] + u'_{0_i}, \;\; i = 1, 2 \qquad (2.36)$$

$$\{u_1, u_2, u_3\} \;=\; f(u'_1, u'_2, x)$$

where y_{sp_i} is the desired set-point value and y_i is the value of the output obtained from the measurement system (y_1 is the volume-based average of particle velocity and y_2 is the volume-based average of particle melting ratio). u'_1 is the combustion pressure and u'_2 is the equivalence ratio. K_{c_i} is the proportional gain and τ_{c_i} is the integral time constant of the ith controller. The third equation makes use of the process model. To keep the problem simple, the ratio of air to oxygen (or x) is fixed. We note that the relationship between the gas temperature and the equivalence ratio is not monotonic. Beyond the optimal equivalence ratio (about 1.2 for $x = 3.97$), the gas temperature decreases as the equivalence ratio increases. Therefore, K_{c_2} and τ_{c_2} should be replaced by $-K_{c_2}$ and $-\tau_{c_2}$ when the equivalence ratio is above this value. The design of a model-based feedback control system, employing nonlinear control techniques for particulate processes, [26, 27, 43, 30, 85, 86, 87] as well as applications of the control system to an experimental system, will be the subject of future work.

Regarding the practical implementation of the proposed control system (see Figure 2.14) on the Diamond Jet hybrid HVOF thermal spray, we note that the chamber pressure and the equivalence ratio can be readily manipulated in real-time by adjusting the mass flow rates of fuel, oxygen and air. The velocity and temperature of individual particles can be measured experimentally using non-intrusive optical techniques, for example, Laser Doppler Velocimetry [50], Particle Imaging Velocimetry [93, 183], and Two Color Pyrometry [177, 66, 48]. However, it is not possible to directly measure the degree of melting of individual particles and consequently, the average degree of melting of the entire particle size distribution. To overcome this
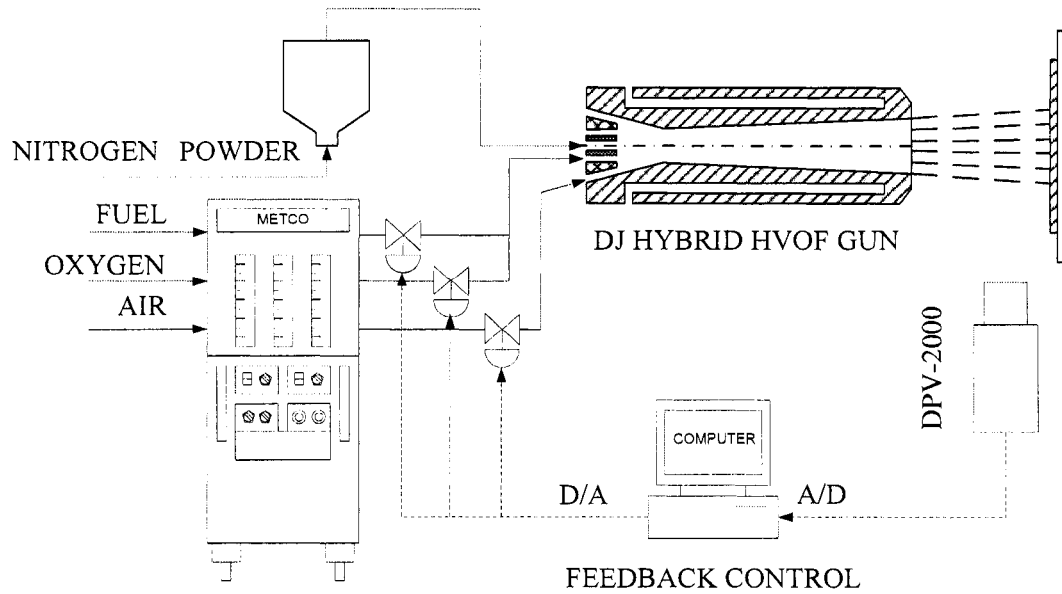
Figure 2.14: Schematic of the proposed feedback control system.

limitation, one needs to use an estimation scheme based on the modeling equations that describe the evolution of particle temperature, velocity and degree of particle melting coupled with the available gas phase measurements to estimate average particle melting ratio at the point of impact on the substrate. The estimates obtained by this model can be further improved through comparison with the particle temperature measurements at various locations across the free jet. In the simulation section, we have included a closed-loop simulation in the presence of measurement errors to evaluate the effect of such errors in closed-loop performance; the detailed development of an estimation scheme for particle melting ratio is the subject of future work. The controller then obtains information from the measurement system, and makes decisions, which are sent to the controlled valves (total flow of gases to the process and oxygen/fuel ratio), to adjust the manipulated input variables until the deviation of the controlled outputs from their corresponding set-point values falls within a tolerable region. One of the great advantages of feedback control is that it

Table 2.7: Process and controller parameters used in the closed-loop simulation.

K_{c_1}	5×10^{-3}
K_{c_2}	0.1
τ_1	5×10^{-2}
τ_2	5×10^{-2}
d_{10}^* (μm)	15
d_{50} (μm)	35
d_{90} (μm)	77
ϕ	1.0

* powders are assumed to be lognormally distributed, and d_{10}, d_{50}, and d_{90} are three characteristic diameters whose corresponding cumulative weight function values are 0.1, 0.5, 0.9.

can compensate for the effect of disturbances in the process operating conditions.

2.5.2 Simulation results of HVOF process model under feedback control

In this subsection, simulation runs of the closed-loop system are presented. The outputs $y_1(t)$ and $y_2(t)$ are computed by averaging the individual particle velocity and melting ratio data obtained from the process model. To account for the powder size distribution, we first fit a lognormal distribution and calculate the size range in order to capture more than 99wt% of all the particles. We then divide this size range into 100 intervals to perform the integration (Further increase on the number of discretization intervals did not change the accuracy of the computed results) [109, 108]. This requires solving simultaneously 400 ordinary differential equations for each process simulation. The parameters used in the closed-loop system simulations are shown in Table 2.7.

Several simulation runs of the process model under the feedback controller were performed to evaluate the ability of the controller to: a) drive the melting ratio

64

Figure 2.15: Profiles of controlled outputs (average particle velocity and melting ratio), manipulated inputs (flow rate of propylene, oxygen and air), and total mass flow rate and equivalence ratio, under the request of 5% increase in average particle velocity and 5% decrease in the melting ratio - Control problem formulation accounts for the effect of powder size distribution.

and velocity of particles at the point of impact on substrate to desired set-point values, b) attenuate the effect of disturbances on process operating conditions, and c) compensate for the effect of measurement errors. The first simulation studies the behavior of the closed-loop system in the presence of changes in the set-point. Initially, the process is assumed to operate at the baseline condition, and at time $t = 10$ sec, the average particle velocity set-point value increases by 5% and the average particle melting ratio set-point value decreases by 5%. Figure 2.15 shows how the controlled outputs and manipulated inputs as well as the total mass flow rate and the equivalence ratio respond in the case of requesting such changes in the set-point values. The feedback controller drives the controlled outputs to the new set-points in about 10 sec (note that 10 sec is the time needed for the controlled outputs to reach the new set-point values, not the time for the particles to hit the substrate, which is on the order of 10^{-3} sec). In a typical HVOF process, the powder feed rate is in the range 20-80 g/min and the thickness of a coating is about 100 - 300 μm [141]. The deposition efficiency of HVOF process is around 70% [179]. Considering the deposition of a coating on a 0.5 m × 0.5 m substrate, the deposition time can be estimated by the following formula:

$$t = \frac{200 \times 10^{-6}m \times 0.5m \times 0.5m \times 8900kg/m^3}{50 \times 10^{-3}kg/min \times 0.7} = 12.7 \ min \qquad (2.37)$$

For a coating with a larger area, the deposition time is even longer, which means that the controller is quite effective (compared with a typical time needed for a full coating) and validates the feasibility of implementation of feedback control on the HVOF process. Note that in the first 0.8 sec, the liquid ratio increases when the equivalence ratio decreases. This is because in this time period the mass flow rate and the pressure increase by 22% and 21% while the equivalence ratio decreases by 6%. As a result, the increase in gas temperature resulting from the increased pressure

outweighs its decrease resulting from the lower equivalence ratio.

To demonstrate that the proposed formulation of the control problem, which explicitly accounts for the effect of powder size distribution, leads to a solution of the control problem that is superior (with respect to the control action needed to achieve the desired control objectives) to a solution that assumes a monodisperse powder size distribution, the two PI controllers are also implemented on the process model using the same controlled outputs but assuming that the velocity and temperature measurements are based on a single particle whose size is taken to be $d_p = 35 \ \mu m$, which is equal to the d_{50} value of the powder size distribution used in our simulation. The corresponding controlled and manipulated variables are given in Figure 2.16. The results show that the desired objectives of 5% change in the set-point values are not achieved (compare the controlled output profiles of Figure 2.15, where the desired set-point change is achieved); this occurs because, as it has been previously shown [109], the behavior of an individual particle is insufficient to represent that of the entire powder size distribution. This makes clear the need to account for the effect of powder size distribution in the control problem formulation and solution.

To test the robustness of the proposed control problem formulation and of the feedback controller, the problem of controlling the HVOF process in the presence of disturbances was studied. Figures 2.17 and 2.18 show the controlled output and manipulated input profiles in the presence of disturbance (20% increase and 20% decrease, respectively) in the spray distance which occurs at t $= 10$ *sec*. Without control, the process jumps to a new steady state in a very short time (owing to the very short time of particle fight), the particle velocity in both cases drop instantaneously. The reason is that the particles are usually accelerated first and then decelerated in the external field and therefore there is an optimal spray distance. Nevertheless, the
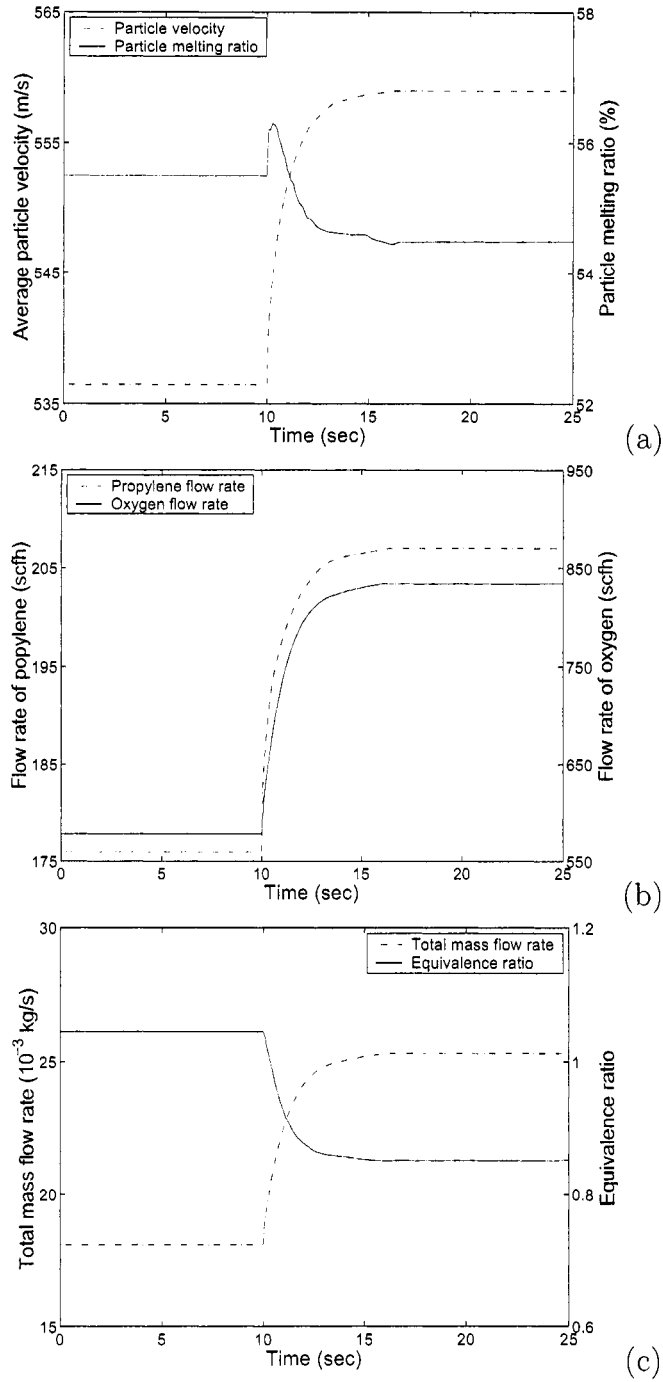
Figure 2.16: Profiles of controlled outputs (average particle velocity and melting ratio), manipulated inputs (flow rate of propylene, oxygen and air), and total mass flow rate and equivalence ratio, under the request of 5% increase in average particle velocity and 5% decrease in the melting ratio - Control problem formulation does not account for the effect of powder size distribution.

68
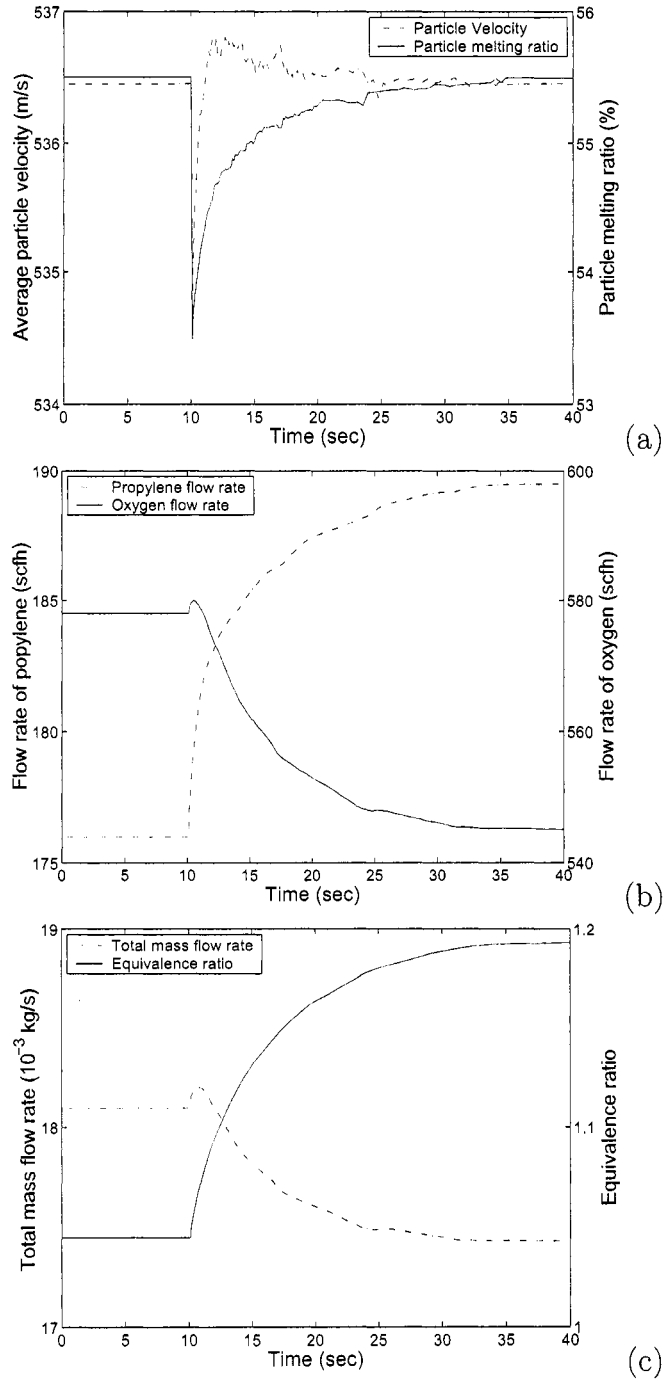
Figure 2.17: Profiles of controlled outputs (average particle velocity and melting ratio), manipulated inputs (flow rate of propylene, oxygen and air), and total mass flow rate and equivalence ratio, in the presence of disturbance (20% increase) in the spray distance.
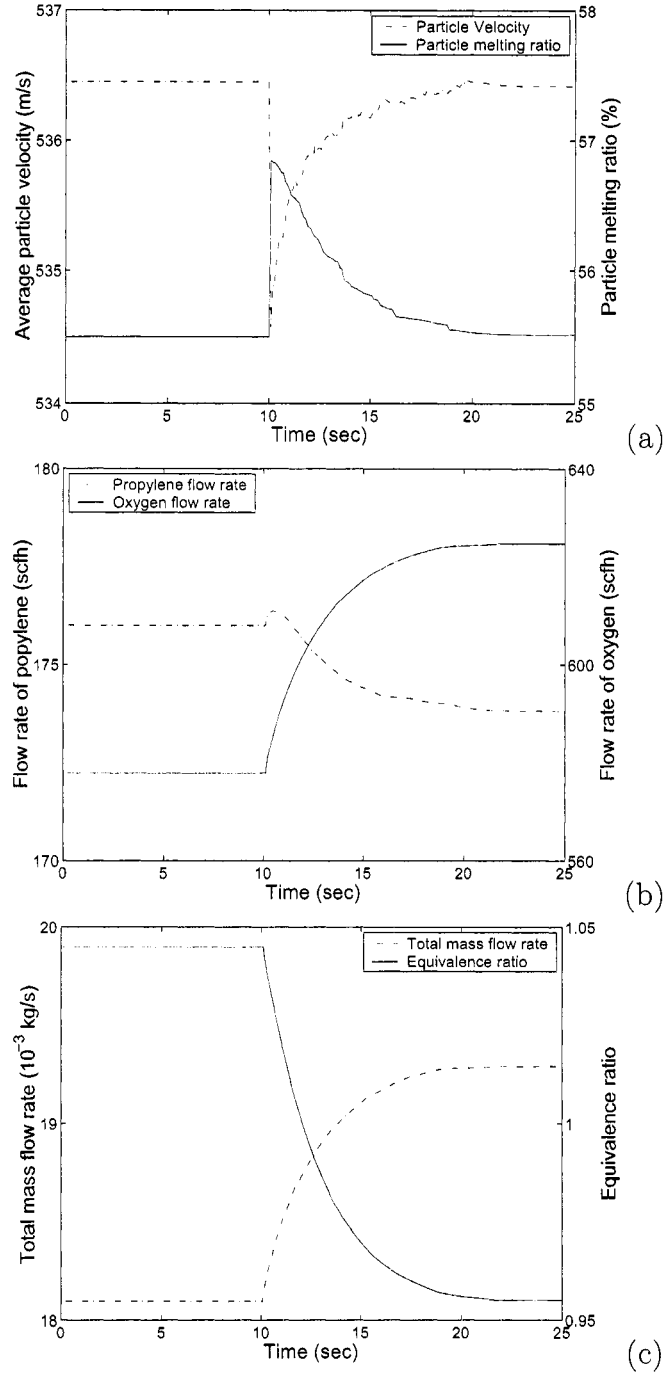
Figure 2.18: Profiles of controlled outputs (average particle velocity and melting ratio), manipulated inputs (flow rate of propylene, oxygen and air), and total mass flow rate and equivalence ratio, in the presence of disturbance (20% decrease) in the spray distance.

disturbances in spray distance do not have a significant effect on particle velocity because the velocity profile of particles is almost flat as they reach the gas velocity. However, the melting ratio of particles at the point of impact on substrate decreases in the former case and increases in the latter case, which can be explained by the change in residence time of particles in the gas flame. Such variations in the molten state of the particle may have a detrimental effect on the coating microstructure evolution. Under feedback control, the manipulated inputs drive the process outputs to their original steady state values in 10 - 25 *sec*. It is also interesting to see how the controller responds to compensate for this velocity decrease. While it is intuitively expected that the mass flow rate increases in the latter case to increase the particle velocity, the total mass flow rate in the former case decreases to drive the particle velocity to its original value. This is because the equivalence ratio increases all the time and the pressure increases even as the total mass flow rate decreases.

Figures 2.19 and 2.20 show the controlled output and manipulated input profiles in the presence of disturbances (10% increase and 20% decrease, respectively) in initial particle velocity at t = 10 *sec*. Without control, the system jumps to a new steady state in a very short time. While the particle velocity changes little in both cases, the particle melting behavior varies a lot. The changes of particle temperature in both cases can be explained by the residence time of particles in the flame gas, which is caused by the variation of the particle velocity along the flight, although the particle velocity at the point of impact remains nearly the same. Under feedback control, the manipulated inputs drive the process outputs to their original steady state values in about 20 *sec*.

Another source of disturbance to the process operation, especially in an industrial environment, is the variation of the size distribution of the powder during the
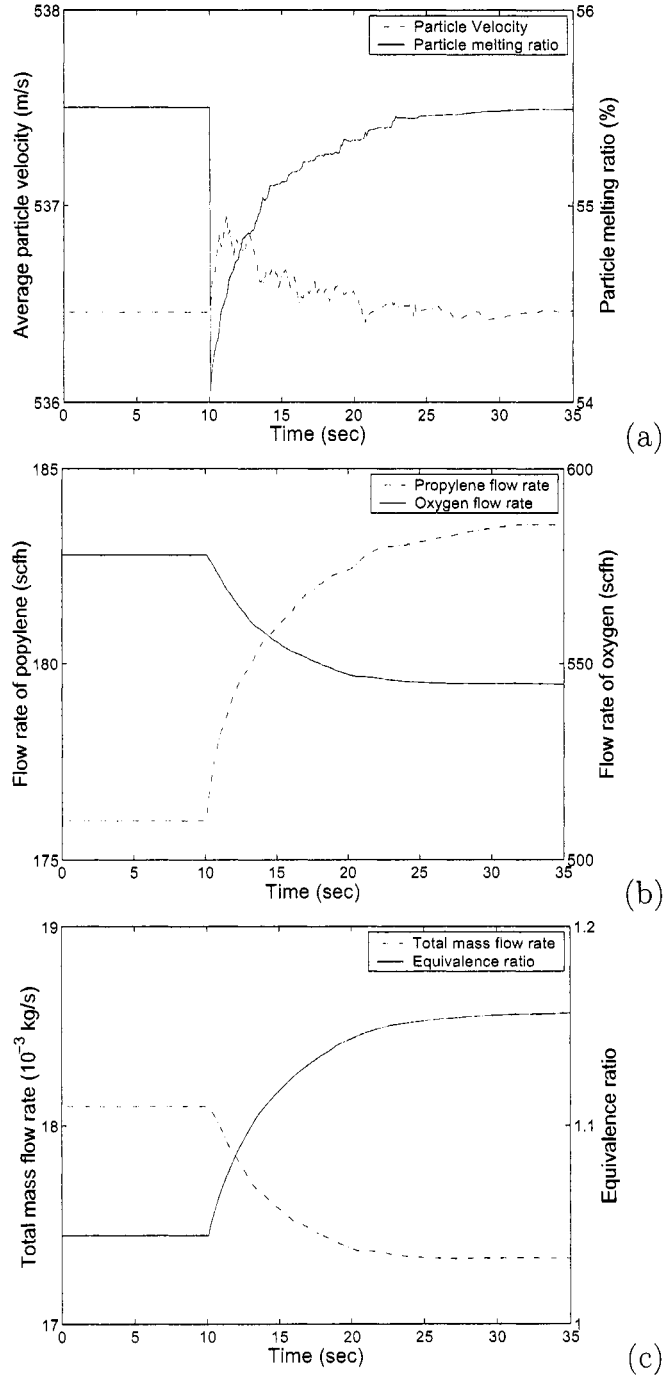
Figure 2.19: Profiles of controlled outputs (average particle velocity and melting ratio), manipulated inputs (flow rate of propylene, oxygen and air), and total mass flow rate and equivalence ratio, in the presence of disturbance (10% increase) in particle injection velocity.
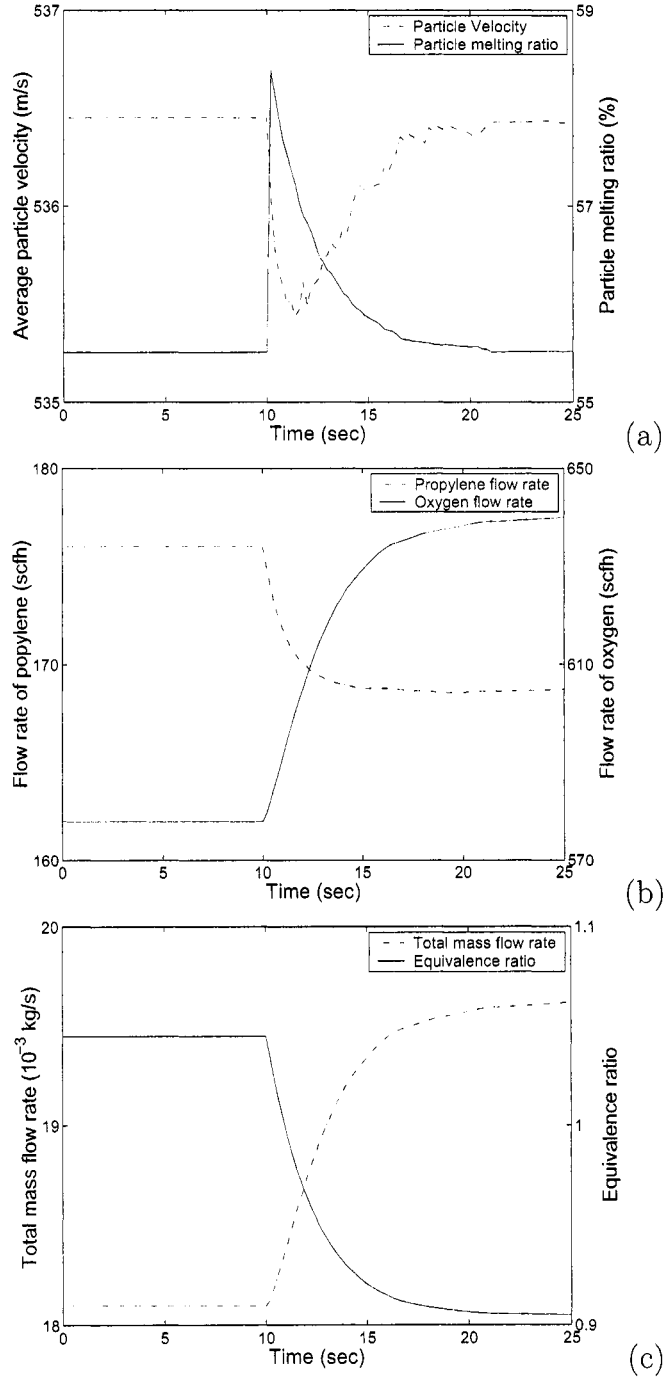
Figure 2.20: Profiles of controlled outputs (average particle velocity and melting ratio), manipulated inputs (flow rate of propylene, oxygen and air), and total mass flow rate and equivalence ratio, in the presence of disturbance (20% decrease) in particle injection velocity.

operation of the HVOF process. This may have a significant influence on the particle velocity and particle temperature at the point of impact on the substrate based on the analysis of the previous sections. In the following simulation, it is assumed that the process is at steady state in the first 100 sec and then the powder size distribution changes gradually (specifically, in the following calculation, μ increases according to the expression $\mu = \mu_0[1 + 0.03(1 - e^{-t/100})]$ and σ^2 is kept constant). Figure 2.21 shows the controlled outputs and the manipulated inputs as well as the total mass flow rate and the equivalence ratio in the presence of such a variation in the powder size distribution. Under feedback control, both particle velocity and melting ratio fluctuate in a very narrow range around the desired set-point values. We note that φ changes rather sharply compared to the change in $\dot{m}_{Fuel}$ and $\dot{m}_{O_2}$ because both $\dot{m}_{Fuel}$ and $\dot{m}_{O_2}$ have an influence on φ ($\varphi = \dot{m}_{Fuel}/\dot{m}_{O_2} \times 4.5$). For example, φ will go up sharply if $\dot{m}_{Fuel}$ increases while $\dot{m}_{O_2}$ decreases and go down sharply in the opposite case. When no control is used, in which case the flow rate of each stream is kept constant, both velocity and melting ratio of particles decrease with time, which may have an undesirable effect on the resulting coating properties.

To demonstrate that the proposed formulation of the control problem is robust with respect to measurement errors, we implemented the developed control system on the process model under the request of 5% decrease in average particle melting ratio set-point value and 5% increase in the average particle velocity set-point value at time $t = 10$ sec but assuming that there are errors in the values of average velocity and degree of melting used in the controller. In the closed-loop simulation, we assume that the estimation errors follow an exponentially-decaying function with an initial error of 10%. The corresponding controlled and manipulated variables are given in Figure 2.22. The results show that the desired control objective of 5% change in
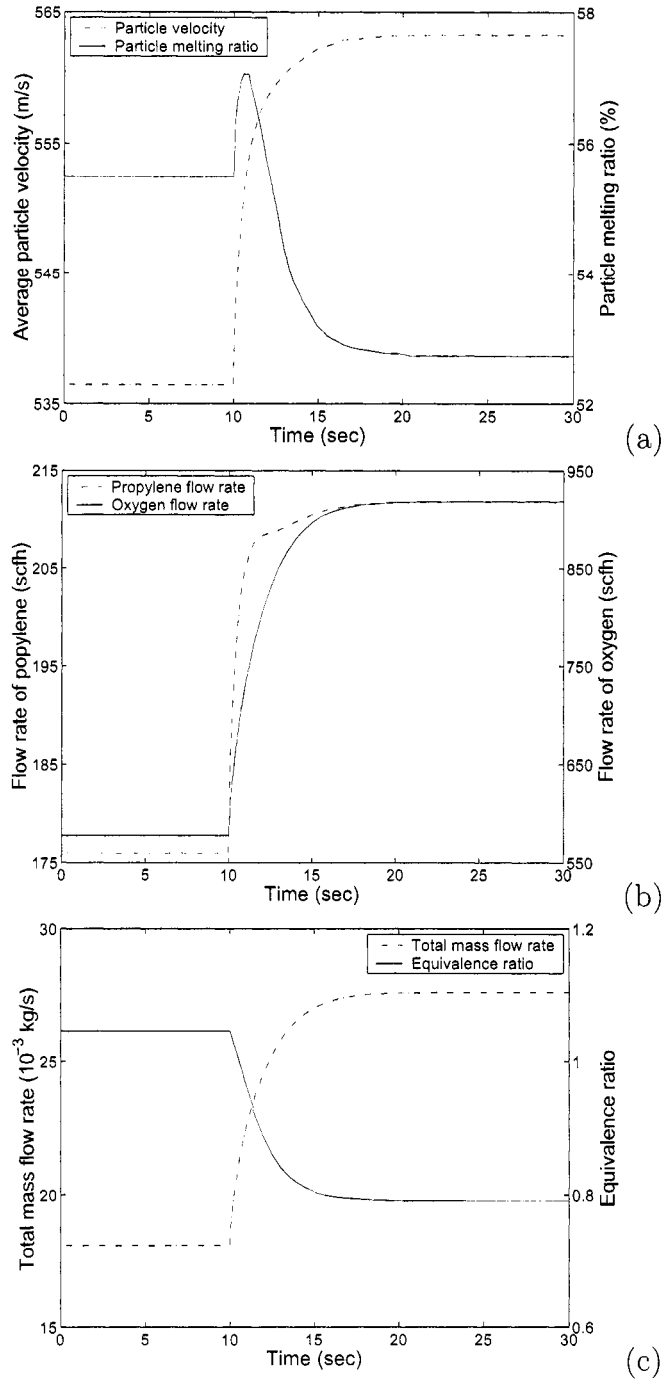
74
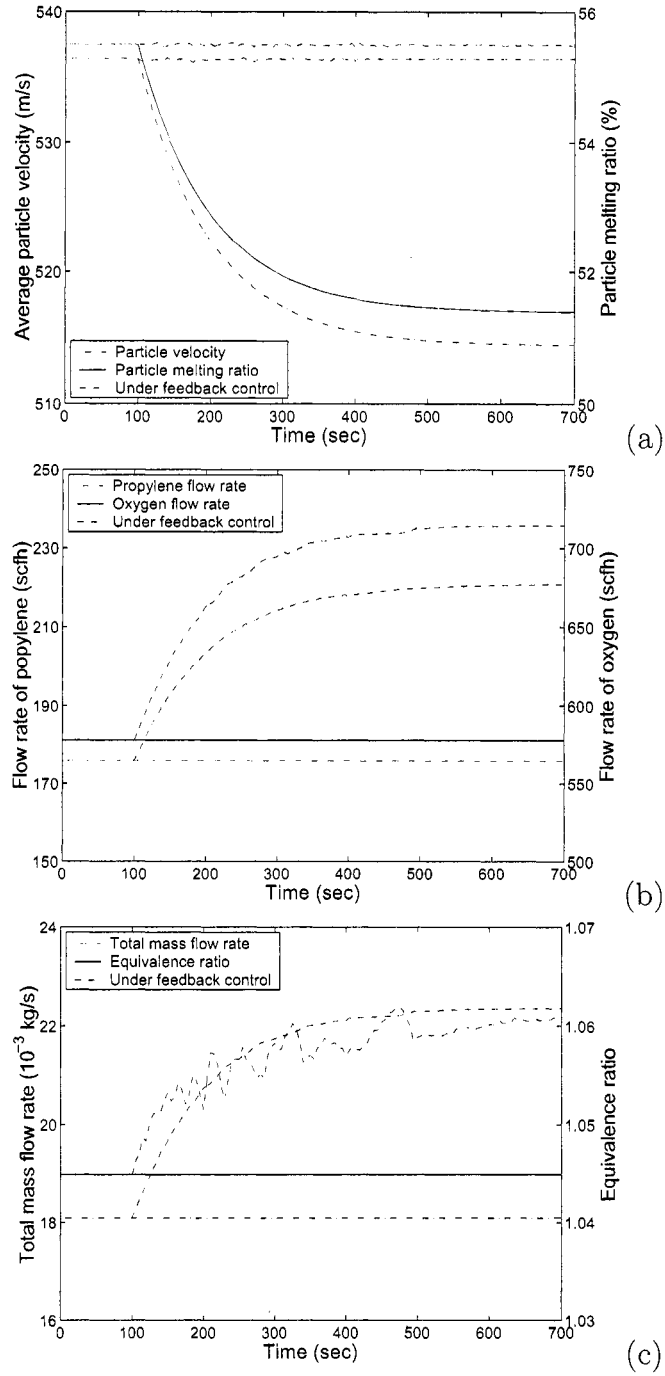
Figure 2.21: Profiles of controlled outputs (average particle velocity and melting ratio), manipulated inputs (flow rate of propylene, oxygen and air), and total mass flow rate and equivalence ratio, in the presence of variation in the powder size distribution.

the set-point values is eventually achieved (compare the controlled output profiles of Figures 2.15 and 2.22); this demonstrates that the proposed formulation of the control problem is robust with respect to measurement errors.

2.6 Conclusions

This chapter presented a fundamental model and a feedback control system for an industrial high velocity oxygen-fuel (HVOF) thermal spray process (Diamond Jet hybrid gun, Sulzer Metco, Westbury, NY). The process model describes the evolution of the gas thermal and velocity fields, the motion and temperature of agglomerate particles of different sizes, and explicitly accounts for the effect of powder size distribution. In addition to providing useful insight into the in-flight behavior of different-size particles, the model was used to make a comprehensive parametric analysis of the HVOF process. This analysis allowed a systematic characterization of the influence of controllable process variables such as combustion pressure, oxygen/fuel ratio, as well as the effect of powder size distribution, on the values of particle velocity and temperature at the point of impact on substrate. Specifically, the study shows that the particle velocity is primarily influenced by the combustion pressure, and the particle temperature is strongly dependent on the fuel/oxygen ratio. These findings are consistent with existing experimental studies and set the basis for the formulation of the control problem for this HVOF process. To develop a feedback controller that can be readily implemented in practice, the control problem was formulated as the one of regulating volume-based averages of the melting ratio and velocity of the particles at the point of impact on the substrate (these are the variables that directly influence coating microstructure and porosity, which, in turn, determine coating strength and hardness) by directly manipulating the flow rate of fuel, oxygen and air at the
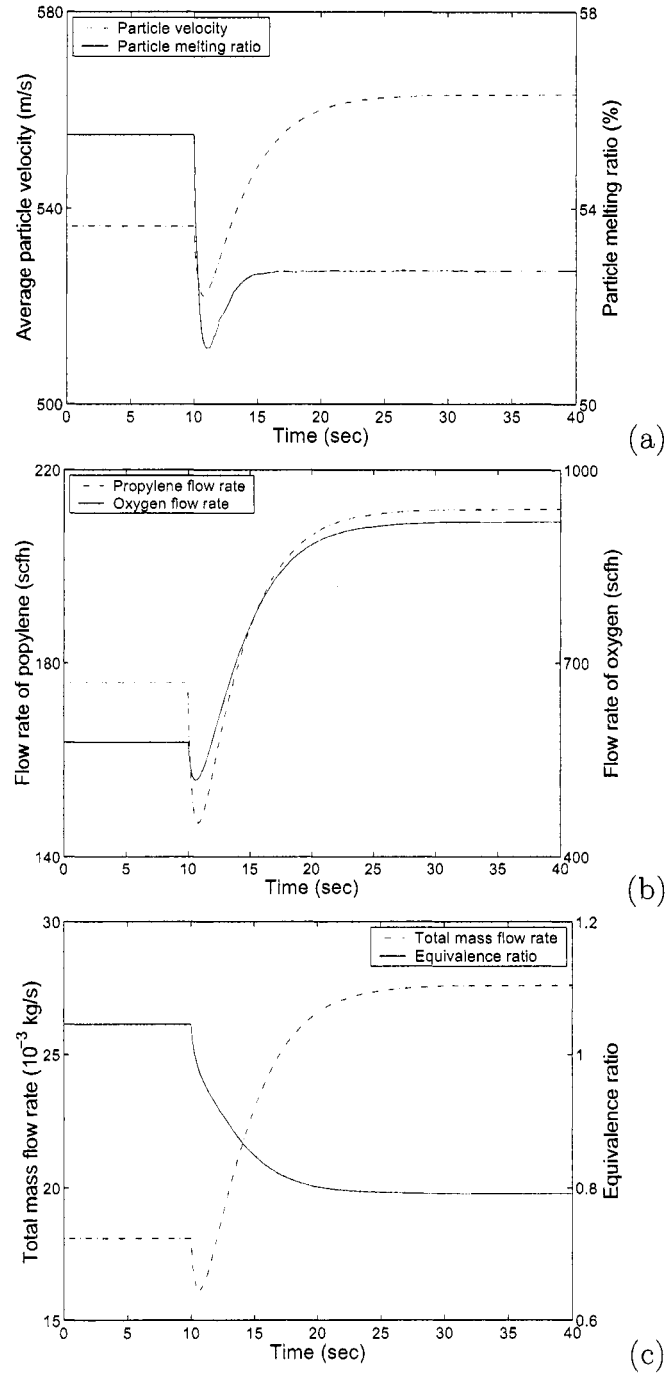
Figure 2.22: Profiles of controlled outputs (average particle velocity and melting ratio), manipulated inputs (flow rate of propylene, oxygen and air), and total mass flow rate and equivalence ratio, under the request of 5% increase in average particle velocity and 5% decrease in the melting ratio - Closed-loop simulation in the presence of measurement error.

entrance of the HVOF gun. A feedback control system was developed and applied to the process model. Closed-loop simulations demonstrated that the particle velocity and melting ratio at the point of impact on substrate reach the desired set-point values in a short time, which validates the feasibility of real-time implementation of feedback control on the HVOF thermal spray system. It was also shown that the proposed control problem formulation and the feedback control system are robust with respect to disturbances in spray distance and particle injection velocity, and variations in powder size distribution.

In the next chapter, we present a mechanistic model which uses information about particle velocity, temperature and degree of melting at the point of impact on substrate from the model developed in this chapter to predict coating porosity and microstructure.

Chapter 3

Diamond Jet Hybrid HVOF Thermal Spray: Rule-Based Modeling of Coating Microstructure

This chapter focuses on computational modeling and simulation of microstructure of coatings produced by an industrial high-velocity oxygen fuel (HVOF) thermal spray process (Diamond Jet hybrid gun, Sulzer Metco, Westbury, NY). Based on the understanding of coating structure and mechanisms of pore formation inside of the coating obtained from experimental studies, a stochastic simulation procedure is used to explore the evolution of the microstructure of the coatings. In the coating growth model, the velocity, temperature and degree of melting of particles hitting on the substrate are determined by a previously developed mathematical model [112] describing gas and particle behavior, and the complex characteristics of the thermally sprayed coatings are captured by applying certain basic rules that encapsulate the main physical features of the deposition process. In addition to providing useful insight into

the pore formation and coating growth, the model is used to make a comprehensive parametric analysis, which allows us to systematically characterize the influence of operating conditions, such as the gas flow rate, spray distance, as well as the effect of particle size, on the particle melting behavior, coating porosity, surface roughness and deposition efficiency. Comparison of simulation results and experimental studies shows that the proposed model can reasonably predict the relationship between macroscopic processing conditions and coating microstructure.

3.1 Introduction

Thermal spray represents a series of particulate deposition processes in which the particles are heated up and propelled in a gas/plasma stream to hit a substrate, forming a thin layer of dense, hard and lamellar-structured coating. Since its development in the early twentieth century, the thermal spray technology has been one of the most cost-efficient means of protecting substrate surfaces, via coating deposition, from wear, corrosion and erosion. The 1980s witnessed the invention of the so-called high-velocity oxygen fuel (HVOF) thermal spray technology, which was a major achievement in the thermal spray industry [141]. Featured with high gas/particle velocity and relatively low gas/particle temperature when compared to plasma spraying, HVOF thermal spray is a powerful tool for the fabrication of coatings of metals, cermets, and composites. On the one hand, the extremely high particle velocity helps to densify the coating and to increase the deposition rate. On the other hand, the very short residence time in the relatively low temperature gas flame makes the powder particles highly plastic and superheating or vaporization is prevented [21, 24, 109, 108]. Nowadays, the HVOF thermal spray has carved out a special niche in the thermal spray industry, particularly in the deposition of nano-

structured coatings, because the nano-crystalline structure of powder particles can be preserved during flight [21].

In order to improve coating repeatability and process performance, much experimental work has been done in the last decade to study the effect of key process parameters such as gas flow rate, fuel/oxygen ratio, and spray distance, on the physical and mechanical properties of HVOF thermally sprayed coatings [30, 36, 60, 64, 71, 120, 113]. The optimization of process parameters involved in these works relies on the conventional Taguchi method, which uses a set of orthogonal arrays that stipulates the way of conducting the minimal number of experiments that could give the full information of all the factors affecting the coating performance parameters [36]. This approach is expensive but reliable for a specific HVOF thermal spray process. However, a lack of fundamental understanding of the dynamics of the gas and particle behavior as well as of the microscopic deposition process significantly restrict its applicability because, the experimentally derived "optimal" solution may be questionable when it is applied to another thermal spray process in which some important parameters, such as the nozzle configuration, powder or fuel type, etc., are different [21]. Mathematical modeling, on the other hand, provides an efficient and versatile alternative to quantify the effect of each one of the key process parameters on coating properties.

In the last decade, significant efforts have been made to simulate the evolution of coating microstructure using mathematical models. For example, stochastic simulation has been applied to model the stochastic deposition and coating growth process in plasma spray [20, 31, 94]. These stochastic models are based on certain rules that govern the splat formation, coating growth and pore formation. Parametric analysis has been made based on these models to study how the coating microstructure

81

and physical properties such as the porosity and roughness, are affected by various process parameters, including the gun scanning velocity, spray angle [20], particle size, gas temperature and velocity [31]. However, the particle temperature, velocity and degree of melting profiles in the plasma spray process are very different from the corresponding profiles in the HVOF thermal spray, and thus, these models cannot be used to predict coating microstructure in the HVOF thermal spray process. Recently, continuum type and stochastic models have been developed to simulate the coating microstructure formation [59, 134] in the HVOF thermal spray process; the continuum type models involve partial differential equations governing particle deformation and spreading. However, in these works, the particles at the point of impact on the substrate are assumed to be fully melted and the important effect of degree of particle melting (i.e., most particles hit the substrate in semi-molten state) is not accounted for in the heat balance that describes the evolution of particle temperature and the formation of coating microstructure.

To develop a methodology to precisely control the coating micro- or nano-structure which determines the coating mechanical and physical properties by manipulating macro-scale operating conditions, the link between the macroscopic operating conditions and the coating microstructure should be established and the relationship between particle size and melting behavior and coating porosity needs to be understood. In this chapter, we focus on the modeling of microstructure of coatings produced by an industrial HVOF thermal spray process (Diamond Jet hybrid gun, Sulzer Metco, Westbury, NY). Based on the understanding of coating structure and mechanisms of pore formation inside of the coating obtained from experimental studies [116, 117, 118], stochastic simulation is used to explore the microstructure evolution behavior of the coatings on the substrate. In the coating growth model, the velocity,

temperature and degree of melting of powders hitting on the substrate are determined by a previously developed mathematical model describing gas and particle behavior [112], and the complex characteristics of the thermally sprayed coatings are captured by applying several basic rules that encapsulate the main physical features of the deposition process. In addition to providing useful insight into the pore formation and coating growth, the model is used to make a comprehensive parametric analysis, which allows us to systematically characterize the influence of operating conditions, such as the gas flow rate, spray distance, as well as the effect of particle size, on the particle melting behavior, coating porosity, surface roughness and deposition efficiency. Comparison of simulation results and experimental studies shows that the proposed model can provide good predictions of the relationship between macroscopic processing conditions and coating microstructure.

3.2   Characteristics of deposition and coating growth

Thermally sprayed coatings consist of lamellar splats interspersed with pores. The splats, which are the fundamental building blocks of the coating, are formed by the impact, deformation, spreading and solidification of individual droplets. The pores, however, are formed by the interaction of the droplets and the previously-deposited coating surface. In this section, several characteristics involved in the deposition and coating growth process, including deformation, pore formation and surface roughness, will be described.

3.2.1   Deformation

In the HVOF thermal spray process, each individual particle is accelerated and heated up in a burning gas flame, and then impinges onto the substrate in a molten, partially-

molten or solid state. At impact, the sudden stagnation of the powder particles leads to a pressure build-up at the particle-surface interface, and deformation occurs. As the particles splash on the substrate, they are also quenched to the substrate temperature in a very short time. For the particle deformation process, if a particle is fully melted, it is assumed that the droplet becomes a cylinder as a result of deformation [122] (see Figure 3.1(a)). The splat flattening degree ξ is defined by the following equation:

$$\xi = \frac{D}{d_p} = \frac{2}{d_p}\sqrt{\frac{A}{\pi}} \tag{3.1}$$

where D and A are the estimated diameter and area of the splat, respectively, and d_p is the particle diameter prior to impact. The analysis of Madejski [122] shows that ξ depends on several dimensionless parameters characterizing the impact and spreading processes, including: the Reynolds number ($Re = d_p v_p/\nu_p$, where ν_p is the kinematic viscosity of the droplets), which represents the viscous dissipation of the inertia forces, the Weber number ($We = d_p v_p^2 \rho_p/\sigma_p$, where σ_p is surface tension of the droplets), which quantifies the conversion of the kinetic energy into surface energy, and the Peclet number ($Pe = v_p d_p/\varepsilon_p$, where ε_p is the thermal diffusivity of the solidified layer), which expresses the freezing rate [122]. Under the operating conditions typically employed in the HVOF thermal spray process, solidification is insignificant before the deformation is complete, and therefore the flattening ratio can be expressed as a function of We and Re as follows [122]:

$$\frac{3\xi^2}{We} + \frac{1}{Re}\left(\frac{\xi}{1.2941}\right)^5 = 1 \tag{3.2}$$

The above equation is valid for $We > 100$ and $Re > 100$. When the surface tension effects are negligible, which is usually true for particles with size larger than 10 μm, Eq.3.2 can be further simplified to:

$$\xi = 1.2941 Re^{0.2} \tag{3.3}$$
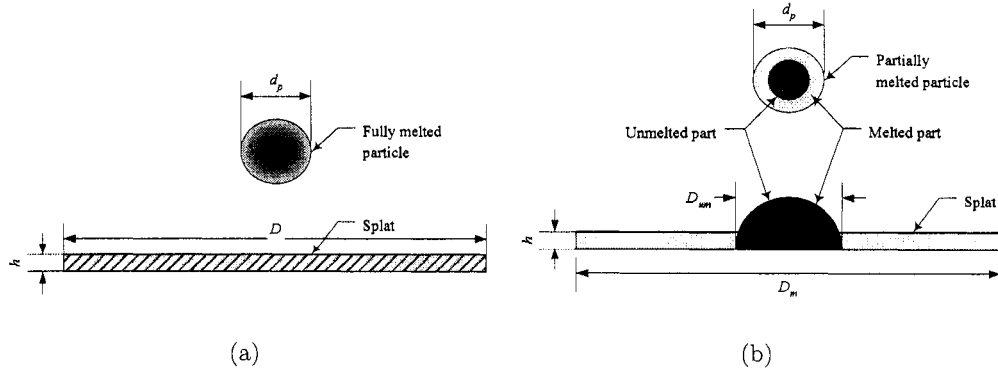
Figure 3.1: Deformation of fully melted particle and partially melted particle upon impact on the substrate.

If a particle is partially melted, our modeling procedure assumes that the unmelted part will form a hemisphere with the equivalent volume and the melted part will form a ring around this hemisphere (see Figure 3.1(b)), whose flattening ratio can be calculated using the same formula.

3.2.2 Pore formation

Porosity, which is defined as the ratio of the volume of the pores inside the coating to the total volume of the coating, is one of the most important quality parameters of the coatings produced by the HVOF thermal spray process. Experimental studies have shown that a lamellar microstructure is consistently observed on cross sections of a coating, and pores are distributed in the lamellar structure, regardless of the processing conditions [141]. However, the amount, size and distribution of pores in the thermally sprayed coatings are dependent to a large extent on the processing conditions. These variables, which significantly affect thermal conductivity and mechanical properties of the coatings, can be controlled more efficiently if an in-depth understanding of the fundamental mechanisms of porosity formation is established.

In this sense, estimation of coating porosity is one of the main objectives of this work.

Liu *et al.* [116, 117, 118] proposed several possible mechanisms of pore formation in the coating microstructure based on their experimental investigations. Five major types of pores are classified (see Figured 3.2). The first one is a macro-pore type, whose size is comparable to the droplet size. It is primarily formed in the vicinity of solidified particles, unmelted or partially melted particles as a result of unfree spreading of subsequent droplets around these slightly flattened particles. The remaining four types of pores are all of micro-pore type, whose size is much smaller than the size of the droplets. Specifically, they are formed by: (1) solidification of voids caused by droplet/droplet and droplet/liquid-surface-layer interactions; (2) separation of liquid from the solid/liquid interface or liquid ejection or rebounding (detached liquid may entrap voids); (3) presence of cavities in droplets before impact; and (4) extraneous inclusions and dispersoids (e.g., carbides, nitrides and oxides) that may be present in droplets. The occurrence of each mechanism depends on the processing conditions. For example, when the degree of melting of the particles at impact is low and there are many solid particles in the sprayed powder at the point of impact on substrate, the first two mechanisms may be dominant. When the deposition layers are thin and the resultant rate of heat extraction in the deposited material is high, mechanism 3 becomes important. If there is a large amount of extraneous particles in the droplets, mechanism 5 will be significant. Because the spray powder used in the current study is nickel, the powder particles are dense and it can be assumed that there is no reaction of carbides or oxides inside them. Therefore, pores formed by mechanisms 4 and 5 can be neglected. Mechanisms 1, 2 and 3 will be included in the microstructure model and their relative importance will vary depending on the operating conditions.
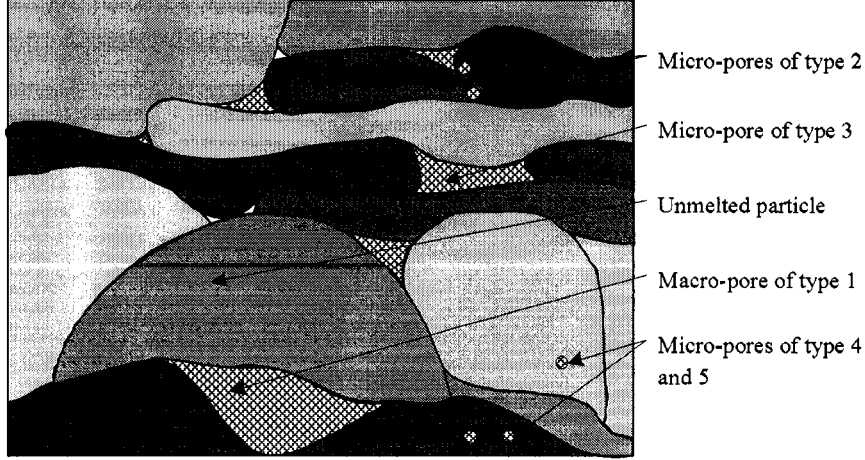
Figure 3.2: Schematic of the five types of pores.

3.2.3 Surface roughness

The roughness of a coating surface is another important factor that affects coating quality. A smooth surface can enhance the coating performance in terms of abrasion, wear, and corrosion resistance. In this work, the roughness is defined as the arithmetic mean of the absolute difference between the surface height of each gird and the average surface height:

$$R_a = \frac{\sum\limits_{i=1}^{n} |h(i) - h_m|}{n} \tag{3.4}$$

where R_a is the roughness, n is the number of grid points used in the model, $h(i)$ is the surface height of grid point i, and h_m is the average surface height calculated by using the expression $\sum_{i=1}^{n} h(i)/n$.

The surface roughness is primarily dependent on the substrate properties as well as the particle size and chemical and physical states of the particles at the point of impact on the substrate. This work considers that the substrate is smooth and does not account for the effect of substrate roughness on the coating properties. However, it should be noted that the substrate surface is usually roughened before

coating processing. Such a treatment can increase the bonding strength between the thermally sprayed coating and the substrate. Mellali *et al.* [128] have concluded that the particle adhesion/cohesion on the surface increases with substrate roughness at least for the well-molten particles.

3.3 Computer simulation of coating formation

Because of the polydisperse nature of the powder size distribution and the stochastic nature of the deposition process, a stochastic simulation method, which is based on random number generation and rule-based modeling of coating formation, is used to explore the particle behavior in the deposition and coating formation processes. In this section, the modeling procedure, coating growth rules, and modeling settings will be presented. While the proposed model will be applied to a coating sprayed by the Diamond Jet hybrid HVOF thermal spray process, the modeling methodology is applicable to coatings sprayed with other HVOF thermal spray processes.

3.3.1 Simulation procedure

The procedure followed for the simulation of coating microstructure is based on the sequential modular method, which is shown in Figure 3.3. At the beginning of each simulation run, the process operating conditions (such as the mass flow rate of oxygen, fuel and air) and the particle size distribution parameters are specified. After the initialization, the simulation repeats a process in which individual particles hit on the surface of the coating, until the coating thickness reaches the desired set-point value. The size of each particle is chosen by using a random number generator according to a lognormally-distributed particle size distribution of the following form [32]:
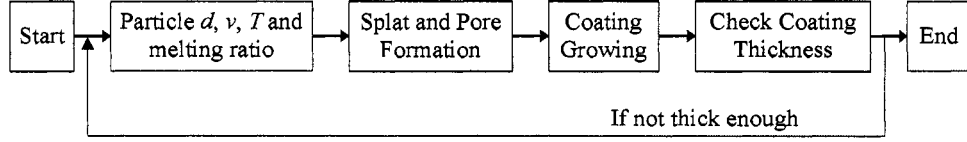
Figure 3.3: Modeling procedure.

$$f(d_p) = \frac{1}{\sqrt{2\pi}\sigma d_p} \exp\left[-\frac{(\ln d_p - \mu)^2}{2\sigma^2}\right] \qquad (3.5)$$

where $f(d_p)$ is the size distribution function, μ and σ^2 are two dimensionless parameters corresponding to the mean and the variance of $\ln d_p$, which obeys the normal distribution. For particles that are lognormally distributed, μ and σ can be determined by the following formulas:

$$\mu = \ln \sqrt[3]{d_{10}d_{50}d_{90}} - 1.831 \left(\ln \sqrt{\frac{d_{90}}{d_{10}}}\right)^2$$

$$\sigma = 0.781 \ln \sqrt{\frac{d_{90}}{d_{10}}} \qquad (3.6)$$

where d_{10}, d_{50} and d_{90} are three characteristic diameters which can be obtained experimentally [100].

Once the particle size is determined, the particle velocity, temperature and melting ratio at the point of impact on the substrate are calculated by using the HVOF thermal spray process model developed in the last chapter [112]. The hitting position of the particle on the substrate is also determined by two independent random numbers. The program then simulates how each individual particle hits on the substrate and forms a splat. For the simulation of splat accumulation, we consider that the coating formation process is a sequence of independent discrete events of each individual particle hitting on the previously formed coating layer. After all the parameters of a particle before hitting the previously deposited coating layer, such as the melting ratio, the flattening ratio etc., are determined, the particle is added to

89

the already-formed coating layer based on certain rules, which will be discussed in subsection 3.3.2 below. When the coating thickness reaches its set-point value, the program saves the configuration of the simulated coating section and calculates the coating porosity, surface roughness and deposition efficiency. The deposition efficiency is defined as the ratio of the volume of particles deposited on the substrate to the total volume of particles sprayed by the HVOF process.

To increase the efficiency of the computation, the model only simulates the cross section of the coating that is perpendicular to the substrate, i.e., simulation of coating growth in two dimensions. The point of impact of a particle on the substrate is determined by two random variables, corresponding to its two dimensional position on the coating surface. The first one represents its position in the x-coordinate (x_p), calculated from a reference point on the simulated section to the center of the splat. The second one stands for its position in the y-coordinate (y_p), calculated from the position where the splat is cut by the cross section to the center of the splat (see Figure 3.4). Specifically,

$$\begin{cases} x_p &= uL + L/2 \\ y_p &= wD \end{cases} \tag{3.7}$$

where u and w are two independent and uniformly distributed random variables in the interval [-0.5, 0.5], L is the length of the simulated coating section and D is the diameter of the splat. Note uniformly but not normally distributed variables are used to describe splat position because the thermal spray gun may move in general back and forth. After the point of impact of a particle on the substrate is determined, the splat is added on the previously deposited coating layer and pores may be formed, depending on the conditions of the previously-deposited coating layer.
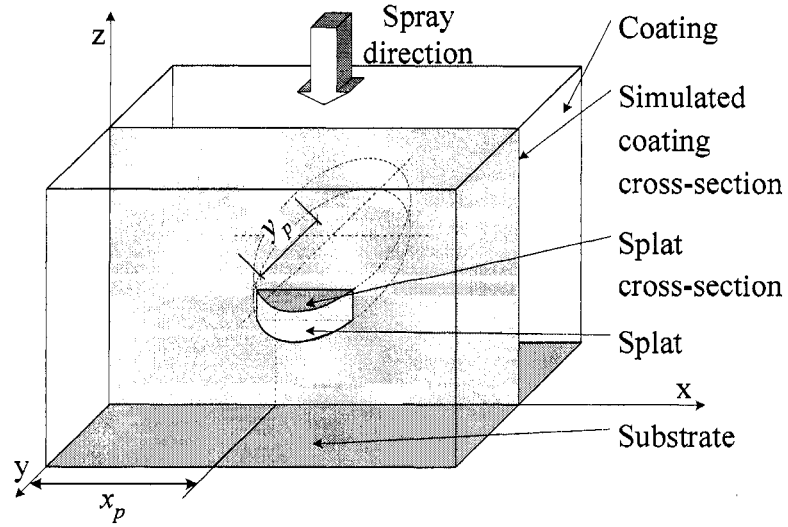
Figure 3.4: Sketch of the splat position used in the model.

3.3.2 Coating growth rules

There are several different events which may take place when a particle hits on the substrate. The occurrence of each event depends on the physical state of the sprayed particle and the condition of the previously deposited layer at the hitting point. The rules governing the geometric shape of the splats and the formation of the pores are described as follows.

1. If a particle at the point of impact on the substrate is partially melted, the unmelted part will form a hemisphere on the previously deposited layer and the melted part will form a ring around this hemisphere (see Figure 3.1(b)). Furthermore, if the unmelted part of the particle hits at the point of the previously deposited layer that is formed by an unmelted particle, it will bounce off, and a hole will be formed in the center of the disk. Otherwise, the hemisphere will hit on the surface and macro-size pores may form under the hemisphere. Figures 3.5(a) and (b) show the coating layer before and after a partially melted particle

91
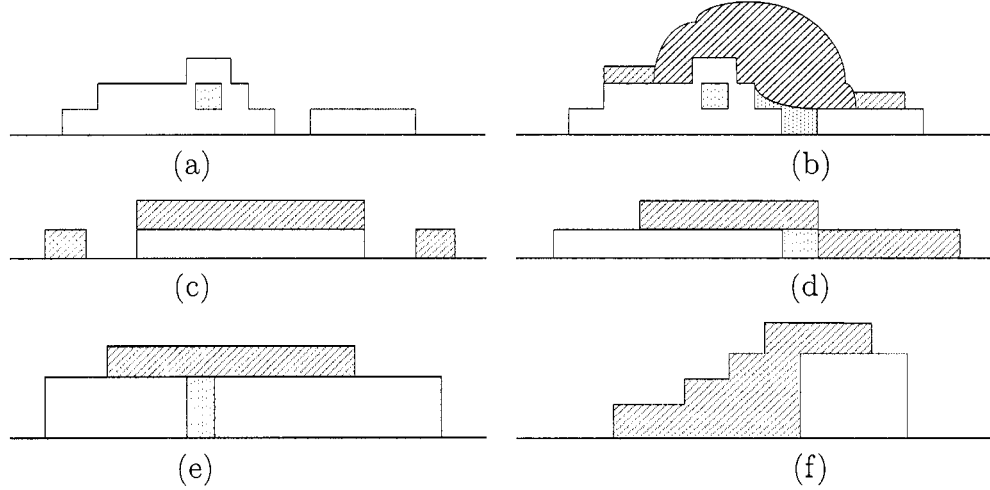
Figure 3.5: Splat formation rules (shaded area corresponds to added splat and dotted area corresponds to pore formation) - (a) coating surface before impact of partially melted particle, (b) coating structure after impact of partially melted particle, (c) splat breaking up, (d) pore formation at the corner of a step, (e) pore formation in a gap and (f) splat pileup on a step.

hits on the surface. It is shown that one pore is formed as the unmelted particle covers the gap. This kind of pore formation is consistent with the first type of pore formation mentioned in the subsection 3.2.2.

2. When a particle hits the substrate, the melted part will fit on the surface as much as possible. The splat will spread outwards, after the impact region of the particle fits on the surface, without forming a new pore. The impact region is determined by the size and the cross-sectional position of the particle.

3. During the splat spreading, if the splat comes to a vertical drop, the program will calculate the ratio of the splat that has not been settled down. If the step does not continue with a gap (shown in Figure 3.5(e)) that can be covered by the splat, the splat will break (Figure 3.5(c)) or cover the corner at the step (Figure 3.5(d)) according to the ratio and the height of the step. Otherwise, the gap

will be covered by the splat (Figure 3.5(e)), and a pore will be formed. Pores formed in this way fall into the second and third categories of pore formation mechanism mentioned in the subsection 3.2.2.

4. If the splat encounters a dead end (Figure 3.5(f)), it first fills the available space, and then it flows over the outer surface if the volume of the remaining splat is big enough.

To successfully simulate the coating microstructure, several important parameters are used in these rules. According to the situations that these parameters are used, there are 5 groups of parameters: (a) One parameter is used to determine how deep the unmelted part of the particle will hit into the gap (Figure 3.5(b), i.e., the vertical distance d_1 at each discretization point between the actual bottom of the unmelted particle and the straight line connected the boundaries of the gap) based on the width of the gap, w, and therefore, this parameter decides the size of a macro-sized pore. Specifically, the vertical distance d_1 is calculated by $c_1 \sqrt{x^2 - wx}$, where the parameter c_1 is set to be 0.5, and x is the horizontal distance between the discretization point and the left boundary of the gap; (b) in the third rule, when a splat meets a vertical drop step (Figure 3.5(c) and (d)), the ratio of the step height to the splat thickness, set to be 5 in the simulation, determines whether the splat will break; (c) if the splat breaks when it meets a vertical drop step (Figure 3.5(c)), the distance that it breaks away is proportional to the difference between the height of the step and the length of the splat that breaks, and the ratio is set to be 0.3 in the simulation. (d) if the splat does not break when it meets a vertical drop step (Figure 3.5(d)), a pore will form at the corner of the step (the size of the pore is decided by a parameter, which is the slope of the splat covering the corner. The slope is set to be 0.5 in the simulation); (e) in the fourth rule, a necessary parameter is the slope of the bulk

formed by the splat at the dead end (Figure 3.5(f)), which is set to be 1 in the simulation. All these parameters were carefully selected based on the consideration of their physical meaning and were tuned to provide results of important coating variables (like coating porosity) which are consistent with the available experimental results [60, 71].

By means of these parameters, these four basic rules control how each particle hits and deforms on the substrate to form a lamellar-structured coating. Based on the simulated coating structure, the coating porosity and roughness can be calculated. Specifically, the coating porosity P is calculated using the following equation:

$$P = \frac{n_1}{n_1 + n_2} \tag{3.8}$$

where n_1 is the number of void grids under the simulated coating surface, and n_2 is the number of grids occupied by splats under the simulated coating surface. The deposition efficiency η is calculated using the following equation:

$$\eta = \frac{V_1}{V_1 + V_2} \tag{3.9}$$

where V_1 is the volume of particles that are added to the coating, and V_2 is the volume of solid particles that are bouncing off by hitting on the surface formed by unmelted particles. Note that all partially-melted and fully-melted particles stick onto the surface independently of the nature of the coating layer at the hitting position.

3.3.3 Simulation settings

The simulation model is based on the operation of the Diamond Jet Hybrid gun, whose geometric configuration can be found in the last chapter [112]. Table 3.1 lists the baseline operating conditions (recommended by the manufacturer), typical particle size distribution and the dimension of the simulated coating section. Especially,

Table 3.1: Baseline operating conditions for the Diamond Jet hybrid thermal spray process used in the simulation.

Parameter	Value
Flow rate of oxygen, O_2 $(scfh)$	578
Flow rate of propylene, C_3H_6 $(scfh)$	176
Flow rate of air $(scfh)$	857
Spray distance, L (mm)	245
Characteristic diameter d_{10} (μm)	15
Characteristic diameter d_{50} (μm)	35
Characteristic diameter d_{90} (μm)	77
Particle injection velocity, v_{p_0} (m/s)	20
Width of the simulated coating section (μm)	819.2
Desired set-point of the coating thickness (μm)	254

Table 3.2: Thermophysical properties of powder particles.

Powder	Nickel
Density (kg/m^3)	8.9×10^3
Melting temperature (K)	1727
Heat capacity $(J/kg/K)$	471
Latent heat of melting (J/kg)	3×10^5
Liquid kinematic viscosity (m^2/s)	6.2×10^{-7}

the three characteristic diameters (d_{10}, d_{50} and d_{90}) are listed as a reference for the lognormal distribution of the powder particles. When particles with different sizes are used in the simulation, these three characteristic diameters are varied proportionally, i.e. only one characteristic diameter is needed to describe a certain lognormal distribution of particles. Therefore, we only mention d_{50} to characterize the size distributions of the various powder used in this chapter. The physical properties of the particles used for coating formation are listed in Table 3.2. The model simulates a section of the coating. The section is assumed to be a rectangle and is discretized by a 8192 × 4096 mesh. The size of each grid in the mesh is 0.1 × 0.1 μm. Such a grid

size is around half of the height of the splat which is formed by a fully melted particle, whose diameter is 40 μm, under the baseline operating conditions. According to the mathematical model describing gas and particle behavior [112], particles whose size is smaller than about 8 μm are mostly fully unmelted. Based on this fact, a grid size of 0.1 μm is small enough to carry out a simulation of coating growth with reasonable computing power. Each splat formed by a particle hitting on the previously formed coating surface is discretized to a combination of grids, and is placed on the coating surface by following certain rules (see section 3.2). The splat with a thickness less than 0.1 μm is rounded to 0.1 μm. Eq.3.10 shows the relationship between the ratio of splat diameter (D) to thickness (h) and the flattening degree (ξ):

$$\frac{D}{h} = 1.5\xi^3 \tag{3.10}$$

Usually, ξ is around 8 according to our calculations, which means that the splat diameter D is around 768 times the splat thickness h. Considering such a high particle deformation, a smaller grid size will not be able to substantially improve the accuracy of the computed results, this point has been verified by running representative simulations with different grid size.

3.4 Simulation results and discussion

3.4.1 Microstructure of coatings made of particles of different molten states

Under normal operating conditions, the gas temperature at the exit of the gun is around 2000 K, which is several hundred Kelvin higher than the melting point of the nickel particle. However, simulation results [112] show that even at such a high temperature, only particles in a certain size range, about 10 - 40 μm, can be fully

melted, while others, either too small or too large, are in a coexistence state of liquid and solid or even in a solid state at the point of impact on substrate. The very small particles, although they may be totally melted during flight, are not in a fully molten state at impact because they are cooled down quickly in the free jet due to the gas temperature decay and their small thermal inertias. Experiments of Zhang et al. [200] also shows that particles at the point of impact on the substrate may be in different molten states (fully melted, partially melted or solid) due to different sizes and different trajectories in the HVOF thermal spray process. Figure 3.6 shows the simulated configuration of the coating sections that are perpendicular to the substrate, for particles with different molten states. The simulated section in Figure 3.6(a) is formed by particles that are all fully melted (ideal case, in which the particle velocity is calculated based on the baseline operating conditions, and the particle melting ratio is assumed to be one), while the one in Figure 3.6(b) is formed by particles with nonuniform molten states (some particles may be partially melted or even unmelted, in which case the particle velocity, temperature and degree of melting are calculated based on the baseline operating conditions). The ideal lamellar structure of the thermally sprayed coating can be easily seen in Figure 3.6(a). However, such a lamellar structure is disturbed by the unmelted part of the particles, as shown in Figure 3.6(b). It is also shown that large unmelted particles affect the coating surface dramatically, thus, leading to high coating roughness. To show the pore size and distribution inside of the coating, we draw the Figure 3.6(b) again by ignoring the difference between each splat; the result is shown in Figure 3.6(c). The white dots in Figure 3.6(c) represent the pores. He et al. [70] and Totemeier et al. [184] have observed similar coating microstructures in their experiments. It can be concluded from this comparison that the particle melting behavior plays a very important role in the coating microstructure evolution and should be accounted for

in the simulation model.

The effect of particle melting behavior on the coating porosity was studied by analyzing the simulation results. Figure 3.7 shows the comparison of the coating porosity simulated by two different models. One model considers the particle melting behavior, i.e. the melting ratio of each particle is calculated by a mathematical model [112] considering the particle size and operating conditions. Another model assumes that all particles are fully melted, while other parameters, such as the particle velocity, are calculated by the same mathematical model [112]. The comparison shows the importance of considering the particle melting behavior, which has not been included in previous coating simulation models [94, 134, 59]. For the model considering that all the particles are fully melted, the coating porosity decreases monotonically as the particle size (d_{50}) increases, shown as the dashed line in Figure 3.7. However, the simulated coating porosity accounting for the particle melting behavior will decrease first and then increase, as the particle size (d_{50}) increases, shown as the solid line in the same figure. The existence of a minimum porosity can be explained by the existence of the maximum particle melting ratio for particles with different size, Figure 3.8. Several experimental studies [71, 60] have proved that a better particle melting condition can lead to a lower coating porosity. It is also found that the error band increases as bigger particles are used in the simulation. Such a phenomenon can be explained by the formation of more macro-pores when larger particles are used for the coating formation. Simulations show that the number of macro-pores is usually less than 50 inside one simulated coating section. Under operating conditions in which macro-pores strongly influence the coating porosity (e.g. large particles are used for the coating formation), a small change of the number of macro-pores will strongly influence the coating porosity.
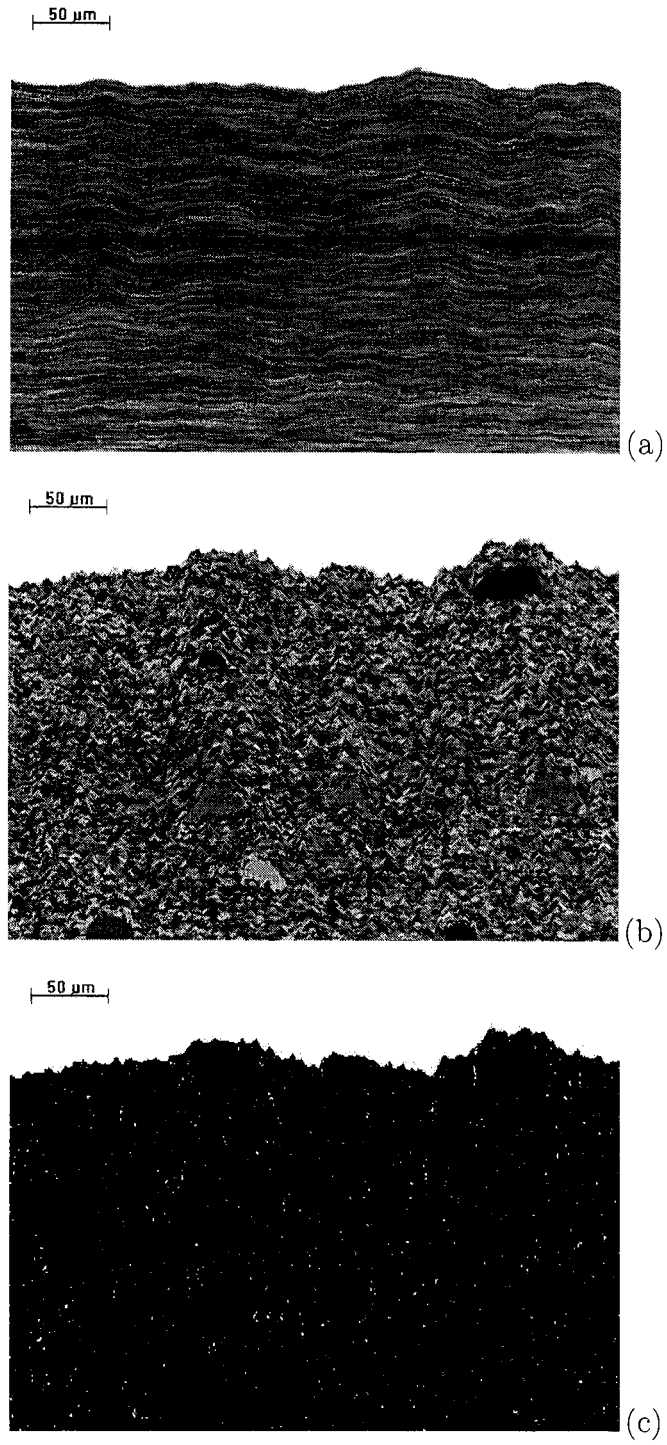
Figure 3.6: Simulated coating section using fully-melted particles and partially-melted particles.
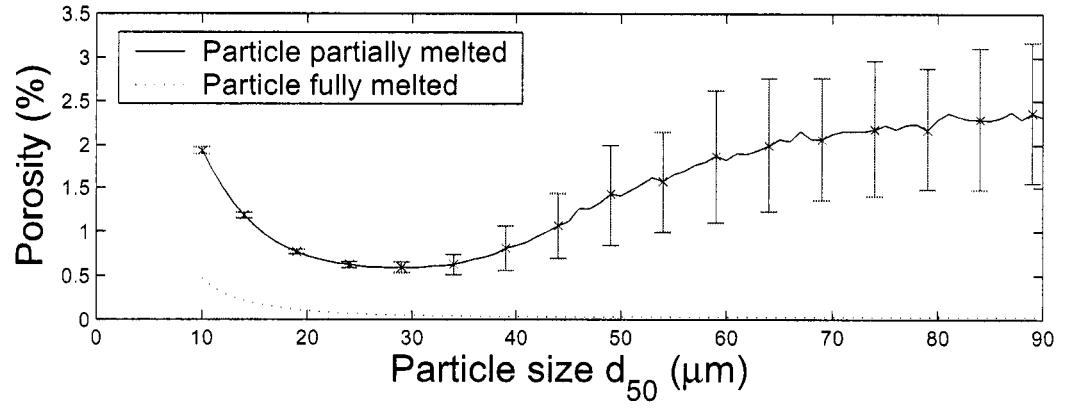
Figure 3.7: Comparison of simulation results for fully melted and partially melted particles under baseline operating conditions.
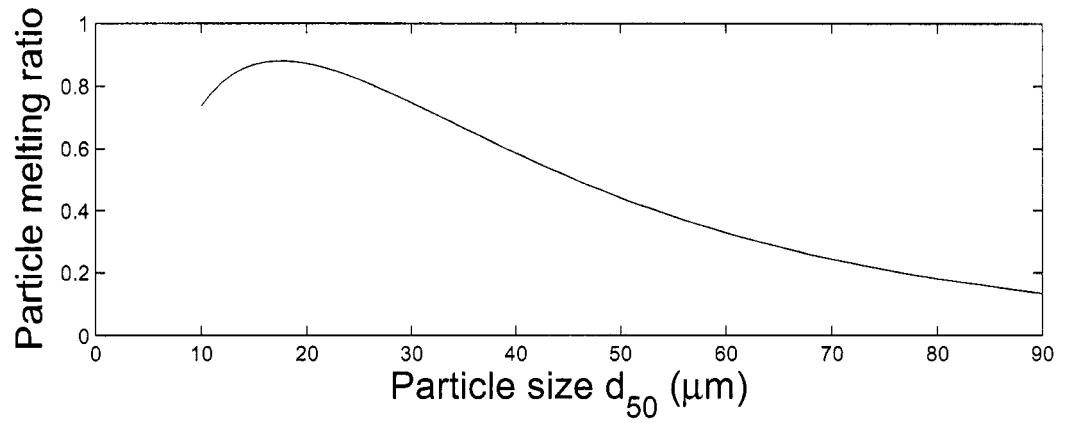
Figure 3.8: The melting ratio of particles with different size under baseline operating conditions.

100

3.4.2 Influence of operating conditions on coating properties

In addition to providing useful insight into coating formation and growth, the developed model is used to make a comprehensive parametric analysis, which allows us to systematically characterize the influence of operating conditions and the effect of particle size on the coating porosity and deposition efficiency. The parametric analysis of macroscopic operating conditions on coating microstructure is based on the "one-factor-at-a-time" method, i.e. each time only one processing parameter is varied from 55% to 150% of its baseline condition value while the other parameters are fixed. The influence of particle size on coating microstructure is also studied by varying powder size distribution parameters, e.g. d_{50} (whose corresponding cumulative weight function is 0.5), from 20 to 60 μm. The simulated results in the following figures are the average of a large number of repeated simulation runs performed under the same operating conditions to obtain a convergent average value and make the variance small enough. The effect of variations of the process parameters is compared with available experimental data.

Effect of oxygen flow rate

Figure 3.9 shows the influence of oxygen flow rate and particle size on the particle melting ratio, coating porosity, surface roughness and deposition efficiency. Figure 3.9(a) reveals that the particle melting ratio increases significantly and becomes almost flat when the oxygen flow rate increases from its lower bound (318 $scfh$) to its upper bound (867 $scfh$); this behavior can be explained by the discussion in Section 2.4. When the oxygen flow rate is small, the equivalence ratio (fuel/oxygen ratio) is very far away from its optimal value. As the oxygen flow rate increases, the equivalence ratio becomes close to its optimal value, and the combustion pressure increases
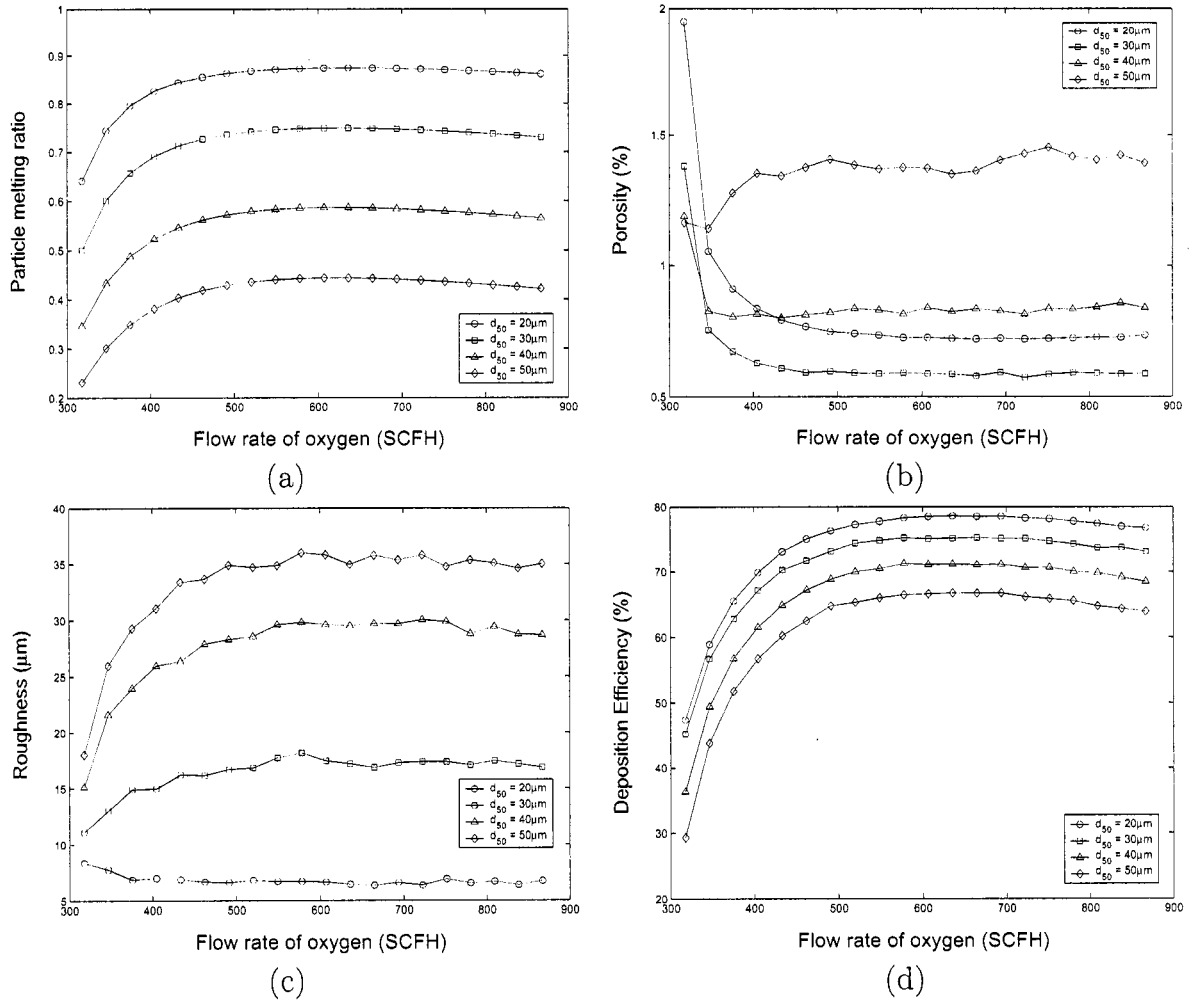
Figure 3.9: The effect of oxygen flow rate on (a) particle melting behavior, (b) coating porosity, (c) surface roughness and (d) deposition efficiency.

(due to an increase in the total mass flow rate of the gas) at the same time. This leads to an increase of the gas temperature, and therefore, the particle temperature goes up sharply. However, after the oxygen flow rate exceeds a critical value in which the equivalence ratio departs significantly from its optimal value, the gas temperature slightly decreases. This is because the effect of an increase in the combustion pressure partially compensates for the effect of a decrease in the equivalence ratio. Accordingly, the coating porosity decreases very fast initially, and then approaches a nearly constant value as the oxygen flow rate spans its entire range of variation, for particles of small size (Figure 3.9(b)). This implies that for small particles, a good particle melting condition (i.e., higher degree of particle melting) helps to decrease coating porosity. For particles of large size, the coating porosity is large, which can be explained by the low melting ratio of large particles at the point of impact on substrate, which results in big pores formed in the coating structure. We should also notice the effect of particle size on the coating porosity. Figure 3.9(b) shows that a coating formed by a powder with $d_{50} = 30 \ \mu m$ has a lower porosity than the coating formed by a powder with $d_{50} = 20 \ \mu m$. The roughness of the coating increases with the particle size, but it is not affected much by the oxygen flow rate, as shown in Figure 3.9(c). This is because the coating roughness is controlled by the unmelted part of the particles, whose amount does not change much when the oxygen flow rate changes. The effect of oxygen flow rate on the deposition efficiency is similar to the one on particle melting ratio, as shown in Figure 3.9(d). When the oxygen flow rate is less than 500 $scfh$, higher oxygen flow rates and smaller particle size lead to higher degree of particle melting and higher deposition efficiency.
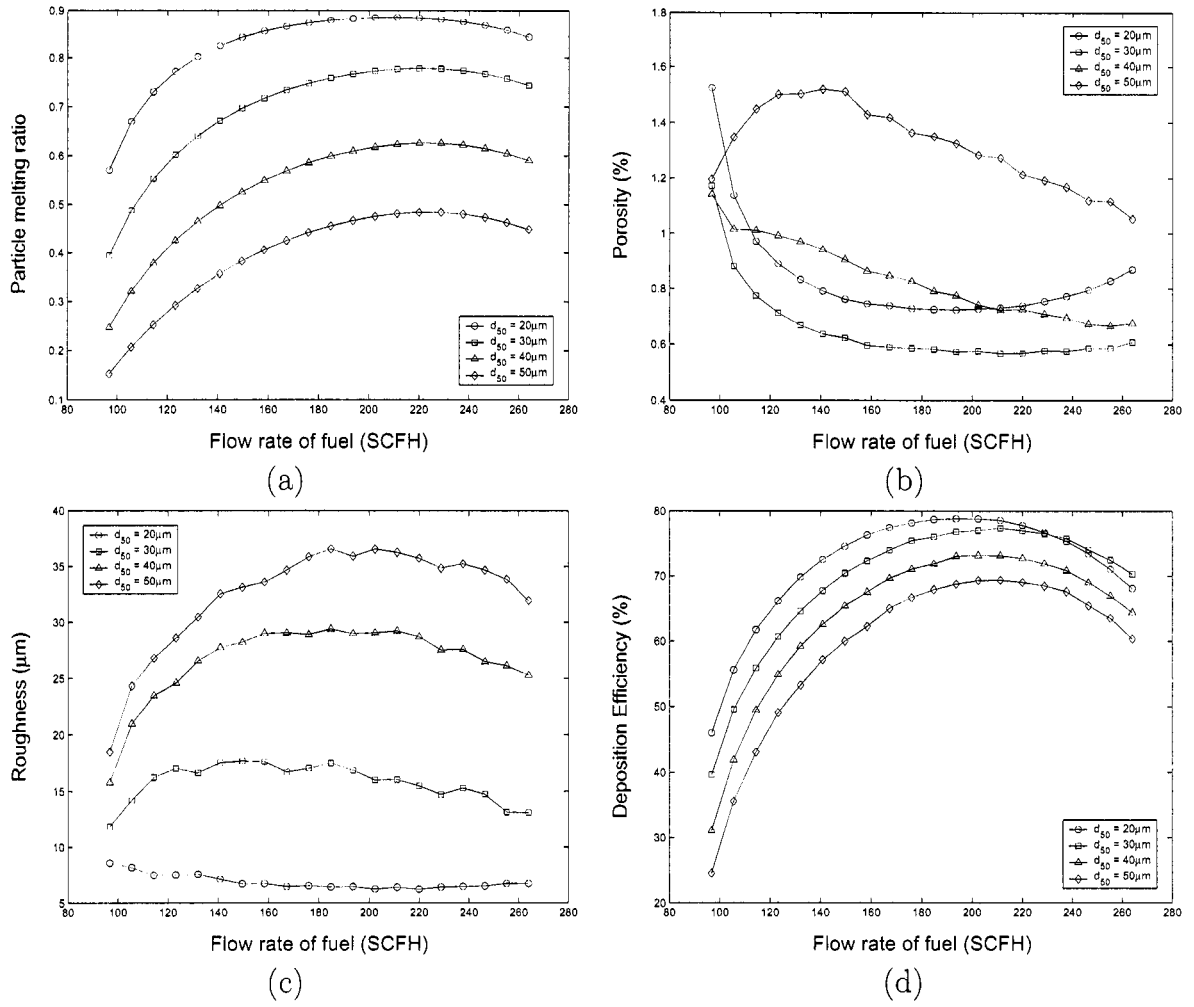
Figure 3.10: The effect of fuel flow rate on (a) particle melting behavior, (b) coating porosity, (c) surface roughness and (d) deposition efficiency.

Effect of fuel flow rate

Compared to the influence of oxygen flow rate, variation in the fuel flow rate has more obvious effects on coating properties, as shown in Figure 3.10. For example, a peak in the fuel flow rate vs. particle melting ratio can be clearly seen in Figure 3.10(a). This is because the total mass flow rate does not increase much in the range of interest (because the flow rate of fuel is small compared to those of oxygen and air) and the gas temperature is only a function of the equivalence ratio. For particles of different size, the maximum melting ratio occurs when the fuel flow rate is about 210 $scfh$, whose corresponding equivalence ratio is about 1.2. Accordingly, as the fuel flow rate increases, the coating porosity decreases first and then increases, and the lowest coating porosity is achieved when the fuel flow rate is around 210 $scfh$. This fact further substantiates the point that a good particle melting condition (i.e., high degree of particle melting) is beneficial to achieve a lower coating porosity. However, it is not the only factor affecting the coating porosity. Figure 3.10(b) shows that a coating formed by a powder with $d_{50} = 30$ μm has a lower porosity than a coating formed by a powder with $d_{50} = 20$ μm, although smaller particles have better melting condition than bigger ones. This is similar to the observation in Figure 3.9(b). Once again, the roughness of the coating increases with the particle size, and the relationship between the coating roughness and the fuel flow rate is not so strong (Figure 3.10(c)). Consistent with the variation of particle melting ratio, the deposition efficiency is shown to increase first and then decrease as the fuel flow rate increases (Figure 3.10(d)).

Effect of air flow rate

The effect of air, which partially functions as coolant in the HVOF thermal spray process, can be seen in Figure 3.11. As the air flow rate increases, the particle melting ratio at the point of impact on the substrate decreases (Figure 3.11(a)). Correspondingly, the porosity of coatings deposited by different size particles increases, as shown in Figure 3.11(b). Regardless of the change of air flow rate, the coating roughness is almost proportional to the particle size (Figure 3.11(c)). A higher air flow rate will lead to a lower deposition efficiency (Figure 3.11(d)). Moreover, an increase in the particle size will decrease the deposition efficiency.

Effect of total mass flow rate

The effect of total mass flow rate can be seen in Figure 3.12. According to Figure 3.12(a), the relative ratio of fuel, oxygen and air flow rate is kept at the baseline condition, while the total mass flow rate varies from 50% to 150% of its baseline condition. For different particle size, the particle melting ratio changes almost linearly with the total mass flow rate. Such a dependence is different from the corresponding effect of the fuel flow rate and of the oxygen flow rate. The increase in degree of particle melting is caused by an increase in the combustion pressure, and therefore, gas temperature [112]. Note that as the total mass flow rate increases, the particle velocity at the point of impact will also increase [112]. From Figure 3.12(b), it can be seen that the coating porosity decreases slowly as the total mass flow rate changes. This is caused by an increase in both degree of particle melting and impact velocity. The deposition efficiency increases dramatically as the total mass flow rate increases. Again, the coating formed by powder particles with mean size $d_{50} = 30$ μm has the lowest porosity and almost the highest deposition efficiency, as shown in Figure
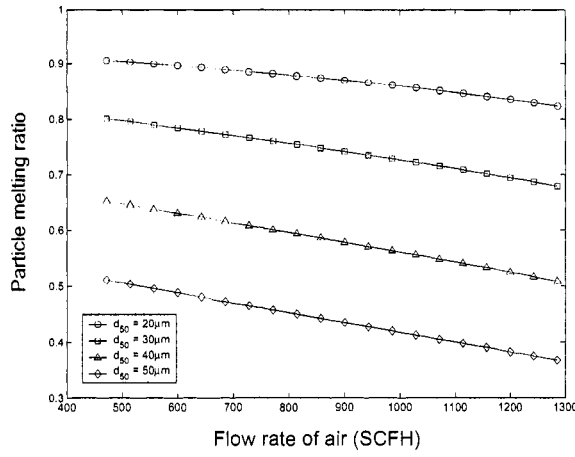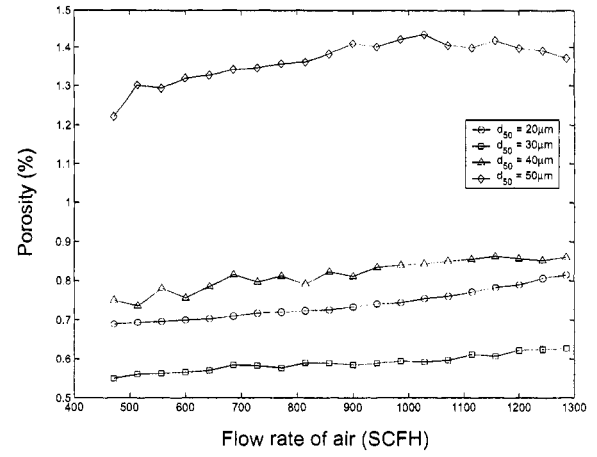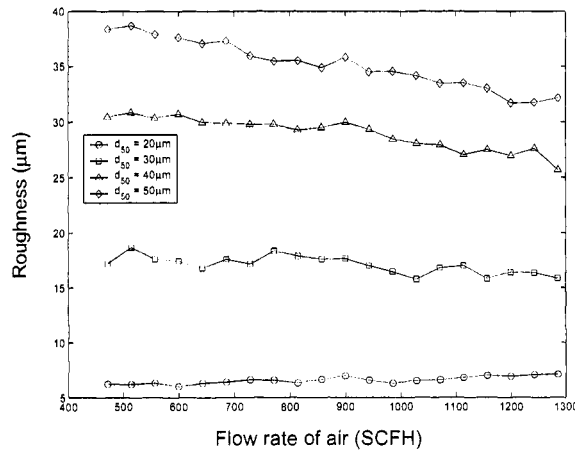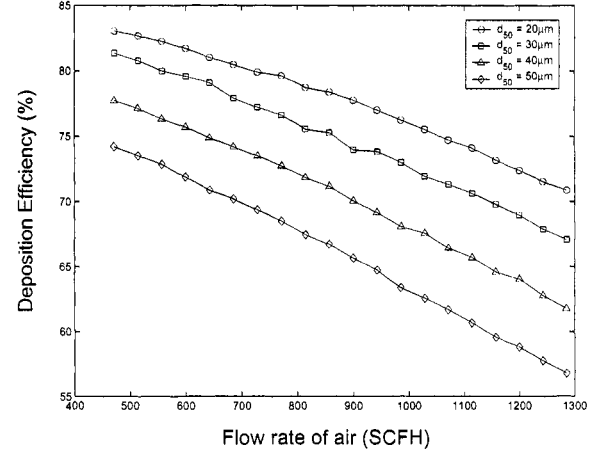
Figure 3.11: The effect of air flow rate on (a) particle melting behavior, (b) coating porosity, (c) surface roughness and (d) deposition efficiency.
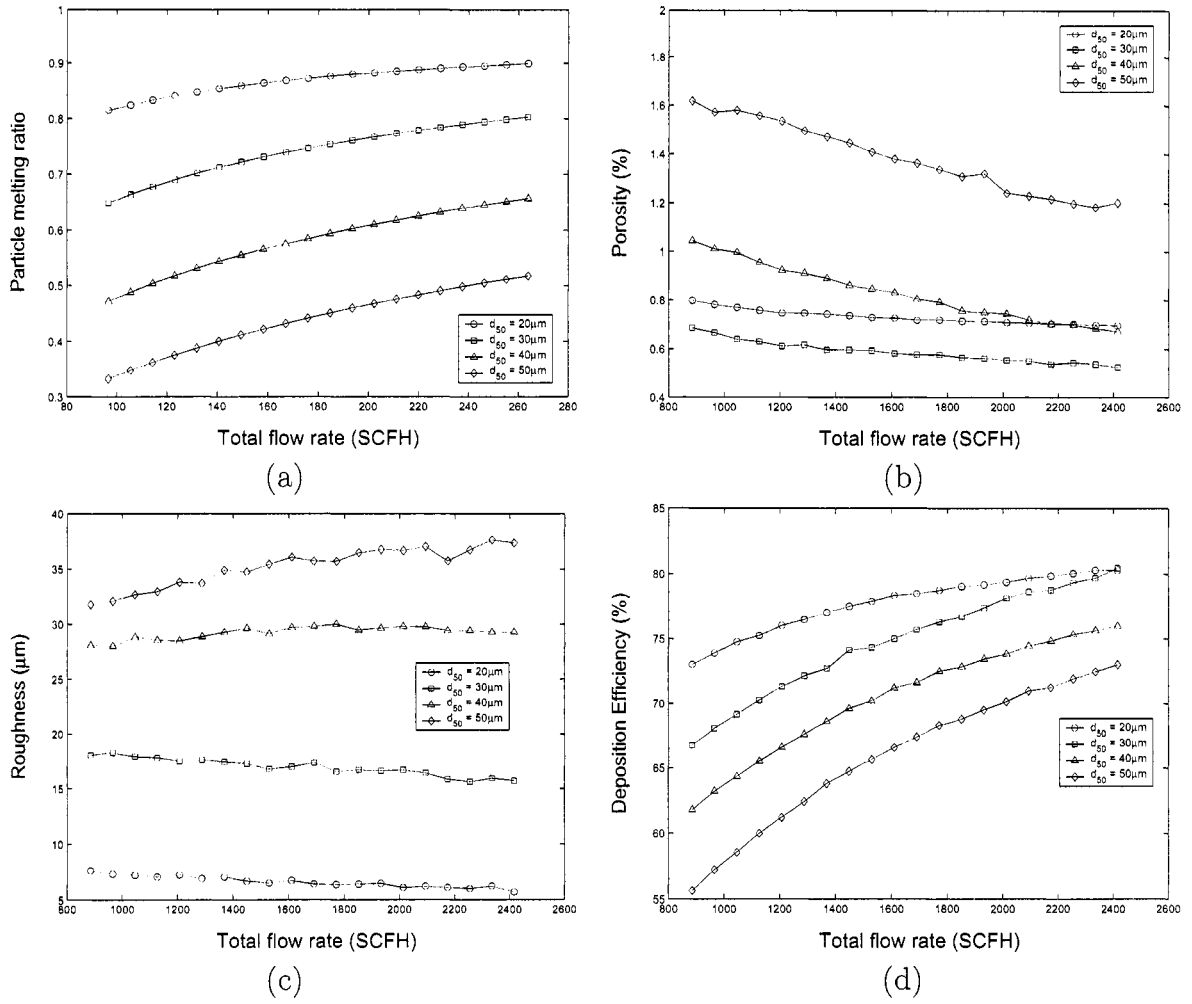
Figure 3.12: The effect of total mass flow rate on (a) particle melting behavior, (b) coating porosity, (c) surface roughness and (d) deposition efficiency.

3.12(d). Also, the coating roughness is mainly a function of the particle size, and is almost independent of the total mass flow rate.
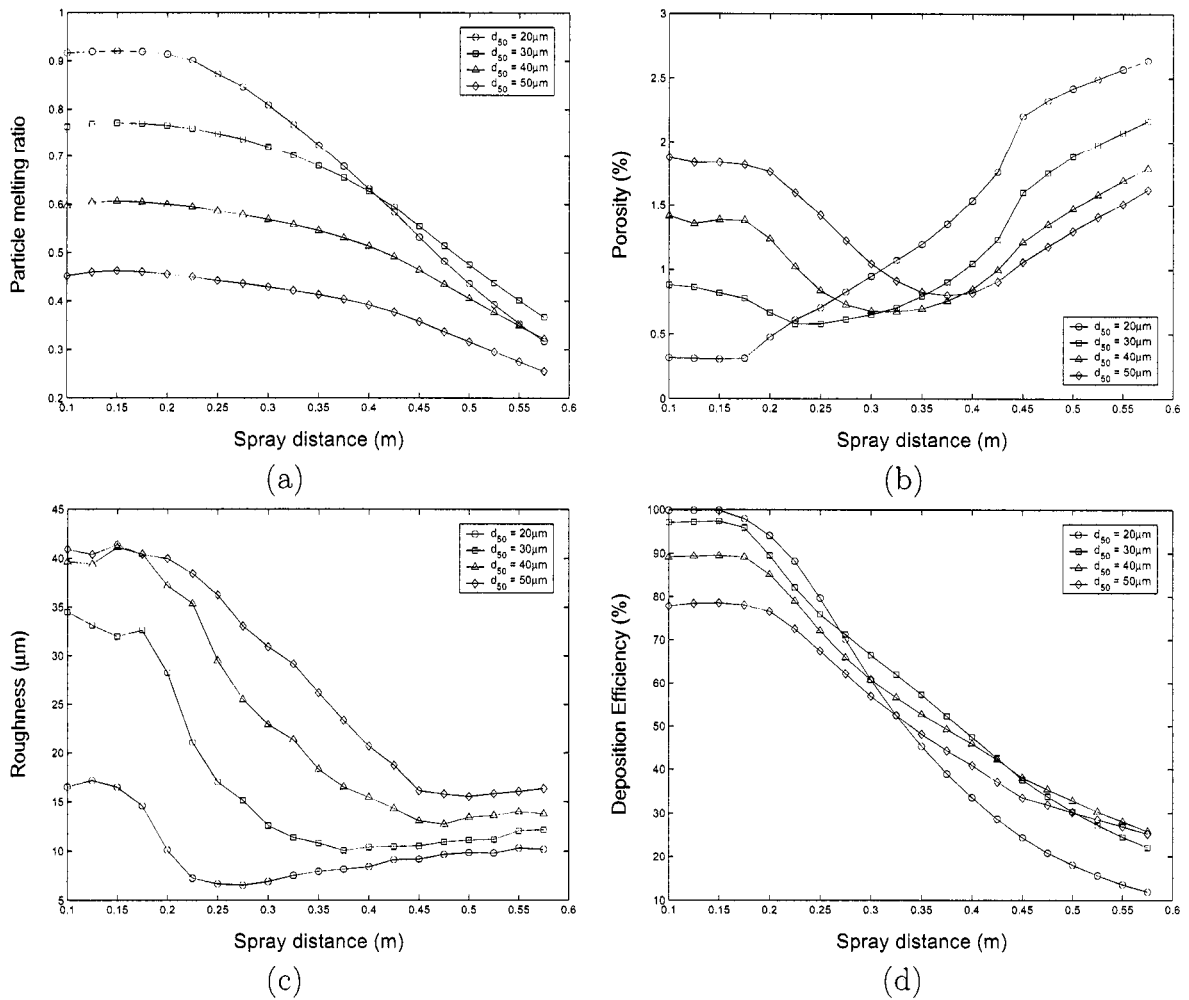
Figure 3.13: The effect of spray distance on (a) particle melting behavior, (b) coating porosity, (c) surface roughness and (d) deposition efficiency.

Effect of spray distance

The spray distance has the most complicated effect on the particle melting behavior and coating porosity. Figure 3.13(a) shows that the particle melting ratio decreases as the spray distance increases. Furthermore, the melting ratio of smaller particles

drops much faster than bigger ones. For instance, the melting ratio of particles with $d_{50} = 20 \ \mu m$ becomes even lower than that of the bigger particles ($d_{50} = 40 \ \mu m$) at large spray distances. As a result, the coating porosity generally increases as the spray distance increases, as shown in Figure 3.13(b). Among all particle sizes of interest, the porosity of coatings produced by particles with $d_{50} = 20 \ \mu m$ increases the fastest as the spray distance increases, and becomes even the largest at a large spray distance. Figure 3.13(c) shows that the coating roughness is high at small spray distances, when the particle melting ratio is high, and decreases as the spray distance increases, especially for large particles. One possible reason for this behavior is that the deposition efficiency is less than 50% for large spray distances (shown in Figure 3.13(d)). Such a low deposition efficiency lead to the result that the increase of the amount of unmelted particles bouncing off the surface outweighs the increase of the amount of unmelted particles caused by the decrease of particle melting ratio. Since only the melted part of particles and small unmelted particles are deposited on the surface, small coating roughness can be achieved at long spray distances. Such a phenomenon can also be observed in Figure 3.9(c) and 3.10(c). When the deposition efficiency is less than 50% , which is caused by low flow rate of oxygen and fuel, the coating roughness is also considerable low. Figure 3.13(d) also shows that the deposition efficiency decreases very fast because the particle melting ratio decreases significantly as the spray distance increases. Specifically, comparing the curves for small particles ($d_{50} = 20 \ \mu m$) in Figure 3.13(a) and 3.13(d), we can see that at large spray distances, the deposition efficiency for particles with $d_{50} = 20 \ \mu m$ becomes the smallest among all the particles of interest and their melting ratio is even less than that of larger particles. Such a result substantiates the conclusion that the particle melting condition has the strongest effect on the deposition efficiency.

110

Table 3.3: Experimental systems for parametric analysis.

Reference	HVOF System	Fuel	Powder	Size (μm)
Hearley et al. [71]	UTP TopGun	Propylene	NiAl	15-45
de Villers Lovelock et al. [36]	JP-5000	Kerosene	WC-17%Co	16-45
Gil and Staia [60]	JP-5000	Kerosene	NiWCrBSi	22-66
Lih et al. [113]	A3000	Propylene	CrC/20NiCr	
Lugscheider et al. [120]	Diamond Jet Hybrid	Hydrogen or Propane	MCrAlY	
Gourlaouen et al. [64]	Diamond Jet Hybrid	Propylene	Stainless Steel	
Swank et al. [179]	JP-5000	Kerosene	Inconel 718	15-63

3.4.3 Comparison of stochastic simulation results and experimental studies

The influence of operating conditions on coating microstructure and deposition efficiency have been experimentally studied by various groups [36, 60, 64, 71, 120, 113]. The gun type and corresponding fuel and powder used in these HVOF thermal spray processes are listed in Table 3.3. In this subsection, we attempt to put into perspective our simulation results described above with respect to the available experimental results.

The important effect of equivalence ratio (which affects to a large extent the degree of particle melting) on coating porosity has been analyzed by several experimental studies. For instance, the porosity of the inert gas atomized (IGA) NiAl coatings produced by the UTP TopGun HVOF gun is 2% when the equivalence ratio is 1.26, which is close to the optimal one [112]. When the equivalence ratio is maintained at 1.68, which is far away from the optimal one, the porosity is 2.54% (or 3.38%) as

a result of increasing fuel flow rate (or decreasing oxygen flow rate) [71]. Although the equivalence ratio is the same in the last two cases, the coating porosity is higher when the total mass flow rate is lower, which validates the conclusion in subsection 3.4.2. By conducting experiments of NiWCrBSi coating processing using a JP-5000 HVOF thermal spray system, Gil and Staia [60] pointed out that the best coating properties are achieved at an equivalence ratio between 1.1 and 1.2, which is very close to our prediction. Note although liquid fuel (kerosene) is used in this process, the relationship between the equivalence ratio and the combustion temperature (see analysis in the work of Swank et al. [178]) is very similar to the Diamond Jet hybrid HVOF thermal spray process studied in our work [112].

One of the main conclusions of our study is that a better particle melting condition (higher degree of particle melting, which occurs under a fuel-rich condition) will increase the deposition efficiency. This conclusion is substantiated by the experiments of Hearley et al. [71]. It is found from their studies that when the equivalence ratio gets close to the optimal one and the total gas flow rate increases, the deposition efficiency also increases. Sakaki and Shimizu [165] have also drawn such a conclusion based on their experiment studies. By analyzing the effects of gun size on HVOF thermal spray, they found that a higher degree of particle melting will lead to a higher deposition efficiency.

3.5   Conclusions

Based on the discussion of the influence of operating conditions on coating microstructure and deposition efficiency, the following main conclusions can be drawn.

1. Particle melting behavior plays a very important role in coating microstructure. A high degree of particle melting tends to achieve a low coating porosity and

a high deposition efficiency. This requires the system to be operated under a fuel-rich condition ($\varphi = 1.2$ for the Diamond Jet Hybrid thermal spray process).

2. Particle size has a significant effect on coating porosity. Particles of mean size (d_{50}) around 35 μm tend to achieve the lowest coating porosity among all the particles of interest under various operating conditions, including the fuel-rich condition. Furthermore, the larger the particle size, the higher the coating surface roughness.

In summary, the comparison of simulation results and available experimental data shows that the stochastic simulation model developed here can be used to properly predict the effects of process parameters, including the particle size, spray distance, flow rate of oxygen, fuel and air, on the microstructure of coatings produced by the Diamond Jet hybrid HVOF thermal spray process.

Chapter 4

Predictive Control of Particle Size Distribution in Particulate Processes

In this chapter, we focus on the development and application of predictive-based strategies for control of particle size distribution (PSD) in continuous and batch particulate processes described by population balance models (PBMs). The control algorithms are designed on the basis of reduced-order models, utilize measurements of principle moments of the PSD, and are tailored to address different control objectives for the continuous and batch processes. For continuous particulate processes, we develop a hybrid predictive control strategy to stabilize a continuous crystallizer at an open-loop unstable steady-state. The hybrid predictive control strategy employs logic-based switching between model predictive control (MPC) and a fall–back bounded controller with a well-defined stability region. The strategy is shown to provide a safety net for the implementation of MPC algorithms with guaranteed stability region. For batch particulate processes, the control objective is to achieve a

final PSD with desired characteristics subject to both manipulated input and product quality constraints. An optimization-based predictive control strategy that incorporates these constraints explicitly in the controller design is formulated and applied to a seeded batch cooling crystallizer example. The strategy is shown to be able to reduce the total volume of the fines by 13.4% compared to a linear cooling strategy, and is shown to be robust with respect to modeling errors.

4.1 Introduction

Particulate processes are prevalent in a number of process industries including agricultural, chemical, food, minerals, and pharmaceuticals. By some estimates, 60% of the products in the chemical industry are manufactured as particulates with an additional 20% using powders as ingredients. Examples of particulate processes include the crystallization of proteins for pharmaceutical applications, the emulsion polymerization reactors for the production of latex, and the titania powder aerosol reactors used in the production of white pigments. One of the key attributes of particulate systems is the co–presence of a continuous phase and a dispersed phase, which leads to the occurrence of physico–chemical phenomena such as particle nucleation, growth, coagulation, and breakage which are absent in homogeneous processes and lead to a distributed characterization of the physical and chemical properties of the particulate product such as particle size, shape, morphology, porosity, molecular weight, etc.

It is now well understood that the physico–chemical and mechanical properties of materials made with particulates are strongly dependent on the characteristics of the corresponding particle size distribution (PSD). For example, a nearly mono–disperse PSD is required for titania pigments to obtain the maximum hiding power per unit mass. Also, in coatings the product's composition, molecular weight and particle size

115

distributions often need to be maintained in specific ranges to ensure the coating has a desired level of film formation, film strength, and gloss. In all of these instances, the PSD provides the critical link between the product quality indices and the operating process variables; and, therefore, the ability to effectively manipulate the PSD is essential for our ability to control the end product quality in these processes. In this light, the problem of synthesizing and implementing high-performance model-based feedback control systems on particulate processes to achieve PSDs with desired characteristics has significant industrial value.

The mathematical models of particulate processes are typically obtained through the application of population, material and energy balances and consist of systems of nonlinear partial integro-differential equations that describe the evolution of the PSD, coupled with systems of nonlinear ordinary differential equations (ODEs) that describe the evolution of the state variables of the continuous phase. There is an extensive literature on population balance modeling, numerical solution, and dynamical analysis of particulate processes, see, for example, [153, 142, 124, 53, 57, 150, 75, 95, 79, 154, 152]; see also [30] for further details and references. Early work on control of particulate processes focused mainly on the understanding of fundamental control-theoretic properties of PBMs [170], and the application of conventional control schemes to crystallizers and emulsion polymerization processes [171, 158, 39], and the references therein. More recently, the realization that PBMs – owing to their infinite-dimensional nature – cannot be used directly for the synthesis of practically implementable controllers, has motivated significant research work on the development of a general order reduction procedure, based on combination of the method of weighted residuals and approximate inertial manifolds, which allows deriving low-order ODE approximations that capture the dominant dynamics of par-

ticulate processes and can, therefore, serve as an appropriate basis for the design of low-order controllers that can be readily implemented in practice [26]. This approach subsequently laid the foundation for the development of a systematic framework for solving a number of important control problems for particulate processes, including the problem of dealing with the highly nonlinear behavior, e.g., owing to complex growth, nucleation, agglomeration and breakage mechanisms, and the Arrhenius dependence of nucleation laws on solute concentration in crystallizers [26], the problem of model uncertainty [27], and the problem of control under actuator constraints [43].

In the operation of particulate processes, constraints typically arise due to physical limitations on the capacity of control actuators and/or desired restrictions on the process state variables, such as temperature and certain properties of the PSD (e.g., crystal concentration and total particle size), in order to meet some safety or product quality requirements. In current industrial practice, the achievement of optimal performance, subject to input and state constraints, relies to a large extent on the use of MPC policies which are well known for their ability to handle multi-variable interactions, constraints, and optimization requirements, all in a consistent, systematic manner. Unlike open-loop model-based optimal control policies (where the optimal operating conditions are calculated off-line), in MPC, the control action is computed by solving repeatedly, on–line, a constrained optimization problem at each sampling time. Owing to this, MPC has the ability to suppress the influence of external disturbances and tolerate model inaccuracies (because of the use of feedback) and force the system to follow the optimal trajectory that respects constraints on the operating conditions.

In this chapter, we focus on the development and application of predictive algorithms for control of PSDs in continuous and batch particulate processes described

by PBMs. The control algorithms are designed on the basis of finite-dimensional models that capture the dominant dynamics of the particulate processes and are tailored to address different control objectives for the batch and continuous processes. The controllers utilize real-time measurements of the principal moments of the PSD (such measurements, for example, can be obtained from PSD measurements made by light scattering techniques as in the case of crystallization processes), as well as measurements of the process temperature and of the concentrations of the continuous-phase species. For continuous particulate processes, we consider the control objective of asymptotic stabilization under constraints and develop a hybrid predictive control methodology that employs logic-based switching between MPC and a fall-back bounded controller with a well-defined stability region. The hybrid predictive control strategy provides a safety net for the implementation of MPC algorithms to particulate processes with guaranteed stability regions. The strategy is successfully used to stabilize a continuous crystallizer at an open-loop unstable steady-state. For batch particulate processes, the control objective is to achieve PSD with desired characteristics subject to both control and product quality constraints. An optimization-based predictive control strategy that incorporates these constraints explicitly in the controller design is formulated and applied to a seeded batch crystallizer of potassium sulfate crystals. The strategy is shown to be able to reduce the volume of fines by 13.4% comparing to linear cooling strategy, and to possess a robustness margin with respect to modeling errors.

4.2 Predictive control of continuous particulate processes

4.2.1 A continuous crystallizer: modeling and dynamics

Crystallization is a particulate process which is widely used in industry for the production of many products including fertilizers, proteins, and pesticides. The fact that the shape of the crystal-size distribution influences significantly the necessary liquid-solid separation, as well as the properties of the product, implies that crystallization requires a population balance in order to be accurately described, analyzed, and controlled. Continuous crystallizers typically exhibit highly oscillatory behavior which suggests the use of feedback control to ensure stable operation and attain a crystal-size distribution with desired characteristics. Under the assumptions of isothermal operation, constant volume, mixed suspension, nucleation of crystals of infinitesimal size, and mixed product removal, a dynamic model for a continuous crystallizer can be derived from a population balance for the particle phase and a mass balance for the solute concentration of the following form [106, 79]:

$$
\begin{aligned}
\frac{\partial n}{\partial \bar{t}} &= -\frac{\partial (R(\bar{t})n)}{\partial r} - \frac{n}{\tau} + \delta(r - 0)Q(\bar{t}) \\
\frac{dc}{d\bar{t}} &= \frac{(c_0 - \rho)}{\bar{\epsilon}\tau} + \frac{(\rho - c)}{\tau} + \frac{(\rho - c)}{\bar{\epsilon}} \frac{d\bar{\epsilon}}{d\bar{t}}
\end{aligned}
\tag{4.1}
$$

where $n(r, \bar{t})$ is the density of crystals of radius $r \in [0, \infty)$ at time $\bar{t}$ in the suspension, τ is the residence time, c is the solute concentration in the crystallizer, c_0 is the solute concentration in the feed, and $\bar{\epsilon} = 1 - \int_0^\infty n(r, \bar{t}) \frac{4}{3}\pi r^3 dr$ is the volume of liquid per unit volume of suspension. $R(\bar{t})$ is the growth rate, $\delta(r - 0)$ is the standard Dirac function, and $Q(\bar{t})$ is the nucleation rate. The term $\delta(r - 0)Q(\bar{t})$ accounts for the production of crystals of infinitesimal (zero) size via nucleation. $R(\bar{t})$ and $Q(\bar{t})$ are
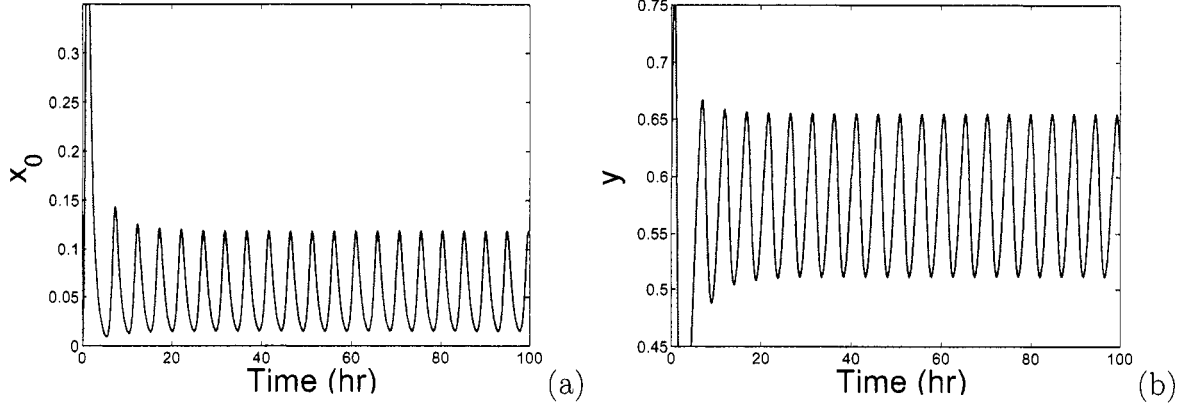
Figure 4.1: Open-loop profiles of (a) crystal concentration and (b) solute concentration obtained from the distributed parameter model.

assumed to follow McCabe's law and Volmer's nucleation law, respectively:

$$
\begin{aligned}
R(\bar{t}) &= k_1(c - c_s) \\
Q(\bar{t}) &= \bar{\epsilon} k_2 \exp\left[-\frac{k_3}{\left(\dfrac{c}{c_s} - 1\right)^2} \right]
\end{aligned}
\tag{4.2}
$$

where k_1, k_2, and k_3 are constants and c_s is the concentration of solute at saturation.

To study the dynamic behavior of the crystallizer in question, a second-order accurate finite-difference spatial discretization scheme with 1,000 discretization points was used to obtain the solution of the system of Eqs.4.1-4.2 (simulations of the system using more discretization points led to identical results). The values of the process parameters used in the simulations can be found in [26].

The solid lines in Figure 4.1 show the open-loop profiles of the total crystal concentration and the solute concentration obtained by solving the distributed parameter model of Eqs.4.1-4.2. It is clear that the crystallizer exhibits highly oscillatory behavior, which is the result of the interplay between growth and nucleation caused by the relative nonlinearity of the nucleation rate as compared to the growth rate (compare the nonlinear dependence of $Q(\bar{t})$ and $R(\bar{t})$ on c in Eq.4.2). To establish

120

that the dynamics of the crystallizer are characterized by a small number of degrees of freedom, the method of moments is applied to the system of Eqs.4.1-4.2 to derive a reduced-order ODE model. Because the nucleation and growth rates are assumed to be independent of particle size, this allows closure of the moments equations, which results in the reduced-order moments model being an exact replication of the evolution of the PBM model. It is noted that the method of moments has been extensively used in the past to analyze the dynamics of particulate processes, e.g., [77, 145].

Defining the jth moment of $n(r, \bar{t})$ as:

$$\mu_j = \int_0^\infty r^j n(r, \bar{t}) dr, \quad j = 0, \ldots, \tag{4.3}$$

multiplying the population balance in Eq.4.1 by r^j, and integrating over all particle sizes, the following system of infinite ordinary differential equations, which describes the rate of change of the moments of the particle size distribution and the solute concentration, is obtained:

$$\frac{d\mu_0}{d\bar{t}} = -\frac{\mu_0}{\tau} + \left(1 - \frac{4}{3}\pi\mu_3\right) k_2 e^{-\frac{k_3}{\left(\frac{c}{c_s} - 1\right)^2}}$$

$$\frac{d\mu_1}{d\bar{t}} = -\frac{\mu_1}{\tau} + \nu k_1 (c - c_s)\mu_0$$

$$\frac{d\mu_2}{d\bar{t}} = -\frac{\mu_2}{\tau} + \nu k_1 (c - c_s)\mu_1$$

$$\frac{d\mu_3}{d\bar{t}} = -\frac{\mu_3}{\tau} + \nu k_1 (c - c_s)\mu_2 \tag{4.4}$$

$$\frac{d\mu_j}{d\bar{t}} = -\frac{\mu_j}{\tau} + \nu k_1 (c - c_s)\mu_{j-1}, \quad j = 4, 5, 6 \ldots,$$

$$\frac{dc}{d\bar{t}} = \frac{c_0 - c - 4\pi k_1 \tau (c - c_s)\mu_2(\rho - c)}{\tau\left(1 - \frac{4}{3}\pi\mu_3\right)}$$

On the basis of the system of Eq.4.4, it is clear that the moments of order four and higher do not affect those of order three and lower, and moreover, the state of the infinite dimensional system is bounded when μ_3 and c are bounded, and it

converges to a globally exponentially stable equilibrium point when $\lim\limits_{t\to\infty} \mu_3 = c_1$ and $\lim\limits_{t\to\infty} c = c_2$, where c_1, c_2 are constants. This implies that the dominant dynamics of the process of Eq.4.1 can be adequately captured by the fifth-order moments model which includes the dynamics of the first four moments and those of the solute concentration. Furthermore, when the following set of dimensionless variables and parameters is introduced:

$$x_0 = 8\pi\sigma^3\mu_0, \ x_1 = 8\pi\sigma^2\mu_1, \ x_2 = 4\pi\sigma\mu_2, \ x_3 = \frac{4}{3}\pi\mu_3, ...,$$

$$t = \frac{\bar{t}}{\tau}, \ \sigma = k_1\tau(c_{0s} - c_s), \ Da = 8\pi\sigma^3 k_2\tau, \tag{4.5}$$

$$F = \frac{k_3 c_s^2}{(c_{0s} - c_s)^2}, \ \alpha = \frac{(\rho - c_s)}{(c_{0s} - c_s)}, \ y = \frac{(c - c_s)}{(c_{0s} - c_s)}, \ u = \frac{(c_0 - c_{0s})}{(c_{0s} - c_s)}$$

The resulting moments model takes the form:

$$
\begin{aligned}
\frac{dx_0}{dt} &= -x_0 + (1 - x_3)Da\exp\left(\frac{-F}{y^2}\right) \\
\frac{dx_1}{dt} &= -x_1 + yx_0 \\
\frac{dx_2}{dt} &= -x_2 + yx_1 \\
\frac{dx_3}{dt} &= -x_3 + yx_2 \\
\frac{dy}{dt} &= \frac{1 - y - (\alpha - y)yx_2}{1 - x_3} + \frac{u}{1 - x_3}
\end{aligned}
\tag{4.6}
$$

where x_i, $i = 0, 1, 2, 3$, are dimensionless moments of the crystal size distribution, y is dimensionless concentration of the solute in the crystallizer, and u is a dimensionless concentration of the solute in the feed (the reader may refer to [43] for a detailed derivation of the moments model, and to [30] for further results and references in this area).

The stability properties of the fifth-order model of Eq.4.6 have been studied thoroughly in [79], see also [106], where it is shown that the global phase space of this model has a unique unstable steady-state surrounded by a stable periodic orbit, and

that the linearization of the system of Eq.4.1 around the unstable steady-state includes two isolated complex conjugate eigenvalues with a positive real part.

4.2.2 Hybrid predictive controller design

Having obtained a low-order ODE model that captures the dominant dynamics of the continuous crystallizer, we proceed in this section to address the controller synthesis problem on the basis of the low-order model. The control objective is to stabilize the crystallizer at an unstable steady-state (which corresponds to a desired PSD) using constrained control action. MPC is a popular method for handling constraints within an optimal control setting. In MPC, the control action is obtained by solving repeatedly, on-line, a finite–horizon constrained open-loop optimal control problem. When the system is linear, the cost quadratic, and the constraints convex, the MPC optimization problem reduces to a quadratic program for which efficient software exists and, consequently, a number of control-relevant issues have been explored, including issues of closed–loop stability, performance, implementation and constraint satisfaction. The crystallizer, however, exhibits highly nonlinear behavior that must be accounted for when designing the controller. While several nonlinear model predictive control (NMPC) schemes have been proposed in the literature (see [126] for a survey of results in this area), the practical implementation of MPC is limited by: (1) the computational difficulties of solving a nonlinear (typically nonconvex) optimization problem at each time step, and (2) the difficulty of characterizing, a priori, the set of initial conditions starting from where a given NMPC controller is guaranteed to be feasible and/or stabilize the closed–loop nonlinear system.

To overcome these difficulties, we have recently developed [47] a hybrid predictive control structure that provides a safety net for the implementation of predictive

control algorithms. The central idea is to use a bounded analytical nonlinear controller, with an explicitly characterized stability region, as a fall–back controller, and embed the operation of MPC within its stability region. In the event that the given predictive controller (which can be based on linear or nonlinear models) is unable to stabilize the closed–loop system (e.g., due to failure of the optimization algorithm, poor choice of the initial condition, insufficient horizon length, etc.), supervisory switching from MPC to the bounded controller safeguards closed–loop stability.

In order to proceed with the hybrid predictive controller design, we initially rewrite the moments model of Eq.4.6 in a more compact form:

$$\dot{\tilde{x}}(t) = f(\tilde{x}(t)) + g(\tilde{x}(t))\tilde{u}(t), \qquad |\tilde{u}| \leq u_{max} \qquad (4.7)$$

where $\tilde{x} = [\tilde{x}_0 \ \tilde{x}_1 \ \tilde{x}_2 \ \tilde{x}_3 \ \tilde{y}]'$, $\tilde{x}_i = x_i - x_i^s$, $i = 0, 1, 2, 3$, $\tilde{y} = y - y^s$, $\tilde{u} = u - u^s$, $u_{max} \geq 0$ denotes the bound on the manipulated input, the superscript at x_i^s refers to the unstable steady-state at which we would like to asymptotically stabilize the system.

In order to provide the necessary background for our main results in section 4.2.3, we will briefly review in the remainder of this section the design procedure for, and the stability properties of, both the bounded and model predictive controllers, which constitute the basic components of our hybrid control scheme. For clarity of presentation, we will focus only on the state feedback problem where measurements of $x(t)$ are assumed to be available for all t; the readers may refer to [129] for results on output feedback hybrid predictive control.

Bounded Lyapunov-based control

Consider the system of Eq.4.7, for which a control Lyapunov function (CLF), $V(\tilde{x})$, is available, for more details on the existence and construction of CLFs, see [52].

Using the control Lyapunov function, we construct, using the results in [115], see also [44, 45], the following continuous bounded control law:

$$u(\tilde{x}) = -k(\tilde{x})L_g V(\tilde{x}) := b(\tilde{x}) \qquad (4.8)$$

where

$$k(\tilde{x}) = \begin{cases} \dfrac{L_f V(\tilde{x}) + \sqrt{(L_f V(\tilde{x}))^2 + (u_{max} L_g V(\tilde{x}))^4}}{(L_g V(\tilde{x}))^2 \left[1 + \sqrt{1 + (u_{max} L_g V(\tilde{x}))^2}\right]}, & L_g V(\tilde{x}) \neq 0 \\ 0, & L_g V(\tilde{x}) = 0 \end{cases} \qquad (4.9)$$

where $L_f V(\tilde{x}) = \dfrac{\partial V(\tilde{x})}{\partial \tilde{x}} f(\tilde{x})$, and $L_g V(\tilde{x}) = \dfrac{\partial V(\tilde{x})}{\partial \tilde{x}} g(\tilde{x})$. An estimate of the constrained stability region of the above controller can be obtained using the level sets of V, i.e.,

$$\Omega = \{\tilde{x} \in \mathbb{R}^n : V(\tilde{x}) \leq c^{max}\} \qquad (4.10)$$

where $c^{max} > 0$ is the largest number for which every nonzero element of Ω is fully contained in the set:

$$\Phi = \{\tilde{x} \in \mathbb{R}^n : L_f V(\tilde{x}) < u_{max}|L_g V(\tilde{x})|\} \qquad (4.11)$$

Model predictive control

In this section, we consider model predictive control of the system under control constraints described by Eq.4.7. In the literature, several MPC formulations are currently available. For the sake of a concrete illustration, we briefly describe here the traditional formulation (we note that any other MPC formulation can be used; see [47] for further details on this issue). For this case, the control action in MPC at state $\tilde{x}$ and time t is conventionally obtained by solving, on-line, a finite horizon optimal control problem of the form

$$P(\tilde{x}, t) \quad : \quad \min\{J(\tilde{x}, t, \tilde{u}(\cdot))|\tilde{u}(\cdot) \in S\}, \qquad s.t. \ \dot{\tilde{x}} = f(\tilde{x}) + g(\tilde{x})\tilde{u} \qquad (4.12)$$

where $S = S(t, T)$ is the family of piecewise continuous functions, with period Δ, mapping $[t, t+T]$ into $\mathcal{U} := \{\tilde{u} \in \mathbb{R} : |\tilde{u}| \leq \tilde{u}_{max}\}$ and T is the specified horizon. The constraint in Eq.4.12 is a nonlinear model describing the time evolution of the states $\tilde{x}$. A control $\tilde{u}(\cdot)$ in S is characterized by the sequence $\{\tilde{u}[k]\}$ where $\tilde{u}[k] := \tilde{u}(k\Delta)$, and satisfies $\tilde{u}(t) = \tilde{u}[k]$ for all $t \in [k\Delta, (k+1)\Delta)$. The performance index is given by

$$J(\tilde{x}, t, \tilde{u}(\cdot)) = \int_t^{t+T} \left[\|\tilde{x}^u(s; \tilde{x}, t)\|_Q^2 + \|\tilde{u}(s)\|_R^2 \right] ds + F(\tilde{x}(t+T)) \tag{4.13}$$

where $\| \cdot \|_Q$ refers to the weighted norm, defined by $\|\tilde{x}\|_Q^2 = \tilde{x}'Q\tilde{x}$ for all $\tilde{x} \in \mathbb{R}^n$, Q and R are strictly positive–definite, symmetric matrices and $\tilde{x}^u(s; \tilde{x}, t)$ denotes the solution of Eq.4.7, due to control $\tilde{u}$, with initial state $\tilde{x}$ at time t and $F(\cdot)$ denotes the terminal penalty. The minimizing control $\tilde{u}^0(\cdot) \in S$ is then applied to the plant over the interval $[k\Delta, (k+1)\Delta]$ and the procedure is repeated indefinitely. This defines an implicit model predictive control law

$$M(\tilde{x}) = argmin(J(\tilde{x}, t, \tilde{u}(\cdot))) = \tilde{u}^0(t; \tilde{x}, t) \tag{4.14}$$

A hybrid predictive control strategy: switching logic design

In this section, we describe a switching strategy that brings together the MPC and bounded controllers in a way that guarantees asymptotic closed-loop stability and provides a safety net for the implementation of MPC. To this end, consider the constrained nonlinear system of Eq.4.7, with any initial condition $\tilde{x}(0) \in \Omega$, where Ω was defined in Eq.4.10, under the model predictive controller of Eqs.4.12-4.14. Also let $\bar{T} \geq 0$ be the earliest time for which either the closed–loop state, under MPC, satisfies

$$L_f V(\tilde{x}(\bar{T})) + L_g V(\tilde{x}(\bar{T}))M(\tilde{x}(\bar{T})) \geq 0 \tag{4.15}$$

126
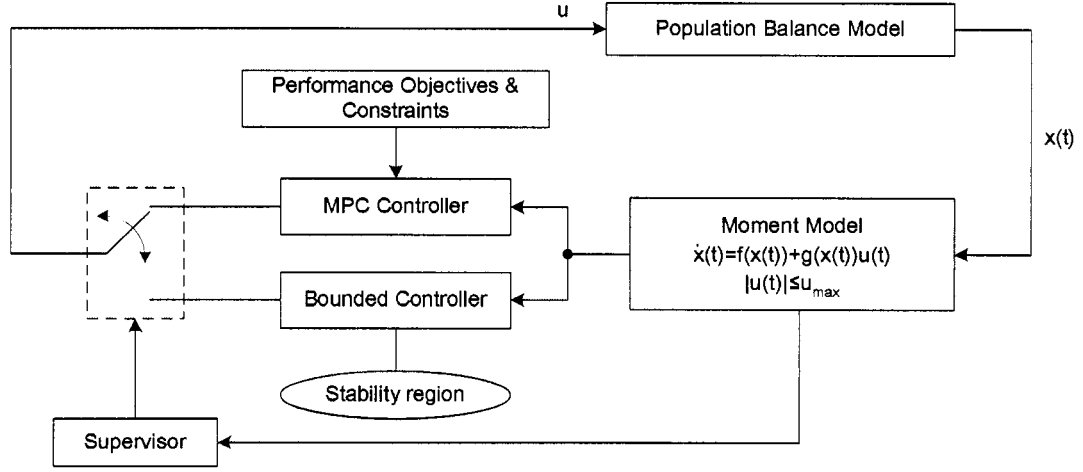
Figure 4.2: Closed-loop system under hybrid predictive control.

or the MPC algorithm fails to prescribe any control move. Then, the switching rule given by

$$\tilde{u}(t) \;=\; \begin{cases} M(\tilde{x}(t)), & 0 \le t < \bar{T} \\ b(\tilde{x}(t)), & t \ge \bar{T} \end{cases} \qquad (4.16)$$

guarantees that the origin of the switched closed–loop system of Eqs.4.7-4.16 is asymptotically stable (see [47] for a detailed proof as well as possible extensions of the switching scheme).

The hybrid predictive control structure consists of the predictive controller, the bounded nonlinear controller with its estimated region of closed-loop stability, and a high–level supervisor that orchestrates the switching between the two controllers. A schematic representation of the hybrid predictive control structure is shown in Figure 4.2. The implementation procedure is outlined below:

1. Consider the population balance model of Eqs.4.1-4.2 and use the model reduction procedure, based on the method of moments, to derive the finite dimensional ODE model of Eq.4.6 that captures the dominant dynamics of the continuous crystallizer.

2. Given the constraints on the manipulated input and an appropriate CLF, design the bounded controller, on the basis of the system of Eq.4.6, using Eqs.4.8-4.9, and compute the stability region using Eqs.4.10-4.11.

3. Given the performance objective and constraints, construct the MPC optimization algorithm, on the basis of the system of Eq.4.6, and choose the MPC parameters.

4. Initialize the closed–loop system under MPC, with the initial condition $x(0)$ belonging to the set Ω.

5. Monitor the temporal evolution of the closed–loop trajectory of x (by checking Eq.4.15 at each time) and denote the earliest time that either Eq.4.15 holds or the MPC algorithm prescribes no control move as $\bar{T}$.

6. If such a $\bar{T}$ exists, discontinue MPC implementation, switch to the bounded controller and implement it for all future times.

4.2.3 Application to control of PSD in a continuous crystallizer

In this section, we demonstrate the application of the hybrid predictive control strategy to the continuous crystallizer of Eqs.4.1-4.2. The control objective is to suppress the oscillatory behavior of the crystallizer and stabilize it at an unstable steady-state that corresponds to a desired PSD by manipulating the inlet solute concentration. To achieve this objective, we assume that the first four moments, as well as the solute concentration, can be measured on line. Following the proposed methodology, we initially use the moments model of Eq.4.6 to design the controllers. The values of the dimensionless model parameters in Eq.4.6 are chosen to be: $F = 3.0$, $\alpha = 40.0$ and $Da = 200.0$. The dimensionless solute feed concentration, u, is subject to the

constraints: $-1 \leq u \leq 1$ (which correspond to the following constraint on the inlet solute concentration; $980kg/m^3 \leq c_0 \leq 1000kg/m^3$). The desired steady-state is $x^s = [x_0^s \ x_1^s \ x_2^s \ x_3^s \ y^s]' = [0.065 \ 0.040 \ 0.024 \ 0.015 \ 0.612]'$, and $u^s = 0.2$.

To facilitate the design of the bounded controller and construction of the CLF, we initially re-write the moments model of Eq.4.6 in deviation variable form – thus translating the steady-state to the origin – to obtain the system of Eq.4.7 which we transform into the normal form. To this end, we define the auxiliary output variable, $\bar{y} = h(x) = \tilde{x}_0$, and introduce the invertible coordinate transformation: $[\xi' \ \eta']' = \Pi(x) = [\tilde{x}_0 \ f_1(\tilde{x}) \ \tilde{x}_1 \ \tilde{x}_2 \ \tilde{x}_3]'$, where $\xi = [\xi_1 \ \xi_2]' = [\tilde{x}_0 \ f_1(\tilde{x})]'$, $\bar{y} = \xi_1$, $f_1(\tilde{x}) = -\tilde{x}_0 + (1 - \tilde{x}_3)Da \exp(-F/\tilde{y}^2)$, and $\eta = [\eta_1 \ \eta_2 \ \eta_3]' = [\tilde{x}_1 \ \tilde{x}_2 \ \tilde{x}_3]'$. The state-space description of the system in the transformed coordinates takes the form:

$$\begin{aligned} \dot{\xi} &= A\xi + bl(\xi, \eta) + b\alpha(\xi, \eta)u \\ \dot{\eta} &= \Psi(\eta, \xi) \end{aligned} \tag{4.17}$$

where $A = \begin{bmatrix} 0 & 1 \\ 0 & 0 \end{bmatrix}$, $b = [0 \ 1]'$, $l(\xi, \eta) = L_f^2 h(\Pi^{-1}(\xi, \eta))$ is the second-order Lie derivative of the scalar function, $h(\cdot)$, along the vector field $f(\cdot)$, and $\alpha(\xi, \eta) = L_g L_f h(\Pi^{-1}(\xi, \eta))$ is the mixed Lie derivative. The forms of $f(\cdot)$ and $g(\cdot)$ can be obtained by re-writing the system of Eq.4.6 in the form of Eq.4.7, and are omitted for brevity.

The partially-linear ξ-subsystem in Eq.4.17 is used to design a bounded controller that stabilizes the full interconnected system of Eq.4.17 and, consequently, the original system of Eq.4.6. For this purpose, a quadratic function of the form, $V_\xi = \xi'P\xi$, is used as a CLF in the controller synthesis formula of Eqs.4.8-4.9, where the positive–definite matrix, P, is chosen to satisfy the Riccati matrix equality: $A'P + PA - Pbb'P = -\bar{Q}$ where $\bar{Q}$ is a positive–definite matrix. An estimate of the region of constrained closed–loop stability for the full system is obtained by defining a composite Lyapunov function of the form $V_c = V_\xi + V_\eta$, where $V_\eta = \eta'P_\eta\eta$ and P_η is
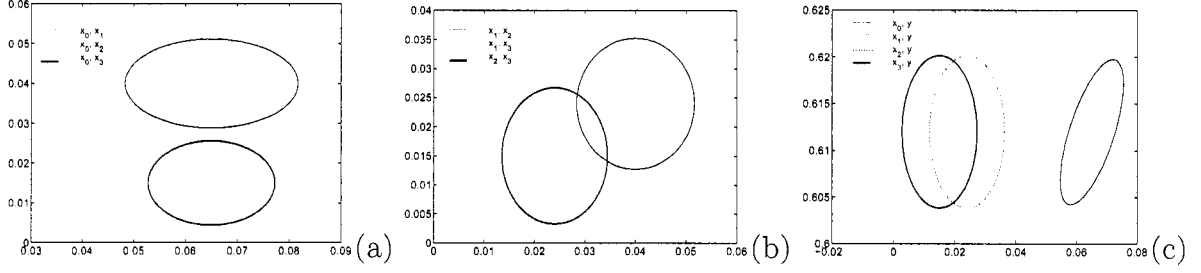
Figure 4.3: Two dimensional projections of the stability region for the 10 distinct combinations of the states of the reduced order system of Eq.4.6.

a positive–definite matrix, and choosing a level set of V_c, Ω_c, for which $\dot{V}_c < 0$ for all x in Ω_c. The two-dimensional projections of the stability region are shown in Figure 4.3 for all possible combinations of the system states.

In designing the predictive controller, a linear MPC formulation, with a terminal equality constraint of the form $x(t + T) = 0$, is chosen (based on the linearization of the reduced order model of Eq.4.6 around the unstable equilibrium point). The parameters in the objective function of Eq.4.13 are taken to be: $Q = qI$, with $q = 1$, $R = rI$, with $r = 1.0$, and $F = 0$. We also choose a horizon length of $T = 0.25$ in implementing the predictive controller. The resulting quadratic program is solved using the MATLAB subroutine QuadProg, and the full nonlinear closed–loop system is integrated using finite-differences.

In the first set of simulation runs, we tested the ability of the predictive controller to stabilize the crystallizer starting from the initial condition, $x(0) = [0.066\ 0.041\ 0.025\ 0.015\ 0.560]'$. The result is shown by the solid lines in Figure 4.4(a)–(e) where it is seen that the predictive controller, with a horizon length of $T = 0.25$, is able to stabilize the closed–loop system at the desired equilibrium point. Starting from the initial condition $x(0) = [0.033\ 0.020\ 0.013\ 0.0075\ 0.570]'$, however, the predictive controller yields no feasible solution. If the terminal equality constraint is removed, to
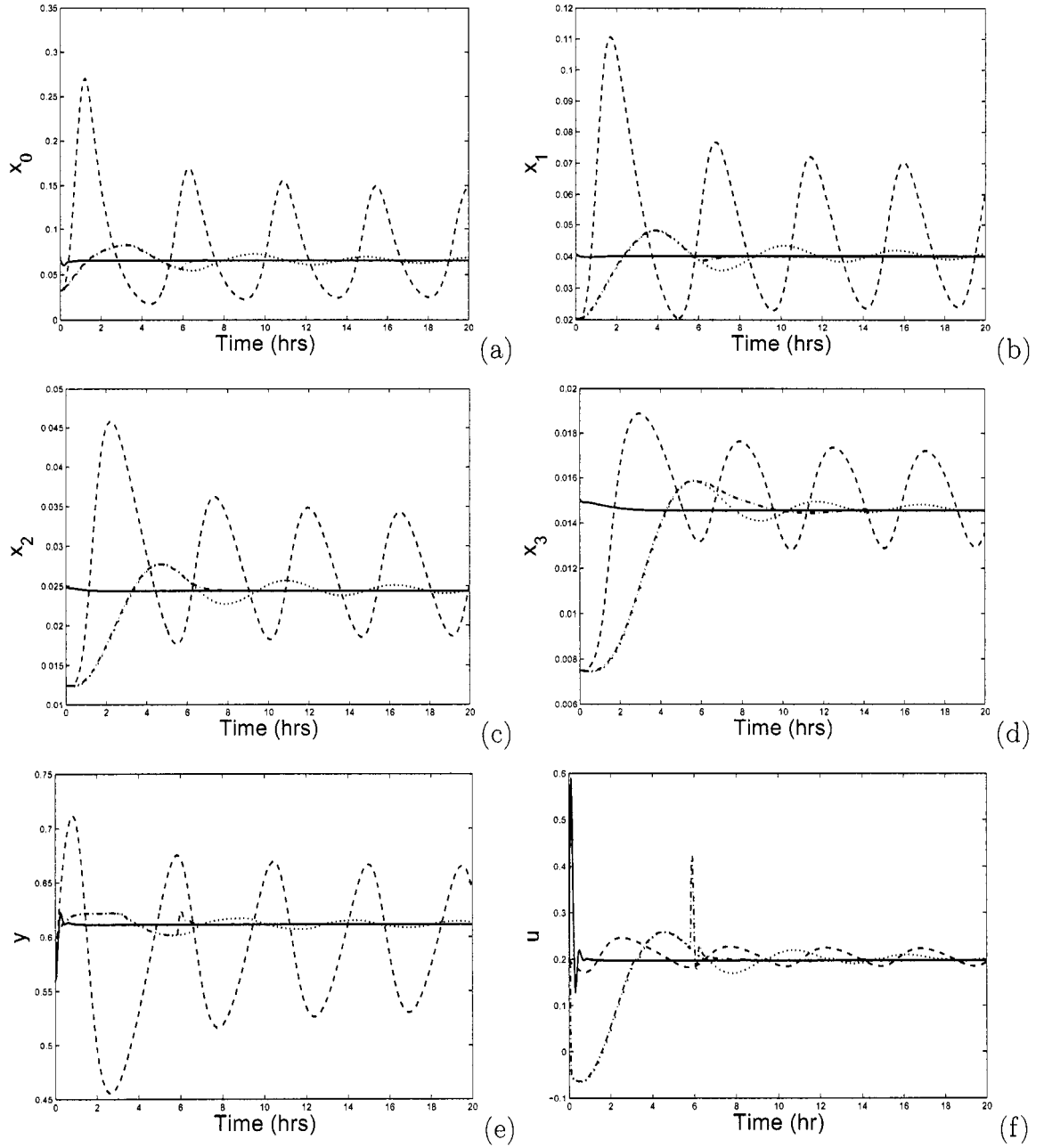
Figure 4.4: Continuous crystallizer example: closed-loop profiles of the dimensionless crystallizer moments (a)-(d), the solute concentration in the crystallizer (e) and the manipulated input (f) under MPC with stability constraints (solid lines), under the bounded controller (dotted lines), and using the hybrid predictive controller (dash-dotted lines).
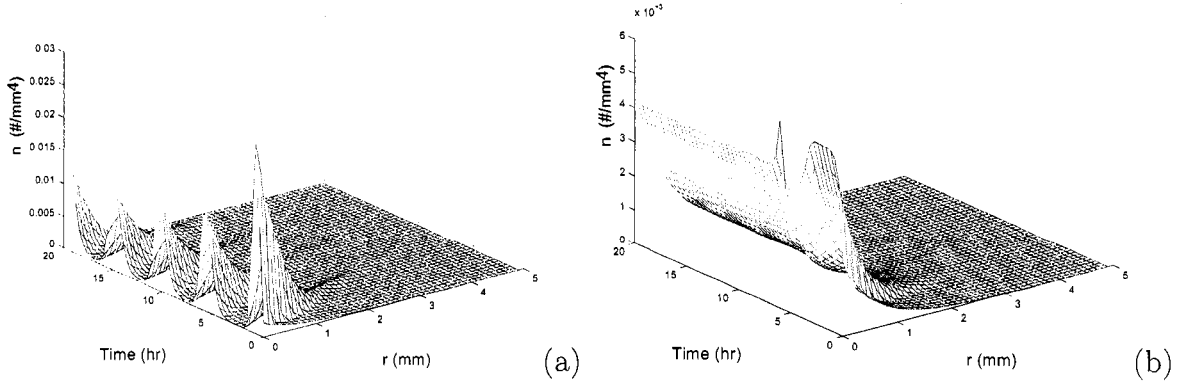
Figure 4.5: Closed-loop profiles of the PSD: (a) under MPC without terminal constraints; (b) under the hybrid predictive controller.

make MPC feasible, we see from the dashed lines in Figure 4.4(a)–(e) that the resulting control action cannot stabilize the closed–loop system, and leads to a stable limit cycle. Figure 4.5(a) shows the resulting sustained oscillations in the PSD under MPC without terminal constraints. On the other hand, when the hybrid predictive controller is implemented, the supervisor detects initial infeasibility of MPC and implements the bounded controller in the closed loop. As the closed–loop states evolve under the bounded controller and get closer to the desired steady–state, the supervisor finds (at $t = 5.8$) that the MPC becomes feasible and, therefore, implements it for all future times. Note that despite the "jump" in the control action profile as we switch from the bounded controller to MPC at $t = 5.8$, (see the difference between dotted and dash-dotted profiles in Figure 4.4(f)), the moments of the PSD in the crystallizer continue to evolve smoothly (dash-dotted lines in Figure 4.4(a)–(e)). The supervisor finds that MPC continuous to be feasible and is implemented in closed–loop to stabilize the closed–loop system at the desired steady-state. The dotted lines in Figure 4.4(a)–(e) shows the simulation results of the closed-loop system under the bounded controller only. Compared with the simulation results under the

bounded controller, the hybrid predictive controller (dash-dotted lines) stabilizes the system much faster, and achieves a better performance, reflected in a lower value of the performance index (0.1282 vs 0.1308). The evolution of PSD under the hybrid predictive controller, shown in Figure 4.5(b), illustrates clearly how the hybrid controller stabilizes the PSD at the desired steady state. The manipulated input profiles for the three scenarios are shown in Figure 4.4(f).

4.3 Predictive control of batch particulate processes

Batch crystallization differs from continuous crystallization in that the withdrawal of product for the batch process is made only once at the end of the batch run. It is commonly used in the chemical, pharmaceutical, photographic, and many other industries as manufacturing process to prepare a wide variety of crystalline products. Compared with continuous particulate processes, batch particulate processes have several desirable features [191]. For instance, in batch particulate processes, the equipment is relatively simple and flexible, and requires a relatively lower level of maintenance. Batch particulate processes are particularly applicable to chemical systems difficult to process, such as processes with toxic or highly viscous properties. Also, experiments on batch particulate processes can be used to examine a large number of operational variables in a short time. Systems that are difficult to operate continuously may conveniently be investigated in a batch-wise manner with relatively minimum development time and investment. For capacity requirements less than 500 kg/h, batch particulate processes are usually more economically advantageous. Furthermore, if the product requires a relatively narrow PSD, a batch particulate process is clearly a better choice.

4.3.1 A seeded batch crystallizer: modeling and dynamics

As an example, we consider the seeded batch cooling crystallizer studied in [153, 155], which produces crystals of potassium sulfate. The population balance model of this crystallizer, describes the evolution of the crystal size distribution, $n(r, t)$, under the joint effects of nucleation (B is the crystal nucleation rate) and crystal growth (G is the crystal growth rate). The evolution of the solute concentration, C, and reactor temperature, T, are described by two ODEs. The process model has the following form:

$$\frac{\partial n(r, t)}{\partial t} + G(t)\frac{\partial n(r, t)}{\partial r} = 0, \quad n(0, t) = \frac{B(t)}{G(t)}$$

$$\frac{dC}{dt} = -3\rho k_v G(t)\mu_2(t) \tag{4.18}$$

$$\frac{dT}{dt} = -\frac{UA}{MC_p}(T - T_j) - \frac{\Delta H}{C_p}3\rho k_v G(t)\mu_2(t)$$

where ρ is the density of crystals, k_v is the volumetric shape factor, U is the overall heat-transfer coefficient, A is the total heat-transfer surface area, M is the mass of solvent in the crystallizer, C_p is the heat capacity of the solution, T_j is the jacket temperature, ΔH is the heat of reaction, and $\mu_2 = \int_0^\infty r^2 n(r, t)dr$ is the second moment of the PSD. The nucleation rate, $B(t)$, and the growth rate, $G(t)$, are given by

$$B(t) = k_b e^{-E_b/RT}\left(\frac{C - C_s(T)}{C_s(T)}\right)^b \mu_3,$$

$$G(t) = k_g e^{-E_g/RT}\left(\frac{C - C_s(T)}{C_s(T)}\right)^g \tag{4.19}$$

where E_b is the nucleation activation energy, E_g is the growth activation energy, b and g are exponents relating nucleation rate and growth rate to supersaturation, C_s is the saturation concentration of the solute, and $\mu_3 = \int_0^\infty r^3 n(r, t)dr$ is the third moment of the PSD. The values of the process parameters are given in Table 5.1. Eq.4.20 is used to calculate the saturation and metastable concentrations corresponding to

Table 4.1: Parameter values for the seeded batch cooling crystallizer of Eqs.4.18–4.19.

b	=	1.45		g	=	1.5	
k_b	=	285.0	$1/(s\,\mu m^3)$	k_g	=	1.44×10^8	$\mu m/s$
E_b/R	=	7517.0	K	E_g/R	=	4859.0	K
U	=	1800	$kJ/m^2 \cdot hr \cdot K$	A	=	0.25	m^2
ΔH	=	44.5	kJ/kg	C_p	=	3.8	$kJ/K \cdot kg$
M	=	27.0	kg	ρ	=	2.66×10^{-12}	$g/\mu m^3$
k_v	=	1.5		t_f	=	30	min

the solution temperature T. These two concentrations represent the constraints on the solution concentration, i.e., $C_s \leq C \leq C_m$ that must hold during the whole batch run. The initial seed distribution of the seeded batch crystallizer is assumed to be a parabolic distribution, from 250 to 300 μm, and the maximum density of initial seed distribution, which is $2/\mu m \cdot g$ solvent, occurs at 275 μm, i.e., $n(r,0) = 0.0032(300 - r)(r - 250)$, for $250\mu m \leq r \leq 300\mu m$, and $n(r,0)$=0, for $r < 250\mu m$ and $r > 300\mu m$.

$$C_s(T) = 6.29 \times 10^{-2} + 2.46 \times 10^{-3}T - 7.14 \times 10^{-6}T^2$$

$$C_m(T) = 7.76 \times 10^{-2} + 2.46 \times 10^{-3}T - 8.10 \times 10^{-6}T^2$$

(4.20)

To study the dynamic behavior of the crystallizer, a second-order accurate finite difference scheme with 1500 discretization points is used to obtain the solution of the system of Eq.4.18. Figure 4.6 shows the evolution of the reactor temperature, T, the solution concentration, C, and the PSD under a linear cooling strategy (where the jacket temperature, T_j, is cooled down linearly from 50°C to 30°C). From Figure 4.6(b), it is clear that there is a gap between the crystals formed by nucleation and those growing from the seeds during the whole reaction period. Based on this observation, we developed two moments models to simulate the dynamics of the crystals formed by nucleation and the crystals growing from the seeds separately. The two models are given by Eqs. 4.21 and 4.22, respectively. The mass and energy
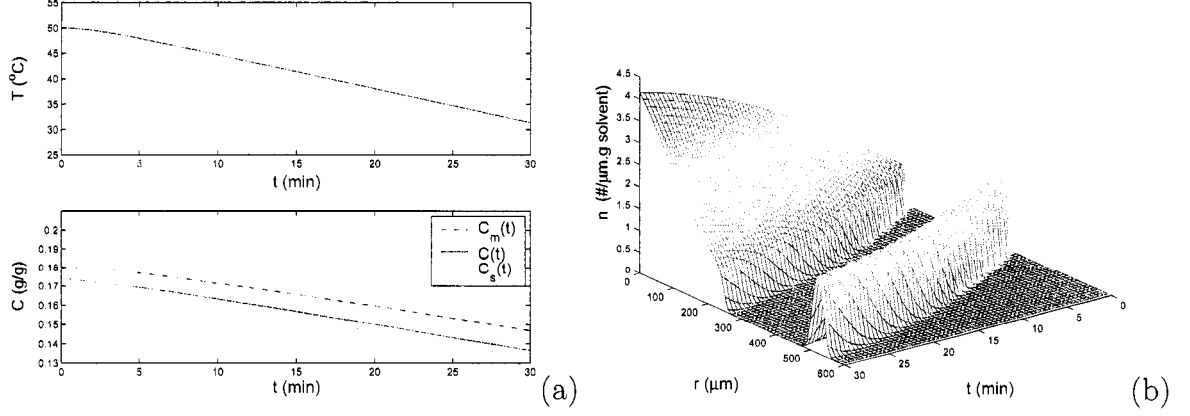
Figure 4.6: Simulation results for the linear cooling strategy: (a) reactor temperature and concentration profiles (dashed and dotted lines represent the upper and lower constraints on the concentration respectively); (b) the evolution of crystal size distribution.

balances in these two models are described by Eq. 4.23.

$$
\begin{aligned}
\frac{d\mu_0^n}{dt} &= B(t) \\
\frac{d\mu_i^n}{dt} &= iG(t)\mu_{i-1}^n(t), \quad i = 1, 2, 3
\end{aligned}
\tag{4.21}
$$

$$
\begin{aligned}
\mu_0^s &= k_4 \\
\frac{d\mu_i^s}{dt} &= iG(t)\mu_{i-1}^s(t), \quad i = 1, 2, 3
\end{aligned}
\tag{4.22}
$$

$$
\begin{aligned}
\frac{dC}{dt} &= -3\rho k_v G(t)(\mu_2^n(t) + \mu_2^s(t)) \\
\frac{dT}{dt} &= -\frac{UA}{MC_p}(T - T_j) - \frac{\Delta H}{C_p}3\rho k_v G(t)(\mu_2^n(t) + \mu_2^s(t))
\end{aligned}
\tag{4.23}
$$

where μ_i^n and μ_i^s (i=0,1,2,3) are the first four moments of the PSD of the crystals formed by nucleation and the crystals growing from the seeds, respectively, and are defined by

$$
\begin{aligned}
\mu_i^n &= \int_0^{r_g} r^i n(r, t) dr \\
\mu_i^s &= \int_{r_g}^{\infty} r^i n(r, t) dr, \quad i = 0, 1, 2, 3.
\end{aligned}
\tag{4.24}
$$

The superscript, n, stands for nucleation, and s stands for seed. r_g is the radius at the middle of the gap between two groups of crystals. This characteristic radius is
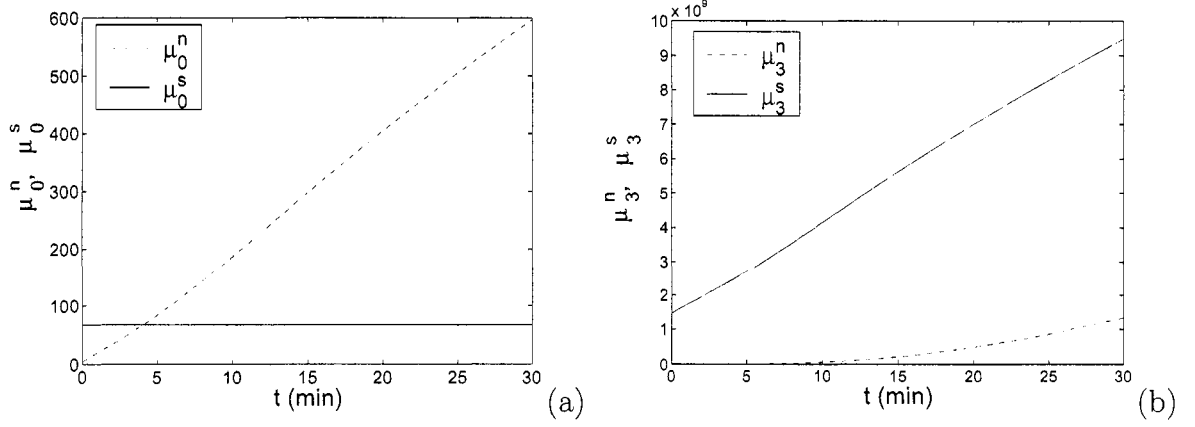
Figure 4.7: Simulation results for the linear cooling strategy: (a) the zeroth and (b) third moments of the PSD of the crystals formed by nucleation (dashed lines) and the those growing from the seeds (solid lines).

a function of time, and can be determined only from the population balance model. Since the model does not consider crystal breakage or agglomeration during the crystallization, μ_0^s, which is the total number of the crystals growing from the seeds, remains constant k_4 during the crystallization period. Figure 4.7 shows a comparison between μ_i^n and μ_i^s, (i=0,3), based on simulations of the two moments models. The purpose of deriving two moments models instead of one is to facilitate the design of the predictive controller for the PSD of each group of crystals discussed in the next section.

4.3.2 Predictive controller design: accounting for state and input constraints

Unlike the control of continuous particulate processes, asymptotic stabilization is not an issue in the control of batch processes. More important is the objective of achieving a desired particle size distribution at the end of the batch and satisfying state and control constraints during the whole batch run. Significant previous work has fo-

cused on PSD control in the batch crystallizers [153, 195]. [137] derived an open-loop optimal control strategy where the objective function involves maximization of the crystal size and the cooling curve is the decision variable. [130] developed a method for assessing parameter uncertainty and studied its effects on the open-loop optimal control strategy, which maximized the weight mean size of the product. [201] developed an on-line optimal control methodology for a seeded batch cooling crystallizer to improve the product quality expressed in terms of the mean size and the width of the distribution. [78] designed a hierarchical multiobjective strategy to control the PSD in semi-batch emulsion polymerization. In these previous works, most efforts were focused on the open-loop optimal control of the batch crystallizer, i.e., the optimal operating condition was calculated off-line and based on mathematical models. The successful application of such a control strategy relies, to a large extent, on the accuracy of the models.

In this section, we focus on developing a closed-loop predictive control system to minimize the total volume of fines (i.e., small crystals formed by nucleation) in the final product. In the operation of industrial crystallizers, the fines usually cause difficulties in downstream processing equipment (e.g., filtration) and affect both product quality and process economics. Such effects are especially important in a seeded batch crystallizer, since its final products mainly grow from the seeds rather than from the crystal formed by nucleation. Excessive fines may also require a relatively long batch run time to achieve the desired final size of the product. Some experimental studies on fines destruction for batch crystallizers have been reported. [83] first described the application of fines destruction in batch crystallization of potassium sulfate solutions. [159] implemented a feedback control fines dissolution strategy in order to maintain the fines slurry density at some constant value over the batch run.

These studies demonstrate the experimental feasibility of dramatically reducing the amount of fines in the final product based on the reactor design.

In this work, a closed-loop predictive control scheme is developed to control the seeded batch cooling crystallizer described by Eq.4.18. The control objective is to minimize the volume of fines in the final product, (i.e., the third moment of the crystals formed by nucleation, μ_3^n), by manipulating the jacket temperature, T_j. The principle moments are calculated from the on-line measured PSD, n, which can be obtained by measurement techniques such as the laser light scattering method. The concentration and reactor temperature are also assumed to be measured in real time. In the closed-loop control structure, the PBM, together with the mass and energy balances of Eq.4.18, are used to describe the process while the reduced-order model of Eqs.4.21–4.22 is used within the MPC for the purpose of prediction. Therefore, the PBM is utilized to simulate the value of the state variables (n, C, T) at $t_i = i\Delta t$, where i=1,2,...,m, $m = t_f/\Delta t$, and t_f is the length of the crystallization period. Thus, the values of the moments $(\mu_j^n(t_i), \mu_j^s(t_i)$, j=0,1,2,3) are calculated from the PSD at every t_i, $n(r, t_i)$. The values of $\mu_j^n(t_i), \mu_j^s(t_i)$, $C(t_i)$, $T(t_i)$, and the optimal trajectory of T_j solved at the previous time step, are used as the initial values for the reduced-order model in MPC to solve an optimization problem for a horizon length of $t_f - t_i$. The first step of the solution (T_j) is implemented to generate the value of state variables at the end of next time step, t_{i+1}. This procedure is repeated every Δt until the end of the batch run.

Manipulated input limitations and concentration specifications are incorporated

as input and state constraints on the optimization problem, which takes the form

$$
\begin{aligned}
\min \quad & \mu_3^n(t_f) \\
s.t. \quad & T_{j,min} \leq T_j \leq T_{j,max}, \\
& C_s \leq C \leq C_m, \\
& \left| \frac{dT_j}{dt} \right| \leq k_5, \\
& \mu_3^s(t_f) \geq V_1
\end{aligned}
\tag{4.25}
$$

where μ_3^n, μ_3^s, T_j and C are obtained by solving the moments models of Eqs.4.21-4.22. $T_{j,min}$ and $T_{j,max}$ are the constraints on the manipulated variable, T_j, and set to 30°C and 50°C in the simulation. C_s and C_m, which can be calculated from Eq.4.20, are the constraints on the solution concentration. The constant, k_5, (chosen to be 2°C/min) is the maximum gradient of the jacket temperature. V_1, chosen as 8.3301×10^9 in the simulations, denotes the lower bound on the total volume of the crystals growing from the seeds. Such constraint on $\mu_3^s(t_f)$ represents a desirable quality of the final product. In the simulation, Δt and t_f are chosen as 30 seconds and 30 min, respectively. The optimization problem is solved using the steepest descent method, which is a gradient-based optimization method and converges faster when compared with other optimization methods such as SQP. Considering the high dimensionality of the nonlinear optimization problem, fast convergence is critical to real time implementation of the feasibility of the predictive control policy. Furthermore, the optimization results based on the steepest descent method and SQP were compared, and only a small difference was observed, while the SQP method took a considerably longer time to converge than the steepest descent method.

4.3.3 Closed-loop simulation results

To illustrate the effect of model accuracy on the ability of the predictive controller to control the crystallizer, we considered two different cases. In the first case, it
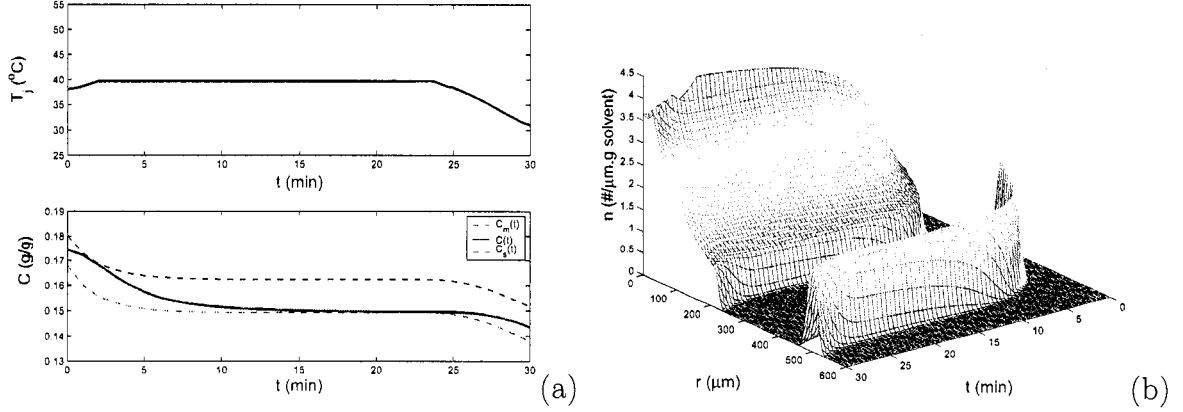
Figure 4.8: Closed-loop simulation results for matched models: (a) Jacket temperature and concentration profiles (dashed and dotted lines represent the upper and lower constraints on the concentration, respectively); (b) the evolution of crystal size distribution.

is assumed that the same model parameters are used in the MPC model (i.e., the moments model) and the process model (i.e., population balance model). In another case, a process–model mismatch is allowed by changing the value of the parameter b, which is the exponent relating nucleation rate to supersaturation, from its nominal value of 1.45 to 1.35 in the moments model used in MPC. The simulation results of these two cases were also compared with the open-loop simulation results obtained under the linear cooling strategy.

Figure 4.8 shows the closed-loop simulation results for the case of a perfect process–model match. Figure 4.8(a) shows the optimal trajectory of the jacket temperature and solution concentration while Figure 4.8(b) shows the evolution of the PSD. Clearly, the constraints on the jacket temperature and concentration are respected during the evolution of the closed-loop profiles. When a process–model mismatch is considered, MPC is unable to satisfy the state and control constraints unless the time step of the closed-loop control system (the hold time in MPC implementation) is lowered from 30 to 15 seconds, indicating that tighter feedback control is
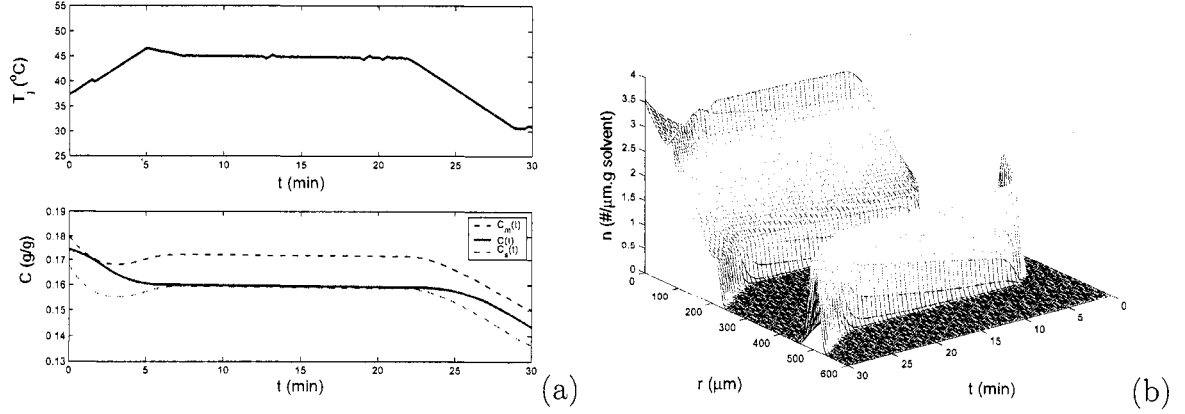
Figure 4.9: Closed-loop simulation results for mismatched models: (a) Jacket temperature and concentration profiles (dashed and dotted lines represent the upper and lower constraints on the concentration, respectively); (b) the evolution of crystal size distribution.

necessary in the case of imperfect model to avoid violation of the constraints. The closed-loop simulation results for the case of a process–model mismatch are shown in Figure 4.9. Comparing Figure 4.8 and Figure 4.9, it is clear that the predictive controller produces a different manipulated input trajectory to enforce constraint satisfaction when the model used in MPC design does not perfectly match the process. It is also noticed that the off-line computed optimal trajectory of T_j based on the mismatched model fails to satisfy the constraints on the solute concentration during the batch run. Such results indicate that feedback control is necessary to guarantee the process operating within the constraints.

Table 4.2: Comparison between the simulation results under four different control strategies.

Control Strategy	μ_3^n ($\mu m^2/g$ solvent)	μ_3^s ($\mu m^2/g$ solvent)
Open-loop with linear cooling	8.9174×10^8	8.3304×10^9
MPC with objective to maximize μ_3^s/μ_3^n	1.7828×10^9	1.0545×10^{10}
MPC with matched moments model	7.7209×10^8	8.3301×10^9
MPC with mismatched moments model	7.8655×10^8	8.3301×10^9
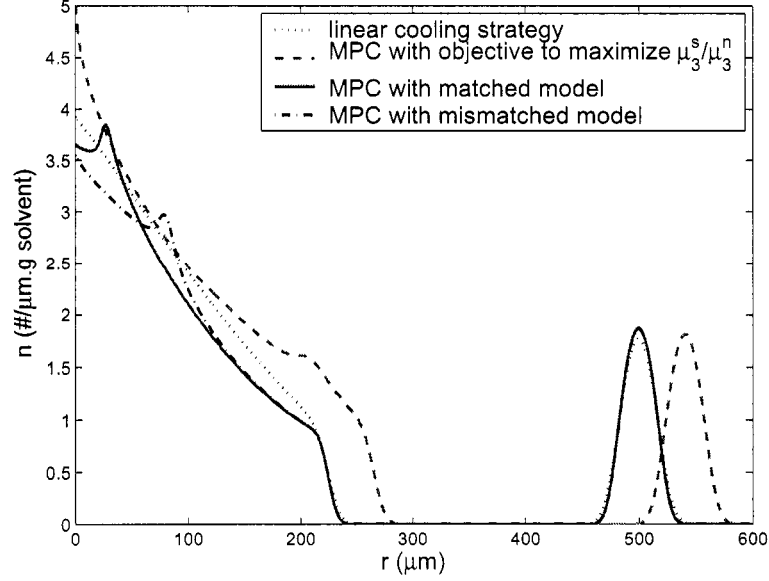
Figure 4.10: Comparison of the final crystal size distributions under 4 different control strategies.

Table 5.3 lists the value of μ_3^n and μ_3^s obtained under four different control strategies: (1) Open-loop with linear cooling, (2) MPC with an objective to maximize μ_3^s/μ_3^n, (3) MPC with the objective of Eq.5.9 under a perfect process–model match, and (4) MPC with the objective of Eq.5.9 under a process–model mismatch. Figure 4.10 compares the final crystal size distribution under these 4 different control strategies. Comparing the results of control strategies (1), (3) and (4), it is clear that MPC can lower the volume of fines (nucleation formed crystals) by 13.4% compared with the linear cooling strategy, while the crystals growing from the seeds in final product still satisfy the product quality requirement. It is also observed that, in the case of process–model mismatch, the predictive control strategy (with a smaller time step) is able to successfully control the system and lower the volume of fines by 11.8% compared with the linear cooling strategy. To demonstrate the effect of the choice of optimization objective in the control strategy on the volume of fines, we carried

143

out simulations with the same control structure, but with a different optimization objective which is to maximize the ratio μ_3^s/μ_3^n. Comparing the results in Table 5.3, it is clear that, when MPC with this objective is applied, even though the volume of crystals growing from the seeds increases by 26.6% (relative to the linear cooling strategy) which is favorable to product quality, the volume of fines actually increases dramatically by 129.2%. Such large difference on the crystal size distribution of final products can be more clearly seen in Figure 4.10. It shows that the control strategy (2) leads to larger crystals both formed by nucleation and grown from seeds compared to the other 3 control strategies, which allow to produce less crystals formed by nucleation while satisfying the minimum requirement of the volume of the crystals grown from seeds. This result suggests that maximizing the ratio μ_3^s/μ_3^n, while favoring product quality, does so at the expense of a significant increase in the volume of fines which is undesirable. In contrast, the optimization problem of Eq.5.9 provides a more meaningful formulation whereby the volume of fines is explicitly minimized, and the product quality is accounted for as a constraint on the optimization problem. This significant difference in the impact on μ_3^s and μ_3^n between the two optimization formulations suggests that the optimization objective should be selected carefully, when attempting to achieve a desired PSD, in order to strike a balance between enhancing product quality and minimizing the difficulties caused by a large volume of fines. Finally, to study the importance of incorporating measurements in the control system, we carried out a simulation of the predictive control system where the values of the state variables at each time step are not updated using measurements from the process, but instead, are updated using the values generated by simulating the moments model with $b = 1.35$. The simulation results (not shown in the manuscript due to space limitation) show that the state constraints are violated at the end of the open-loop simulation run because of the discrepancy between the PBM and the

mismatched moments model, and the lack of measurement feedback.

4.4 Conclusions

In this chapter, we focused on the development and application of predictive algorithms for control of PSDs in continuous and batch particulate processes described by PBMs. The control algorithms were designed on the basis of finite-dimensional models that capture the dominant dynamics of the particulate processes and were tailored to address different control objectives for the continuous and batch processes. Closed-loop simulations have demonstrated the effectiveness of the proposed control algorithms.

Chapter 5

Predictive Control of Crystal Size Distribution in Protein Crystallization

This chapter focuses on the modeling, simulation and control of a batch protein crystallization process that is used to produce the crystals of tetragonal hen egg-white (HEW) lysozyme. First, a model is presented that describes the formation of infinitesimal-size protein crystals via nucleation and the subsequent growth of the crystals via condensation, and predicts the temporal evolution of the crystal size distribution in the size range of $0 - 300 \ \mu m$. To this end, existing experimental data are used to develop empirical models of the nucleation and growth mechanisms of the tetragonal HEW lysozyme crystal. The developed growth and nucleation rate expressions are used within a population balance model to simulate a batch crystallization process that produces the tetragonal HEW lysozyme crystals. Then, model reduction techniques are used to derive a reduced-order moments model for the purpose of controller design. Online measurements of the solute concentration and reactor tem-

perature are assumed to be available, and a Luenberger-type observer is developed to estimate the moments of the crystal size distribution based on the available measurements. A predictive controller, that uses the available state estimates, is designed to achieve the objective of maximizing the volume-averaged crystal size while respecting constraints on the manipulated input variables (which reflect physical limitations of control actuators) and on the process state variables (which reflect performance considerations). Simulation results demonstrate that the proposed predictive controller is able to increase the volume-averaged crystal size by 30% and 8.5% compared to Constant Temperature Control (CTC) and Constant Supersaturation Control (CSC) strategies, respectively, while reducing the number of fine crystals produced. Furthermore, a comparison of the crystal size distributions (CSDs) indicates that the product achieved by the proposed predictive control strategy has larger total volume and lower polydispersity compared to the CTC and CSC strategies. Finally, the robustness of the proposed method with respect to plant-model mismatch is evaluated. The proposed method is demonstrated to successfully achieve the task of maximizing the volume-averaged crystal size in the presence of plant-model mismatch, and is found to be robust in comparison to open-loop optimal control strategies.

5.1 Introduction

Proteins play a vital role in most biological processes. In addition to constructing large-scale biological structures, such as muscle fibers, smaller protein molecules can function as antibodies, which help the immune system to destroy invading substances like viruses and bacteria, and enzymes, which can catalyze the synthesis of complex compounds, the transformation of complex substances into simpler ones, or the generation of energy in organisms. A protein molecule is a chain of amino acids that are

linked by peptide bonds formed by dehydration synthesis. Many pharmaceuticals act by binding to and blocking an active site (the active site is a region on the protein composed of some of the protein's amino acids which have a specific three dimensional arrangement to which a molecule can bind) of a protein [160]. The three-dimensional arrangement of amino acids, especially, at the active site, determines the specific biological function of the protein molecule.

X-ray and neutron diffraction techniques are the only available methods that can be used to obtain structural information of proteins with molecular weight over 20,000. To be able to study the structure of proteins using these techniques, large protein crystals of high structural perfection, typically with diameters of several hundred microns, are needed. Extensive research studies, using model proteins, such as ferritin, insulin, haemoglobin and lysozyme, that are able to crystallize easily under normal operating conditions, have focussed on growing large protein crystals of high structural perfection under various operating conditions, including low gravity [17], different pressure conditions [138], flow condition of the solution [149], purity [186], temperature [35] and concentrations of precipitants and buffers [148, 111]. In addition, numerous research studies have considered the problem of modeling of protein nucleation [54, 147] and growth [42, 96, 51]. The reader may also refer to [127, 163. 192, 185] for excellent reviews on this subject. Among these model proteins, the tetragonal form of HEW lysozyme is most popular and widely used [19]. HEW lysozyme is composed of 129 amino acids, with a molecular weight of 14,388. It is a naturally occurring enzyme, and has antibacterial activity against gram-positive bacteria.

The experimental studies not only benefit the determination of the protein structure, but also provide, through an understanding of the nucleation and growth mech-

anisms of protein crystallization, a way of determining the operating conditions necessary to achieve protein crystals of desired properties, which can often be expressed in the form of a desired size distribution. In the pharmaceutical industry, the size distribution of the protein crystal is a very critical variable and in many applications a predetermined, typically narrow, crystal size distribution is necessary in order to guarantee a desired drug delivery performance.

Protein crystals intrinsically grow much slower than most inorganic crystals at the same supersaturation [161]. This is probably one of the reasons why it has been widely believed that implementation of advanced control algorithms is not important for growing perfect crystals in protein crystallization. However, experimental results show that even in protein crystallization processes, certain growth conditions lead to crystal defect formation (for example, the structural defect density increases when the growth rate is relatively high [132]), which necessitates appropriately choosing the operating conditions. Furthermore, for a given choice of operating conditions, it is critical to implement real-time control to mitigate the affect of disturbances that might drive the operating conditions off the desired values.

While numerous experimental studies of the nucleation and growth mechanisms of protein crystallization have been carried out, very few results on control of protein crystallization are available. The feasibility and effectiveness of temperature control in protein crystallization was discussed in [162], where a series of preliminary experiments were conducted to demonstrate the ability of temperature control to manipulate the supersaturation in the protein crystallization. In [38], a method for control of nucleation in small protein solutions was developed and focused on control of a relatively smaller number of protein crystals. In [189], an experiment system was developed to control a crystallization cell, and focused on the develop-

ment of the control system, including the hardware and software for measurement and communication, rather than on the control algorithm. A Constant Supersaturation Concentration (CSC) control strategy was developed in [169] to achieve large protein crystals. Although this strategy shows significant advantage in increasing the crystal size compared to the case where, for instance, the temperature in the crystallizer is held steady, it is not optimal with respect to maximizing the crystal size. Furthermore, being an open-loop control strategy, it is not robust with respect to modeling errors and disturbances affecting the operation of the crystallizer.

Motivated by the above considerations, this chapter focuses on the modeling, simulation and control of a batch protein crystallization process that is used to produce the crystals of tetragonal hen egg-white (HEW) lysozyme. First, a model is presented that describes the formation of infinitesimal-size protein crystals via nucleation and the subsequent growth of the crystals via condensation, and predicts the temporal evolution of the crystal size distribution in the size range of $0 - 300 \ \mu m$. To this end, existing experimental data are used to develop empirical models of the nucleation and growth mechanisms of the tetragonal HEW lysozyme crystal. The developed growth and nucleation rate expressions are used within a population balance model to simulate a batch crystallization process that produces the tetragonal HEW lysozyme crystals. Then, model reduction techniques are used to derive a reduced-order moments model for the purpose of controller design. Online measurements of the solute concentration and reactor temperature are assumed to be available, and a Luenberger-type observer is developed to estimate the moments of the crystal size distribution based on the available measurements. A predictive controller, that uses the available state estimates, is designed to achieve the objective of maximizing the volume-averaged crystal size while respecting constraints on the manipulated input

variables (which reflect physical limitations of control actuators) and on the process state variables (which reflect performance considerations). Simulation results demonstrate that the proposed predictive controller is able to increase the volume-averaged crystal size by 30% and 8.5% compared to Constant Temperature Control (CTC) and Constant Supersaturation Control (CSC) strategies, respectively, while reducing the number of fine crystals produced. Furthermore, a comparison of the crystal size distributions (CSDs) indicates that the product achieved by the proposed predictive control strategy has larger total volume and lower polydispersity compared to the CTC and CSC strategies. Finally, the robustness of the proposed method with respect to plant-model mismatch is evaluated. The proposed method is demonstrated to successfully achieve the task of maximizing the volume-averaged crystal size in the presence of plant-model mismatch, and is found to be robust in comparison to open-loop optimal control strategies.

5.2 Modeling of nucleation and growth rate of tetragonal lysozyme crystal

The formation of a single crystal can be modeled as comprising of two sequential processes: crystal nucleation and growth. Experimental studies [42, 51, 54, 92, 147] have considered various operating conditions and developed empirical models for the nucleation and growth of the tetragonal HEW lysozyme crystal. Owing to large differences in operating conditions, significant discrepancies exist in the nucleation and growth data obtained in these works. In the current study, we focus on one operating condition (fixed buffer, pH value and salt concentration; these values are selected based on the availability of experimental results), and develop an empirical model of the nucleation and growth mechanisms by using the existing experimental

151

results available for these operating conditions. In the remainder of this section, experimental results on the solubility, nucleation and growth of the tetragonal HEW lysozyme crystal are analyzed and an empirical model of the nucleation and growth mechanisms is developed.

5.2.1 Solubility of the tetragonal HEW lysozyme crystals

The main driving force for the crystal nucleation and growth is understood to be supersaturation, i.e., the concentration of the solution in excess of the saturation concentration (solubility). The solubility of lysozyme at different pH and precipitant concentrations has been studied by [12, 161, 168]. In [12], the solubility experiments covered a pH range from 4.0 to 5.4, NaCl concentration (weight/volume) range from 2.0% to 7.0% and temperature range from 4 to 25°C. The solubility of HEW lysozyme was also studied in [161], for pH at 4.5, NaCl concentration at 2.1%, 2.5% and 3.0%, and a temperature range from 11 to 30°C. By implementing a more accurate measurement technique (two-beam interferometry), the solubility in a solution with pH of 4.5 and NaCl concentration of 2.5% was measured in [168].

Since purer samples and more advanced measurement techniques were used in [168], this solubility data, shown as circles in Figure 5.1, is considered to be more accurate and used to derive parameters of the empirical model in our work. A third-order polynomial is used to fit the data, and the fitted curve is shown as the solid curve in Figure 5.1. Also shown in Figure 5.1 is the solubility data in [12, 161, 168] which exhibit trends similar to the data set obtained in [168], with solubility being low at low temperature and increasing significantly with increasing temperature. The resulting expression for the solubility, $C_s(T)$, is as follows:

$$C_s(T) = 1.0036 \times 10^{-3}T^3 + 1.4059 \times 10^{-2}T^2 - 0.12835T + 3.4613 \qquad (5.1)$$
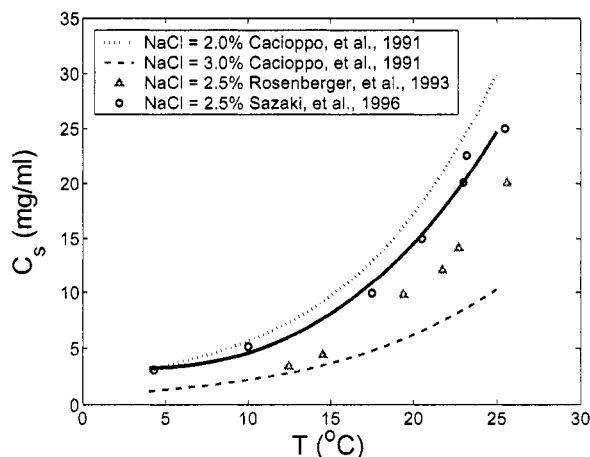
Figure 5.1: Solubility data of tetragonal lysozyme crystal: dotted and dashed lines show the data in [12], $\triangle$ shows data in [161], $\circ$ shows data in [168], and the solid line shows the empirical model of Eq.5.1).

5.2.2 Modeling of the nucleation rate of the tetragonal HEW lysozyme crystals

For biological molecules, crystals are most often grown with no seeding, where primary nucleation must precede crystal growth. Thus, an understanding of the nucleation process and the effect of various parameters on nucleation is essential for successful production of protein crystals. Recently, significant progress has been made in understanding the nucleation and crystallization of globular proteins, including the formation of compositional and structural crystal defects [163].

Insight into the interactions of protein macro-ions in solution, obtained from light scattering, small angle X-ray scattering and osmotic pressure studies shows that the nucleation of globular proteins is governed by the same principles as those of small molecules. In particular, supersaturation, the difference between solute concentra-

tion and solubility, is understood to be the main driving force for both nucleation and growth of the protein crystals. Changes of operating conditions, such as lowering temperature, increasing salt concentration, pH or protein concentration influence nucleation [84] via influencing the solubility. Therefore, to develop an empirical model, it is assumed that the homogenous nucleation rate of the tetragonal HEW lysozyme crystal is only a function of solute concentration and supersaturation. The following two-parameter empirical expression is used as an empirical model to describe the crystal nucleation rate $B(t)$ [54, 5]:

$$B(t) = k_a C exp\left(-\frac{k_b}{\sigma^2}\right) \tag{5.2}$$

where σ, the supersaturation, is defined as $\sigma = ln(C/C_s)$, where C is the solute concentration and C_s is the solubility and k_a and k_b are parameters that are obtained using experimental results.

Different techniques, including light scattering [5], temperature jump [54] and microcalorimetry [35] have been implemented to measure the nucleation rate of the tetragonal HEW lysozyme crystal. We initially use the measurements of concentration and temperature to compute the solubility according to Eq.5.1 and the supersaturation. The experimentally obtained values of the nucleation rate, and the computed concentration and supersaturation values, are then used to obtain the parameters k_a and k_b in Eq.5.2. Both sets of data yield the same values for $k_a = 1044.4/min.cm^3$ and $k_b = 51.33$ and a single straight line serves as the best fit for both sets of data (see Figure 5.2).

5.2.3 Modeling of the growth rate of tetragonal HEW lysozyme crystals

Figure 5.3 shows the structure of a tetragonal HEW lysozyme crystal, which shows well-defined facets similar to inorganic crystals. This observation indicates that
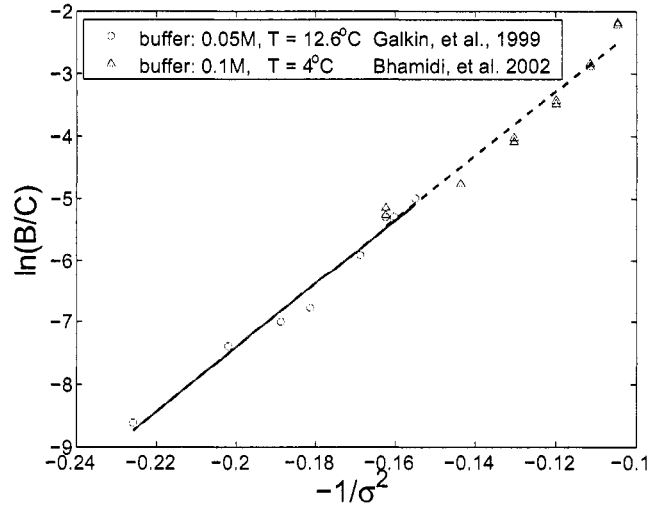
Figure 5.2: Comparison of the experimental results on the nucleation rate of tetragonal HEW lysozyme crystal: o show the data in [54], $\triangle$ show the data in [5], and the empirical model of Eq.5.2 is shown by the solid line.

growth occurs via the spreading of layers from growth step sources such as dislocations and 2D nuclei [41]. The microstructure of the faces of protein crystals has been revealed by implementing advanced measurement techniques, such as electron microscopy and atomic force microscopy (AFM). Experimental results have shown that the growth step generation at screw dislocations outcrops and 2D nucleation islands is the dominant growth mechanism in the growth of tetragonal lysozyme crystals [41]. Experimental studies have also shown that screw dislocation and 2D nucleation are the rate-limiting steps for the growth of tetragonal HEW lysozyme crystals [42, 41, 185]. Detailed spiral growth and 2D nucleation theories have been developed [4]. Experiments in [186] also showed the existence of a critical supersaturation, above which the crystal growth is dominated by 2D nucleation. When the supersaturation is higher than about 1.6, the increase in the growth rate with increasing supersaturation is much faster than at low supersaturation. This is consistent with the results in [42] which concludes that the growth rates at high and

low supersaturation are dominated by two different mechanisms. The experimental results suggest that dislocations may be involved in the lysozyme crystal growth at low supersaturation, and 2D nucleation could be dominant at high supersaturation which leads to equal growth rates on all crystal facets, thereby leading to the formation of symmetrical crystals. Furthermore, it was found that orthorhombic lysozyme crystals, rather than tetragonal crystals, tend to be formed at low supersaturation [51]. This suggests that the supersaturation should be maintained within appropriate bounds to obtain crystals of desired morphology. Empirical and theoretical models
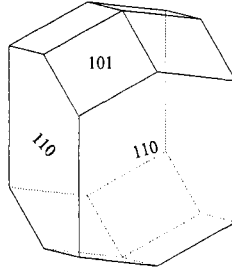
Figure 5.3: Structure of a tetragonal HEW lysozyme crystal.

of crystal growth mechanisms have been developed and compared to experimental results [42, 111, 96]. These works studied the growth rate of the tetragonal HEW lysozyme crystal under various operating conditions, such as different precipitation concentration, solute concentration and temperature. All of them concluded the power-law dependence of the growth rate on supersaturation σ. Some experimental results of the studies of the growth rate of the tetragonal HEW lysozyme crystal are shown in Figure 5.4 [148, 42, 96]. The growth rate data corresponding to the supersaturation are plotted on log-log scale. It is clear that the growth rate changes exponentially with the supersaturation, and that the value of the exponents obtained from different experiments are very close. In our work, we use the following empirical model to describe the growth rate of the tetragonal HEW lysozyme crystals as a
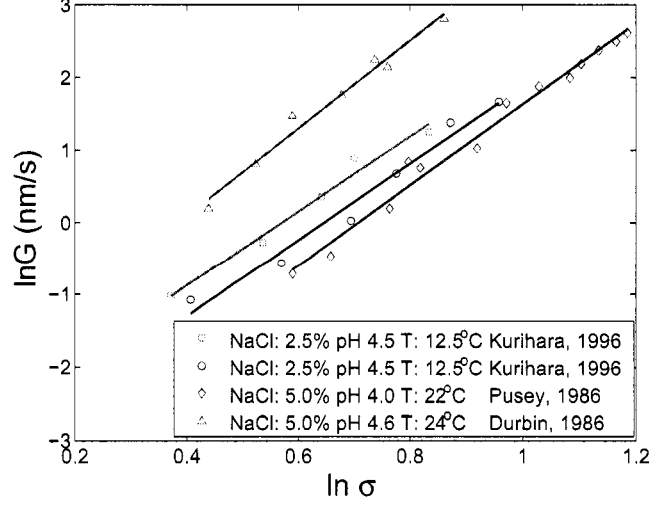
Figure 5.4: Comparison of the experimental results on the growth rate of tetragonal HEW lysozyme crystal: ◇ shows the data in [148], △ shows data in [42], and □ and ○ show the data in [96].

function of supersaturation:

$$G(t) = k_g \sigma^g \tag{5.3}$$

where k_g is the pre-exponential factor of the growth rate. Since the composition of the solution considered in the present study is the same as that in [96]; the experimental data of [96], shown as the circles in Figure 5.4, are used to compute the values of k_g and g in Eq.5.3; this yields $k_g = 3.1451 \times 10^{-9} cm/min$ and $g = 5.169$.

5.3 Modeling of a batch crystallizer for protein crystallization

The mathematical models of particulate processes, including the protein crystallization process in question, are typically obtained through the application of population, material and energy balances and consist of systems of nonlinear partial integro-differential equations that describe the evolution of the particle size distribu-

157

tion (PSD), coupled with systems of nonlinear ordinary differential equations (ODEs) that describe the evolution of the state variables of the continuous phase. There is an extensive literature on population balance modeling, numerical solution, and dynamical analysis of particulate processes, see, for example, [151]; see also [30] for further details and references.

For the batch crystallizer considered in this chapter, a population balance model can be used to describe the evolution of the crystal size distribution (CSD), $n(r, t)$. The evolution of the solute concentration, C, and crystallizer temperature, T, are described by two ODEs. The process model has the following form:

$$\frac{\partial n(r, t)}{\partial t} + G(t) \frac{\partial n(r, t)}{\partial r} = 0, \quad n(0, t) = \frac{B(t)}{G(t)}$$

$$\frac{dC}{dt} = -24 \rho k_v G(t) \mu_2(t)$$

$$\frac{dT}{dt} = -\frac{UA}{MC_p}(T - T_j)$$

(5.4)

where $G(t)$ is the growth rate, $B(t)$ is the nucleation rate, ρ is the density of crystals, k_v is the volumetric shape factor, U is the overall heat-transfer coefficient, A is the total heat-transfer surface area, M is the mass of solvent in the crystallizer, C_p is the heat capacity of the solution and $\mu_2 = \int_0^\infty r^2 n(r, t) dr$ is the second moment of the CSD. The nucleation rate, $B(t)$, and the growth rate, $G(t)$, are given by Eqs. 5.2 and 5.3, respectively, where the parameters obtained from experimental results are used, and reported in Table 5.1. Note that because of the tetragonal form of the crystals and the existence of about 46% of solvent in each crystal [107], the volumetric shape factor, k_v, is set equal to 0.54. To simulate the population balance model of Eq.5.4, a second-order accurate finite difference scheme with sufficient (3000) discretization points is used (while not shown here for the sake of brevity, it was verified that simulations with higher number of discretization points yield results that are almost indistinguishable from those obtained using 3000 discretization points). Figure 5.5

158

Table 5.1: Parameter values for the batch crystallizer model of Eqs.5.3 and 5.4.

k_a	$1044.4/(min\ cm^3)$	k_g	$3.1451 \times 10^{-9} cm/min$
k_b	51.33	g	5.169
k_v	0.54	ρ	$1.40 \times 10^3 mg/cm^3$
U	$1800 kJ/m^2 \cdot hr \cdot K$	A	$0.25 m^2$
M	$10 kg$	C_p	$4.13 kJ/K \cdot kg$

shows the evolution of the solute concentration (C), the supersaturation (σ) and the CSD at a constant crystallizer temperature $(T = 15°C)$.
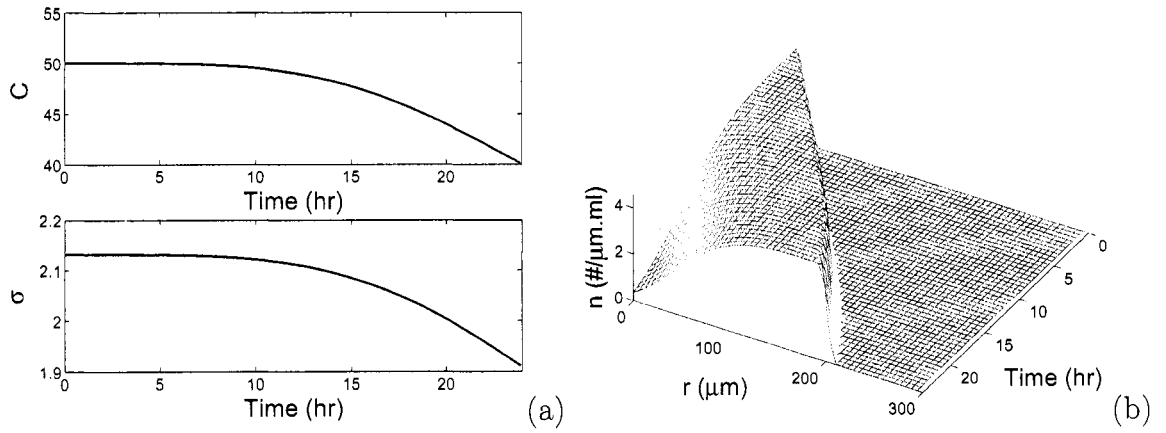
Figure 5.5: Open-loop simulation results of the solute concentration (C), the supersaturation (σ) and the CSD at a constant crystallizer temperature $(T = 15°C)$.

5.4 Predictive control of the batch protein crystallizer

Early work on control of particulate processes focused mainly on the understanding of fundamental control-theoretic properties of PBMs and the application of conventional control schemes to crystallizers and emulsion polymerization processes, see, e.g., [158], and the references therein. More recently, the realization that PBMs – owing to their infinite-dimensional nature – cannot be used directly for the synthesis of practically implementable model-based controllers, has motivated significant

research work on the development of a general order reduction procedure, based on combination of the method of weighted residuals and approximate inertial manifolds, which allows deriving low-order ODE approximations that capture the dominant dynamics of particulate processes and can, therefore, serve as an appropriate basis for the design of low-order controllers that can be readily implemented in practice, see, for example, [26]. This approach subsequently laid the foundation for the development of a systematic framework for solving a number of important control problems for particulate processes, including the problem of dealing with the highly nonlinear behavior, e.g., owing to complex growth, nucleation, agglomeration and breakage mechanisms, and the Arrhenius dependence of nucleation laws on solute concentration in crystallizers [26], the problem of control under model uncertainty [27], and the problem of control under actuator constraints [43].

The crystal size distribution or the moments of the crystal size distribution are often not available as online measurements. Solute concentration and temperature, on the other hand, are more readily available as measurements and can be used to generate estimates of the moments which are required for implementation of feedback control strategies based on the reduced order moments model. Also, given the availability of a reduced order moments model and estimates of the moments, desirable product characteristics need to be appropriately expressed in terms of constraints on the crystal size distribution, and physical limitations on the manipulated variable (jacket temperature) must be accounted for in the control design. In the remainder of this section we first use model reduction techniques to develop a reduced order model suitable for the purpose of real-time control. Next, we present the design of a state estimator, to provide estimates of the states of the reduced order model using available measurements. Then we present a predictive controller design that uses

the state estimates for the purpose of real-time control, while incorporating performance considerations as appropriate constraints on the moments of the crystal size distribution and accounting for the constraints on the manipulated input variable.

5.4.1 Model reduction

Owning to the fact that the dominant dynamics of the crystallizer are characterized by a small number of degrees of freedom [26], the method of moments [77] (see also [30, 172, 123]) is applied to the system of Eq.5.4 to derive an approximate ODE model. Defining the ith moment of $n(r,t)$ as:

$$\mu_i = \int_0^\infty r^i n(r,t)dr, \quad i = 0, 1, ..., \infty \tag{5.5}$$

multiplying the population balance in Eq.5.4 by r^i, and integrating over all crystal sizes, the following infinite set of ordinary differential equations, which describes the rate of change of the moments of the crystal size distribution, solute concentration and temperature, is obtained:

$$
\begin{aligned}
\frac{d\mu_0}{dt} &= B(t) \\
\frac{d\mu_i}{dt} &= iG(t)\mu_{i-1}(t), \quad i = 1, 2, ..., \infty \\
\frac{dC}{dt} &= -24\rho k_v G(t)\mu_2(t) \\
\frac{dT}{dt} &= -\frac{UA}{MC_p}(T - T_j)
\end{aligned} \tag{5.6}
$$

Note that in Eq.5.6, the ODEs describing the dynamics of the first N moments, where N is any positive integer greater than or equal to 3, the solute concentration and the crystallizer temperature are independent of the moments of order $N + 1$ and higher. This implies that a set of ordinary differential equations, which include the first N moments and the evolution of the solute concentration and crystallizer temperature, would provide an accurate description of the evolution of the first N

moments, the solute concentration and the crystallizer temperature. In this case, the nucleation and growth rates are independent of crystal size and this allows closure of the moment equations (note that closure can still be achieved if the nucleation and growth mechanism are dependent on certain moments of the crystal size distribution). In cases where the moments do not close, a finite set of ordinary differential equations describing the evolution of the moments would provide an approximation that gets increasingly better as the number of moments included in the reduced-order model is increased.

As will be seen in section 5.4.3, the control objective will require computation of μ_3 and μ_4, hence N is chosen as 4 and the following reduced-order model is used for the purpose of controller design:

$$
\begin{aligned}
\frac{d\mu_0}{dt} &= B(t) \\
\frac{d\mu_i}{dt} &= iG(t)\mu_{i-1}(t), \quad i = 1, 2, 3, 4 \\
\frac{dC}{dt} &= -24\rho k_v G(t)\mu_2(t) \\
\frac{dT}{dt} &= -\frac{UA}{MC_p}(T - T_j)
\end{aligned}
\tag{5.7}
$$

5.4.2 State estimator design

In this section, we present an observer design that uses measurements of the solute concentration, C, and temperature T and the reduced order moments model, to generate estimates of the moments. Note that building an observer for a nonlinear system of the form of Eq.5.7 with guaranteed convergence properties is in general a difficult task. In this chapter, an extended Luenberger-type observer is used to estimate the values of the moments of the CSD and takes the following form:

Table 5.2: Parameter values for the Luenberger-type observer of Eq.5.8.

L_0	-0.4	L_1	0.05
L_2	0.001	L_3	1.7×10^{-5}
L_4	3×10^{-7}	L_5	-0.1

$$\frac{d\hat{\mu}_0}{dt} = \hat{B}(t) + L_0(C_m - \hat{C})$$

$$\frac{d\hat{\mu}_i}{dt} = i\hat{G}(t)\hat{\mu}_{i-1}(t) + L_i(C_m - \hat{C}), \quad i = 1, ..., 4 \qquad (5.8)$$

$$\frac{d\hat{C}}{dt} = -24\rho k_v \hat{G}(t)\hat{\mu}_2(t) + L_5(C_m - \hat{C})$$

where C_m is the online measurement of the solute concentration, $\hat{B}(t)$ and $\hat{G}(t)$ are the nucleation and growth rates computed using the online measurement of T and values of the estimates of $\hat{\mu}_i$ and $\hat{C}$, and L_i, $i = 0, ..., 5$ are the observer gains (these values were obtained via running open-loop simulations and comparing the evolution of the state with the state estimates for different choices of the observer gains), reported in Table 5.2. Figures 5.6a-f show a comparison between the evolution of the solute concentration (solid line in Figure 5.6(a)) and the moments $\mu_i, i = 0, 1, ..., 4$ (solid lines in Figures 5.6(b)-(f)) and the estimates of the solute concentration C and the moments, for the perfect model case (dotted lines), and for two instances of plant-model mismatch, where the parameter g in the moment model is 90% and 110% of its nominal value, respectively (denoted by o and *), under open–loop simulations. In all instances, the effect of measurement noise, often found in experimental readings, is simulated by introducing a white noise with variance of 0.5 mg/ml in the measurement of the solute concentration. Furthermore, to evaluate the convergence of the estimates to the true state values, the initial value of the estimated solute concentration, $\hat{C}$, is set to 40 mg/ml, while the true value is 50 mg/ml.

Note that for the batch crystallization considered in this chapter, the initial values
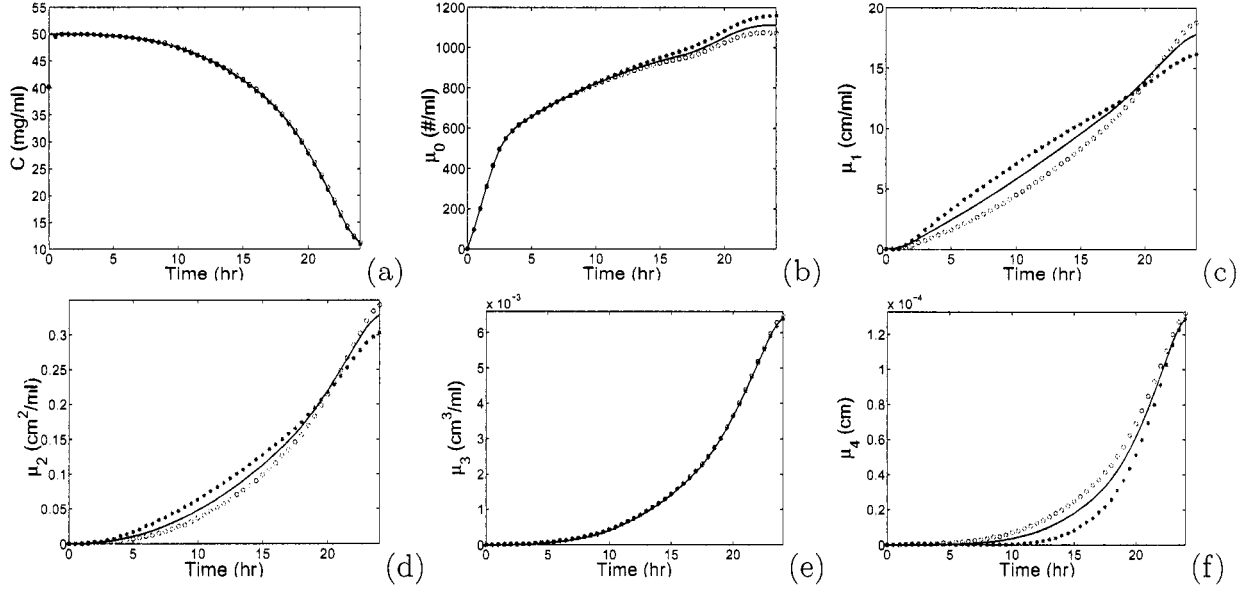
Figure 5.6: Comparison between the true value and the estimates of C (the solute concentration) and $\mu_i, i = 0, 1, ..., 4$.

of the moments at the beginning of the batch run are identically equal to zero, because there are no crystals initially inside the crystallizer. In the case of a perfect model, the state estimates converge quickly to the true values, and in both cases of plant-model mismatch, the observer generates satisfactory estimates of the states (see Figure 5.6(a)-(f)).

5.4.3 Predictive controller formulation

Significant previous work has focused on CSD control in batch crystallizers, e.g., [153, 195]. In [137], an open-loop optimal control strategy was derived, where the objective function involves maximization of the crystal size, and the cooling curve is the decision variable. In [130], a method was developed for assessing parameter uncertainty and studied its effects on the open-loop optimal control strategy, which maximized the weight mean size of the product. An on-line optimal control method-

ology was developed for a seeded batch cooling crystallizer in [195, 201]. Most of these works focused on open-loop optimal control of the batch crystallizer, i.e., the optimal operating condition is calculated off-line and implemented during the batch operation. The successful achievement of the control objective in such a control strategy depends heavily on the accuracy of the models, and disturbances affecting the batch operation may easily drive the process off the desired trajectory.

The volume-averaged crystal size is an important parameter that characterizes the crystal size distribution [201], especially for pharmaceuticals. A larger volume-averaged crystal size facilitates downstream processing of the crystals, such as filtration. As mentioned previously, experimental results show low supersaturation leads to the cessation of the crystal growth, while needle like, instead of tetragonal crystals, form if the supersaturation is too high and this necessitates maintaining the supersaturation (and similarly, temperature) within an acceptable range. Constraints on the jacket temperature reflect the physical limitations in supplying the coolant at a prescribed temperature.

Based on these considerations, we present in the remainder of this section a predictive controller formulation that uses the available estimates of the process states for the purpose of feedback control to maximize the volume-averaged crystal size, while respecting the constraints on the reactor temperature, solute concentration and the jacket temperature. Specifically, at time t_i, the control trajectory is computed by

solving an optimization problem of the form:

$$\min \quad -\frac{\mu_4(t_f)}{\mu_3(t_f)}$$

$$s.t. \quad \frac{d\mu_0}{dt} = k_a C \exp\left(-\frac{k_b}{\sigma^2}\right)$$

$$\frac{d\mu_i}{dt} = i k_g \sigma^g \mu_{i-1}(t), \quad i = 1, ..., 4$$

$$\frac{dC}{dt} = -24\rho k_v k_g \sigma^g \mu_2(t)$$

$$\frac{dT}{dt} = -\frac{UA}{MC_p}(T - T_j) \tag{5.9}$$

$$\mu_i(t_i) = \hat{\mu}_i(t_i)$$

$$C(t_i) = \hat{C}(t_i)$$

$$t_i \leq t \leq t_f,$$

$$T_{min} \leq T \leq T_{max},$$

$$T_{j\,min} \leq T_j \leq T_{j\,max},$$

$$\sigma_{min} \leq \sigma \leq \sigma_{max},$$

$$\left|\frac{dC_s}{dt}\right| \leq k_1$$

$$n(0, t) \leq n_{fine}, \forall\ t \geq t_f/2 \tag{5.10}$$

where T_{min} and T_{max} are the constraints on the crystallizer temperature, T, and are specified as 4°C and 22°C, respectively. $T_{j\,min}$ and $T_{j\,max}$ are the constraints on the manipulated variable, T_j, and are specified as 3°C and 22°C, respectively. The constraints on the supersaturation σ are $\sigma_{min} = 1.73$ and $\sigma_{max} = 2.89$. The constant, k_1, (chosen to be 0.065mg/ml·min) specifies the maximum rate of change of the saturation concentration C_s. n_{fine} is the largest allowable number of nuclei at any time instant during the second half of the batch run, and is set to be $5/\mu m.ml$. Previous work has shown that the objective of maximizing the volume-averaged crystal size can result in a large number of fines in the final product [121]. The constraint of Eq.5.10, by restricting the number of nuclei formed at any time instant during the second half of the batch run limits the fines in the final product.

In the closed-loop control structure, the PBM, together with the mass and energy

balances of Eq.5.4, are used to simulate the batch crystallization process. Measurements of the solute concentration and the crystallizer temperature are assumed to be available, and are used by the Luenberger-type observer of Eq.5.8 to generate estimates of the moments. These estimates are used as initial conditions of the states in the moments model, which is used in the predictive controller to compute the control trajectory. Specifically, the PBM is utilized to simulate the value of the state variables (n, C, T) at $t_i = i\Delta t$, where i=1,2,...,m, $m = t_f/\Delta t$, and t_f is the length of the crystallization period. The measurements of C and T are used to compute estimates of $\hat{\mu}_j(t_i)$. These estimates are used as initial values of the states in the reduced order moments model, and used within the optimization problem over a horizon length of $t_f - t_i$ to compute the optimal control trajectory. The first step of the solution (T_j) is implemented in the closed-loop, and this procedure is repeated every Δt until the end of the batch run. In the simulations, Δt and t_f are chosen as 5 minutes and 24 hours, respectively. Eq. 5.4, that describes the evolution of the batch crystallizer, is solved by a second-order accurate finite difference scheme with 3000 spatial discretization points and 7200 temporal discretization points and the optimization problem is solved using sequential quadratic programming (SQP).

5.5   Closed-loop simulation results

In this section, we first demonstrate the effect of the unavailability of measurements of the moments on the evolution of the closed–loop system. To this end, we compare the following scenarios: 1) state feedback control (i.e., the measurements of the moments are available); the control trajectory initially computed by the optimization problem is shown by the dotted line, and the closed–loop control trajectory under state feedback is shown by the dash-dotted line in Figure 5.7(a), and 2) output feed-

back control; the control trajectory initially computed by the optimization problem is shown by the dashed line in Figure 5.7(a), and the closed–loop control trajectory under output feedback control is shown by the solid line in Figure 5.7(a) (the corresponding supersaturation profiles are shown in Figure 5.7(b)).

Note that in the case of state feedback control, the control trajectory computed initially coincides with that under the closed–loop implementation (the dotted and dash-dotted lines overlap), since the tail of the control trajectory continues to be the solution to the optimization problem at the successive times. In the case of output feedback control, however, the control trajectory is initially computed based on the available (incorrect) estimates of the state variables, and leads to state constraints violation if implemented for the entire duration of the batch run (see dashed lines in Figure 5.7(b), where the supersaturation hits the lower constraint at $t = 18.2$ hours).

(a)   (b)
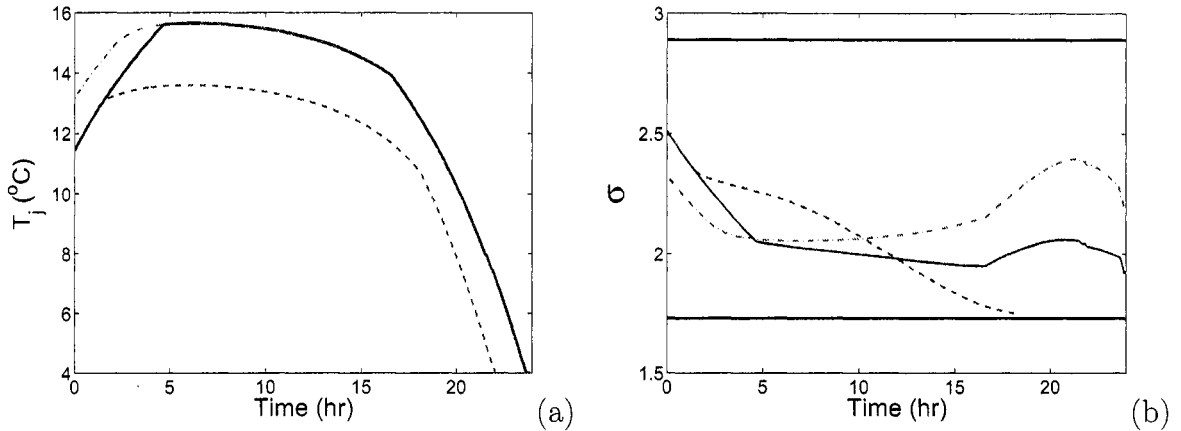
Figure 5.7: (a) Jacket temperature and (b) supersaturation profiles under 1) state feedback control: dotted (implementation of the initially computed manipulated input trajectory) and dash-dotted (closed–loop state feedback control) lines, and 2) output feedback control; dashed (implementation of the initially computed manipulated input trajectory) and solid (closed–loop output feedback control) lines.

Next, we compare the performance of the proposed predictive controller to that

of three other control strategies, Constant Temperature Control (CTC), Constant Supersaturation Control (CSC) and open-loop optimal control strategy. To study the ability of the proposed predictive control strategy to maximize the performance objective while avoiding the formation of a large number of fines in the final product, the predictive controller of Eq.5.9 is implemented with the additional constraint (Eq.5.10) on the fines in the final product. Also, to evaluate the robustness of the proposed method with respect to plant-model mismatch, we consider a 10% error in the nominal value of the parameter g - which is the exponent relating growth rate to supersaturation - in the moments model used in the predictive controller.
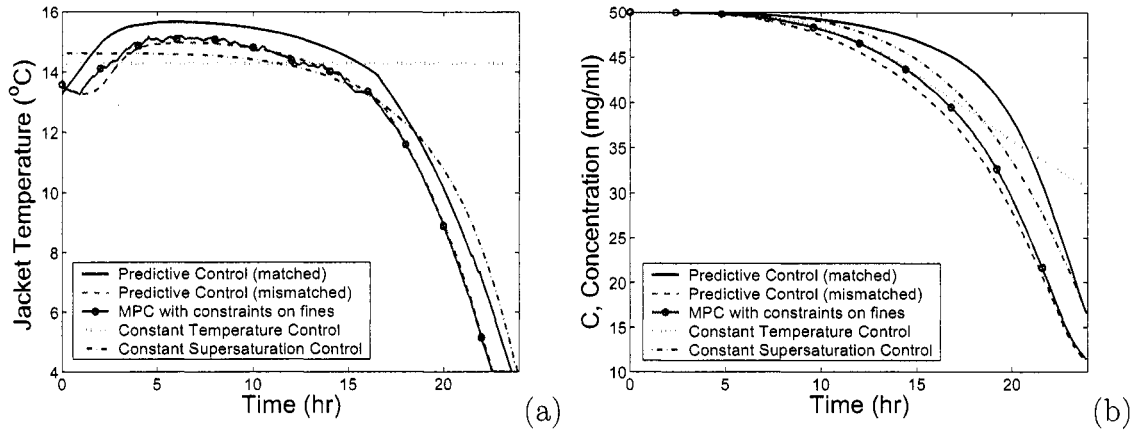
Figure 5.8: Comparison of the simulation results for (a) jacket temperature and (b) solute concentration under four different control strategies.

In Figures 5.8 and 5.9, four important variables, the jacket temperature, the solute concentration, the supersaturation, and the volume distribution of the CSD ($P(r)$) at the end of the batch run, are shown. The volume distribution of the CSD, $P(r)$, defined as:

$$P(r) = \frac{r^3 n(r, t_f)}{\int_0^\infty r^3 n(r, t_f) dr}$$ (5.11)

where t_f is the time at the end of the batch run, is an important variable in determining the product characteristics. The two horizontal lines at 1.73 and 2.89 in Figure
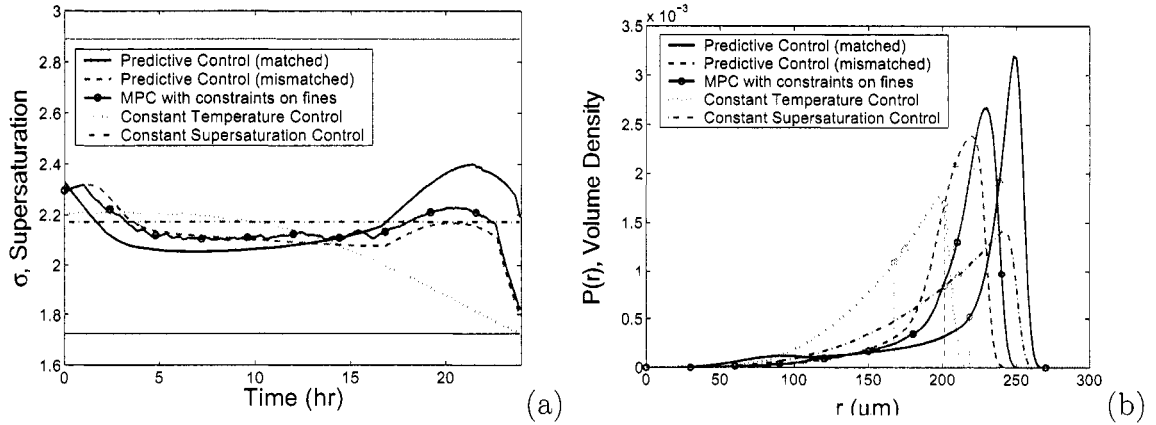
Figure 5.9: Comparison of the simulation results for (a) supersaturation and (b) volume density under four different control strategies.

5.9(a) are the lower and upper constraints on the supersaturation. The evolution of the CSD under different control strategies is shown in Figure 5.10.

Figure 5.8(a) shows the comparison of the manipulated variable trajectories, the jacket temperature T_j, for the five scenarios. Note that while the trajectories of the jacket temperature under CSC (dash-dotted line) and under the predictive controller with a matched model (solid line) are close; the slight difference causes the behavior of CSD evolution under these two different control strategies to be significantly different (shown in Figure 5.10(a) and (e)), indicating the necessity to implement control to achieve a desired product quality.

Since the supersaturation σ is the main driving force for the crystal nucleation and growth, the evolution of supersaturation under various control strategies, shown in Figure 5.9(a), can be subsequently used to explain the behavior of the CSD evolution. Specifically, the solid line in Figure 5.9(a) shows that the predictive controller computes a manipulated input trajectory that results in the supersaturation first decreasing, then staying almost constant at a low level, and finally increasing at the end of the batch run. In view of the fact that the control objective is to maximize

170
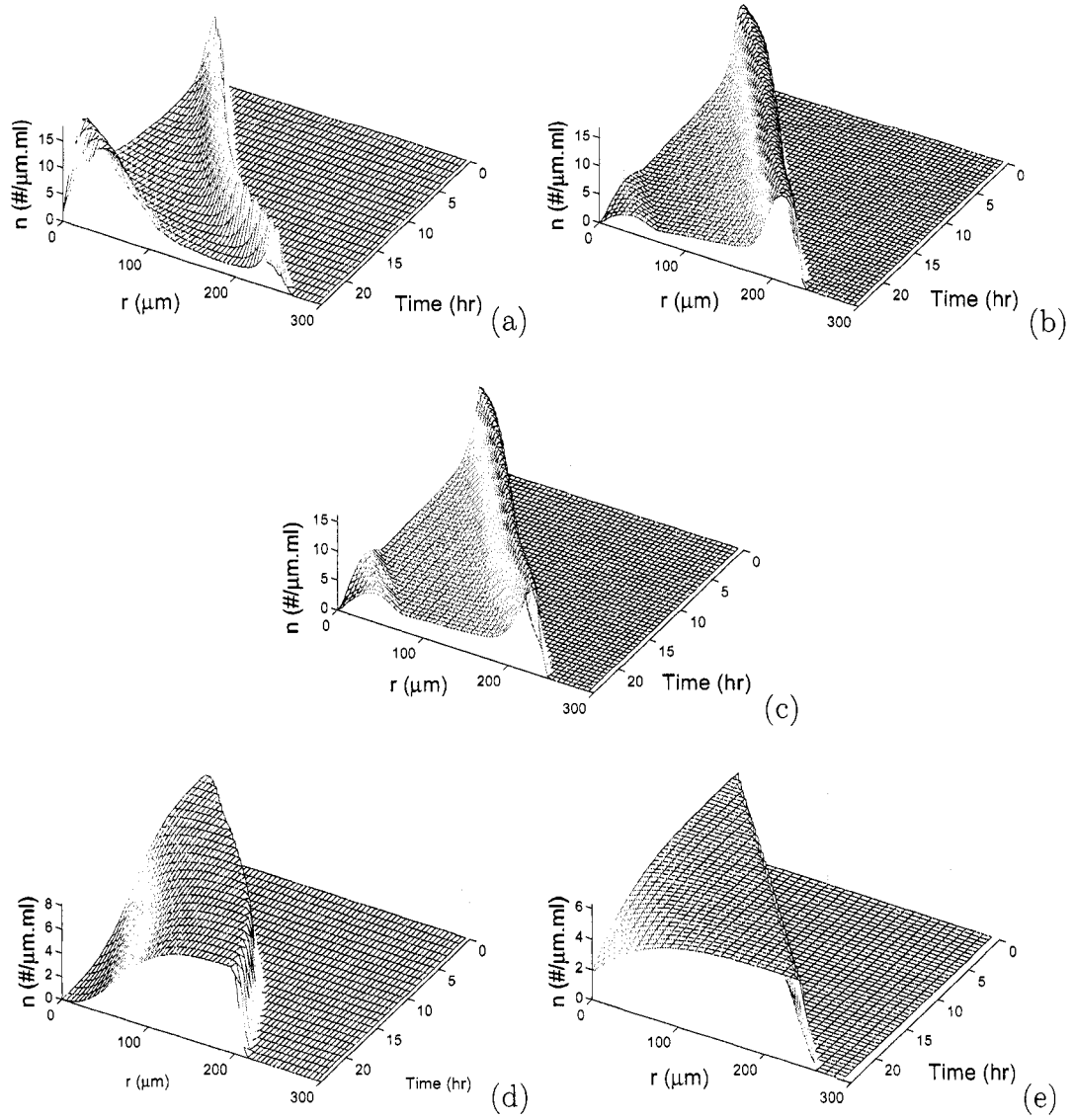
Figure 5.10: Evolution of crystal size distribution under four different control strategies: (a) Predictive control with matched model, (b) Predictive control with mismatched model, (c) Predictive control with constraint on fines, (d) constant temperature control, (e) constant supersaturation control.

the volume-averaged crystal size at the end of the batch run, i.e., to maximize the volume of big crystals while minimizing the volume of small crystals, the result can be understood as follows: after high initial levels of supersaturation, that results in a number of nuclei formed, a drop in the supersaturation results in the nucleation rate dropping more drastically than the growth rate (note that while the nucleation rate in Eq.5.2 shows exponential dependence on the supersaturation, the growth rate in Eq.5.3 exhibits a power law dependence), and favors growth of the initially formed crystals instead of formation of new crystals. Towards the end of the batch run, it is advantageous to increase the growth rate (by increasing the supersaturation) to maximize the size of the crystals in the batch reactor, even at the cost of forming a small number of new nuclei because the net result is a favorable increase in the volume-averaged crystal size.

Note that towards the end of the batch run, the solute concentration has depleted due to the formation of crystals. Supersaturation, however, is the solute concentration in excess of the solubility, and may be increased by decreasing the solubility, which is a function of the reactor temperature. Therefore, the desired increase in the supersaturation at the end of the batch run is achieved by lowering the jacket temperature (to lower the reactor temperature, which lowers the solubility, and hence, increases the supersaturation), until it hits the lower constraint (4 °C) on the jacket temperature.

The closed-loop simulation results for the case of a process–model mismatch are shown by the dashed line in Figures 5.8, 5.9 and 5.10(b). Comparing Figure 5.10(a) and Figure 5.10(b), it is clear that through feedback, the predictive controller 'corrects' for plant-model mismatch and produces a different manipulated input trajectory to enforce constraint satisfaction and achieve the desired objective. Simulation

results, shown in Figure 5.7, also demonstrate that if the off-line optimized trajectory of jacket temperature, based on the mismatched model, is implemented for the entire duration of the batch run without using the measurements to update the control trajectory, the state constraints are violated at the end of the batch run underscoring the importance of feedback to achieve robustness with respect to modeling errors.

Note that predictive control without constraint on fines can result in a product with a large number of fines (see Figure 5.10(a)) which is undesirable. The implementation of the predictive controller with the constraint of Eq.5.10, designed to reduce the fines in the product, results in a product with much less fines while still maximizing the volume-averaged crystal size (see Figure 5.10(c) and Table 5.3).

Compared to predictive control, the crystal size distribution evolves very differently under CTC and CSC. Under CTC, where a constant reactor temperature is maintained throughout the batch run, the control strategy results in a constant solubility during the batch run, and the depletion in the solute concentration is reflected in the decrease of supersaturation, which eventually hits its lower constraint (the dotted line in Figure 5.9(a)). In contrast, under CSC, which tries to maintain a constant value of the supersaturation during the entire batch run, the reactor temperature is lowered during the entire batch run (via the continued lowering of the jacket temperature) to keep up with the falling concentration levels (see the dash-dotted line in Figures 5.8(a) and 5.9(a)). Under CSC, therefore, the growth rate stays constant during the batch run, since it is only dependent on the supersaturation. The nucleation rate, which also depends directly on the solute concentration itself, is lowered gradually because of the depletion of the solute. Unlike the CSD evolution under predictive control, in the case of CTC and CSC, a constant number of new nuclei are continuously formed during the whole batch run until the depletion of the solute

and this leads to a relatively low volume-averaged crystal size compared to the case of crystallizer operation under predictive control.

Table 5.3 summarizes the simulation results obtained under the five different control strategies: (1) Predictive control with a matched model, (2) Predictive control with a mismatched model, (3) Predictive control with constraint on fines, (4) Open-loop operation under CTC, and (5) Open-loop operation under CSC. In Table 5.3, six characteristic parameters of the product at the end of the batch run are compared, including the value of the volume-averaged crystal size (μ_4/μ_3), total volume (μ_3), r_{10}, r_{50}, r_{90} and the span. r_{10}, r_{50} and r_{90} are the 10%, 50% and 90% volume fractions of the CSD, respectively, denoting the percentage of crystals smaller than that size. The span, defined as $(r_{90} - r_{10})/r_{50}$, is an important characteristic of the CSD, and is widely used in the pharmaceutical industry. A high span value indicates a wide distribution in size and a high polydispersity, which is undesirable. Comparing the results of the five control strategies listed in Table 5.3, it is clear that the predictive controller increases the volume-averaged crystal size by 30% compared to CTC, and 8.5% compared to CSC. It is also observed that, in the case of process–model mismatch (a 10% error of the exponent relating growth rate to supersaturation), the predictive control strategy is able to increase the volume-averaged crystal size by

Table 5.3: Comparison between the simulation results under five different control strategies.

Control Strategy	μ_4/μ_3	μ_3	r_{10}	r_{50}	r_{90}	Span
	μm	$\times 10^3$	μm	μm	μm	
Predictive control (matched)	218	5.589	143	239	253	0.463
Predictive control (mismatched)	201	6.459	167	208	226	0.284
Predictive control with constraint on fines	208	6.374	166	219	235	0.315
Open-loop CTC	168	3.186	123	175	201	0.445
Open-loop CSC	201	5.583	143	211	244	0.478

20% compared to CTC. Although the predictive controller with a mismatched model results in a similar volume-averaged crystal size compared to CSC, it leads to a much higher volume of the product, 103% compared to CTC and 16% compared to CSC. Note also that the CSD under predictive control has the largest r_{10}, r_{50} and r_{90}. Figure 5.9(b) shows that the CSDs under the proposed predictive controller with perfect model (solid line), plant-model mismatch (dashed line) and constraint on fines (solid line marked with circles) have lower polydispersity. A lower span and much larger volume-averaged crystal size are achieved under predictive control with constraint on fines compared to the one under CTC and CSC, as shown in Figure 5.10 and Table 5.3. In summary, the implementation of the proposed predictive controller increases the volume-averaged crystal size, satisfies state and input constraints, and is found to be robust with respect to plant-model mismatch.

5.6 Conclusions

In this chapter, we considered the problem of modeling, simulation and control of a batch protein crystallization process that is used to produce the tetragonal HEW lysozyme crystals. First, a population balance model, using empirically obtained rate expressions, was developed to simulate the batch crystallization process. Then, model reduction techniques were used to derive a reduced-order moments model for the purpose of controller design. Online measurements of the solute concentration and reactor temperature were assumed to be available, and a Luenberger-type observer was developed to estimate the moments of the crystal size. A predictive controller, that uses these state estimates, was designed to achieve the objective of maximizing the volume-averaged crystal size while respecting constraints on the manipulated input variables (which reflect physical limitations of control actuators) and

on the process state variables (which reflect performance considerations). Simulation results showed that the proposed predictive controller was able to increase the volume-averaged crystal size by 30% and 8.5% compared to Constant Temperature Control (CTC) and Constant Supersaturation Control (CSC) strategies, respectively, while reducing the number of fine crystals produced. Furthermore, a comparison of the crystal size distributions (CSDs) indicated that the product achieved by the proposed predictive control strategy has larger total volume and lower polydispersity compared to the CTC and CSC strategies. Finally, the robustness of the proposed method with respect to plant-model mismatch was evaluated. In contrast to open–loop control strategies, which led to violation of constraints in the presence of plant-model mismatch, the proposed method was demonstrated to successfully achieve the task of maximizing the volume-averaged crystal size while satisfying the state and input constraints.

Chapter 6

Conclusions and future research directions

6.1 Conclusions

This work is focused on the modeling and control of particulate processes, including high-velocity oxygen fuel (HVOF) thermal spray and protein crystallization processes. The first part of this work is focused on the modeling and feedback control of the HVOF thermal spray processing of nanostructured coatings, which is motivated by the superior qualities of nanostructured coatings and high sensitivity of the coated material to arbitrary variation in the operating environment. In the second part of this work, we developed a novel and practical framework for the synthesis of practically-implementable predictive controllers for regulation of particle size distribution (PSD) in particulate processes.

In the first part of this work, we developed a multiscale modeling and control framework for the HVOF thermal spray processing of nanostructured coatings. In the modeling part, we developed a comprehensive multiscale model, which includes

continuum type differential equations that describe the evolution of gas and particle temperature and velocity, and a rule-based stochastic simulator that predicts the evolution of coating microstructure. On the macroscopic gas/particle dynamics side, the Reynolds and Favre-averaged Navier-Stokes equations and energy balance equations are solved with the renormalization group (RNG) k-ϵ turbulence model to capture the complex fluid/thermal behavior, and the particle trajectories, temperature histories and melting ratio are determined using the 4th order Runge-Kutta method. On the microscopic particle deposition process, the formation of coating microstructure is captured by certain rules that encapsulate the main physical features of particle deformation, solidification and coating growth. Based on the proposed model, a detailed comprehensive parametric analysis is carried out to study the relationship between the key process parameters and the particle inflight behavior as well as the resulting coating properties. Specifically, the modeling and analysis work shows the following:

1. Particles in the HVOF thermal spray process are not uniformly accelerated or heated, i.e., particles of moderate sizes usually achieve highest velocities, temperatures and melting ratio. Small particles, due to their small momentum inertia, may follow the gas stream and not stick on the substrate. (Note that the existence of the substrate will change that pattern of the supersonic free jet. In the vicinity of substrate, the gas velocity in the axial direction decreases to zero and the gas flows in parallel to the substrate.) They are most likely in a solid state upon impact, although they might experience a fully molten state during flight. Particles with sizes larger than 50 μm, however, are hard to be either accelerated (or heated up) or decelerated (or cooled down). The nonuniform acceleration and heating of particles of different sizes have been validated by

experiments [70, 91, 200].

2. The particle velocity and melting ratio play an important role in the formation of coating microstructure. The higher the particle velocity, the larger the flattening ratio and the denser the coating. Moreover, a high ratio of particle melting tends to decrease the coating porosity and increase the deposition efficiency [133]. Therefore, to improve process performance, both the velocity and melting ratio of particles at the point of impact on the substrate should be maintained above certain levels. However, for the processing of nanostructured coatings, the particle melting ratio should not be too high since it is the nanocrystalline structure preserved in most of the particles deposited on the substrate that leads to the unique characteristics of nanostructured coatings [24].

3. Chamber pressure and fuel/oxygen ratio are two key parameters directly related to the gas momentum flux (ρu^2) and gas temperature, which provide driving forces for particle motion and particle heating. To enhance momentum transfer, the chamber pressure should be maintained as high as possible, however, the pressure in the chamber maintained is usually limited by the maximum reservoir pressure. Moreover, an increase in the total mass flow rate typically results in an increase in the chamber pressure. And, increasing the total mass flow rate tends to lengthen the potential core in the supersonic free jet, or both gas velocity and temperature are maintained at high values for a longer distance, which enhances momentum and heat transfer. However, the relationship between the fuel/oxygen ratio and the gas temperature is not monotonic. The maximum gas temperature is usually achieved at the equivalence ratio around 1.1-1.2, a fuel rich condition.

Based on the comprehensive process model, a simplified one dimensional model,

179

which is computationally tractable (from a control point of view) while capable of capturing the dominant characteristic occurring within the HVOF thermal spray process, is developed. The control problem is then formulated as the one of regulating volume-based averages of the melting ratio and velocity of the particles at the point of impact on the substrate (these are the variables that directly influence coating microstructure and porosity, which, in turn, determine coating strength and hardness) by directly manipulating the flow rate of fuel, oxygen and air at the entrance of the HVOF thermal spray gun. A feedback control system is developed and applied to the fundamental process model. Closed-loop simulations demonstrate that the particle velocity and melting ratio at the point of impact on substrate reach the desired set-point values in a short time, which validates the feasibility of real-time implementation of feedback control on the HVOF thermal spray system. It is shown that the proposed formulation of the control problem (which accounts for the effect of powder size distribution) leads to a solution of the control problem that is superior (with respect to the achievement of the desired control objectives) to a solution that assumes a monodisperse powder size distribution. It is also demonstrated that the proposed control problem formulation and the feedback control system are robust with respect to disturbances in spray distance and particle injection velocity, and variations in powder size distribution.

In the second part of this work, we focused on the development and application of predictive-based strategies for control of PSD in continuous and batch particulate processes described by population balance models. The control algorithms were developed on the basis of reduced-order models that capture the dominant dynamics of the particulate process, utilize measurements of principle moments of the PSD, and are tailored to address different control objectives for the continuous and batch

processes.

For continuous particulate processes, we considered the control objective of asymptotic stabilization under constraints and developed a hybrid predictive control strategy that employs logic-based switching between model predictive control (MPC) and a fall–back controller with a well-defined stability region. The control objective is to stabilize the crystallizer at an unstable steady-state (which corresponds to a desired PSD) using constrained control action. MPC is a popular method for handling constraints within an optimal control setting. For linear systems, a number of control-relevant issues have been explored, including issues of closed–loop stability, performance, implementation and constraint satisfaction. However, because of the highly nonlinear behavior exhibited by the continuous crystallizer, the practical implementation of MPC is limited by: (1) the computational difficulties of solving a nonlinear (typically nonconvex) optimization problem at each time step, and (2) the difficulty of characterizing, *a priori*, the set of initial conditions starting from where a given NMPC controller is guaranteed to be feasible and/or stabilize the closed–loop nonlinear system. To overcome these difficulties, we used a recently developed hybrid predictive control structure [47] that provides a safety net for the implementation of predictive control algorithms. The central idea is to use a bounded analytical nonlinear controller, with an explicitly characterized stability region, as a fall–back controller, and embed the operation of MPC within its stability region. In the event that the given predictive controller (which can be based on linear or nonlinear models) is unable to stabilize the closed–loop system (e.g., due to failure of the optimization algorithm, poor choice of the initial condition, insufficient horizon length, etc.), supervisory switching from MPC to the bounded controller safeguards closed–loop stability. The strategy was shown to provide a safety net for the imple-

mentation of MPC algorithms to particulate processes, and was successfully used to stabilize a continuous crystallizer at an open-loop unstable steady-state.

For batch particulate processes, the control objective is to achieve PSD with desired characteristics subject to both manipulated input and product quality constraints. An optimization-based predictive control strategy that incorporates these constraints explicitly in the controller design was formulated. The developed control methods were successfully applied via computer simulations to batch cooling crystallizer which produce protein (tetragonal hen egg-white lysozyme) crystals. First, a model was presented that describes the formation of infinitesimal-size protein crystals via nucleation and the subsequent growth of the crystals via condensation, and predicts the temporal evolution of the crystal size distribution in the size range of $0 - 300 \ \mu m$. To this end, existing experimental data were used to develop empirical models of the nucleation and growth mechanisms of the tetragonal HEW lysozyme crystal. The developed growth and nucleation rate expressions were used within a population balance model to simulate a batch crystallization process that produces the tetragonal HEW lysozyme crystals. Then, model reduction techniques were used to derive a reduced-order moments model for the purpose of controller design. Online measurements of the solute concentration and reactor temperature were assumed to be available, and a Luenberger-type observer was developed to estimate the moments of the crystal size distribution based on the available measurements. A predictive controller, that uses the available state estimates, was designed to achieve the objective of maximizing the volume-averaged crystal size while respecting constraints on the manipulated input variables (which reflect physical limitations of control actuators) and on the process state variables (which reflect performance considerations). Simulation results demonstrated that the proposed predictive controller is able to

increase the volume-averaged crystal size by 30% and 8.5% compared to Constant Temperature Control (CTC) and Constant Supersaturation Control (CSC) strategies, respectively, while reducing the number of fine crystals produced. Furthermore, a comparison of the crystal size distributions (CSDs) indicated that the product achieved by the proposed predictive control strategy has larger total volume and lower polydispersity compared to the CTC and CSC strategies. Finally, the robustness of the proposed method with respect to plant-model mismatch was evaluated. The proposed method was demonstrated to successfully achieve the task of maximizing the volume-averaged crystal size in the presence of plant-model mismatch, and was found to be robust in comparison to open-loop optimal control strategies.

6.2   Future research directions

For the purpose of modeling and control of HVOF thermal spray processes, a more comprehensive CFD model should be developed for HVOF thermal spray systems which takes into account reactions, transport, phase change and microstructure development phenomena taking place in the process. The model should include the gas dynamics of in the torch and in the free jet, particle injection and the interaction (heat and momentum transfer) between the injected particles and the turbulent gas flow inside the outside the barrel, particle interaction with the barrel walls, phase change of the nanosize powders, droplet motion, distribution and impact on the substrate, microstructure development, and dependence of coated material end-properties on microstructure. Since most of the factors have been taken into account in our present work, this comprehensive model to be developed will focus on the three dimensional tracking of particles in the gas flow/thermal field and the interaction between particles and gas, especially the heating and melting of particles during flight. Moreover,

the impact of particles on the substrate and the interaction between melted parts and unmelted ones of the splats will be explored. The detailed model will be used to predict the dependence of the thermal and mechanical properties of the nanostructured coatings on the size, velocity, temperature and molten state of the droplets which hit on the substrate, along with the consolidation rate of the sprayed droplets. In addition, the model will predict the dependence of these parameters on the heat and momentum transfers between the flame and the particles of the nanopowder, and on the other hand by the morphology, size and injection velocity distribution of the particles. Moreover, the relationship of the nature, roughness and temperature of the substrate and the previously deposited layers on the impact, flattening, cooling and solidification of the droplets will be explicitly modeled.

3-D particle tracking: Most of the previous modeling work is based on the one dimensional particle tracking, in which case the particle properties are only functions of particle size and axial position. However, because of the stochastic behavior of particle motion due to injection velocity distribution, collision of wall, turbulence of the gas phase, particles of the same size may take totally different trajectories during flight and have different melting experience. Therefore, the properties of particles at the point of impact will be not only size dependent but also spatially distributed. The 3-D particle tracking will provide a more accurate description of the evolution of velocity, temperature and melting ratio of particles in the HVOF gas flow field.

Interaction between melted parts and unmelted parts in coating microstructure evolution: Most previous studies of particle deposition and coating growth rely on the assumption of fully molten state of particles on the substrate. However, both experiments [70, 91, 200] and numerical modeling [112, 110] have shown that particles at the point of impact on the substrate may be in different molten states (fully

184

melted, partially melted or solid) due to different sizes and different trajectories in the HVOF thermal spray process. We first included the nonuniform molten states of particles upon impact on the substrate [173]. However, the rules governing the coating growth, for example, the threshold for particle bouncing off, the interaction between the melted parts and the unmelted parts of the splats, can be further improved to have more accurate predictions. Moreover, further efforts should be devoted to the modeling of solid particle impingement and the microstructural evolution, particularly the grain growth behavior, and chemical reactions during impingement.

Model validation: Model validation should be conducted in collaboration with Sulzer Metco, the manufacturer of the Diamond Jet hybrid HVOF thermal spray gun. Comparison between the CFD predicted gas phase data such as pressure, velocity, temperature, mach number and density etc., and the corresponding experimental measurements will point out various modeling assumptions and equations that have been suggested in the literature to improve the process model. Based on the validated process model, a comprehensive parametric analysis will be made to find out the key parameters that affect coating microstructure, including particle velocity, temperature, melting ratio, and oxidant content etc. This model would allow precise simulation of HVOF thermal spray processes using any combination of carries gases and nanostructured powders under any operating conditions, which would facilitate testing of different operating conditions with minimum cost compared to expensive laboratory or pilot-scale testing.

We note that although a comprehensive CFD model is adequate to capture the reaction, transport, phase change, microstructure development phenomena involved in the HVOF thermal spray process, however, from a control point of view, such a model is computationally untractable because its solution time can not be comparable

to the evolution of the process dynamics. Therefore, a well-characterized, simplified model that is capable of capturing the dominant gas and particle dynamics should be developed and validated. Combination of experimental data and model predictions will determine whether some mechanisms in the thermal spray process may be neglected in the models used for controller design in order to simplify the controller design task. This can be done by running a bunch of comprehensive CFD simulations under different gas flow rates and equivalence ratios and applying interpolation method to estimate the gas thermal and flow characteristics in a certain range. Our preliminary study has shown that the gas dynamics can be adequately described by the weighted sum of several characteristic functions, thus the gas flow/thermal field can be reasonably estimated in a very short time. Based on the reduced model, model-based estimation and control algorithms will be then synthesized which use the information from the measurements and the simulator to manipulate external variables to achieve the desired performance specifications.

To develop a practical control system for the HVOF thermal spray process, it is also important to note several physical constraints on this process. Firstly, although it is found that an increase in the total gas flow rate leads to an increase in the gas momentum flux and the flame temperature, which is beneficial to the particle inflight behavior, especially the ratio of particle melting, and eventually, the coating microstructure. However, It should be noted that the reservoir pressure of the inlet gases limits the increase of pressure in the combustion chamber. Secondly, the flame temperature cannot increase unboundedly. Although the gas temperature increases a little as the total gas flow rate increases, the flame temperature is almost a sole function of the equivalence ratio, and the highest temperature is achieved at an optimal equivalence ratio around 1.2. If the process is operated under or around this

optimal conditions, it will be difficult to further increase the particle temperature and melting ratio by changing the total mass flow rate and the equivalence ratio. One possible way to solve this is to adjust the spray distance. This leads to the development of control systems with switching scheme (see, for example, [129, 47, 46]). Thirdly, significant uncertainty in the parameters of the process model (time-varying unknown process parameters such as unknown reaction rates, heat transfer coefficients, heat of reaction, etc.) and external disturbances (arbitrary variations in the concentration and temperature of inlet streams), and large dead-times in the measurement instruments and the control actuators should be accounted for in the synthesis of controllers for implementation into practice.

Further studies in control of the particle size distribution in particulate processes include model development, molecular simulation and model validation. To simulate the crystallization processes more accurately, a more detailed model, which considers the effects of secondary nucleation and multidimensional crystallization, should be developed to simulate crystallization processes. Molecular simulation is a powerful tool to capture the stochastic behaviors of the crystallization processes. Deep understanding on the mechanisms of crystal nucleation and growth can be achieved by molecular simulation methods, such as Monte Carlo simulation method. The population balance model and molecular model should also be validated through experiment studies.

Modeling of secondary nucleation and multidimensional crystallization processes: Population balance models were developed in this work to simulate the crystallization processes. Existing experimental data were used to develop empirical models of the nucleation and growth mechanisms of the tetragonal HEW lysozyme crystal. Because of the complex nature of the crystallization process, some important

phenomena that were not considered in this work, such as secondary nucleation and multidimensional crystallization, should also be carefully studied to develop a comprehensive model for crystallization processes. Other phenomena with minor effects include heterogeneous nucleation and size-dependant growth. Furthermore, as the population balance model becomes more complex by accounting for more complex reaction mechanisms, method of moments may not be able to use as the model reduction technique. Other model reduction techniques, such as method of weighted residuals, should be implemented to achieve lower-order models for the purpose of controller design.

Molecular simulation of crystallization processes: Crystallization processes can be viewed and modeled as a molecular assembly process. Molecular simulation is a powerful tool to capture the stochastic behaviors of such processes. Based on molecular simulation, the effects of operating conditions on the crystal nucleation and growth rate can be numerically analyzed. The molecular simulation can also reveal the mechanisms of defect formation and shape dynamics, which can be used to validate the setting of constraints on the operating conditions. At this stage, a close look in the literature indicates that significant research is needed to explore the crystallization process both from a microscopic (study of the nucleation and growth mechanisms by molecular simulation) and macroscopic (control of the crystal size distribution) point of view. Therefore, a multiscale model, which combines both the molecular simulation and the population balance model, should be developed to provide a comprehensive view of crystallization processes, and to facilitate the design of advanced control strategies.

Model validation: Experiments on the control of crystallization processes should be conducted to validate the process models and control strategies. Comparison

between the experimental measurements and simulation results, including the solute concentration, temperature, and crystal size distributions, can be used to validate the model assumptions and equations that have been suggested in the literature. Because of the difficulties of the online measurements of solute concentration and crystal size distribution, different measurement techniques and methods should be tested to guarantee the accuracy of the measurements. Based on the validated process model, more accurate and reliable controllers can be designed, and the performance of the proposed control strategies will be able to be analyzed and validated.

To improve the performance of the proposed control strategies, several important issues respect to control algorithms should also be further explored. Firstly, the optimization algorithm should be extensively studied to be more robust and efficient. In this work, optimization problems formulated in the controllers are high-dimensional, highly nonlinear and nonconvex, and incorporate a large number of linear and nonlinear constraints. Optimization algorithms for such problems are typically very complex, and do not guarantee the solution to be global optimal. Although the sequential quadratic programming methods represent the state-of-the-art in nonlinear programming methods, there still exist several issues that need to be carefully studied, for example, how to achieve the initial guess of a feasible control trajectory. The optimal objectives and constraints considered in the optimization problem should also be carefully selected to guarantee the performance of the closed-loop system. Secondly, the robustness of the proposed control strategies should be more extensively analyzed. In this work, the robustness is numerically tested by introducing a modeling error on a process parameter. Besides the numerical study, theoretical study should be conducted to thoroughly analyze the robustness of the proposed control strategies.

Bibliography

[1] L. Ajdelsztajn, J. Lee, K. Chung, F. L. Bastian, and E. J. Lavernia. Synthesis and nanoindentation study of high-velocity oxygen fuel thermal-sprayed nanocrystalline and near-nanocrystalline Ni coatings. *Metall. Mater. Trans. A*, 33:647–655, 2002.

[2] S. Annavarapu, D. Apelian, and A. Lawley. Spray casting of steel strip: Process analysis. *Metall. Trans. A*, 21:3237–3256, 1990.

[3] M. Benaissa, M. JoseYacaman, T. D. Xiao, and P. R. Strutt. Microstructural study of hollandite-type MnO_2 nano-fibers. *Appl. Phys. Lett.*, 70:2120–2122, 1997.

[4] P. Bennema. Spiral growth and surface roughening: Developments since Burton, Cabrera and Frank. *J. Cryst. Growth*, 69:182–197, 1984.

[5] V. Bhamidi, S. Varanasi, and C. A. Schall. Measurement and modeling of protein crystal nucleation kinetics. *Crystal Growth & Design*, 2:395–400, 2002.

[6] F. Biancaniello, J. J. Conway, P. I. Espina, G. E. Mattingly, and S. D. Ridder. Particle size measurement of inert-gas-atomized powder. *Mater. Sci. Eng.*, A124:9–14, 1990.

[7] F. Biancaniello, C. Presser, and S.D. Ridder. Real-time particle size analysis during inert gas atomization. *Mater. Sci. Eng.*, A124:21–29, 1990.

[8] R. B. Bird, W. E. Stewart, and E. N. Lightfoot. *Transport Phenomena*. John Wiley & Sons, New York, USA, 1960.

[9] C. M. Bouko, T. H. Le, and H. Henein. Ensemble and single particle laser probe sizing results for gas atomized zinc powders. *Particle & Particle Systems Characterization*, 10:266–270, 1993.

[10] R. D. Braatz and S. Hasebe. Particle size and shape control in crystallization processes. In J. B. Rawlings, B. A. Ogunnaike, and J. W. Eaton, editors, *Chemical Process Control VI*, pages 307–327, Tucson, AZ, 2002.

[11] M. Bussmann, J. Mostaghimi, and S. Chandra. On a three-dimensional volume tracking model of droplet impact. *Physics of Fluids*, 11:1406–1417, 1999.

[12] E. Cacioppo and M. L. Pusey. The solubility of the tetragonal form of hen egg white lysozyme from pH 4.0 to 5.4. *J. Cryst. Growth*, 114:286–292, 1991.

[13] W. D. Cai and E. J. Lavernia. Sensors and techniques used to monitor processing parameters during spray atomization and deposition. *J. Mater. Sci.*, 30:1125–1138, 1995.

[14] W. D. Cai and E. J. Lavernia. Modeling of porosity during spray forming. *Mat. Sci. Eng. A*, 226:8–12, 1997.

[15] W. D. Cai and E. J. Lavernia. Numerical simulation of porosity evolution during spray forming of Ta-2.5 wt% Fe. *J. Mater. Synth. Proces.*, 5:39–44, 1997.

[16] R. C. Cammarata. Surface and interface stress effects on interfacial and nanostructured materials. *Mater. Sci. & Eng.*, A237:180–184, 1997.

[17] D. C. Carter, K. Lim, J. X. Ho, B. S. Wright, P. D. Twigg, T. Y. Miller, J. Chapman, K. Keeling, J. Ruble, P. G. Vekilov, B. R. Thomas, F. Rosenberger, and A. A. Chernov. Lower dimer impurity incorporation may result in higher perfection of HEWL crystals grown in microgravity: A case study. *J. Cryst. Growth*, 196:623–637, 1999.

[18] B. M. Cetegen and W. Yu. In-situ particle temperature, velocity, and size measurements in DC arc plasma thermal sprays. *J. Therm. Spray Techn.*, 8:57–67, 1999.

[19] N. E. Chayen and E. Saridakis. Is lysozyme really the ideal model protein? *J. Cryst. Growth*, 232:262–264, 2001.

[20] Y. Chen, G. Wang, and H. Zhang. Numerical simulation of coating growth and pore formation in rapid plasma spray tooling. *Thin Solid Films*, 390:13–19, 2001.

[21] D. Cheng, G. Trapaga, J. W. McKelliget, and E. J. Lavernia. Mathematical modeling of high velocity oxygen fuel thermal spraying: an overview. *Key Eng. Mat.*, 197:1–25, 2001.

[22] D. Cheng, G. Trapaga, J. W. McKelliget, and E. J. Lavernia. Mathematical modelling of high velocity oxygen fuel thermal spraying of nanocrystalline materials: an overview. *Modelling Simul. Mater. Sci. Eng.*, 11:R1–R31, 2003.

[23] D. Cheng, Q. Xu, G. Trapaga, and E. J. Lavernia. The effect of particle size and morphology on the in-flight behavior of particles during high-velocity oxyfuel thermal spraying. *Metall. Mat. Trans. B*, 32:525–535, 2001.

[24] D. Cheng, Q. Xu, G. Trapaga, and E. J. Lavernia. A numerical study of high-velocity oxygen fuel thermal spraying process. part I: Gas phase dynamics. *Metall. Mat. Trans. A*, 32:1609–1620, 2001.

[25] T. S. Cheng, J. A. Wehrmeyer, R. W. Pitz, O. Jarrett, and G. B. Northam. Raman measurement of mixing and finite-rate chemistry in a supersonic hydrogen-air diffusion flame. *Combustion and Flame*, 99:157–173, 1994.

[26] T. Chiu and P. D. Christofides. Nonlinear control of particulate processes. *AIChE J.*, 45:1279–1297, 1999.

[27] T. Chiu and P. D. Christofides. Robust control of particulate processes using uncertain population balances. *AIChE J.*, 46:266–280, 2000.

[28] T. Chraska and A. H. King. Interfaces in rapidly solidified zirconia-yttria. *Mat. Sci. Forum*, 294:779–782, 1999.

[29] P. D. Christofides. Control of nonlinear distributed process systems: recent developments and challenges. *AIChE J.*, 47:514–518, 2001.

[30] P. D. Christofides. *Model-Based Control of Particulate Processes.* Kluwer Academic Publishers, Particle Technology Series, Netherlands, 2002.

[31] S. Cirolini, J. H. Harding, and G. Jacucci. Computer simulation of plasma-sprayed coatings I coating deposition model. *Surf. Coat. Tech.*, 48:137–145, 1991.

[32] E. L. Crow and K. Shimizu. *Lognormal Distributions: Theory and Applications.* Marcel Dekker, New York, USA, 1988.

[33] C. T. Crowe, M. Sommerfeld, and Y. Tsuji. *Multiphase Flows with Droplets and Particles.* CRC Press, Boca Raton, FL, USA, 1997.

[34] C. T. Crowe and D. E. Stock. A computer solution for two-dimensional fluid-particle flows. *International Journal for Numerical Methods in Engineering*, 10:185–196, 1976.

[35] P. A. Darcy and J. M. Wiencek. Identifying nucleation temperatures for lysozyme via differential scanning calorimetry. *J. Cryst. Growth*, 196:243–249, 1999.

[36] H. L. de Villiers Lovelock, P. W. Richter, J. M. Benson, and P. M. Young. Parameter study of HP/HVOF deposited WC-Co coatings. *J. Therm. Spray Techn.*, 7:97–107, 1998.

[37] L. DelCastillo, Y. Wu, H. M. Hu, and E. J. Lavernia. The mechanism of porous column formation during spray forming. *Metall. Mater. Trans. A*, 30:1381–1389, 1999.

[38] R. C. DeMattei and R. S. Feigelson. Controlling nucleation in protein solutions. *J. Cryst. Growth*, 122:21–30, 1992.

[39] J. Dimitratos, G. Elicabe, and C. Georgakis. Control of emulsion polymerization reactors. *AIChE J.*, 40:1993–2021, 1994.

[40] A. Dolatabadi, J. Mostaghimi, and V. Pershin. Effect of a cylindrical shroud on particle conditions in high velocity oxy-fuel spray process. *J. Mater. Process. Tech.*, 137:214–224, 2003.

[41] S. D. Durbin, W. E. Carlson, and M. T. Saros. In-situ studies of protein crystal-growth by atomic-force microscopy. *J. Phys. D: Appl. Phys.*, 26:B128–B132, 1993.

[42] S. D. Durbin and G. Feher. Crystal growth studies of lysozyme as a model for protein crystallization. *J. Cryst. Growth*, 76:583–592, 1986.

[43] N. H. El-Farra, T. Chiu, and P. D. Christofides. Analysis and control of particulate processes with input constraints. *AIChE J.*, 47:1849–1865, 2001.

[44] N. H. El-Farra and P. D. Christofides. Integrating robustness, optimality and constraints in control of nonlinear processes. *Chem. Eng. Sci.*, 56:1841–1868, 2001.

[45] N. H. El-Farra and P. D. Christofides. Bounded robust control of constrained multivariabe nonlinear processes. *Chem. Eng. Sci.*, 58:3025–3047, 2003.

[46] N. H. El-Farra and P. D. Christofides. Coordinated feedback and switching for control of hybrid nonlinear processes. *AIChE J.*, 49:2079–2098, 2003.

[47] N. H. El-Farra, P. Mhaskar, and P. D. Christofides. Hybrid predictive control of nonlinear systems: Method and applications to chemical processes. *Int. J. Rob. & Non. Contr.*, 14:199–225, 2004.

[48] J. R. Fincke, D. C. Haggard, and W. D. Swank. Particle temperature measurement in the thermal spray process. *J. Therm. Spray Techn.*, 10:255–266, 2001.

[49] J. R. Fincke, W. D. Swank, R. L. Bewley, D. C. Haggard, M. Gevelber, and D. Wroblewski. Diagnostics and control in the thermal spray process. *Surf. Coat. Tech.*, 146-147:537–543, 2001.

[50] J. R. Fincke, W. D. Swank, and C. L. Jeffrey. Simultaneous measurement of particle size, velocity and temperature in thermal plasmas. *IEEE Trans. Plasma Sci.*, 18:948–957, 1990.

[51] E. L. Forsythe, A. Nadarajah, and M. L. Pusey. Growth of (101) faces of tetragonal lysozyme crystals: measured growth-rate trends. *Acta Crystallographica Section D - Biological Crystallography*, 55:1005–1011, 1999.

[52] R. A. Freeman and P. V. Kokotovic. *Robust Nonlinear Control Design: State-Space and Lyapunov Techniques*. Birkhauser, Boston, 1996.

[53] S. K. Friedlander. *Smoke, Dust, and Haze: Fundamentals of Aerosol Behavior*. Wiley, New York, 1977.

[54] O. Galkin and P. G. Vekilov. Direct determination of the nucleation rates of protein crystals. *Journal of Physical Chemistry B*, 103:10965 – 10971, 1999.

[55] G. H. Ganser. A rational approach to drag prediction of spherical and nonspherical particles. *Powder Technol.*, 77:143–152, 1993.

[56] C. J. Geankoplis. *Transport Processes and Unit Operations, 3rd ed.* Prentice-Hall, New Jersey, USA, 1993.

[57] F. Gelbard and J. H. Seinfeld. Numerical solution of the dynamic equation for particulate processes. *J. Comp. Phys.*, 28:357–375, 1978.

[58] M. Gell. The potential for nanostructured materials in gas turbine engines. *Nanostructured Materials*, 6:997–1000, 1995.

[59] R. Ghafouri-Azar, J. Mostaghimi, S. Chandra, and M. Charmchi. A stochastic model to simulate the formation of a thermal spray coating. *J. Therm. Spray Techn.*, 12:53–69, 2003.

[60] L. Gil and M. H. Staia. Influence of HVOF parameters on the corrosion resistance of NiWCrBSi coatings. *Thin Solid Films*, 420–421:446–454, 2002.

[61] S. L. Girshick and C. P. Chiu. Numerical study of MGO powder synthesis by thermal plasma. *J. Aerosol. Sci.*, 21:641–650, 1990.

[62] N. G. Glumac, Y. J. Chen, and G. Skandan. Diagnostics and modeling of nanopowder synthesis in low pressure flames. *J. Therm. Spray Techn.*, 13:2572–2579, 1998.

[63] S. Gordon and B. J. McBride. Computer program for calculation of complex chemical equilibrium compositions and applications. NASA Reference Publication 1311, Lewis Research Center, Cleveland, Ohio, USA, 1994.

[64] V. Gourlaouen, E. Verna, and P. Beaubien. Influence of flame parameters on stainless steel coatings properties. In *Thermal Spray: Surface Engineering Via Applied Research, Proceedings of the International Thermal Spray Conference*, pages 487–493, Montreal, QC, Canada, 2000.

[65] S. Gu, C. N. Eastwick, K. A. Simmons, and D. G. McCartney. Computational fluid dynamic modeling of gas flow characteristics in a high-velocity oxy-fuel thermal spray system. *J. Therm. Spray Techn.*, 10:461–469, 2001.

[66] T. C. Hanson, C. M. Hackett, and G. S. Settles. Independent control of HVOF particle velocity and temperature. *J. Therm. Spray Techn.*, 11:75–85, 2002.

[67] B. Hassan, A. R. Lopez, and W. L. Oberkampf. Computational analysis of a three-dimensional high-velocity oxygen fuel (HVOF) thermal spray torch. *J. Therm. Spray Techn.*, 7:71–77, 1998.

[68] J. He, M. Ice, S. Dallek, and E. J. Lavernia. Synthesis of nanostructured WC-12 pct Co coating using mechanical milling and high velocity oxygen fuel thermal spraying. *Metall. Mater. Trans. A*, 31:541–553, 2000.

[69] J. He, M. Ice, and E. J. Lavernia. Synthesis and characterization of nanostructured Cr3C2-NiCr. *Nanostructured Materials*, 10:1271–1283, 1998.

[70] J. He, M. Ice, and E. J. Lavernia. Particle melting behavior during high-velocity oxygen fuel thermal spraying. *J. Therm. Spray Techn.*, 10:83–93, 2001.

[71] J. A. Hearley, J. A. Little, and A. J. Sturgeon. The effect of spray parameters on the properties of high velocity oxy-fuel NiAl intermetallic coatings. *Surf. Coat. Tech.*, 123:210–218, 2000.

[72] H. Henein, P. L. Meyer D. J. Holve, and M. A. Kuhni. On-line measurement of powder size distribution in zinc atomization. *Int. J. Powder Metall.*, 28:149–165, 1992.

[73] K. Hollis and R. Neise. Analysis of the nonthermal emission signal present in a molybdenum particle-laden plasma-spray plume. *J. Therm. Spray Techn.*, 7:383–391, 1998.

[74] K. Hollis and R. Neiser. Particle temperature and flux measurement utilizing a nonthermal signal correction process. *J. Therm. Spray Techn.*, 7:392–402, 1998.

[75] M. J. Hounslow. A discretized population balance for continuous systems at steady-state. *AIChE J.*, 36:106–116, 1990.

[76] B. Huang, R. J. Perez, and E. J. Lavernia. Grain growth of nanocrystalline Fe-Al alloys produced by cryomilling in liquid argon and nitrogen. *Mat. Sci. Eng. A.*, 255:124–132, 1998.

[77] H. M. Hulburt and S. Katz. Some problems in particle technology: A statistical mechanical formulation. *Chem. Eng. Sci.*, 19:555–574, 1964.

[78] C. D. Immanuel and F. J. Doyle III. Hierarchical multiobjective strategy for particle-size distribution control. *AIChE J.*, 49:2383–2399, 2003.

[79] G. R. Jerauld, Y. Vasatis, and M. F. Doherty. Simple conditions for the appearance of sustained oscillations in continuous crystallizers. *Chem. Eng. Sci.*, 38:1675–1681, 1983.

[80] G. M. Jiang, H. Henein, and M. W. Siege. Overview - intelligent sensors for atomization. *Int. J. Powder Metall.*, 26:253–268, 1990.

[81] H. G. Jiang, M. L. Lau, and E. J. Lavernia. Grain growth behavior of nanocrystalline Inconel 718 and Ni powders and coatings. *Nanostructured Materials*, 10:169–178, 1998.

[82] L. Y. Jiang and J. P. Sislian. Velocity and density measurements in supersonic high-temperature exhaust plumes. *AIAA J.*, 36:1216–1222, 1998.

[83] A. G. Jones, A. Chianese, and J. W. Mullin. Effect of fines destruction on batch colling crystallization of potassium sulphate solutions. In S. J. Jancic and E. J. de Jong, editors, *Industrial crystallization 84 : Proceedings of the 9th Symposium on Industrial Crystallization*, pages 191–195, 1984.

[84] R. A. Judge, R. S. Jacobs, T. Frazier, E. H. Snell, and M. L. Pusey. The effect of temperature and solution pH on the nucleation of tetragonal lysozyme crystals. *Biophysical Journal*, 77:1585–1593, 1999.

[85] A. Kalani and P. D. Christofides. Nonlinear control of spatially-inhomogeneous aerosol processes. *Chem. Eng. Sci.*, 54:2669–2678, 1999.

[86] A. Kalani and P. D. Christofides. Modeling and control of a titania aerosol reactor. *Aer. Sci. & Tech.*, 32:369–391, 2000.

[87] A. Kalani and P. D. Christofides. Simulation, estimation and control of size distribution in aerosol processes with simultaneous reaction, nucleation, condensation and coagulation. *Comp. & Chem. Eng.*, 26:1153–1169, 2002.

[88] J. Karthikeyan, C. C. Berndt, S. Reddy, J. Y. Wang, A. H. King, and H. Herman. Nanomaterial deposits formed by DC plasma spraying of liquid feedstocks. *J. Amer. Cer. Soc.*, 81:121–128, 1998.

[89] J. Kartikeyan, C. C. Berndt, J. Tikkanen, J. Y. Wang, A. H. King, and H. Herman. Nanomaterial powders and deposits prepared by flame spray processing of liquid precursors. *Nanostructured Materials*, 8:61–74, 1997.

[90] D. Katoshevski and J. H. Seinfeld. Analytical solution of the multicomponent aerosol general dynamic equation - without coagulation. *Aer. Sci. & Tech.*, 27:541–549, 1997.

[91] K. A. Khor, H. Li, and P. Cheang. Significance of melt-fraction in hvof sprayed hydroxyapatite particles, splats and coatings. *Biomaterials*, 25:1177–1186, 2004.

[92] A. M. Kierzek and P. Zielenkiewicz. Models of protein crystal growth. *Biophysical Chemistry*, 91:1–20, 2001.

[93] R. Knight, R. W. Smith, and Z. Xiao. Particle velocity measurements in HVOF and APS systems. In *Thermal Spray Industrial Applications, Proceedings of 7th National Thermal Spray Conference*, pages 331–336, 1994.

[94] O. Knotek and R. Elsing. Monte carlo simulation of the lamellar structure of thermally sprayed coatings. *Surf. Coat. Tech.*, 32:261–271, 1987.

[95] S. Kumar and D. Ramkrishna. On the solution of population balance equations by discretization-II. a moving pivot technique. *Chem. Eng. Sci.*, 51:1333–1342, 1996.

[96] K. Kurihara, S. Miyashita, G. Sazaki, T. Nakada, Y. Suzuki, and H. Komatsu. Interferometric study on the crystal growth of tetragonal lysozyme crystal. *J. Cryst. Growth*, 166:904–908, 1996.

[97] M. L. Lau, V. V. Gupta, and E. J. Lavernia. Mathematical modeling of particle behavior of nanocrystalline Ni during high velocity oxy-fuel thermal spray. *Nanostructured Materials*, 10:715–722, 1998.

[98] M. L. Lau, V. V. Gupta, and E. J. Lavernia. Particle behavior of nanocrystalline 316-stainless steel during high velocity oxy-fuel thermal spray. *Nanostructured Materials*, 12:319–322, 1999.

[99] M. L. Lau, J. He, R. Schweinfest, M. Rhle, C. G. Levi, and E. J. Lavernia. Synthesis and characterization of nanocrystalline Cu-Al coatings. *Mater. Sci. Eng. A*, 347:231–242, 2003.

[100] M. L. Lau, H. G. Jiang, W. Nuchter, and E. J. Lavernia. Thermal spraying of nanocrystalline Ni coatings. *Phys. Stat. Sol. A - Appl. Res.*, 166:257–268, 1998.

[101] M. L. Lau, E. Strock, A. Fabel, C. J. Lavernia, and E. J. Lavernia. Synthesis and characterization of nanocrystalline Co-Cr coatings by plasma spraying. *Nanostructured Materials*, 10:723–730, 1998.

[102] W. Lauterborn, A. Judt, and E. Schmitz. High-speed off-axis holographic cinematography with a copper-vapor-pumped dye laser. *Optics Letters*, 18:4–6, 1993.

[103] E. J. Lavernia and Y. Wu. *Spray Atomization and Deposition*. Wiley, New-York, 1996.

[104] T. Le, R. Stefaniuk, H. Henein, and J. Huot. Measurement and analysis of melt flowrate in gas atomization. *Int. J. Powder Metall.*, 35:51–59, 1999.

[105] Z. H. Lee, M. M. Hu, E. J. Lavernia, and D. R. White. The mechanism of porous column formation during spray forming. *Metall. Mater. Trans. A*, 30:1679–1682, 1999.

[106] S. J. Lei, R. Shinnar, and S. Katz. The stability and dynamic behavior of a continuous crystallizer with a fines trap. *AIChE J.*, 17:1459–1470, 1971.

[107] A. K. W. Leung, M. M. V. Park, and D. W. Borhani. An improved method for protein crystal density measurements. *J. Appl. Cryst.*, 32:1006–1009, 1999.

[108] M. Li and P. D. Christofides. Modeling and Analysis of HVOF Thermal Spray Process Accounting for Powder Size Distribution. *Chem. Eng. Sci.*, 58:849–857, 2003.

[109] M. Li and P. D. Christofides. Feedback control of HVOF thremal spray process accounting for powder size distribution. *J. Therm. Spray Techn.*, 13:108–120, 2004.

[110] M. Li and P. D. Christofides. Multiscale modeling and analysis of HVOF thermal spray process. *Chem. Eng. Sci.* provisionally accepted, 2004.

[111] M. Li, A. Nadarajah, and M. L. Pusey. Modeling the growth rates of tetragonal lysozyme crystals. *J. Cryst. Growth*, 156:121–132, 1995.

[112] M. Li, D. Shi, and P. D. Christofides. Diamond jet hybrid HVOF thermal spray: Gas-phase and particle behavior modeling and feedback control design. *Ind. & Eng. Chem. Res.*, 43:3632–3652, 2004.

[113] W. C. Lih, S. H. Yang, C. Y. Su, S. C. Huang, I. C. Hsu, and M. S. Leu. Effects of process parameters on molten particle speed and surface temperature and the properties of HVOF CrC/NiCr coatings. *Surf. Coat. Tech.*, 133, 2000.

[114] R. S. Lima, A. Kucuk, and C. C. Berndt. Integrity of nanostructured partially stabilized zirconia after plasma spray processing. *Mat. Sci. Eng. A*, 313:75–82, 2001.

[115] Y. Lin and E. D. Sontag. A universal formula for stabilization with bounded controls. *Systems & Control Letters*, 16:393–397, 1991.

[116] H. Liu, E. J. Lavernia, and R. H. Rangel. Numerical simulation of substrate impact and freezing of droplets in plasma spray processes. *J. Phys. D: Appl. Phys.*, 26:1900–1908, 1993.

[117] H. Liu, E. J. Lavernia, and R. H. Rangel. Numerical stimulation of impingement of molten Ti, Ni, and W droplets on a flat substrate. *J. Therm. Spray Techn.*, 2:369–378, 1993.

[118] H. Liu, E. J. Lavernia, and R. H. Rangel. Modeling of molten droplet impingement on a nonflat surface. *Acta Metall. Mater.*, 43:2053–2072, 1995.

[119] H. M. Liu, R. H. Rangel, and E. J. Lavernia. Modeling of reactive atomization and deposition processing of NI_3AL. *Acta Metall. Mater.*, 42:3277–3289, 1994.

[120] E. Lugscheider, C. Herbst, and L. Zhao. Parameter studies on high-velocity oxy-fuel spraying of MCrAlY coatings. *Surf. Coat. Tech.*, 108-109:16–23, 1998.

[121] D. L. Ma, D. K. Tafti, and R. D. Braatz. Optimal control and simulation of multidimensional crystallization processes. *Comp. & Chem. Eng.*, 26:1103–1116, 2002.

[122] J. Madejski. Solidification of droplets on a cold surface. *Int. J. Heat Mass Transfer*, 19:1009–1013, 1976.

[123] N. V. Mantzaris and P. Daoutidis. Cell population balance modeling and control in continuous bioreactors. *Journal of Process Control*, 14:775–784, 2004.

[124] N. V. Mantzaris, P. Daoutidis, and F. Srienc. Numerical solution of multi-variable cell population balance models, i. finite difference methods. *Comp. & Chem. Eng.*, 25:1411–1440, 2001.

[125] P. Marthur, S. Annavarapu, D. Apelian, and A. Lawley. Spray casting: An integral model for process understanding and control. *Mat. Sci. Eng. A*, 142:261–276, 1991.

[126] D. Q. Mayne, J. B. Rawlings, C. V. Rao, and P. O. M. Scokaert. Constrained model predictive control: Stability and optimality. *Automatica*, 36:789–814, 2000.

[127] A. McPherson. A brief history of protein crystal growth. *J. Cryst. Growth*, 110:1–10, 1991.

[128] M. Mellali, P. Fauchais, and A. Grimaud. Influence of substrate roughness and temperature on the adhesion/cohesion of alumina coatings. *Surf. Coat. Tech.*, 81:275–286, 1996.

[129] P. Mhaskar, N. H. El-Farra, and P. D. Christofides. Hybrid predictive control of process systems. *AIChE J.*, 50:1242–1259, 2004.

[130] S. M. Miller and J. B. Rawlings. Model identification and control strategies for batch cooling crystallizers. *AIChE J.*, 40:1312–1327, 1994.

[131] D. Mills. Personal communication, sulzer metco, 2003.

[132] L. A. Monaco and F. Rosenberger. Growth and etching kinetics of tetragonal lysozyme. *J. Cryst. Growth*, 129:465–484, 1993.

[133] C. Moreau and L. Leblanc. Optimization and process control for high performance thermal spray coatings. *Key Eng. Mat.*, 197:27–57, 2001.

[134] J. Mostaghimi, S. Chandra, R. Ghafouri-Azar, and A. Dolatabadi. Modeling thermal spray coating processes: a powerful tool in design and optimization. *Surf. Coat. Tech.*, 163-164:1–11, 2003.

[135] R. Mueller, R. Jossen, S. E. Pratsinis, M. Watson, and M. K. Akhtar. Zirconia nanoparticles made in spray flames at high production rates. *J. Am. Ceram. Soc.*, 87:197–202, 2004.

[136] R. Mueller, L. Madler, and S. E. Pratsinis. Nanoparticle synthesis at high production rates by flame spray pyrolysis. *Chem. Eng. Sci.*, 58:1969–1976, 2003.

[137] J. W. Mullin and J. Nyvlt. Programmed cooling of batch crystallizers. *Chem. Eng. Sci.*, 26:369–377, 1971.

[138] Y. Nagatoshi, G. Sazaki, Y. Suzuki, S. Miyashita, T. Matsui, T. Ujihara, K. Fujiwara, N. Usami, and K. Nakajima. Effects of high pressure on the growth kinetics of orthorhombic lysozyme crystals. *J. Cryst. Growth*, 254:188–195, 2003.

[139] W. L. Oberkampf and M. Talpallikar. Analysis of a high-velocity oxygen-fuel (HVOF) thermal spray torch part 1: Numerical formulation. *J. Therm. Spray Techn.*, 5:53–61, 1996.

[140] D. Oliver and R. Enikov. Micro-particles temperature measurements in a plasma jet. *Vacuum*, 58:244–249, 2000.

[141] L. Pawlowski. *The Science and Engineering of Thermal Spray Coatings*. John Wiley & Sons, Chichester, England, 1995.

[142] P. Pladis and C. Kiparissides. A comprehensive model for the calculation of molecular weight-long-chain branching distribution in free-radical polymerizations. *Chem. Eng. Sci.*, 53:3315–3333, 1998.

[143] G. D. Power, T. J. Barber, and L. M. Chiappetta. Analysis of a high velocity oxygen-fuel (HVOF) thermal torch. In *the 28th AIAA/SAE/ASME/ASEE Joint Propulsion Conference and Exhibit*, AIAA92-3598, Nashville, Tennessee, 1992.

[144] G. D. Power, E. B. Smith, T. J. Barber, and L. M. Chiappetta. Analysis of a combustion (HVOF) spray deposition gun. Report 91-8, United Technologies Research Center, East Hartford, Connecticut, USA, 1991.

[145] S. E. Pratsinis. Simultaneous nucleation, condensation, and coagulation in aerosol reactors. *J. Coll. Inter. Sci.*, 124:416–426, 1988.

[146] W. H. Press, S. A. Teukolsky, W. T. Vetterling, and B. P. Flannery. *Numerical recipes in C++ : the art of scientific computing, 2nd ed.* Cambridge University Press, New YorK, USA, 1997.

[147] M. L. Pusey and A. Nadarajah. A model for tetragonal lysozyme crystal nucleation and growth. *Crystal Growth & Design*, 2:475–483, 2002.

[148] M. L. Pusey and R. Naumann. Growth kinetics of tetragonal lysozyme crystals. *J. Cryst. Growth*, 76:593–599, 1986.

[149] M. L. Pusey, W. Witherow, and R. Naumann. Preliminary investigations into solutal flow about growing tetragonal lysozyme crystals. *J. Cryst. Growth*, 90:105–111, 1988.

[150] D. Ramkrishna. The status of population balances. *Rev. Chem. Eng.*, 3:49–95, 1985.

[151] D. Ramkrishna. *Population Balances – Theory and Applications to Particulate Systems in Engineering*. Academic Press, San Diego, 2000.

[152] A. D. Randolph and M. A. Larson. *Theory of Particulate Processes*. Academic press, Second edition, San Diego, 1988.

[153] J. B. Rawlings, S. M. Miller, and W. R. Witkowski. Model identification and control of solution crystallizatin process – a review. *Ind. & Eng. Chem. Res.*, 32:1275–1296, 1993.

[154] J. B. Rawlings and W. H. Ray. Stability of continuous emulsion polymerization reactors: a detailed model analysis. *Chem. Eng. Sci.*, 42:2767–2777, 1987.

[155] J. B. Rawlings, C. W. Slink, and S. M. Miller. Control of crystallization processes. In Allan S. Myerson, editor, *Handbook of Industrial Crystallization. Second Edition*, pages 201–230. Butterworth-Heinemann, 2001.

[156] D. E. Reisner, A. J. Salkind, P. R. Strutt, and T. D. Xiao. Nickel hydroxide and other nanophase cathode materials for rechargeable batteries. *Journal of Power Sources*, 65:231–233, 1997.

[157] J. A. Roberson and C. T. Crowe. *Engineering Fluid Dynamics, 6th ed.* John Wiley & Sons, New York, USA, 1997.

[158] S. Rohani and J. R. Bourne. Self-tuning control of crystal size distribution in a cooling batch crystallizer. *Chem. Eng. Sci.*, 12:3457–3466, 1990.

[159] S. Rohani, N. S. Tavare, and J. Garside. Control of crystal size distribution in a batch cooling crystallizer. *Can. J. Chem. Eng.*, 68:260–267, 1990.

[160] F. Rosenberger. Protein crystallization. *J. Cryst. Growth*, 166:40–54, 1996.

[161] F. Rosenberger, S. B. Howard, J. W. Sowers, and T. A. Nyce. Temperature dependence of protein solubility determination and application to crystallization in x-ray capillaries. *J. Cryst. Growth*, 129:1–12, 1993.

[162] F. Rosenberger and E. J. Meehan. Control of nucleation and growth in protein crystal growth. *J. Cryst. Growth*, 90:74–78, 1988.

[163] F. Rosenberger, P. G. Vekilov, M. Muschol, and B. R. Thomas. Nucleation and crystallization of globular proteins – what we know and what is missing. *J. Cryst. Growth*, 168:1–27, 1996.

[164] Biancaniello F. S., P. I. Espina, G. E. Mattingly, and S. D. Rider. A flow visualization study of supersonic inert gas-metal atomization. *Mat. Sci. Eng. A*, 119:161–168, 1989.

[165] K. Sakaki and Y. Shimizu. Effect of the increase in the entrance convergent section length of the gun nozzle on the high-velocity oxygen fuel and cold spray process. *J. Therm. Spray Techn.*, 10:487–496, 2001.

[166] S. K. Sampath, D. G. Kanhere, and R. Pandey. Electronic structure of spinel oxides: zinc aluminate and zinc gallate. *J. Phys.: Condens. Matter*, 11:3635–3644, 1999.

[167] A. K. Sandrowitz, J. M. Cooke, and N. G. Glumac. Flame emission spectroscopy for equivalence ratio monitoring. *Applied Spectroscopy*, 52:658–662, 1998.

[168] G. Sazaki, K. Kurihara, T. Nakada, S. Miyashita, and H. Komatsu. A novel approach to the solubility measurement of protein crystals by two-beam interferometry. *J. Cryst. Growth*, 169:355–360, 1996.

[169] C. A. Schall, J. S. Riley, E. Li, E. Arnold, and J. M. Wiencek. Application of temperature control strategies to the growth of hen egg-white lysozyme crystals. *J. Cryst. Growth*, 165:299–307, 1996.

[170] D. Semino and W. H. Ray. Control of systems described by population balance equations-I. controllability analysis. *Chem. Eng. Sci.*, 50:1805–1824, 1995.

[171] D. Semino and W. H. Ray. Control of systems described by population balance equations-II. emulsion polymerization with constrained control action. *Chem. Eng. Sci.*, 50:1825–1839, 1995.

[172] D. Shi, N. H. El-Farra, M. Li, P. Mhaskar, and P. D. Christofides. Predictive control of particle size distribution in particulate processes. *Chem. Eng. Sci.*, accepted, 2005.

[173] D. Shi, M. Li, and P. D. Christofides. Diamond jet hybrid HVOF thermal spray: Rule-based modeling of coating microstructure. *Ind. & Eng. Chem. Res.*, 43:3653–3665, 2004.

[174] D. Shi, P. Mhaskar, N. H. El-Farra, and P. D. Christofides. Predictive control of particle size distribution in protein crystallization. submitted, *Nanotechnology*, 2005.

[175] V. V. Sobolev and J. M. Guilemany. Dynamic processes during high velocity oxyfuel spraying. *International Materials Reviews*, 41:13–32, 1996.

[176] H. D. Steffens, H. Kern, and M. Fathi-Torbaghan. An expert system for diagnosis of low pressure plasma spraying. In *Proceedings of Conference on Thermal Spray Technology*, pages 67–74, Cincinnati, OH, 1989.

[177] W. D. Swank, J. R. Fincke, and D. C. Haggard. A particle temperature sensor for monitoring and control of the thermal spray process. In *Proceedings of the 8th National Thermal Spray Conference*, pages 111–116, Houston, Texas, 1995.

[178] W. D. Swank, J. R. Fincke, D. C. Haggard, and G. Irons. HVOF gas flow field characteristics. In *Thermal Spray Industrial Applications, Proceedings of the 7th National Thermal Spray Conference*, pages 313–318, 1994.

[179] W. D. Swank, J. R. Fincke, D. C. Haggard, G. Irons, and R. Bullock. HVOF particle flow field characteristics. In *Thermal Spray Industrial Applications, Proceedings of the 7th National Thermal Spray Conference*, pages 319–324, Boston, Massachusetts, 1994.

[180] H. H. Tawfik and F. Zimmerman. Mathematical modeling of the gas and powder flow in HVOF systems. *J. Therm. Spray Techn.*, 6:345–352, 1997.

[181] V. L. Tellkamp, S. Dallek, D. Cheng, and E. J. Lavernia. Grain growth behavior of a nanostructured 5083 Al-Mg alloy. *J. Mater. Res.*, 16:938–944, 2001.

[182] V. L. Tellkamp, M. L. Lau, A. Fabel, and E. J. Lavernia. Thermal spraying of nanocrystalline Inconel 718. *Nanostructured Materials*, 9:489–492, 1997.

[183] I. Thomson, V. Pershin, J. Mostaghimi, and S. Chandra. Experimental testing of a curvilinear gas shroud nozzle for improved plasma spraying. *Plasma Chem. Plasma Process.*, 21:65–82, 2001.

[184] T. C. Totemeier, R. N. Wright, and W. D. Swank. Microstructure and stresses in HVOF sprayed iron aluminide coatings. *J. Therm. Spray Techn.*, 11:400–408, 2002.

[185] P. G. Vekilov and A. A. Chernov. The physics of protein crystallization. *Solid State Physics - Advances in Research and Applications*, 57:1–147, 2002.

[186] P. G. Vekilov and F. Rosenberger. Dependence of lysozyme growth kinetics on step sources and impurities. *J. Cryst. Growth*, 158:540–551, 1996.

[187] N. Wagner, K. Gnadig, H. Kreye, and H. Kronewetter. Particle velocity in hypersonic flame spraying of WC-Co. *Surface Technology*, 22:61–71, 1984.

[188] G-X Wang, V. Prasad, and S. Sampath. Rapid solidification in thermal spray deposition: Microstructure and modelling. *Sadhana-Academy Proceedings in Engineering Sciences*, 26:35–57, 2001.

[189] K. B. Ward, W. M. Zuk, M. A. Perozzo, M. A. Walker, G. I. Birnbaum, W. Kung, A. Cavaliere, D. R. Uffen, and H. Scholaert. Dynamic telerobotic control of crystallization experiments. *J. Cryst. Growth*, 122:235–241, 1992.

[190] K. Wegner and S. E. Pratsinis. Nozzle-quenching process for controlled flame synthesis of titania nanoparticles. *AIChE J.*, 49:1667–1675, 2003.

[191] J. S. Wey and P. H. Karpinski. Batch crystallization. In Allan S. Myerson, editor, *Handbook of Industrial Crystallization. Second Edition*, pages 231–248. Butterworth-Heinemann, 2001.

[192] J. M. Wiencek. New strategies for protein crystal growth. *Annual Review of Biomedical Engineering*, 1:505–534, 1999.

[193] T. D. Xiao, M. Benaissa, R. Perez, P. R. Strutt, and M. J. Yacaman. Microstructural characteristics of chemically processed manganese oxide nanofibres. *Acta Materialia*, 45:1685–1693, 1997.

[194] T. D. Xiao, P. R. Strutt, M. Benaissa, H. Chen, and B. H. Kear. Synthesis of high active-site density nanofibrous MnO_2-base materials with enhanced permeabilities. *Nanostructured Materials*, 10:1051–1061, 1998.

[195] W. Xie, S. Rohani, and A. Phoenix. Dynamic modeling and operation of a seeded batch cooling crystallizer. *Chem. Eng. Comm.*, 187:229–249, 2001.

[196] Q. Xu, V. V. Gupta, and E. J. Lavernia. On the mechanism of mushy layer formation during droplet-based processing. *Metall. Mater. Trans. B*, 30:527–539, 1999.

[197] Y. W. Xun, E. J. Lavernia, and F. A. Mohamed. Synthesis of nanocrystalline Zn-22 pct Al using cryomilling. *Metall. Mater. Trans. A*, 35:573–581, 2004.

[198] X. Yang and S. Eidelman. Numerical analysis of a high-velocity oxygen-fuel thermal spray system. *J. Therm. Spray Techn.*, 5:175–184, 1996.

[199] A. V. Zagorski and F. Stadelmaier. Full-scale modelling of a thermal spray process. *Surf. Coat. Tech.*, 146-147:162–167, 2001.

[200] D. Zhang, S. J. Harris, and D. G. McCartney. Microstructure formation and corrosion behaviour in HVOF-sprayed Inconel 625 coatings. *Mat. Sci. Eng. A*, 344:45–56, 2003.

[201] G. P. Zhang and S. Rohani. On-line optimal control of a seeded batch cooling crystallizer. *Chem. Eng. Sci.*, 58:1887–1896, 2003.